



# **Nanocomposite materials for membrane separation processes**

Inaugural-Dissertation

zur Erlangung des Doktorgrades  
der Mathematisch-Naturwissenschaftlichen Fakultät  
der Heinrich-Heine-Universität Düsseldorf

vorgelegt von

**Daniel Sieffert**

aus Düsseldorf

Düsseldorf, Mai 2013

aus dem Institut für Organische und Makromolekulare Chemie  
der Heinrich-Heine Universität Düsseldorf

Gedruckt mit der Genehmigung der  
Mathematisch-Naturwissenschaftlichen Fakultät der  
Heinrich-Heine-Universität Düsseldorf

Referent: Prof. Dr. Claudia Staudt  
Korreferent: Prof. Dr. Joaquín Coronas  
Korreferent: Prof. Dr. Rainer Weinkauff

Tag der mündlichen Prüfung: 10. Juli 2013

# Danksagung

Vielen Menschen möchte ich an dieser Stelle ganz herzlich für ihr Zutun im Rahmen meiner Promotion danken.

Frau Prof. Dr. Claudia Staudt gilt besonderer Dank für die herzliche Aufnahme in ihren Arbeitskreis, die interessante Aufgabenstellung, die Betreuung dieser Arbeit und die organisatorische Unterstützung meiner binationalen Promotion.

Prof. Joaquín Coronas und Prof. Carlos Téllez danke ich für die gute Betreuung während meiner Aufenthalte an der Universität Zaragoza und die herzliche Aufnahme in Ihre Arbeitsgruppe. Prof. Coronas möchte ich außerdem für die Übernahme eines Koreferats und die Unterstützung meiner binationalen Promotion danken.

Ebenso danke ich Prof. Weinkauf für die Übernahme des Koreferats.

Für die gute Arbeitsatmosphäre und Zusammenarbeit sowohl in Düsseldorf als auch in Zaragoza bin ich vielen Menschen sehr dankbar, mit denen ich in den vergangenen Jahren zusammen arbeiten durfte. Stellvertretend für alle Kollegen und Mitarbeiter möchte ich an dieser Stelle ausdrücklich danken: Sonja, Alex, Patrick, Ines, Jan und Nadine, sowie Beba, Cesar, Clara, Marian, Patricia und besonders Alejandro.

Bei Roman und David bedanke ich mich für das Lesen und Korrigieren dieser Arbeit.

Dem Deutschen Akademischen Austauschdienst (DAAD) danke ich vielmals für die finanzielle Unterstützung meiner Forschungsaufenthalte an der Universität Zaragoza.

Meinen Eltern bin ich sehr dankbar für Ihre Unterstützung während des gesamten Studiums. Zu guter Letzt danke ich Charlotte ganz besonders für ihre Geduld und ihr Verständnis, die ich insbesondere während meiner Zeit in Spanien in Anspruch genommen habe.

Für meine Familie

# Content

1	Summaries.....	1
1.1	Summary .....	1
1.2	Zusammenfassung.....	4
1.3	Resumen.....	7
2	Motivation.....	9
2.1	Introduction to membrane-based separation processes.....	9
2.2	Pervaporation – state of the art.....	11
2.3	Gas separation – state of the art.....	14
2.4	Aim of the work.....	18
3	Theoretical background.....	21
3.1	Membrane separation processes.....	21
3.1.1	The solution-diffusion model .....	22
3.1.2	Separation characteristics of membranes.....	25
3.1.3	Plasticization and cross-linking of membrane polymers.....	27
3.2	Membrane materials.....	28
3.2.1	Polyimide.....	28
3.2.1.1	General properties of polyimides.....	28
3.2.1.2	Synthesis of polyimides.....	29
3.2.1.3	Copolyimide used for membrane preparation.....	30
3.2.2	Carbon nanotubes .....	30
3.2.2.1	General properties of CNTs.....	31
3.2.2.2	Major synthesis methods of CNTs.....	32
3.2.2.3	Functionalization methods for CNTs .....	33
3.2.3	Titanosilicate JDF-L1 .....	35
3.2.4	Nanocomposites.....	37
3.2.4.1	Hybrid materials .....	39
3.2.5	Mixed matrix membranes .....	40
4	Experimental section.....	41
4.1	Copolyimide synthesis.....	41
4.2	Functionalization of carbon nanotubes .....	42
4.2.1	Preparation of MWCNT-COOH.....	42

## Content

---

4.2.2	Preparation of MWCNT-OH.....	42
4.3	Preparation and modification of titanosilicate JDF-L1 .....	43
4.3.1	JDF-L1 synthesis.....	43
4.3.2	Disaggregation of JDF-L1 .....	43
4.3.3	Exchange of interlamellar cations .....	43
4.3.4	Simultaneous disaggregation and cation exchange .....	44
4.4	Membrane fabrication .....	44
4.4.1	Preparation of copolyimide membranes.....	45
4.4.2	Preparation of mixed matrix membranes .....	45
4.4.3	Preparation of MWCNT/copolyimide membranes .....	45
4.5	Characterization methods .....	46
4.5.1	Characterization of basic materials .....	46
4.5.1.1	<sup>1</sup> H-NMR spectroscopy .....	46
4.5.1.2	Gel permeation chromatography (GPC).....	48
4.5.1.3	Differential scanning calorimetry (DSC) .....	48
4.5.1.4	Infrared spectroscopy.....	49
4.5.1.5	Thermogravimetric analysis .....	49
4.5.1.6	Electron microscopy .....	50
4.5.1.7	X-Ray diffraction .....	50
4.5.1.8	Elementary analysis.....	50
4.5.1.9	Adsorptive surface analyses .....	50
4.5.2	Membrane characterization.....	51
4.5.2.1	Film formation tests .....	51
4.5.2.2	Stress-strain experiments.....	51
4.5.2.3	Thermogravimetric analysis .....	51
4.5.2.4	Electron microscopy .....	52
4.5.2.5	Raman spectroscopy .....	52
4.6	Pervaporation experiments.....	54
4.6.1	Equipment setup .....	54
4.6.2	Measurement procedure .....	55
4.6.3	Calculation of separation characteristics .....	57
4.7	Gas separation experiments.....	58
4.7.1	Equipment setup .....	58
4.7.2	Measurement procedure .....	59
4.7.3	Calculation of separation characteristics .....	60
5	Results and discussion.....	61
5.1	Basic material characterization .....	61
5.1.1	Copolyimide batches .....	61

---

5.1.2	Functionalized MWCNTs .....	64
5.1.2.1	Dispersion stability of MWCNTs.....	64
5.1.2.2	Surface analysis of MWCNTs.....	66
5.1.2.3	Infrared spectroscopy of MWCNTs .....	66
5.1.2.4	Thermogravimetric analysis of MWCNTs.....	67
5.1.2.5	Elementary analyses of MWCNTs .....	68
5.1.2.6	Electron microscopy of MWCNTs.....	69
5.1.3	Titanosilicate materials .....	70
5.1.3.1	Characterization of disaggregated JDF-L1.....	70
5.1.3.2	Characterization of cation exchanged JDF-L1 .....	71
5.1.3.3	Characterization of one-step disaggregated and ion exchanged JDF-L1 .....	77
5.2	MWCNT/polyimide nanocomposites for pervaporation .....	78
5.2.1	Development of MWCNT/copolyimide membrane preparation.....	78
5.2.2	Pervaporation with MWCNT/copolyimide membranes.....	83
5.2.2.1	Concentration-dependent measurements.....	83
5.2.2.2	Temperature-dependent measurements .....	85
5.2.2.3	Determination of activation energies for the permeation.....	86
5.2.2.4	Summary of pervaporation results.....	88
5.3	Gas separation with titanosilicate/copolyimide MMM .....	90
5.3.1	Development of titanosilicate/copolyimide MMM membranes .....	90
5.3.1.1	Thermogravimetric analyses of titanosilicate containing MMMs.....	90
5.3.1.2	Scanning electron microscopy of titanosilicate containing MMMs.....	91
5.3.1.3	Polarized light microscopy of titanosilicate containing MMMs.....	93
5.3.1.4	X-ray diffraction of titanosilicate containing MMMs .....	94
5.3.1.5	Raman spectroscopy of titanosilicate containing MMMs.....	96
5.3.1.6	Results of stress-strain experiments with MMMs .....	98
5.3.2	Gas separation with JDF-L1/copolyimide MMMs .....	98
5.3.2.1	Influence of filler orientation .....	99
5.3.2.2	Influence of disaggregation.....	101
5.3.2.3	Influence of cross-linking.....	102
5.3.2.4	Influence of interlamellar cation.....	103
5.3.2.5	Summary of gas separation results .....	106
6	Appendix.....	109
6.1	Copolyimide synthesis.....	109
6.2	Exchange of interlamellar cations in disaggregated JDF-L1 .....	117
6.2.1	Preparation of (H)-JDF-L1.....	117
6.2.2	Preparation of (Li)-JDF-L1 4h.....	117
6.2.3	Preparation of (Li)-JDF-L1 24h.....	118
6.2.4	Preparation of (K)-JDF-L1 .....	118
6.2.5	Preparation of (Mg)-JDF-L1 1.1 .....	119

## ***Content***

---

6.2.6	Preparation of (Mg)-JDF-L1 1.2 .....	119
6.2.7	Preparation of (Mg)-JDF-L1 1.3 .....	120
6.2.8	Preparation of (Ca)-JDF-L1 .....	120
6.3	Calibration data for gas separation experiments.....	121
6.3.1	Calibration data oxygen/nitrogen .....	121
6.3.2	Calibration data hydrogen/methane.....	122
7	Bibliography.....	125
8	List of figures and tables .....	133
8.1	List of figures .....	133
8.2	List of tables .....	138

# 1 Summaries

## 1.1 Summary

Membrane based separation processes represent a growing technique with many industrial applications that are even unrivaled in some cases. To further maintain a growth it is necessary to adapt the technique to new fields of application or increase the efficiency for existing separation tasks. The availability of suitable membrane materials often represents the bottleneck in this regard. For polymeric materials the fabrication of nanocomposites represents a promising approach towards a new generation of membranes. By incorporating a nanoscale component into a polymer matrix it is possible to drastically improve material properties or even introduce new characteristics. This strong improvement is usually due to the extremely high surface area to volume ratios and extreme aspect ratios of the incorporated nanometer sized components and is thus often referred to as a “nano-effect”. Most importantly many characteristics of polymers affecting their eligibility as membrane materials can be modified, such as glass transition temperature, material aging and free volume. The aim of this work now was to prepare novel nanocomposite materials based on the copolyimide 6FDA-4MPD/6FDA-DABA 4:1. This polymer exhibits outstanding separation characteristics for a broad range of applications and allows further chemical modification. Moreover it is well processable which facilitates the fabrication of nanocomposite materials. On the one hand functionalized multi walled carbon nanotubes (MWCNTs) were added with the aim of preparing swelling resistant pervaporation membranes with enhanced permeability for the separation of aromatic mixtures. On the other hand titanosilicate nanosheets were incorporated in order to obtain gas separation membranes with increased selectivity based on size exclusion.

In order to assess the potential of nanocomposites comprising 6FDA-4MPD/6FDA-DABA 4:1 and multi walled carbon nanotubes (MWCNTs) pervaporation experiments were performed with toluene/cyclohexane mixtures. In this case toluene is used as a less hazardous substitute for benzene which actually occurs in industrial mixtures. Conventionally this separation is a very challenging task in chemical industry due to the close boiling points of the two components. In such cases membranes offer a big advantage as the separation is not based on phase transitions but rather depends on solubility and diffusivity. Admittedly high aromatic concentrations can induce swelling of the membrane material which leads to increased permeabilities but drastically lowers the selectivity. This requires stronger interaction of the membrane material on the molecular level to enhance its cohesion. Usually cross-linking is used here which however often leads to compaction of the membrane material which then again decreases permeability but increases selectivity. Copolyimide/functionalized MWCNT nanocomposites represent an approach to surpass this tradeoff.

The capabilities of nanocomposites containing 6FDA-4MPD/6FDA-DABA 4:1 and JDF-L1 nanosheets were evaluated via gas separation with hydrogen/methane, a separation task that is of growing industrial interest. In particular hydrogen recovery becomes a more and more important technique as the hydrogen demand is rising due to increasing environmental regulations. In this field membrane processes still exhibit growth potential provided that the separation characteristics can be improved further. On this background it was intended to increase the selectivity of

## 1.1 Summary

---

6FDA-4MPD/6FDA-DABA 4:1 by adding JDF-L1 nanosheets and thus incorporating the size exclusion effect of the titanosilicate. It was attempted to obtain a horizontal orientation of the sheets in order to further enhance this effect. Experiments with oxygen/nitrogen were also conducted as a control mixture in which both feed components cannot permeate through the filler. In additional experiments the interlamellar sodium cations in JDF-L1 were exchanged so as to facilitate the permeation of hydrogen through the membrane. The central cation position in front of the pores across the layers was assumed to have influence on the permeation of gases through the filler. Commonly membranes composed of inorganic fillers dispersed within usually organic matrices are also referred to as mixed matrix membranes (MMMs), so as well in this work.

The first step towards MWCNT/copolyimide nanocomposites was the preparation of functionalized MWCNT samples via a two step reaction. First commercial MWCNTs (Baytubes C 150 P) were oxidized in concentrated nitric acid for 24 hours to introduce carboxylic acid groups on defect sites of the nanotubes. These samples of MWCNT-COOH were subsequently subjected to a reduction treatment with lithium aluminum hydride in order to convert the carboxylic acid groups into hydroxyl groups and obtain MWCNT-OH. The introduction of functional groups was best visualized by elemental analysis. The commercial tubes exhibit an oxygen content of only 0.38 at.-% which is increased to 9.9 and 11.0 at.-% respectively in oxidized samples. The reductive treatment then again lowers the oxygen content by 3 at.-%. For MWCNT-OH oxygen contents of 7.8 and 6.7 at.-% were found. Neither in scanning nor in transmission electron microscopy (SEM, TEM), any alterations of the physical properties of the MWCNTs were observed. From this it can be assumed that the functionalization treatment does not alter the structure of the nanotubes.

A successful method to prepare MWCNT-OH/copolyimide nanocomposite membranes was developed using tetrahydrofuran as the solvent and moderate ultrasound treatment. In thermogravimetric analyses (TGA) of the nanocomposite membranes it was found that the incorporation of MWCNT-OH drastically increases the thermal stability of the material in nitrogen atmosphere. While the pure polymer completely decomposes between 500 and 600 °C residues of around 50 % are left at 800 °C in case of the nanocomposites containing 1 and 3.5 wt.-% MWCNT-OH.

Concentration dependent pervaporation experiments pointed out that the incorporation of 1 wt.-% MWCNT-OH notably enhances the separation characteristics of the polymer. In 50:50 wt.-% mixtures of toluene/cyclohexane the toluene flux is increased from 8.8 and 10.5  $\text{kg}\cdot\mu\text{m}\cdot\text{m}^{-2}\cdot\text{h}^{-1}$  for the copolyimide to values of 17.3 and 16.5  $\text{kg}\cdot\mu\text{m}\cdot\text{m}^{-2}\cdot\text{h}^{-1}$  for nanocomposite membranes while the permeate composition remains unaltered. By incorporating more than the threefold amount of nanotubes this trend could not be extended much further. A nanocomposite membrane containing 3.5 wt.-% MWCNT-OH exhibits an only slightly higher flux of 19.3  $\text{kg}\cdot\mu\text{m}\cdot\text{m}^{-2}\cdot\text{h}^{-1}$ . Moreover the pervaporation results show that the incorporation of MWCNTs enhances swelling resistance. At high aromatic concentrations swelling occurs which increases the toluene flux. This effect is much lower for the nanocomposites than for the pure copolyimide, indicating a certain degree of cross-linking. The activation energies for the permeation of the feed components were determined in temperature dependent pervaporation experiments. It was found that the addition of MWCNT leads to noticeably reduced values. The activation energies declined from 34.5  $\text{kJ}\cdot\text{mol}^{-1}$  to 27.9 and 29.3  $\text{kJ}\cdot\text{mol}^{-1}$  for toluene and from 43.3  $\text{kJ}\cdot\text{mol}^{-1}$  to 36.2 respectively 34.0  $\text{kJ}\cdot\text{mol}^{-1}$  for cyclohexane.

Nanosheets of JDF-L1 were obtained by disaggregating the as-synthesized titanasilicate through a treatment with cetyltrimethylammonium bromide and tetrapropylammonium hydroxide. Hereby the material was not swollen and the crystal structure was not affected as seen in X-ray diffraction (XRD). SEM showed little fragmentation of the sheet crystals and slight damage to their borders. Ion exchanged JDF-L1 samples containing  $H^+$ ,  $Li^+$ ,  $K^+$ ,  $Mg^{2+}$  and  $Ca^{2+}$  were obtained by exposing the disaggregated titanasilicate to an excess of the desired cation in aqueous solution. XRD spectra show that exchanging sodium with protons leads to drastic structural changes including a decreased layer distance in the titanasilicate. Very similar structural changes were observed in parts of the sample in which large amounts of sodium have been exchanged with lithium. It is possible to influence the sodium exchange rate in the final material by varying the excess of the cation or the duration of the reaction. Based on the finding that a disaggregation of JDF-L1 can also be achieved with an aqueous solution of sodium hydroxide simultaneous ion exchange and disaggregation processes using lithium and potassium hydroxide were also successfully conducted.

MMMs containing 5, 8 and 10 wt.-% of disaggregated JDF-L1 were cast from 10 and 13 wt.-% polymer solutions. In TGA slightly higher actual loads of 7.0, 8.7 and 13.0 wt.-% were found. Multiple analysis methods consistently showed that MMMs cast from 10 wt.-% polymer solutions exhibit a preferential horizontal filler orientation while in MMMs cast from 13.-% polymer solutions the sheet crystals are more randomly oriented. This could be especially well observed in SEM images of the membrane cross section, but also in light microscopic images. The incorporation of individual JDF-L1 sheet crystals was observed in XRD. The spectra of MMMs showed peaks related to the layered structure of the filler ([001], [002] and [003] indexations). Moreover angle dependent XRD and polarized Raman spectroscopy indicate a higher degree of horizontal filler orientation for membranes cast from 10 wt.-% polymer solutions. In stress-strain experiments it was pointed out that the incorporation of disaggregated JDF-L1 increases the Young's modulus from 2100 - 2200 MPa to values between 2500 and 3000 MPa. From this finding a very good phase interaction was deduced.

Gas permeation experiments were performed with MMMs cast from 10 and 13 wt.-% polymer solutions containing 5, 8 and 10 wt.-% disaggregated JDF-L1 using  $H_2/CH_4$  and  $O_2/N_2$  mixtures. For all gases a strong decrease of permeabilities was found with increasing filler loads. The reduction was noticeably stronger for methane than for hydrogen which drastically increased the selectivity. The  $H_2$  permeability was reduced from 360 Barrer for the pure polymer to 189 Barrer for a MMM containing 5 wt.-% JDF-L1 cast from a 10 wt.-% polymer solution. At the same time the selectivity increased notably from 21.3 to 30.2. In the case of MMMs cast from a 13 wt.-% polymer solution the decrease of methane permeability was not as strong. For  $O_2/N_2$  mixtures the selectivity remained unaltered but the permeabilities decreased drastically with higher loads of JDF-L1. This trend is slightly higher in case of the oriented MMMs cast from 10 wt.-% polymer solution. When using as-synthesized JDF-L1 as filler no gain of  $H_2/CH_4$  selectivity was found. Then again cross-linking of MMMs containing disaggregated JDF-L1 is also not recommended as it strongly increases the inhomogeneity of the membrane material and leads to heavily diverging results. Finally, it was shown that separation characteristics for  $H_2/CH_4$  cannot be enhanced further using ion exchange in JDF-L1. For  $O_2/N_2$  mixtures however results close to and in some cases even above the upper bound of 1991 were obtained. In this case slightly higher selectivities but somewhat lower permeabilities than the pure polymer were found. For example an  $O_2$  permeability of 76.8 Barrer and an  $O_2/N_2$  selectivity of 4.5 were determined for a MMM containing (Ca)-JDF-L1. In both investigated mixtures the ion exchanged filler materials with bivalent cations and such that were protonated exhibit higher permeabilities than the other materials containing a monovalent cation (Li, K, Na). Taking into

## 1.2 Zusammenfassung

---

account the extremely small size of  $H^+$  and the fact that bivalent cations replace two interlamellar sodium cations this indicates that the interlamellar cation in fact noticeably influences the permeation of gases through the filler.

## 1.2 Zusammenfassung

Die Auftrennung von Mischungen mittels Membranen ist eine wachsende Technologie, die industriell vielfach Anwendung findet und in manchen Bereichen sogar konkurrenzlos ist. Um das Wachstum beizubehalten muss die Effizienz vorhandener Membranmaterialien stetig verbessert und die Technologie an neue Aufgaben angepasst werden, indem neue geeignete Membranen entwickelt werden. Gerade bei polymeren Materialien ist die Herstellung von Nanocompositen ein vielversprechender Ansatz auf dem Weg zu einer neuen Generation von Membranen. Durch das Einbringen nanoskalierter Komponenten in die Polymermatrix können Materialcharakteristika entscheidend verbessert und sogar neue Eigenschaften eingeführt werden. Dies beruht oftmals auf den sehr großen Oberfläche-zu-Volumen Verhältnissen bzw. Seitenverhältnissen der Nanopartikel und wird daher als „Nano-Effekt“ bezeichnet. Gerade die für den Einsatz als Membranen wichtigen Polymereigenschaften wie Glasübergangstemperatur, Alterungsverhalten und freies Volumen können auf diese Weise merklich verbessert werden. Das Ziel dieser Arbeit war es, neuartige Nanocomposite basierend auf dem Copolyimid 6FDA-4MPD/6FDA-DABA 4:1 herzustellen. Dieses Polymer weist für verschiedene Mischungen bereits herausragende Trenneigenschaften auf und kann leicht chemisch modifiziert werden. Außerdem zeichnet es sich durch gute Verarbeitbarkeit aus, was die Herstellung von Nanocompositen erleichtert. Zum einen wurden funktionalisierte mehrwandige Kohlenstoffnanoröhren (MWCNTs) zugegeben, mit dem Ziel quellungsresistente Membranen mit erhöhtem Fluss für die Pervaporation von aromatischen Mischungen herzustellen. Zum anderen wurden Titanosilikat Nanoplättchen zum Polymer gegeben, um mittels Größenausschluss die Selektivität der Membranen für die Gastrennung zu erhöhen.

Um das Potenzial der Nanocompositmembranen aus 6FDA-4MPD/6FDA-DABA 4:1 und funktionalisierten MWCNTs beurteilen zu können, wurden Pervaporationsexperimente mit Toluol/Cyclohexan Mischungen durchgeführt. Aufgrund seiner geringeren Gesundheitsgefährdung aber vergleichbaren Trenneigenschaften wird hierbei Toluol an Stelle von Benzol verwendet, das eigentlich in industriellen Mischungen vorliegt. Aus Sicht konventioneller Trenntechniken ist diese eng-siedende Mischung schwierig zu separieren. Gerade in diesem Fall sind Membranen von Vorteil, da hier die Auftrennung nicht auf einer Phasenumwandlung sondern auf der Löslichkeit und Diffusivität der Komponenten beruht. Hohe Aromatenkonzentrationen können jedoch zum Aufquellen der Membran führen, wodurch der Fluss ansteigt aber die Selektivität drastisch absinkt. In diesem Fall muss der molekulare Zusammenhalt verbessert werden, was meist mittels Vernetzung erreicht wird. Durch die erhöhte Kohäsion wird das Membranmaterial allerdings oftmals auch verdichtet und die Permeabilität sinkt während die Selektivität ansteigt. Nanocomposite aus Copolyimid und funktionalisierten MWCNTs sind ein Ansatz um diesen Kompromiss zu umgehen.

Die Eigenschaften von Nanocompositen aus 6FDA-4MPD/6FDA-DABA 4:1 und JDF-L1 Nanoplättchen wurden mittels Gastrennung von Wasserstoff/Methan-Mischungen untersucht. Dieses Trennproblem

gewinnt stetig an industrieller Relevanz, da das Interesse an Wasserstoffrückgewinnung insbesondere aufgrund einer zunehmenden Anzahl umweltpolitischer Regulierungen immer weiter zunimmt. Deshalb ist hier das Wachstumspotenzial für Membrantrennprozesse besonders hoch, sofern die Trenneigenschaften weiter verbessert werden können. Vor diesem Hintergrund wurde in dieser Arbeit versucht die Selektivität von 6FDA-4MPD/6FDA-DABA 4:1 zu erhöhen indem JDF-L1 Nanoplättchen zugegeben werden, die einen intrinsischen Größenausschlusseffekt aufweisen. Um diesen Effekt zu verstärken war es außerdem das Ziel eine vorwiegend horizontale Ausrichtung des Füllmaterials zu erreichen. Als Kontrollmischung für Gastrennexperimente wurde Sauerstoff/Stickstoff verwendet, da hier beide Feedkomponenten zu groß sind, um durch JDF-L1 zu permeieren. In weitergehenden Experimenten wurden die interlamellaren Natriumkationen in JDF-L1 ausgetauscht. Dies sollte die Permeation von Wasserstoff durch die Membran erleichtern, da die zentrale Position des interlamellaren Kations vor den Poren durch die Schichten vermutlich Einfluss auf die Permeation des Gases durch das Füllmaterial hat. Im Allgemeinen werden Membranen in denen ein anorganisches Füllmaterial in einer organischen Matrix dispergiert vorliegt „Mixed Matrix Membran“ (MMM) genannt, so auch in dieser Arbeit.

Für die Herstellung von MWCNT/Copolyimid-Nanocompositen wurden zunächst funktionalisierte MWCNTs mittels einer Zweistufigen Reaktion hergestellt. Im ersten Schritt wurden kommerzielle Kohlenstoffnanoröhrchen (Baytubes C 150 P) für 24 Stunden in konzentrierter Salpetersäure oxidiert um an Defektstellen der Röhren Carboxylgruppen einzuführen. Anschließend wurden diese im zweiten Schritt mittels Reduktion mit Lithiumaluminiumhydrid in Hydroxylgruppen überführt. Den Verlauf der Funktionalisierung bis hin zu MWCNT-OH konnte am besten mittels Elementaranalyse beobachtet werden. Während die kommerziellen Nanotubes nur einen Sauerstoffgehalt von 0,38 at.-% aufweisen steigt dieser nach der Oxidation auf 9,9 bzw. 11,0 At.-% an. Durch die nachfolgende Reduktion sinkt der Gehalt dann wieder um 3 At.-% auf 7,8 bzw. 6,7 At.-% ab. Raster- und Transmissionselektronenmikroskopie zeigten keine Veränderungen der physikalischen Eigenschaften der MWCNTs. Daher kann angenommen werden, dass die Funktionalisierung die Struktur der Nanoröhrchen nicht beeinflusst.

Zur Herstellung von Nanocompositen aus dem Copolyimid und MWCNT-OH wurde eine Methode mit Tetrahydrofuran als Lösemittel und moderater Ultraschallbehandlung entwickelt. Thermogravimetrische Untersuchungen zeigten, dass durch Zugabe von MWCNT-OH die thermische Stabilität unter Stickstoffatmosphäre stark zunimmt. Das reine Polymer wird zwischen 500 und 600 °C komplett zersetzt, während von Nanocompositen mit 1 bzw. 3,5 Gew.-% MWCNT-OH bei 800 °C noch etwa 50 % des Startgewichts vorliegen.

In konzentrationsabhängigen Pervaporationsexperimenten konnte gezeigt werden, dass die Trenneigenschaften des Polymers durch Zugabe von 1 Gew.-% MWCNT-OH deutlich verbessert werden. In 50:50 Gew.-% Mischungen von Toluol und Cyclohexan stieg der Fluss von 8,8 bzw. 10,5  $\text{kg}\cdot\mu\text{m}\cdot\text{m}^{-2}\cdot\text{h}^{-1}$  beim Copolyimid auf 17,3 bzw. 16,5  $\text{kg}\cdot\mu\text{m}\cdot\text{m}^{-2}\cdot\text{h}^{-1}$  bei Nanocompositmembranen. Die Permeatzusammensetzung blieb dabei nahezu gleich. Dieser Trend konnte durch Zugabe der über dreifachen Menge Nanotubes nur geringfügig gesteigert werden. Eine Membran mit 3,5 Gew.-% MWCNT-OH zeigte einen nur leicht höheren Fluss von 19,3  $\text{kg}\cdot\mu\text{m}\cdot\text{m}^{-2}\cdot\text{h}^{-1}$ . Aus den Pervaporationsexperimenten konnte überdies geschlossen werden, dass die Quellungsresistenz der Membran durch MWCNT-Zugabe verstärkt wird. Bei hohen Aromatenkonzentrationen quillt die

## 1.2 Zusammenfassung

---

Membran und der Toluol-Fluss steigt. Dieser Effekt ist bei den Nanocompositmembranen deutlich geringer ausgeprägt als bei den reinen Copolyimidmembranen. Hieraus kann auf einen gewissen Grad an Vernetzung geschlossen werden. Die Aktivierungsenergien für die Permeation der Feedkomponenten wurden in temperaturabhängigen Pervaporationsexperimenten ermittelt. Durch Zugabe von MWCNT-OH sinken die Werte deutlich ab. Für Toluol fällt die Aktivierungsenergie von  $34,5 \text{ kJ}\cdot\text{mol}^{-1}$  auf  $27,9$  bzw.  $29,3 \text{ kJ}\cdot\text{mol}^{-1}$  während sie bei Cyclohexan von  $43,3 \text{ kJ}\cdot\text{mol}^{-1}$  auf  $36,2$  bzw.  $34,0 \text{ kJ}\cdot\text{mol}^{-1}$  absinkt.

Die JDF-L1 Nanoplättchen wurden mittels Disaggregation aus dem synthetisierten Titanosilikat gewonnen. Hierfür wurde eine wässrige Lösung aus Cetyltrimethylammoniumbromid und Tetrapropylammoniumhydroxid verwendet. Röntgenbeugung zeigte, dass bei dieser Behandlung das Material weder gequollen noch dessen Kristallstruktur verändert wurde. Allerdings zeigten rasterelektronenmikroskopische Aufnahmen eine leichte Fragmentierung der Plättchen sowie geringe Beschädigung der Kanten. Ionenausgetauschtes JDF-L1 wurde hergestellt, indem das Titanosilikat einer wässrigen Lösung mit einem Überschuss an  $\text{H}^+$ ,  $\text{Li}^+$ ,  $\text{K}^+$ ,  $\text{Mg}^{2+}$  und  $\text{Ca}^{2+}$  ausgesetzt wurde. Im Röntgendiffraktogramm von (H)-JDF-L1 zeigt sich, dass der Austausch von  $\text{Na}^+$  mit  $\text{H}^+$  zu drastischen Strukturveränderungen führt. Unter anderem sinkt der interlamellare Abstand deutlich. Sehr ähnliche Veränderungen wurden auch in einer Probe gefunden, in der  $\text{Na}^+$  zu großen Teilen mit  $\text{Li}^+$  ausgetauscht wurde. Durch Variation des Überschusses und der Rührdauer kann die Austauschrate für  $\text{Na}^+$  gesteuert werden. Basierend auf der Erkenntnis, dass JDF-L1 auch mit Natronlauge disaggregiert werden kann, wurde eine Methode auf Basis von Lithium- bzw. Kaliumhydroxid entwickelt mit der Ionenaustausch und Disaggregation gleichzeitig erfolgen können.

MMMs mit 5, 8 und 10 Gew.-% disaggregiertem JDF-L1 wurden aus Polymerlösungen von 10 und 13 Gew.-% hergestellt. In TGA wurden etwas höhere tatsächliche Anteile des Füllmaterials von 7,0, 8,7 und 13,0 Gew.-% gefunden. Verschiedene Analyseverfahren zeigen übereinstimmend, dass die Nanoplättchen in MMMs die aus 10 Gew.-% Polymerlösungen hergestellt wurden bevorzugt horizontal ausgerichtet sind. In MMMs aus 13 Gew.-% Polymerlösungen hingegen ist eine eher zufällige Ausrichtung des Füllmaterials zu finden. Dies ist besonders gut in Aufnahmen von REM und Lichtmikroskop zu sehen. Mittels Röntgenbeugung konnte gezeigt werden, dass die Polymermatrix einzelne JDF-L1 Plättchen enthält. In den Spektren der MMMs wurden Signale gefunden, die direkt der Schichtstruktur entsprechen (Indexierung [001], [002] und [003]). Darüber hinaus wurden winkelabhängige Röntgendiffraktogramme und Raman Spektren mit polarisiertem Licht aufgenommen die ebenfalls eine stärkere horizontale Ausrichtung des Füllmaterials in Membranen aus einer 10 Gew.-% Polymerlösung zeigen. In Zug-Dehnungs-Experimenten wurde gefunden, dass das E-Modul durch Zugabe von disaggregiertem JDF-L1 von 2100 – 2200 MPa (Copolyimid) auf Werte zwischen 2500 und 3000 MPa ansteigt. Hieraus kann auf eine sehr gute Wechselwirkung zwischen organischer und anorganischer Phase geschlossen werden.

Mit den MMMs aus 10 bzw. 13 Gew.-% Polymerlösung wurden Gastrennexperimente mit  $\text{H}_2/\text{CH}_4$  und  $\text{O}_2/\text{N}_2$  Mischungen durchgeführt. Mit zunehmendem Gehalt an Füllmaterial sinkt für alle Gase die Permeabilität. Der Rückgang ist jedoch für Methan viel stärker als für Wasserstoff und folglich steigt die  $\text{H}_2/\text{CH}_4$ -Selektivität deutlich an. Die  $\text{H}_2$ -Permeabilität sinkt von 360 Barrer für das Copolyimid auf 189 Barrer für eine MMM mit 5 Gew.-% JDF-L1, die aus einer 10 Gew.-% Polymerlösung hergestellt wurde. Gleichzeitig steigt aber die Selektivität von 21,3 auf 30,2. Bei den MMMs die aus einer

13 Gew.-% Polymerlösung hergestellt wurden, war der Rückgang der CH<sub>4</sub>-Permeabilität allerdings nicht gleich stark. In O<sub>2</sub>/N<sub>2</sub>-Mischungen veränderte sich die Selektivität kaum, während die Permeabilitäten extrem abfielen. Dieser Effekt ist bei den MMM, in denen das Füllmaterial stärker horizontal ausgerichtet ist, deutlicher ausgeprägt. Mit nicht disaggregiertem JDF-L1 als Füllmaterial konnte die H<sub>2</sub>/CH<sub>4</sub>-Selektivität nicht gesteigert werden. Desweiteren ist das Vernetzen von MMMs nicht empfehlenswert, da dies die Inhomogenität in der Membran verstärkt und dadurch zu stark streuenden Ergebnissen führt. Die Trenneigenschaften der MMMs für H<sub>2</sub>/CH<sub>4</sub> konnten nicht mithilfe von Ionenaustausch in JDF-L1 verbessert werden. Für O<sub>2</sub>/N<sub>2</sub>-Mischungen konnten allerdings Ergebnisse nahe bzw sogar oberhalb der Robeson Upper Bound von 1991 erzielt werden. Zum Beispiel wurde für eine MMM mit 8 Gew.-% (Ca)-JDF-L1 eine O<sub>2</sub>-Permeabilität von 76,8 Barrer und eine O<sub>2</sub>/N<sub>2</sub>-Selektivität von 4,5 gefunden. Die höchsten Permeabilitäten fanden sich bei beiden Gasmischungen mit Füllmaterialien, die entweder portioniert worden waren oder in denen Natrium gegen zweiwertige Kationen ausgetauscht wurde. Aufgrund der sehr geringen Größe von H<sup>+</sup> und der Tatsache, dass zweiwertige Kationen zwei Natriumkationen ersetzen, kann darauf geschlossen werden, dass das interlamellare Kation tatsächlich die Permeation von Gasmolekülen durch das Füllmaterial beeinflusst.

### 1.3 Resumen

Los procesos de separación basados en membranas tienen muchas aplicaciones industriales y en los últimos años han despertado un interés creciente. Para incrementar su uso es importante mejorar y desarrollar nuevos materiales para las membranas. La fabricación de nanocomposites representa una prometedora aproximación a una nueva generación de membranas poliméricas. Mediante la incorporación de materiales nanométricos en la matriz polimérica es posible incrementar notablemente las características del polímero o incluso introducir características nuevas. Estas mejoras se deben normalmente a la elevada relación de aspecto de las nanopartículas (“efecto nano”). El objetivo de este trabajo fue preparar nuevos materiales nanocompuestos basados en la copoliimida 6FDA-4MPD/6FDA-DABA 4:1, un polímero con muy buenas propiedades para diferentes procesos de separación. Este polímero puede ser modificado químicamente y además se procesa fácilmente, facilitando la fabricación de nanocomposites. En el desarrollo de esta tesis se añadieron nanotubos de carbono “multi wall” (MWCNTs) funcionalizados con el objetivo de preparar membranas resistentes al proceso de plastificación con propiedades de separación mejoradas para mezclas de compuestos aromáticos. Además, se añadieron nanoláminas del titanosilicato JDF-L1 para obtener membranas para separación de gases que mostrasen selectividad mejorada debida a efecto tamiz.

El potencial de los nanocomposites de MWCNT/copoliimida se comprobó en los experimentos de pervaporación de mezclas tolueno/ciclohexano, un proceso de separación complicado según el estado de la tecnología. Se ha comprobado que altas concentración del compuesto orgánico provocan la plastificación de la membrana incrementando la permeabilidad pero disminuyendo drásticamente la selectividad. Esto requiere una fuerte interacción del material de la membrana a nivel molecular. Normalmente se utiliza “cross-linking” en estos casos, que produce una compactación del material de la membrana disminuyendo la permeabilidad e incrementando la selectividad. Los nanocomposites MWCNT/copoliimida son una posibilidad para evitar este compromiso. En este trabajo los nanotubos de carbono se funcionalizaron con éxito con grupos OH y se desarrollo un nuevo método para preparar membranas MWCNT-OH/copoliimida. Los

### 1.3 Resumen

---

experimentos de pervaporación mostraron que una incorporación de un 1% de MWCNT-OH incrementaba el flujo de los valores de copoliimida de 8,8 y 10,5  $\text{kg}\cdot\mu\text{m}\cdot\text{m}^{-2}\cdot\text{h}^{-1}$  a unos valores de 17,3 y 16,5  $\text{kg}\cdot\mu\text{m}\cdot\text{m}^{-2}\cdot\text{h}^{-1}$ , la selectividad permaneció constante. La adición de MWCNT reduce notablemente la energía de activación para la permeación de ambos componentes. El flujo no se pudo incrementar añadiendo un 3,5% de MWCNT-OH, sin embargo se encontró que la adición de MWCNT-OH mejora generalmente la resistencia del material a la plastificación a altas concentraciones del compuesto aromático.

Las propiedades de permeación de las membranas JDF-L1/copoliimida se evaluaron mediante la separación de la mezcla gaseosa  $\text{H}_2/\text{CH}_4$ . La separación de esta mezcla tiene una importancia creciente debido a la demanda de hidrógeno, además las tecnologías de recuperación de hidrógeno son cada vez más importantes por las normativas medioambientales. Los procesos basados en membranas tienen potencial de crecimiento ya que las propiedades de separación de las membranas pueden ser mejoradas. Sobre esta base el objetivo fue incrementar la selectividad de la copoliimida 6FDA-4MPD/6FDA-DABA 4:1 añadiendo nanoláminas de JDF-L1 e incorporando el efecto tamiz que muestra la carga. Se buscó incrementar este efecto consiguiendo una orientación horizontal de las láminas en la matriz polimérica. Se realizaron experimentos adicionales con JDF-L1 en la que se intercambiaron los cationes interlaminares  $\text{Na}^+$  por  $\text{H}^+$ ,  $\text{Li}^+$ ,  $\text{K}^+$ ,  $\text{Mg}^{2+}$  or  $\text{Ca}^{2+}$  para facilitar la permeación de hidrógeno a través de las láminas. Se comprobó que variando la concentración de polímero en la disolución inicial es posible modificar la orientación de las láminas dentro de la membrana. Mediante varias técnicas analíticas se comprobó que las membranas con carga 5, 8 y 10% de JDF-L1 preparadas a partir de una disolución 10% en peso de polímero tenían una orientación de las láminas de JDF-L1 mayor que las membranas preparadas a partir de una disolución 13% en peso de polímero. Se realizaron experimentos de permeación de la mezcla gaseosa  $\text{H}_2/\text{CH}_4$  para estas membranas. Para ambos gases se redujo la permeabilidad incrementándose la selectividad ya que la reducción de permeabilidad fue mucho mayor para el metano que para el hidrógeno. En el caso de membranas conteniendo 5% en peso de JDF-L1 y preparadas a partir de una disolución 10% en peso de polímero la permeabilidad de  $\text{H}_2$  se redujo de 360 Barrer para el polímero puro hasta 189 Barrer mientras que la selectividad se incrementó desde 21,3 hasta 30,2. En el caso de membranas con una peor orientación de las láminas de JDF-L1 (preparadas a partir de disoluciones 13% en peso de polímero) el descenso de la permeabilidad de  $\text{CH}_4$  no fue tan grande y por lo tanto el incremento de la selectividad no fue tan fuerte. Mediante el intercambio de los cationes interlaminares no fue posible mejorar más las propiedades de separación para  $\text{H}_2/\text{CH}_4$ . Los resultados para el JDF-L1 intercambiado muestran que se obtienen mayores permeabilidades con cationes bivalentes o  $\text{H}^+$  que con cationes monovalentes ( $\text{Li}^+$ ,  $\text{K}^+$ ,  $\text{Na}^+$ ). Teniendo en cuenta el pequeño tamaño del  $\text{H}^+$  y el hecho de que los cationes bivalentes reemplazan dos cationes interlaminares de sodio se desprende que el catión interlaminares probablemente tenga una influencia importante en la propiedades de permeación del material inorgánico.

## 2 Motivation

This chapter gives a short introduction to membrane-based separation processes. Then the investigated processes pervaporation and gas separation are classified and the respective state of the art is presented. On the background of this information this part concludes with the aim of this work.

### 2.1 Introduction to membrane-based separation processes

Membrane-based separation processes are important for many industrial applications. For certain tasks this technique is even unrivaled. Exemplarily the hemodialysis should be mentioned here. In other applications e.g. water purification membrane-based techniques have already grown to lead the way<sup>[1]</sup>. In chemical industry the membrane processes of gas separation and pervaporation are slowly replacing more and more conventional separation processes. The different development levels are also reflected in the life-cycle curve for membrane processes<sup>[2]</sup>. As shown in figure 2.1 reverse osmosis and hemodialysis have the longest lifetimes and are considered to be in the high sales phase. Processes in this phase are characterized by high production efficiency and rather low profits. In contrast to this the processes gas separation and pervaporation are still in the growth phase. This implies only moderate profits but high growth rates are possible, hence the name of this phase. However such growth presupposes the availability of sufficient application know-how<sup>[3]</sup>.

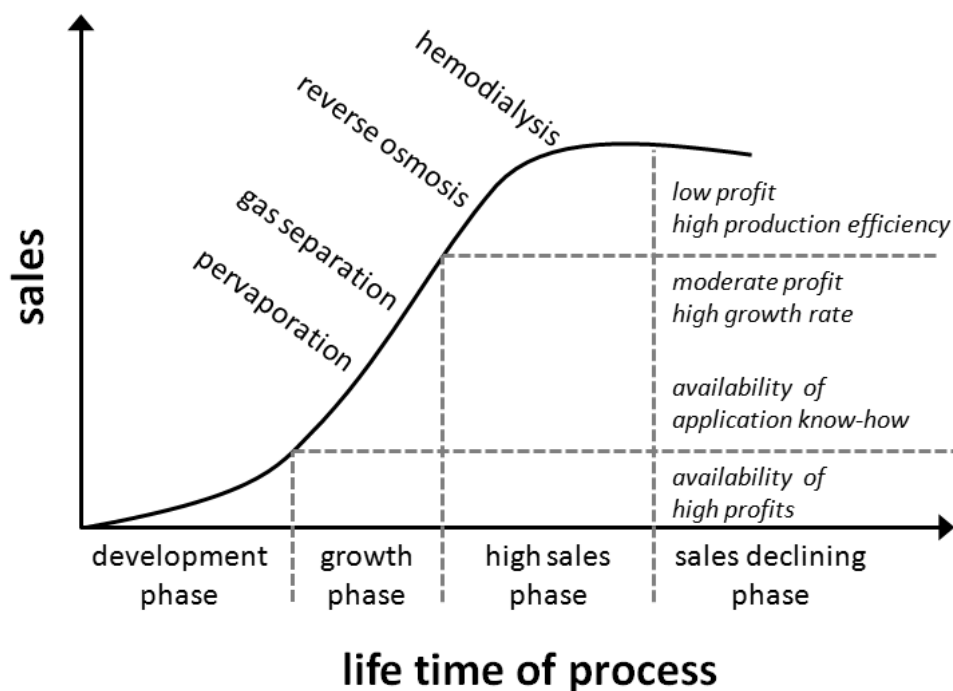


Figure 2.1: Life-cycle curve for several membrane processes displaying the sale as a function of the development state of a process based on [3,4].

## 2.1 Introduction to membrane-based separation processes

For gas separation and in particular for pervaporation the growth could be more pronounced if more suitable membrane materials would exist<sup>[2]</sup>.

For different membrane-based processes very different types of membrane materials are used. Basically there are three groups of membrane materials: modified natural products, synthetic polymers and inorganic substances<sup>[5]</sup>. A detailed overview of these three types including some examples is given in table 2.1.

**Table 2.1: Most commonly used materials for membrane fabrication<sup>[5]</sup>.**

Type of material	Examples
modified natural products	chitin, cellulose and its derivatives, polyelectrolytes
synthetic polymers	polyvinyl alcohol, polysiloxane, polypropylene, polytetrafluorethylene, polyamide, polyester, polyvinyl chloride, polyvinylidene fluoride, polyacrylonitrile, polyimide, polyurethane
inorganic materials	metals and alloys (Ti/Ag, Ti/Ni, Pd) metal oxides (Al <sub>2</sub> O <sub>3</sub> , ZrO <sub>2</sub> , SiO <sub>2</sub> ) carbon, glass, ceramics

Membranes can be divided into two important groups according to the underlying transport mechanism: porous membranes and solution-diffusion membranes. Porous membranes on the one hand contain pores with diameters larger than 1 nm and can consist of ceramics, metals, glass or polymers. Separation here takes place due to size-exclusion, thus the transmembrane flux depends on the applied pressure and pore diameter. Solution-diffusion membranes on the other hand contain pores with diameters smaller than 1 nm and are composed of polymers. The separation is based on the solution-diffusion model where the permeation of a component depends on its permeability. High solubility and diffusivity within the membrane material result in a high permeability of that component. This means that even the larger component can be separated from a smaller one when the latter shows a noticeably smaller solubility or diffusivity. The permeation of a binary mixture through membranes of the two types is shown schematically in figure 2.2 illustrating the respective underlying transport mechanism.

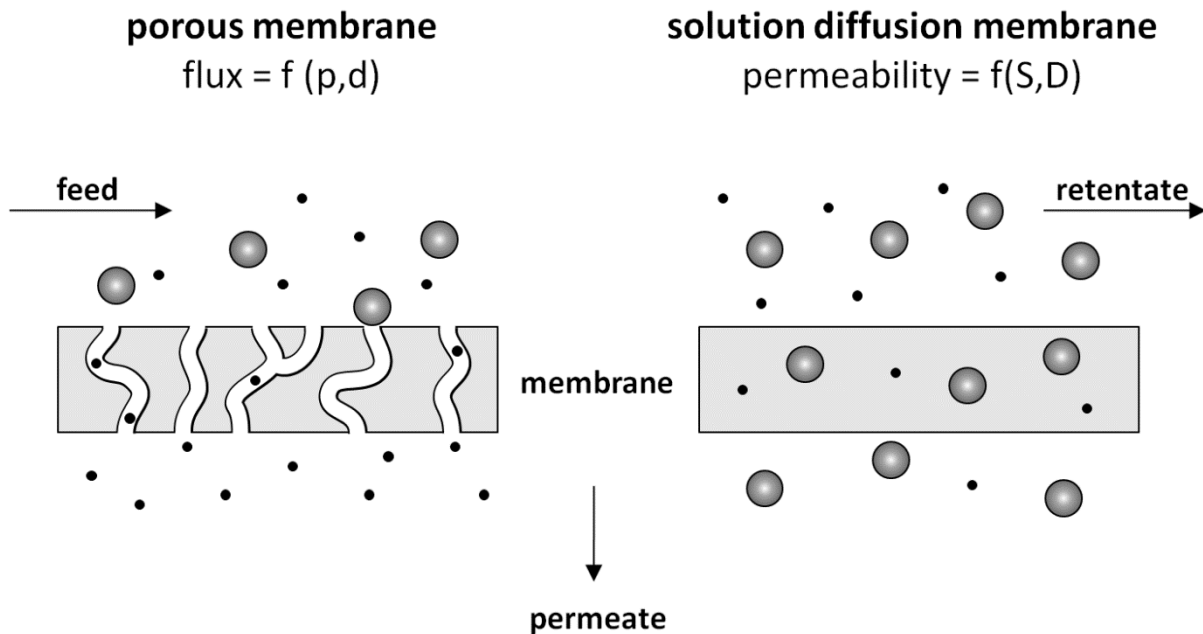


**Figure 2.2:** Schematic of the permeation of a binary mixture through a porous (left) and a solution diffusion membrane (right) based on [5]. The transmembrane flux through a porous membrane is described as a function of pressure  $p$  and pore diameter  $d$ . The permeability  $P$  of a solution diffusion membrane depends on solubility  $S$  and diffusivity  $D$  of the feed components.

It is also possible to incorporate materials usually only found in porous membranes into solution-diffusion membranes. A wide variety of materials is used as fillers for membranes. Here the incorporation of zeolites<sup>[6]</sup>, ordered mesoporous silica<sup>[7,8]</sup> or non-porous silica<sup>[9]</sup> as well as carbon molecular sieves<sup>[10]</sup> into polymeric materials is investigated. Also metal organic frameworks (MOFs)<sup>[11,12]</sup> and delaminated materials<sup>[13]</sup> are used as filler in this regard. A membrane containing matrices of both of the above described membrane types is called mixed-matrix-membrane (MMM). With this technique disadvantages of one material can, to a certain extent, be compensated by advantages of the other material<sup>[14]</sup>. The separation with such a membrane therefore bases not solely on the solution-diffusion mechanism. However MMMs can still be considered solution diffusion membranes because the corresponding matrix generally is the dominant one<sup>[10]</sup>.

## 2.2 Pervaporation – state of the art

Pervaporation is a membrane process for the separation of liquid mixtures. Due to the particular characteristic of membrane techniques it can have the edge over conventional separation methods such as adsorption, crystallization, extraction, or distillation for certain applications. Most notably are the economical, ecological and safety-related advantages of pervaporation<sup>[15]</sup>. Generally this technique can surpass conventional processes which are thermally or procedurally complex. Furthermore with pervaporation it is possible to separate mixtures that exhibit restricted concentration boundaries, for instance azeotropic mixtures<sup>[16]</sup>. For these reasons pervaporation could be an especially interesting alternative in chemical industry for the separation of aromatic/aliphatic mixtures. These are often composed of close or high boiling components but also azeotropes can occur. In a broad variety of refining and petrochemical processes aromatic/aliphatic

## 2.2 Pervaporation – state of the art

---

mixtures have to be processed. Examples are the reforming of naphtha streams, the production of cyclohexane and the desulphurization of gasoline<sup>[17–19]</sup>. Conventional technologies competing with pervaporation in the field of aromatic/aliphatic separation are extractive and azeotropic distillation as well as liquid–liquid extraction which are however energy intensive and expensive<sup>[20,21]</sup>. For the separation of mixtures containing less than 20 wt.-% aromatics no suitable industrial processes are available<sup>[22]</sup>. This context explains the ample interest in research on aromatic/aliphatic separation using pervaporation, whose recent highlights are presented in the following.

Usually for basic research on pervaporation of aromatic/aliphatic mixtures not the actual mixtures that incur in industry are used. Instead experiments are conducted mostly with binary model systems of controllable compositions in order to obtain better reproducible results. One widely used model system is toluene/n-heptane. The separation characteristics of many materials have already been investigated. Roizard et al. investigated cross linked polyurethanes<sup>[23]</sup>. With a membrane synthesized from a polyurethane based on 1,6 diisocyanatohexane and polyethyleneglycole a flux of  $4.0 \text{ kg}\cdot\mu\text{m}\cdot\text{m}^{-2}\cdot\text{h}^{-1}$  at 80 °C was achieved. The concentration of the aromatic component was hereby increased from 50 wt.-% in the feed to 87 wt.-% in the permeate, which equates to a selectivity of 6.7.

Polyvinylchloride and nanocomposites containing 30 wt.-% of different filler materials were investigated as membrane materials by Aouinti et al.<sup>[24]</sup>. The addition of the filler materials always led to reduced selectivity compared to the pure polymer. In some cases also the fluxes decreased. With some other nanocomposites however, selectivity decreased while the flux was drastically increased. In pervaporation experiments with 50 wt.-% toluene mixtures at 80 °C a flux of  $2.2 \text{ kg}\cdot\mu\text{m}\cdot\text{m}^{-2}\cdot\text{h}^{-1}$  and a selectivity of 8.1 was found for the pure polymer. The polyvinylchloride nanocomposite containing 30 wt.-% nanocor I30 exhibited a selectivity of 2.03, which is a fourth compared to pure polyvinylchloride. However the flux increased by a factor of more than six to  $14 \text{ kg}\cdot\mu\text{m}\cdot\text{m}^{-2}\cdot\text{h}^{-1}$ .

The separation characteristics for membranes prepared from several different fluorine containing polyimides have been studied by Ye et al.<sup>[25]</sup>. Altogether fluxes between  $0.1$  and  $2.0 \text{ kg}\cdot\mu\text{m}\cdot\text{m}^{-2}\cdot\text{h}^{-1}$  and selectivities between 1.3 and 11.5 were found. Most promising results were obtained for the polyimide composed of 4,4'-(hexafluoroisopropylidene)-diphthalic anhydride (6FDA) and 2,2-bis[4-(4-aminophenoxy)phenyl] hexafluoropropane (BDAF). In pervaporation experiments at 80 °C with mixtures containing 20 wt.-% toluene a flux of  $1.08 \text{ kg}\cdot\mu\text{m}\cdot\text{m}^{-2}\cdot\text{h}^{-1}$  and a selectivity of 5.29 were found.

Ribeiro et al. synthesized a series of other aromatic polyimides and polybenzoxazoles<sup>[26]</sup>. Overall good results were obtained for the separation of mixtures containing  $40 \pm 1$  wt.-% toluene at 80 °C. Most notable separation characteristics were found for the polyimide based on 6FDA and 2,3,5,6-Tetramethyl-1,4-phenylenediamine (4MPD) with a flux of  $53.2 \text{ kg}\cdot\mu\text{m}\cdot\text{m}^{-2}\cdot\text{h}^{-1}$  and a selectivity of 2.40.

For better comparability and visibility all data of the so far mentioned groups for the separation of toluene/n-heptane mixtures is presented in figure 2.3. Here selectivity is plotted against the total flux in a double logarithmic diagram. In gas separation a very similar way to report membrane characteristics is known as “upper bound diagram”<sup>[27,28]</sup> (see chapter 2.3).

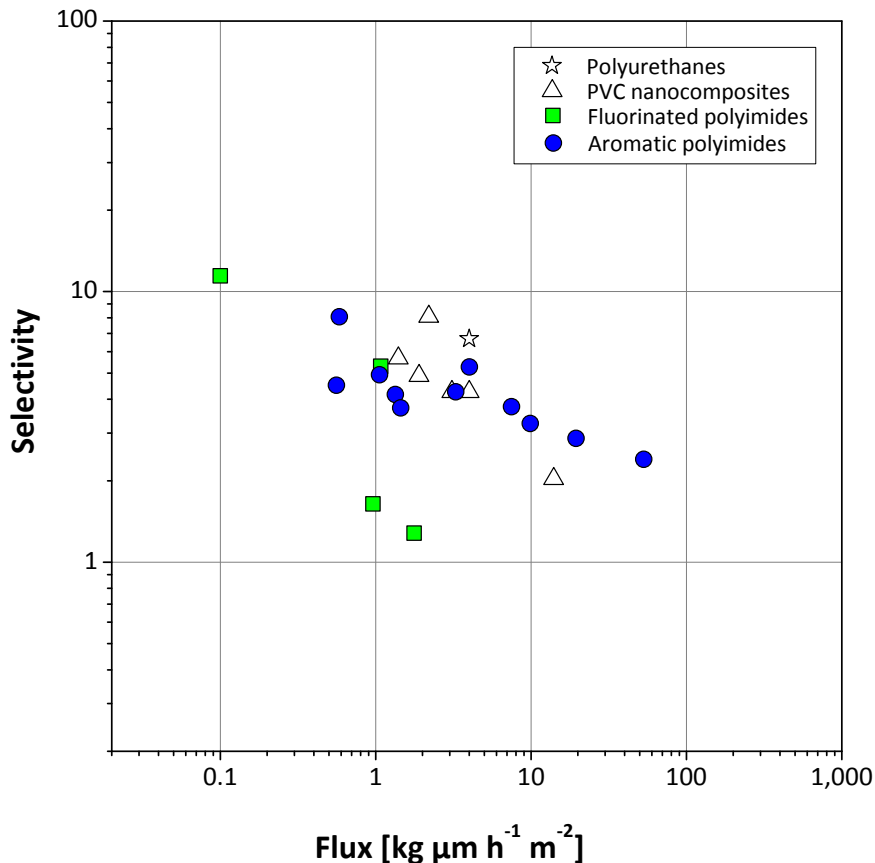


Figure 2.3: Presentation of different separation characteristics for the pervaporation of toluene/n-heptane mixtures with 20 - 50 wt.-% aromatic content at 80°C in the style of an upper bound diagram. Membrane data sources are as follows: polyurethanes (star) by Roizard et al.<sup>[23]</sup>, PVC membranes (triangle) by Aouinti et al.<sup>[24]</sup>, fluorinated polyimides (square) by Ye et al.<sup>[25]</sup> and aromatic polyimides by Ribeiro et al.<sup>[26]</sup>.

From this comparison of data it can be seen that aromatic polyimides generally possess average selectivities, however stand out with high fluxes. This and the chemical adjustability of their characteristics through the choice of different monomers make them particularly interesting as a membrane material for the separation of aromatic/aliphatic mixtures.

An even more challenging process in petrochemical industry is the separation of benzene/cyclohexane mixtures which are very close boiling. Less than 1 K lies in between their boiling points and therefore azeotropic distillation and extractive distillation have to be used conventionally. Here pervaporation particularly emerges as an alternative with good prospects<sup>[22]</sup>. As shown by Katarzynski et al. aromatic polyimides are a promising membrane material for this mixture too, especially at high aromatic concentrations<sup>[29,30]</sup>. In particular 6FDA-based copolyimides containing the diamines 4MPD and 3,5-diaminobenzoic acid (DABA) showed good results in pervaporation of aromatic/aliphatic mixtures (abbreviation of the polymer: 6FDA-4MPD/6FDA-DABA). However it has to be noted that benzene is harmful to health. Therefore in laboratory research great care has to be bestowed on the handling of this component and its mixtures. By using toluene as a substitute aromatic instead, the health risk can be reduced. Pithan showed for the membrane material 6FDA-4MPD/6FDA-DABA 4:1 that at aromatic feed contents below 50 wt.-% the

## 2.3 Gas separation – state of the art

---

separation characteristics are nearly identical when using toluene instead of benzene as the aromatic component<sup>[31]</sup>.

Experiments with 50:50 wt.-% mixtures of cyclohexane and benzene or toluene respectively using membranes made from the copolyimide 6FDA-4MPD/6FDA-DABA 4:1 (containing the diamines 4MPD and DABA in a molar ratio of 4:1) were conducted by Ren and Pithan<sup>[32,33]</sup>. In pervaporation experiments at 60 °C with pure polymer membranes and feed mixtures containing 50 wt.-% toluene a flux of  $12.83 \text{ kg}\cdot\mu\text{m}\cdot\text{m}^{-2}\cdot\text{h}^{-1}$  and a selectivity of 3.84 was found.

Some promising results in terms of membranes from carbon nanotube/polymer nanocomposites were shown by Peng et al.<sup>[34]</sup>. They prepared membranes from a nanocomposite based on polyvinyl alcohol (PVA),  $\beta$ -cyclodextrin and multiwall carbon nanotubes containing glutaraldehyde as cross-linker. Pervaporation experiments with benzene/cyclohexane mixtures were conducted at 50 °C. The normalized flux of the nanocomposite could be enhanced to a maximum of  $3.6 \text{ kg}\cdot\mu\text{m}\cdot\text{m}^{-2}\cdot\text{h}^{-1}$  compared to a flux of nearly  $2 \text{ kg}\cdot\mu\text{m}\cdot\text{m}^{-2}\cdot\text{h}^{-1}$  for a native PVA membrane. The selectivity also increased from around 10 for a pure polymer membrane to 41. In another work of the same group membranes were prepared from hybrid materials of PVA and chitosan wrapped CNTs, which were also glutaraldehyde cross-linked<sup>[35]</sup>. These were then used for the same pervaporation experiments at 50 °C. Here the normalized flux could be enhanced to a maximum of  $5 \text{ kg}\cdot\mu\text{m}\cdot\text{m}^{-2}\cdot\text{h}^{-1}$  and the selectivity increased to 53. These examples show that adding non-covalently modified CNTs to polymers is a promising approach since selectivity and permeability can be increased considerably.

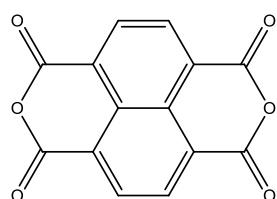
## 2.3 Gas separation – state of the art

The separation of gaseous mixtures using membranes, called gas separation in short, is a pressure-driven process that up to date is used in a broad range of industrial applications. The production of the first commercial polymeric membranes started in 1980. Since then gas separation has become an ever-expanding alternative separation process to conventional methods such as cryogenic distillation and adsorption processes<sup>[36]</sup>. The advantages of gas separation over conventional separation mainly result from the smaller energy input required, like in most membrane processes. In the case of gas separation additionally no phase transition of the feed components occurs<sup>[36]</sup>. Most notably gas separation is used for the separation of air to enrich nitrogen or oxygen respectively, but also in the separation of carbon dioxide from methane and furthermore in the recovery of hydrogen from methane amongst other gases<sup>[37]</sup>.

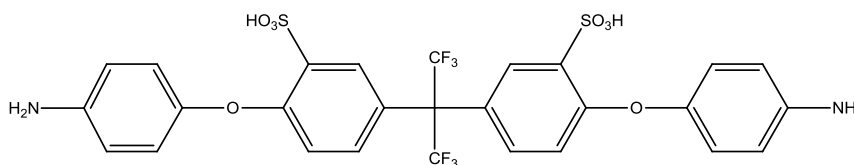
One of the first commercial applications of hydrogen recovery with membranes was the separation of hydrogen from nitrogen, methane, and argon in ammonia purge gas streams as found in the Haber process<sup>[38]</sup>. Today the recovery of hydrogen in refineries represents one of the largest applications for hydrogen-permeable membranes. Also the need for hydrogen is growing due to increasing environmental regulations<sup>[37,39,40]</sup>. Cheap and therefore attractive sources for hydrogen in this industry are refinery fuel gas streams, the tail gas of pressure swing adsorption processes, gas from fluid catalytic cracking units (FCCU) and hydrocracker/hydrotreater off-gas. These streams contain between 30 and 80 % hydrogen together with light hydrocarbons (C1-C5)<sup>[37]</sup>. Competing conventional

techniques are cryogenic, catalytic and pressure swing adsorption processes<sup>[41]</sup>. However several membrane based processes are already commercially available here. The PRISM<sup>®</sup> membranes distributed by Air Products provide the highest market maturity. Operation conditions with these membranes typically are 113 bar at 40 °C but at most 110 °C are possible. This allows a hydrogen recovery of above 97 vol.-%<sup>[39]</sup>. The MEDAL<sup>™</sup> membranes offered by Air Liquide represent another prominent product and can be operated at pressures up to 120 bar while typically providing a hydrogen recovery of 98 vol.-%<sup>[40]</sup>. However further membrane development would be interesting in terms of increased hydrocarbon resistance and higher selectivity and permeability in order to enhance the attractiveness of this technique<sup>[41]</sup>. Therefore in this work the focus has been put on the separation of hydrogen/methane mixtures. Some recently investigated polymeric membrane materials with outstanding separation characteristics are presented below.

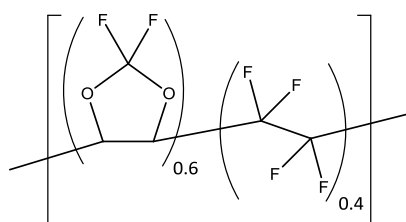
Sulfonated polyimide membranes were prepared by Tanaka et al. and the single gas permeabilities for H<sub>2</sub>, CO<sub>2</sub>, O<sub>2</sub>, N<sub>2</sub> and CH<sub>4</sub> were investigated<sup>[42]</sup>. Experiments were conducted at 35 °C applying a feed pressure of 1 atm and evacuating the permeate to 93 mbar. The most notable results for the gas pair H<sub>2</sub>/CH<sub>4</sub> were obtained with the polymer NTDA-BAPHFDS(H) which is prepared from the dianhydride 1,4,5,8-naphthalene tetracarboxylic dianhydride (NTDA) and the sulfonated diamine 4,4'-(hexafluoroisopropylidene) bis(*p*-phenyleneoxy) dianiline (BAPHFDS(H)). Here a hydrogen permeability of 52 Barrer and an ideal selectivity of 330 were found.



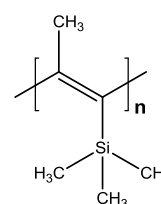
**NTDA**  
1,4,5,8-naphthalene  
tetracarboxylic dianhydride



**BAPHFDS(H)**  
2,2- Bis[4-(4-aminophenoxy)phenyl]  
hexafluoro propane disulfonic acid



**Hyflon AD60X**  
60 % 2,2,4 trifluoro 5 trifluoromethoxy-1,3-dioxole  
and 40 % tetrafluoroethylene



**PTMSP**  
poly(1-trimethylsilyl-1-propyne)

**Figure 2.4: Structures and monomers comprising polymers with outstanding hydrogen/methane separation characteristics.**

Macchione et al. studied the separation characteristics of the perfluorinated copolymer Hyflon AD60X<sup>[43]</sup>. It is composed of tetrafluoroethylene and 2,2,4-trifluoro-5-trifluoromethoxy-1,3-

## 2.3 Gas separation – state of the art

dioxole repeating units in a molar ratio of 40:60. In single gas permeation experiments with hydrogen/methane mixtures at 25 °C and feed pressures of 1 bar a hydrogen permeability of 187 Barrer and an ideal selectivity of 67 were determined.

Pinnau and Toy worked on the single gas permeabilities of a poly(1-trimethylsilyl-1-propyne) membranes<sup>[44]</sup>. Gas permeation experiments were conducted at 23 °C with a feed pressure of 4.5 bar and atmospheric permeate pressure. Hydrogen showed a permeability of 16,700 Barrer and for the gas pair H<sub>2</sub>/CH<sub>4</sub> a selectivity of 1.08 was found.

The so far reviewed results represent some of the uppermost permeabilities and selectivities for the separation of hydrogen and methane and the data are very close to the upper bound. This line was established by Robeson in 1991 when he found a direct correlation between permeability and selectivity that conventional polymers are not able to surpass<sup>[27]</sup>. It has recently been revisited<sup>[28]</sup> and is presented along with the above-mentioned separation characteristics as well as a few more data of outstanding membrane materials in figure 2.5.

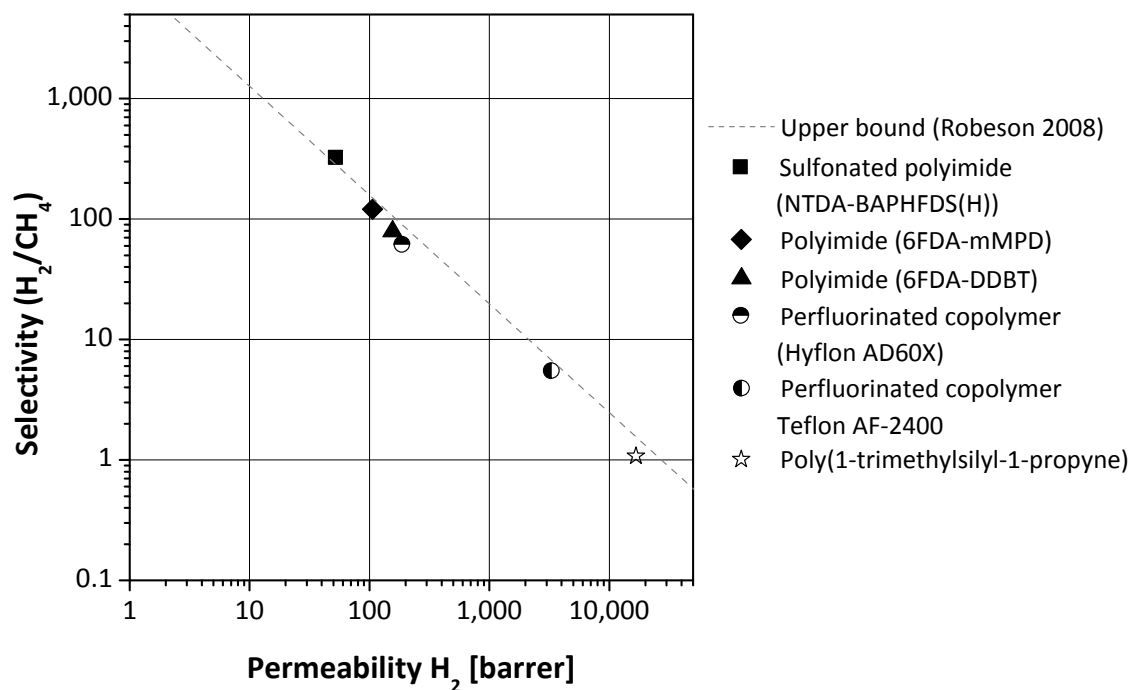


Figure 2.5: Diagram showing the Robeson upper bound correlation for the membrane based separation of hydrogen and methane<sup>[28]</sup>. A selection of membrane materials close or above the upper bound is shown<sup>[42–48]</sup>.

The most important characteristics of inorganic membranes are their outstanding separation characteristics whereas polymeric membranes are easy to produce at low cost. As mentioned above the advantages of the two membrane materials can be combined in form of mixed matrix membranes. Due to the combination of properties it is possible to surpass the Robeson upper bound limit with MMMs<sup>[28]</sup>. The discovery of this material class dates back to as early as 1980 and research interest has increased heavily in recent years<sup>[49]</sup>. Depending on their shape and structure filler materials used in MMMs are divided into several different types. The by far most common materials are particulate inorganic fillers. However sheet-shaped materials represent another promising filler type that has gained much research interest during the last years. Depending on their dimensions these materials are also called flakes or nanosheets. A further subdivision according to the filler pore

size in relation to the size of the feed molecules is made. This leads to either selective flakes where at least one feed component can permeate through the filler or non-selective flakes where the filler is impermeable for all components. The latter type can therefore also be referred to as barrier material. Moreover the orientation of the filler inside the polymer matrix can be influenced providing either random or preferentially horizontally oriented flakes. As the focus in this work lies on the oriented incorporation of selective flakes into a polyimide matrix some important results in the fields of MMMs containing sheet shaped filler materials are present hereafter.

Yang et al. investigated the flake alignment in composite coatings for aluminum coupons<sup>[50]</sup>. In their work it was shown that epoxy coatings containing aligned mica flakes dramatically reduced the permeabilities of solutes such as hydrochloric acid. It was found that the reduction however depends on the volume fraction of the flakes which again depends on the shape and loading.

In terms of selective flakes in MMMs for gas separation a notable example are the results obtained by Jeong et al.<sup>[51]</sup>. The group prepared membranes from the copolyimide 6FDA-6FpDA/6FDA-DABA 21:1 and lamellar aluminum phosphate. For the separation of O<sub>2</sub>/N<sub>2</sub> MMMs containing 10 wt.-% of the filler showed notably increased separation characteristics compared to the pure polymer. The O<sub>2</sub> permeability was reduced from 36.0 Barrer for the pure polymer to 18.5 Barrer for the MMM. At the same time however the O<sub>2</sub>/N<sub>2</sub> selectivity increased drastically from 3.6 for the copolyimide to 8.9 for the MMM. The addition of the filler consequently allowed surpassing the upper bound.

Another example of delaminated porous materials is the work of Choi et al. who have studied MMM comprising polybenzimidazole and delaminated AMH-3<sup>[52]</sup>. In gas separation experiments at 35 °C it was found that addition of only 3 wt.-% of the inorganic filler led to an increase of H<sub>2</sub>/CO<sub>2</sub> selectivity by a factor of 2 compared to pure polymer membranes.

Rubio et al. prepared MMMs from the delaminated material UZAR-S1 and polysulfone (Udel®)<sup>[53]</sup>. By incorporating 4 wt.-% of the filler the H<sub>2</sub>/CH<sub>4</sub> selectivity increased from 58.9 to 69.2 while the hydrogen permeability almost remained unaltered (11.8 Barrer for the pure polymer and 11.5 Barrer for the MMM).

Also Gorgojo et al. investigated a delaminated porous filler for MMM fabrication. They prepared membranes from exfoliated Nu-6(2) and 6FDA-based copolyimides with the diamines 4MPD and DABA in different molar ratios<sup>[13]</sup>. Addition of 5.3 wt.-% of the filler to 6FDA-4MPD/6FDA-DABA 4:1 increases the H<sub>2</sub> permeability from 360 to 500 Barrer while the H<sub>2</sub>/CH<sub>4</sub> selectivity increased from 30.0 to 37.9. In case of 6FDA-4MPD/6FDA-DABA 49:1 as membrane polymer the addition of 5.9 wt.-% exfoliated Nu-6(2) leads to an increase of H<sub>2</sub> permeability from 809 to 839 Barrer while H<sub>2</sub>/CH<sub>4</sub> selectivity increased from 17.8 to 26.2.

As an example for oriented selective flake nanocomposites with the aim of application in hydrogen separation the work of Choi et al. should be mentioned<sup>[54]</sup>. Membranes comprising of MCM-22/silica composites were fabricated through layer-by-layer deposition. These membranes were tested in hydrogen/nitrogen gas separation experiments. Here a H<sub>2</sub> permeability of 65.0 Barrer and a H<sub>2</sub>/N<sub>2</sub> selectivity of 124 were found which is very close to the corresponding Robeson upper bound.

## ***2.4 Aim of the work***

---

The examples presented above point out that the preferentially horizontal oriented incorporation of selective sheet-shaped filler materials is a promising route to enhance the separation characteristics of polymer membranes.

## **2.4 Aim of the work**

As shown in chapters 2.2 and 2.3 polyimides are very eligible membrane materials. In particular those based on 6FDA are often among the polymers with the highest separation characteristics. This was exemplarily shown for the pervaporation of benzene/cyclohexane and the gas separation of hydrogen/methane. These represent two challenging separation tasks in petrochemical industry. So far commercial membrane processes only exist for the separation of hydrogen/methane and the materials used here still possess potential for improvement. The central goal of this work is to further improve the separation characteristics of the copolyimide 6FDA-4MPD/6FDA-DABA 4:1 regarding the previously presented separation tasks. For the two techniques two completely different approaches are used which are described below.

The first aim is to prepare nanocomposites from the copolyimide with functionalized multiwalled carbon nanotubes (MWCNTs) in order to enhance the separation characteristics for the pervaporation of aromatic/aliphatic mixtures. As shown above carbon nanotubes can increase the permeability and especially selectivity in PVA membranes. However in that case additionally a dispersing auxiliary and a cross linking agent are necessary to obtain suitable nanocomposites for membrane preparation. In this work MWCNTs shall be incorporated into the polymer matrix without the need of additional substances. In order to facilitate good interaction between polymer and nanotubes it is necessary that both components possess the right functional groups. The polymer exhibits several functional groups, particularly the carboxylic acid group provided by the DABA unit. Hydroxyl-functionalized MWCNTs (MWCNT-OH) shall be prepared via defect group chemistry starting from pure MWCNTs. Therefore nanotubes have to be oxidized using nitric acid to introduce carboxylic acid groups on the walls end especially ends of the tubes. These can then be reduced to obtain the desired hydroxyl groups. Homogeneous distribution of the nanotubes within the polymer matrix shall be achieved with ultrasound treatment. The right conditions for this step also have to be developed. Figure 2.6 schematically shows the structure of the desired nanocomposite membranes.

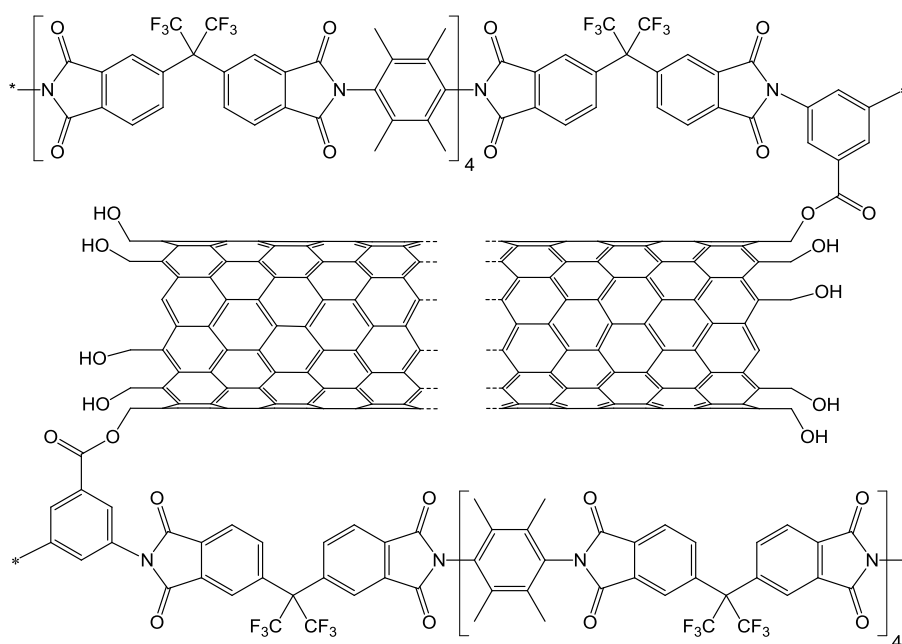


Figure 2.6: Scheme of the desired nanocomposite membrane material comprised of the copolyimide 6FDA-4MPD/6FDA-DABA 4:1 and hydroxyl functionalized MWCNTs.

The second aim is the preparation of mixed matrix membranes (MMMs) for gas separation. In this work selective flakes obtained from the layered titanosilicate JDF-L1 are to be used as filler. Due to the fact that this material exhibits a high selectivity based on size exclusion it is supposed to noticeably increase the selectivity of the polymer. Such an effect would become especially noticeable in the separation of hydrogen and methane, because these two molecules exhibit very different sizes. It is considered that even higher selectivity could be achieved if the filler is predominantly horizontally oriented inside the membrane. By altering the membrane casting conditions the filler orientation shall be influenced. Figure 2.7 illustrates the alteration of permeation paths in the desired MMMs containing preferentially horizontally oriented sheets compared to MMMs containing a particular filler.

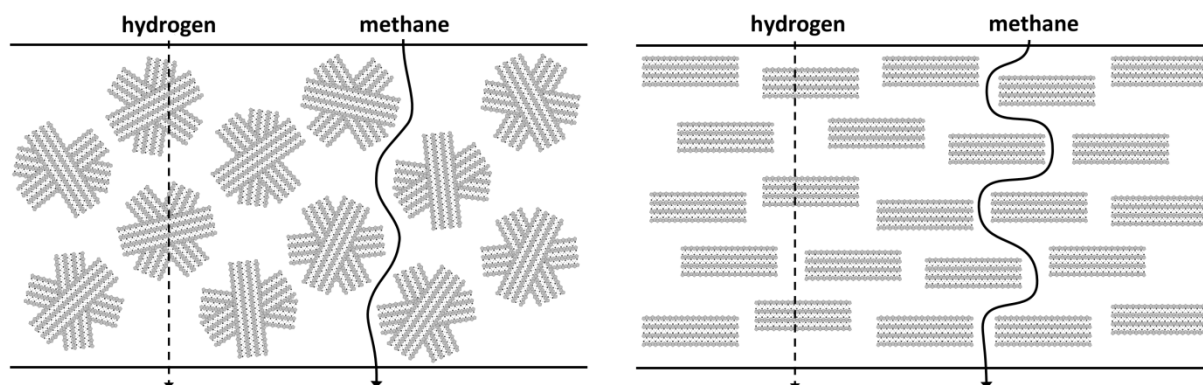


Figure 2.7: Schematic of permeation paths through mixed matrix membranes for gas molecules smaller (hydrogen) and larger (methane) than the pore size of the filler. On the left the MMM contains an agglomerated filler while on the right nanosheets are used which extend the permeation path of the larger gas molecules.



## 3 Theoretical background

This chapter provides an introduction to the principles and mechanisms behind the investigated membrane processes of gas separation and pervaporation. Furthermore the materials used for membrane preparation are presented herein. For polyimides and the investigated filler materials, carbon nanotubes and the titanosilicate JDF-L1, synthesis and general properties are displayed. Finally nanocomposites and MMMs respectively are defined. These are the material classes to be obtained by combining the polymer with the mentioned filler materials.

### 3.1 Membrane separation processes

The operation principle of membrane separation is based on the ability of a membrane to separate a mixture by controlling the rates at which the components pass through it. Generally the mixture to be separated is called feed. It is brought in contact with a membrane where a driving force is applied to the mixture, due to which the components are moved across the membrane at individual rates. This rate is referred to as permeability which indicates the facility of a component to move through the membrane. The stream collected below the membrane is called permeate while the remaining mixture above the membrane is referred to as retentate. As the membrane exhibits noticeably different permeabilities for the individual feed components the higher permeable component will be accumulated in the permeate. Correspondingly the lower permeable component will be enriched in the retentate. An illustration showing the process schematically is presented in figure 3.1.

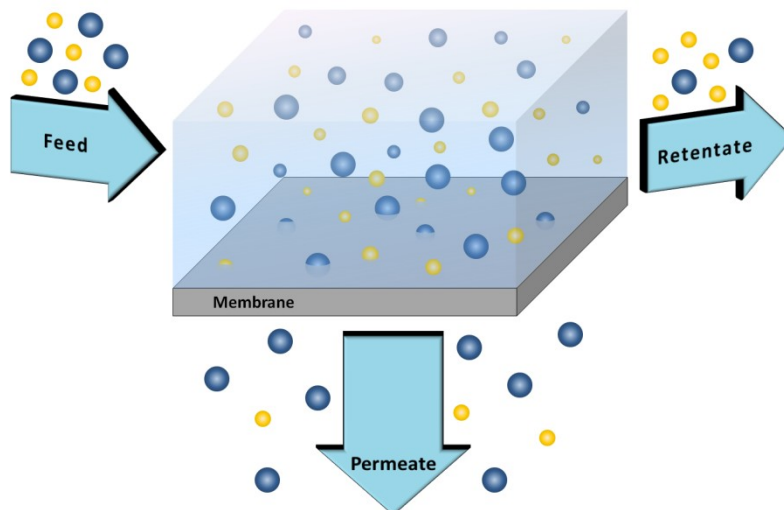


Figure 3.1: Schematic illustration of a membrane separation process for a mixture composed of a higher permeable component (blue spheres) and a lower permeable one (yellow spheres) <sup>based on [55]</sup>.

The driving force in membrane processes can be a gradient of pressure, temperature, concentration or electro motive force between feed and permeate. In pervaporation and gas separation for example the driving force is a pressure gradient. The model used to describe the separation in these

### 3.1 Membrane separation processes

two processes is the solution-diffusion model which is explained in detail later (see chapter 3.1.1). It basically considers that the above mentioned driving forces are interrelated through the chemical potential  $\mu$  which in fact induces the permeation of a component through the membrane<sup>[56]</sup>. With this assumption the solution-diffusion model can be used to mathematically describe the mass transport in membranes for pervaporation, gas separation, dialysis and reverse osmosis.

For different membrane processes the states of matter of feed, retentate and permeate streams may vary. Figure 3.2 visualizes the process streams and their states of matter for the processes investigated in this work.

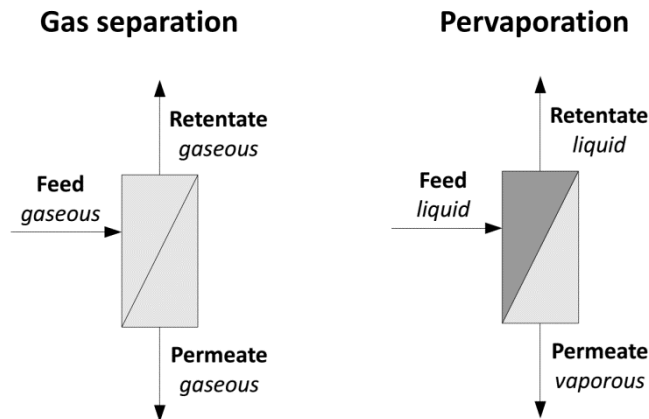


Figure 3.2: Schematic of the mass streams and states of matter in gas separation and pervaporation. The rectangular box is commonly used to depict a membrane module with separated feed and permeate side. The diagonal line represents the membrane.

As distinguished from gas separation, where all phases are gaseous, in pervaporation a phase transition takes place. Here feed and retentate are liquid while the permeate is obtained in the vaporous phase, which has influence on the mathematical description of the separation.

#### 3.1.1 The solution-diffusion model

The solution-diffusion model has been developed in order to describe the separation of mixtures using membranes with pores smaller than 1 nm. Here components are not discriminated based upon their sizes as described by the pore-flow model. The solution-diffusion model was first established by Graham in 1866, when he investigated the permeation through a membrane made of caoutchouc<sup>[57]</sup>. He applied a vacuum on one side of a membrane while the other side was in contact to air and found an enrichment of oxygen in the vacuum. Basing on his approach to explain this observation Binning et al. subdivided the permeation of a component through a membrane into the following three crucial steps<sup>[58]</sup>:

- 1) **Sorption:** On the feed facing side the component is absorbed into the surface of the membrane.
- 2) **Diffusion:** Migration of the component across the bulk of the membrane takes place.
- 3) **Desorption:** The substance is vaporized into the permeate stream on the downstream membrane surface.

An illustration of the three steps is shown in figure 3.3.

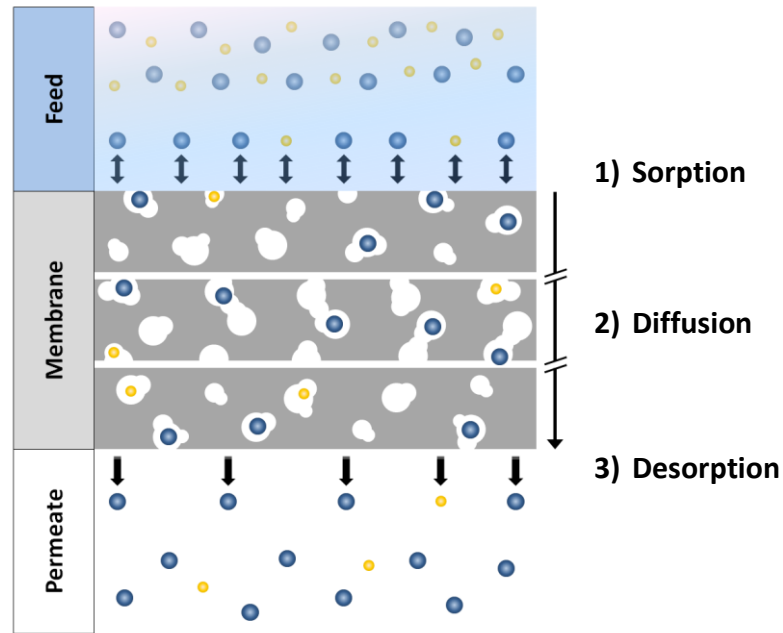


Figure 3.3: Depiction of the permeation across a membrane according to the three underlying steps of the solution-diffusion model.

The most widely accepted explanation for the diffusion of a feed component through dense polymeric membrane materials was found in 1979 by Pace and Datyner<sup>[59]</sup>. Accordingly a molecule permeating through a membrane is located in the micro voids of the polymer. These voids are a result of suboptimal chain stacking and their sum is also referred to as the free volume of the polymer. Due to the thermally induced statistical movement of chain segments micro canals are formed between micro voids. This allows a molecule to move across the membrane from one void to another corresponding to the applied driving force. To visualize this model the membrane in figure 3.3 shows micro voids as white areas. In the middle of the membrane the passage of a molecule (blue sphere) is illustrated from the upper micro void to the lower one by formation of micro canals in between.

In gas separation, pervaporation and most other membrane separation processes the pressure of a component on the permeate side is maintained constant but at a much lower level than on the feed side. Therefore the desorption is fast and can basically be neglected as a step influencing the permeation rate<sup>[56]</sup>. This means the permeability  $P$  of a component  $i$  can be represented as follows:

$$P_i = S_i \cdot D_i \quad (\text{Eq. 3.1})$$

$S_i$  : Solubility coefficient of component  $i$

$D_i$  : Diffusivity coefficient of component  $i$

The solubility coefficient hereby describes the physical and chemical interactions between a feed component and the membrane material. The diffusivity coefficient is a kinetic factor specifying the mobility of a component inside the membrane material.

### 3.1 Membrane separation processes

---

Three presuppositions are made to facilitate the mathematical description of the separation according to the solution-diffusion model. First it is assumed that the membrane is a homogenous layer. Second for all components a chemical equilibrium is presumed on the interface between membrane/feed and membrane/permeate respectively. Third all potential coupling effects between the partial fluxes remain disregarded<sup>[56]</sup>.

Building on that it is possible to mathematically approach the mass transport according to the solution-diffusion model using Fick's first law of diffusion<sup>[60]</sup>. It states that under steady state condition the flux is proportional to the concentration gradient which leads us to the following relationship:

$$J_i = -D_i \cdot \frac{dc_{i,M}}{dl} \quad (\text{Eq. 3.2})$$

- $J_i$  : flux of component  $i$  across the membrane
- $D_i$  : diffusivity coefficient of  $i$
- $c_{i,M}$  : concentration of component  $i$  within membrane
- $l$  : linear spatial coordinate across membrane in the direction of flux

After integration over the thickness of the membrane we obtain the following equation:

$$J_i = \frac{D_i}{\delta_M} \cdot (c_{i,M}^F - c_{i,M}^P) \quad (\text{Eq. 3.3})$$

- $\delta_M$  : membrane thickness
- $c_{i,M}^F$  : steady state concentration of  $i$  on the feed facing side of the membrane
- $c_{i,M}^P$  : steady state concentration of  $i$  on the permeate facing side of the membrane

Up to this point only the diffusivity was considered for the calculation of the flux. As stated above the solubility describes the physical and chemical interactions between the membrane and a feed component. Thus the solubility coefficient has influence on the amount of a component that can be absorbed from the feed into the surface of the membrane. The steady state concentration  $c_{i,M}$  can thus be expressed as:

$$c_{i,M} = S_i \cdot p_i \quad (\text{Eq. 3.4})$$

- $S_i$  : solubility coefficient of  $i$  in gaseous phase
- $p_i$  : partial pressure of  $i$  in gaseous phase

Substitute equation 3.4 into 3.3 we obtain:

$$J_i = D_i \cdot S_i \cdot \frac{(p_i^F - p_i^P)}{\delta_M} = P_i \cdot \frac{(p_i^F - p_i^P)}{\delta_M} \quad (\text{Eq. 3.5})$$

- $p_i^F$  : partial pressure of  $i$  in the feed
- $p_i^P$  : partial pressure of  $i$  in the permeate

The final equation obtained describes the transport of a gas according to the solution-diffusion model and thus holds true for gas separation. By exchanging the partial pressure with the partial vapor pressure however the equation can also be applied for pervaporation.

#### 3.1.2 Separation characteristics of membranes

The key characteristics for evaluating the separation capacity of a membrane are its selectivity and the rate of permeation or flux<sup>[41]</sup>. Selectivity on the one hand can be referred to as the separation efficiency. This is because in order to achieve a specific separation ratio with a high selective membrane a lower driving force (and thus energy) is required compared to a less selective membrane. The permeation rate on the other hand directly relates to the process productivity. High permeable membranes for example allow the use of a smaller membrane area for a given separation task which lowers the investment costs of a membrane process.

Admittedly a variety of different units and dimensions are used to describe the separation efficiency and productivity of a membrane. The dissent in literature has been addressed repeatedly by Wijmans and Baker<sup>[61,62]</sup>. They suggest the use of values which are normalized to the driving force, e.g. permeability, permeance and selectivity. However when evaluating experiments with nearly identical operational conditions (feed concentration, pressure difference and temperature) it is also appropriate to compare non-normalized information such as fluxes. The latter case is often applicable for pervaporation data. Due to the variety of values found in literature the values used to describe the separation characteristics in this work are explained in the following.

Usually the total flux  $J_{total}$  is the most readily available value related to the permeation rate and thus the productivity of a membrane process. In pervaporation experiments the total flux is usually obtained by weighing out the mass of permeate collected during a given time. From this value the partial fluxes  $J_{i,j}$  can be calculated by analyzing the permeate composition. Generally the flux is reported as the quantity of permeate  $m$  obtained over a certain period of time  $t$  using a given membrane area  $A$ :

$$J_i = \frac{m}{A \cdot t}; \quad \left[ \frac{kg}{m^2 \cdot h} \right] \quad (\text{Eq. 3.6})$$

- $J_i$  : partial flux of component  $i$
- $m$  : mass of permeate [kg]
- $A$  : membrane area [ $m^2$ ]
- $t$  : time interval of the measurement [h]

For better comparison of experimental series with different membranes the normalized flux is calculated. Here it is also taken into account that the flux is linearly dependent on the membrane thickness:

$$J_{n,i} = \frac{m \cdot d}{A \cdot t}; \quad \left[ \frac{kg \cdot \mu m}{m^2 \cdot h} \right] \quad (\text{Eq. 3.7})$$

### 3.1 Membrane separation processes

---

$J_{n,i}$  : normalized partial flux of component  $i$   
 $d$  : membrane thickness

In the present work normalized fluxes  $J_n$  were used to report permeation rates in pervaporation experiments. Up to date this is the most common unit used in literature relating to pervaporation. In gas separation however the typical way to report the productivity of a membrane is through permeability, which is used nearly exclusively. Therefore in this work permeabilities were used as well. The calculation of  $P$  from experimental data is explained in chapter 4.7.3.

In the majority of cases selectivity is used to specify the separation efficiency of a membrane for a binary mixture. It is defined as the ratio of the individual permeabilities as shown in equation 3.5. From equation 3.1 it follows that the selectivity can be subdivided into a selectivity of solubility and diffusivity respectively:

$$\alpha_{i,j} = \frac{P_i}{P_j} = \frac{S_i \cdot D_i}{S_j \cdot D_j} = \alpha_{i,j}^{Solubility} \cdot \alpha_{i,j}^{Diffusivity} \quad (\text{Eq. 3.8})$$

The mixture hereby consists of the two components  $i$  and  $j$ , of which  $i$  is the preferentially permeating one. Depending on whether the permeabilities were obtained from experiments with mixtures or by individual testing (e.g. by pure gas permeation tests in gas separation) it has to be distinguished between real and ideal selectivities. When permeabilities are determined individually possible interactions between the components are disregarded which means that only an ideal selectivity is obtained ( $\alpha^{ideal}$ ). The real selectivity ( $\alpha^{real}$ ) on the opposite is calculated using permeabilities obtained from experiments with the according mixtures. This accounts for the interaction between the components and its potential influence on the permeability values.

In this work real selectivities obtained from mixed gas separation experiments were used for gas separation. Also in pervaporation and in industrial application the real selectivity is used to describe the separation efficiency. However in these cases it is most conventionally calculated on the basis of feed and permeate compositions. For this either weight fractions or concentrations can be used:

$$\alpha_{i,j}^{real} = \frac{w_i^P / w_j^P}{w_i^F / w_j^F} \quad \text{or} \quad \alpha_{i,j}^{real} = \frac{c_i^P / c_j^P}{c_i^F / c_j^F} \quad (\text{Eq. 3.9})$$

$w_{i/j}^{P/F}$  : weight fraction of  $i$  or  $j$  in the permeate or feed respectively  
 $c_{i/j}^{P/F}$  : concentration of  $i$  or  $j$  in the permeate or feed respectively

In the case of pervaporation real selectivities were calculated from the weight fractions of the components in feed and permeate.

#### 3.1.3 Plasticization and cross-linking of membrane polymers

When exceeding a certain concentration feed components can act as an external plasticization agent on polymers. This alters the thermal and mechanical characteristics of a membrane material. Most importantly a plasticizer leads to a decreased rigidity of the polymer and a lower glass transition temperature  $T_g$ <sup>[63]</sup>. The plasticizer basically increases the chain distance in the polymer and reduces the chain interaction. Accordingly both the flexibility of the polymer chains and the free volume increase, the polymer swells. Membrane plasticization has two important consequences. The first is the drastically declined mechanical stability which can cause membrane failure due to material disintegration in the worst case. Secondly the permeation rates increase noticeably due to the expanded and more flexible polymer structure. This especially applies for the less preferably permeating component resulting in a loss of selectivity. The effects of membrane plasticization can be circumvented by cross-linking of the polymer material. Additional connections between the polymer chains are introduced that cannot be broken by the plasticizer. The membrane is now affected to a much lower extent by swelling. Figure 3.4 shows the plasticization of both an untreated as well as a cross-linked polymer.

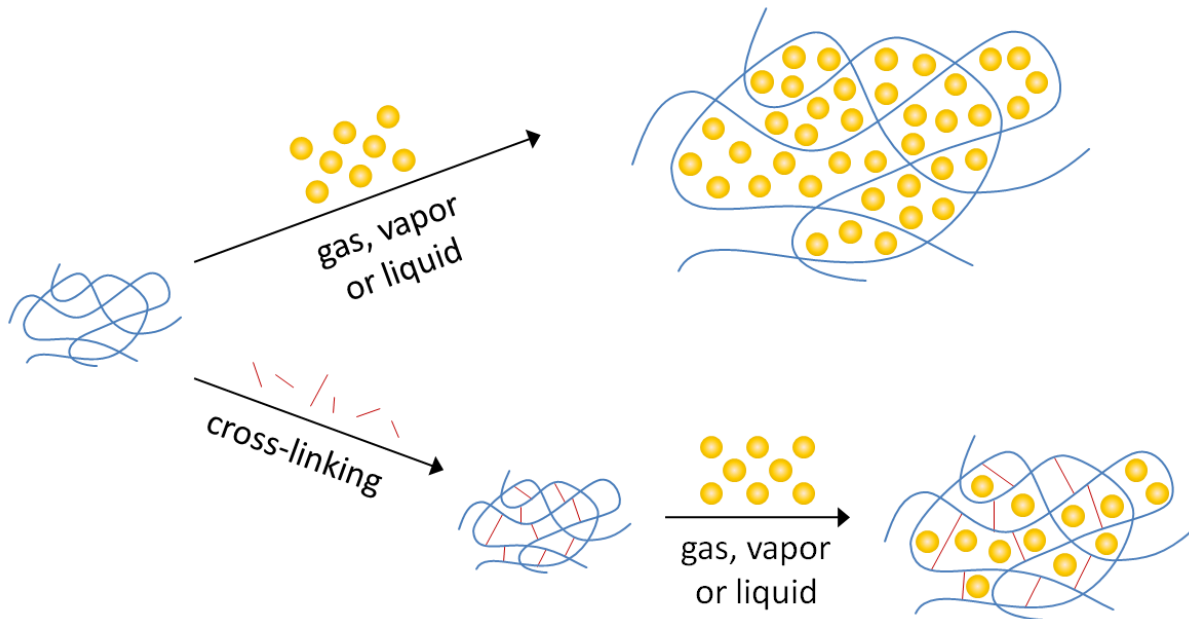


Figure 3.4: Schematic of the plasticization of a polymer with and without cross-linking. Based on [64]

Cross-linking not only hinders plasticization but also affects the separation characteristics. Most commonly the opposite effect of plasticization is observed. In comparison to a pure polymer a cross-linked polymer often shows decreased permeability and increased selectivity. For instance Pithan found a flux of  $12.8 \text{ kg} \cdot \mu\text{m} \cdot \text{m}^{-2} \cdot \text{h}^{-1}$  and a selectivity of 3.8 for the pure polyimide 6FDA-4MPD/6FDA-DABA 4:1. A membrane of the same polyimide which was cross-linked with 1,4-butanediol however showed a lower flux of  $4.5 \text{ kg} \cdot \mu\text{m} \cdot \text{m}^{-2} \cdot \text{h}^{-1}$  and a higher selectivity of 5.7<sup>[31]</sup>.

### 3.2 Membrane materials

The aim of this work was to enhance the separation characteristics of the copolyimide 6FDA-4MPD/6FDA-DABA 4:1. Therefore this polymer can be considered as the central starting material in this work. As filler materials for membrane preparation multi walled carbon nanotubes and the titanosilicate JDF-L1 were used. This section now focuses on these materials. An introduction as well as basic information is given not only for the membrane materials itself but also for the material classes obtained from their combination.

#### 3.2.1 Polyimide

Eponymous for polyimides is the imide group which is composed of two carbonyl groups adjacent to a  $sp^3$  hybridized nitrogen atom. Although polyimides can be composed of either linear or cyclic imide groups cyclic polyimides are technically much more interesting. Figure 3.5 shows the molecular structure of linear and cyclic polyimides. One imide group is exemplarily highlighted in red.

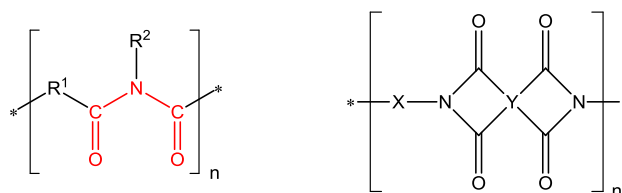


Figure 3.5: Chemical structures of linear and cyclic polyimides. In the linear structure the imide group is exemplarily highlighted in red.

When aromatic structures are used as groups X or Y respectively the polymer is referred to as an aromatic polyimide. The general properties as well as the most common synthesis route are explained in the following.

##### 3.2.1.1 General properties of polyimides

Due to their special properties polyimides are counted among the high-performance plastics and especially qualify as heat resistant polymers. Of all commercial polyimides aromatic polyimides exhibit the most outstanding properties. These possess a high durability across a broad temperature range (-240 up to 370 °C) as well as an extraordinary dimensional stability under heat. Usually short term exposure of up to 400 °C is possible. Continuous service temperatures of above 250 °C when air-exposed and even above 315 °C under inert conditions are found. In addition to their non-flammability and their capabilities as electric insulators polyimides also exhibit resistance to diluted acids, many common solvents, fats and oils. However they are not resistant against strong acid or alkali, boiling water and oxidizing agents<sup>[65,66]</sup>.

These characteristics fulfill many material requisitions therefore polyimides have a variety of industrial applications. In aeronautics for instance thermal insulation of space suits are made of polyimides. In the electrical and electronic industry polyimides are used for example as wire coating enamels or as base material of printed circuit boards. They are also suitable in automotive and mechanical engineering industry where e.g. roll bearings, slide rails or piston rings are made from

this polymer. Generally polyimides are used as plastic moldings, in the form of fibers or foams and as already mentioned for the preparation of membrane films<sup>[65,67]</sup>. Some well-known commercially available polyimides are Kapton from DuPont and P84 from Evonik Industries shown in figure 3.6.

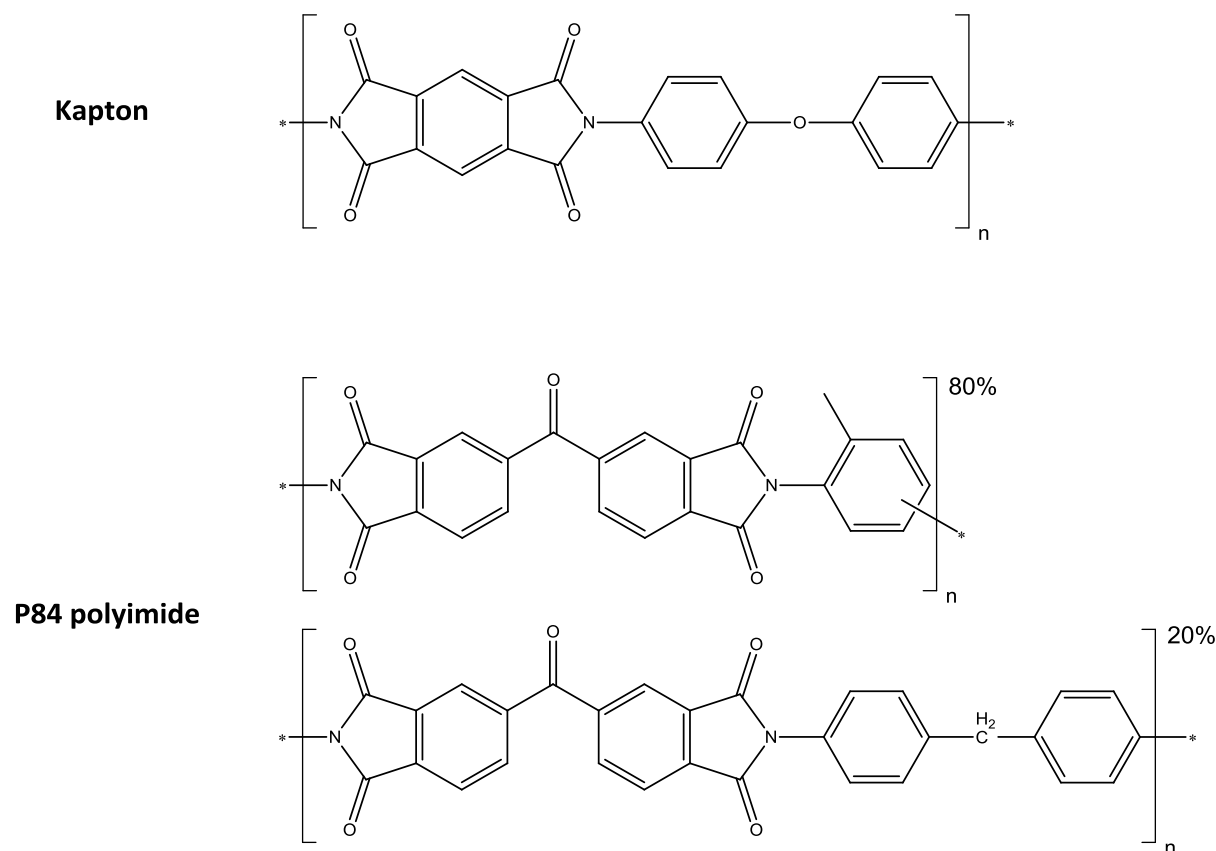


Figure 3.6: Structures of the commercial polyimides Kapton and P84.

#### 3.2.1.2 Synthesis of polyimides

The first polyimide synthesis dates back to as early as 1908 when Bogert and Renshaw described the preparation of a polymer based on 4-aminophthalic acid<sup>[68]</sup>. A big advancement came in 1955 with the first two step synthesis route for high molecular weight polyimides based on pyromellitic acid which was patented by Edwards and Robinson<sup>[69]</sup>. A few years later this route was adapted by Endrey to the preparation of aromatic polyimides<sup>[70,71]</sup>. In the first step a diamine and a dianhydride are reacted forming a polyamic acid. In the second step the cyclic imide groups are obtained by elimination of water at the amic acid groups. Figure 3.7 shows a schematic of the synthesis route.

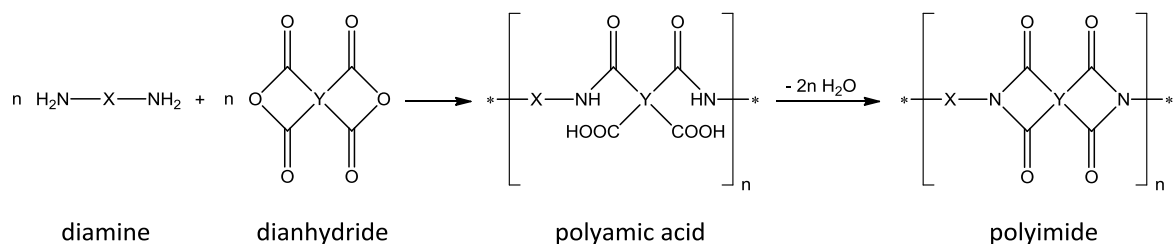


Figure 3.7: Two step synthesis for aromatic polyimides. The rests X and Y represent aromatic groups.

## 3.2 Membrane materials

The dehydration of the amic acid is called imidization. It can be achieved thermally as well as chemically. In this work chemical imidization using an equimolar mixture of triethylamine and acetic anhydride was chosen.

### 3.2.1.3 Copolyimide used for membrane preparation

The copolyimide used in this work is a statistical copolyimide based on the dianhydride 6FDA (4,4'-hexafluoroisopropylidene diphthalic acid anhydride) and the two diamines 4MPD (2,3,5,6-tetramethylphenylene-1,4-diamine) and DABA (3,5-diaminobenzoic acid) in a molar ratio of 4:1. The abbreviation for the polymer material is 6FDA-4MPD/6FDA-DABA 4:1 and the structure is given in figure 3.8.

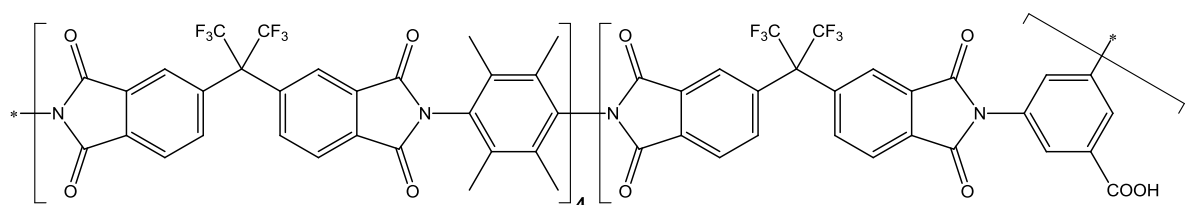


Figure 3.8: Structure of the copolyimide 6FDA-4MPD/6FDA-DABA 4:1.

As it has been shown in chapters 2.2 and 2.3. 6FDA based polyimides often exhibit very prominent separation characteristics. Another advantage of using this dianhydride is the fact that the resulting polyimide is soluble in certain solvents such as tetrahydrofuran and dimethylacetamide<sup>[72]</sup>. This drastically facilitates membrane preparation. In earlier studies the 4MPD diamino monomer turned out to provide high permeable membrane materials, which is a result of an increased free volume due to the bulky methyl side groups. This was also found by Tanaka et al. who investigated the effects of different methyl substituted diamines on the gas separation characteristics of several polyimides<sup>[48]</sup>. The carboxylic acid group inserted by the DABA allows further modifications of the membrane material using polymer-analogous reactions with that functional group<sup>[73]</sup>. Also, if necessary e.g. in pervaporation, cross-linking is possible, which is known to improve the selectivity<sup>[74]</sup>.

## 3.2.2 Carbon nanotubes

The element carbon occurs in different allotropic modifications. Among these are graphite, the most common elemental form, diamond, which is one of the most precious materials in the world, the spherical fullerenes and carbon nanotubes (CNTs) which are described here. CNTs were discovered at the beginning of the 1990s. The first works describing preparation and characterization of the novel material were published simultaneously by the groups around Iijima<sup>[75]</sup> and Bethune<sup>[76]</sup>. Still today it is a standing discussion to whom the honor of discovery is due<sup>[77]</sup>. However it is generally accepted that especially the work of Iijima raised scientific interest in CNTs<sup>[78]</sup>.

The carbon atoms in carbon nanotubes are arranged in the same honeycomb lattice as in graphene. However in CNTs these mono-atomic layers are wrapped up to form cylindrical hollow tubes. The C-C bonds are sp<sup>2</sup>-hybridized but slightly strained owing to the curvature. The C-C atom distance is 141.5 pm as expected for graphene like structures<sup>[79]</sup>. Nanotubes can consist of only one or multiple interleaved tubes which can also be considered as walls. Depending on the number of walls

nanotubes are divided into single walled carbon nanotubes (SWCNTs) and multi walled carbon nanotubes (MWCNTs)<sup>[78]</sup>. In literature also the term double walled carbon nanotube (DWCNT) can be found sometimes. The end of the tubes can either be plain open or closed by an end cap. These caps can be considered as half fullerene spheres with the diameter of the tube. Figure 3.9 shows the general structures of single and multi walled CNTs.

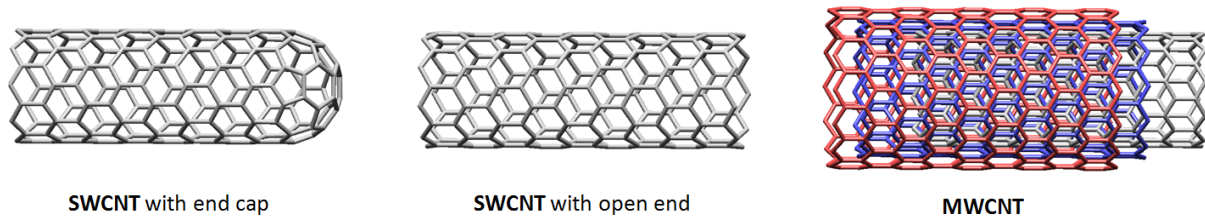


**Figure 3.9: Structures of single and multi walled carbon nanotubes. The ends of CNTs can either be open or closed with end caps.**

Typically for CNTs are diameters in the nanometer scale while lengths of up to several millimeters are most common<sup>[79]</sup>. The thinnest CNT reported so far has a diameter of 3 Å and was found in the center of a MWCNT<sup>[80]</sup>. Under the right conditions even macroscopic nanotubes with lengths over 18 cm can be produced<sup>[81]</sup>. In the present work the commercial nanotubes C 150 P from Bayer MaterialScience were used. These multi walled carbon nanotubes possess between 3 and 15 walls, an outer mean diameter of 13-16 nm and an inner mean diameter of 4 nm. Their length is between 1 and 10 μm.

#### 3.2.2.1 General properties of CNTs

Theoretically the structure of CNTs can be explained as an imaginary graphene layer wrapped up according to a chiral vector  $C_h$ . This vector can be expressed by integral multiples  $n$  and  $m$  (with  $n > m$ ) of the two unit vectors  $a_1$  and  $a_2$  in the graphene layer. Depending on the values of  $n$  and  $m$  three structure types with different electronic properties are possible. These types and their theoretic construction are shown in figure 3.10 exemplarily.

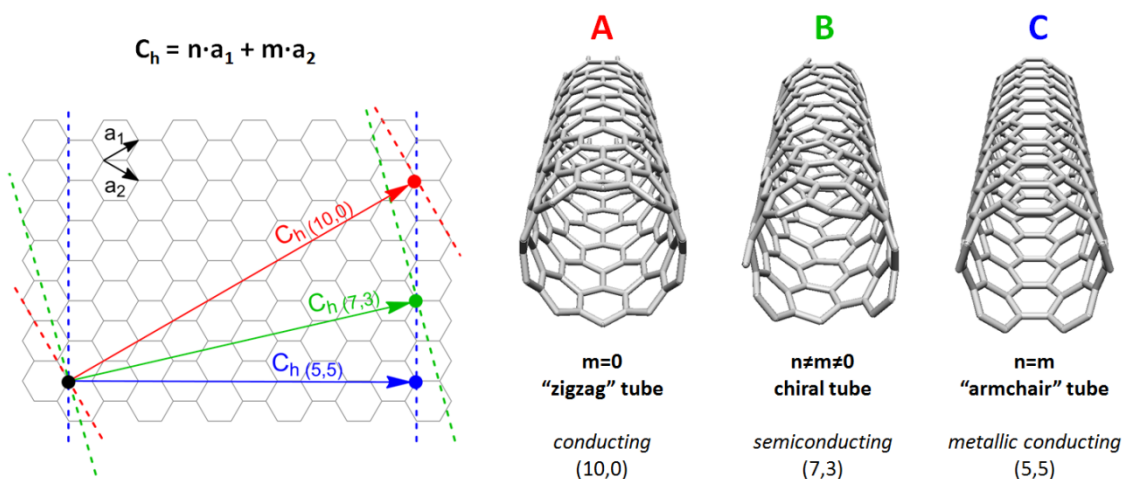


**Figure 3.10: Theoretic construction and structure of the CNTs (10,0), (7,3) and (5,5) as examples of the three possible CNT structures. Also the electronic properties of the tubes are related to the direction of  $C_h$ .**

## 3.2 Membrane materials

With  $m=0$  a “zigzag” structure is obtained (**A**) leading to conducting tubes while  $n=m$  results in an “armchair”-structure (**C**) which exhibits a metallic conducting behavior. For all  $n,m$  in between chiral tubes are obtained (**B**). Here semiconducting properties are found<sup>[79]</sup>.

The electronic properties are not the only extraordinary characteristics of carbon nanotubes. Basically the number of walls affects how pronounced these properties are. This becomes clear in view of the distinct structural appearance of single and multi walled CNTs. SWCNTs on the one hand consist of only one uniform tube with a homogenous surface. For this reason the electrical properties are especially pronounced here<sup>[78]</sup>. In MWCNTs on the other hand the individual tubes do not necessarily have to be intact over the full length of the tube but instead can exhibit gaps. An intermittent outer wall therefore leads to a rough CNT surface. However the nested structure of MWCNTs allows extraordinary mechanical properties. For a certain MWCNT a Young’s modulus of 63 GPa was found<sup>[82]</sup> which is ca. 50 times higher than that of steel. Considering their low density nanotubes have the highest known specific tensile strength<sup>[79]</sup>. MWCNTs also stand out with high thermal conductivities of over 3000 W / (m · K) which is due to the facile phonon propagation along the tubes<sup>[83]</sup>. This is even higher than in diamond or across the base plane of graphite where the thermal conductivity is 2000 W / (m · K). Due to strong  $\pi$ - $\pi$  interaction carbon nanotubes possess a high affinity to agglomeration and especially SWCNTs preferably form bundles<sup>[79]</sup>.

### 3.2.2.2 Major synthesis methods of CNTs

A variety of techniques are used for the synthesis of carbon nanotubes however three main methods are most commonly applied. They provide different yields and also lead to nanotubes with different characteristics. Figure 3.10 gives an overview of the three major synthesis methods which are described in detail in the following.

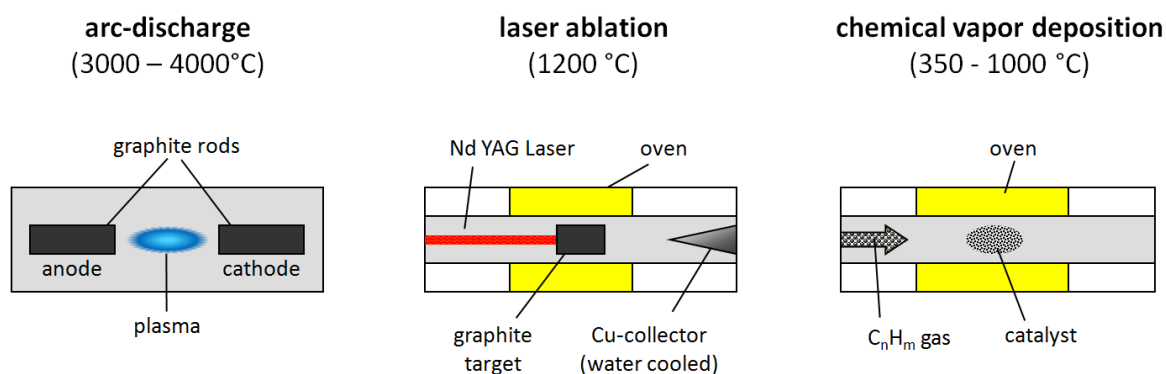


Figure 3.11: Schematics of the three major synthesis methods for the production of CNTs.

The **arc-discharge** method has already been used before the discovery of CNTs for the first mass production of fullerenes<sup>[84]</sup>. In an inert atmosphere an electric arc is induced between two graphite rods serving as electrodes by applying high currents of 80-100 A<sup>[85]</sup>. In the hot reaction conditions inside the plasma arc (3000 - 4000 °C) carbon atoms of the anode are vaporized and then condensate on the cathode where among soot also around at least 30 wt.-% of MWCNTs are formed<sup>[79]</sup>. By doping the anode with metals as catalyst it is possible to obtain SWCNT and furthermore optimize the yield. Journet et al. found a method to obtain SWCNT with a yield of more than 90% using Ni-Y as catalyst, which is frequently used today<sup>[86]</sup>. With the arc-discharge method it is however not possible to control length and diameter of the tubes and also many by-products are obtained. Mostly this is

amorphous carbon but in MWCNT production also polyhedral graphite particles are found. Due to the addition of catalyst for SWNTs formation also encapsulated metal particles are found in this case<sup>[85]</sup>.

**Laser ablation** is of historical significance as it was used by later nobel prize winners Curl, Kroto and Smalley in their work that led to the discovery of fullerenes<sup>[87]</sup>. In this method high energetic laser light e.g. from a Nd-YAG laser is directed at a graphite target which is heated to temperatures around 1200 °C and purged by an inert gas, usually argon<sup>[79]</sup>. Under these conditions a plasma of carbon vapor is generated. The carbon then condenses on a cooled copper collector where the nanotubes grow. In the absence of metal atoms in the target MWCNTs are formed while for the synthesis of SWCNTs metallic catalysts are necessary<sup>[78]</sup>. Thess et al. were the first to obtain SWCNT bundles with laser ablation on a cobalt and nickel doped graphite target<sup>[88]</sup>. Generally for this method extremely pure targets and a high energetic laser are needed. Together with typically small yields this means that laser ablation is a cost-intensive and thus uneconomical method. However it provides high quality nanotubes whose narrow diameter distribution can also be controlled by choosing the right process parameters. Therefore this method is very interesting for the selective synthesis of specific CNTs e.g. in basic research<sup>[78]</sup>.

In **chemical vapor deposition (CVD)** a stream of a volatile carbon precursor is brought into contact with catalyst particles in an oven at temperatures between 350 – 1000 °C. Either supported or floating catalysts (particles moving freely in the reactor) can be used. By deposition of carbon from the precursor gas stream onto the surface of the catalyst particles nanotube growth is induced<sup>[79]</sup>. In this method numerous variables can be altered leading to a broad variety of different CVD-processes<sup>[78]</sup>. One important and today widely used process is the HiPCO method developed by Nikolaev in 1999<sup>[89]</sup>. It allows the bulk synthesis (up to g/h) of high quality single walled carbon nanotubes. As carbon source CO at maximum 10 atm is used and the catalyst particles are formed by thermolysis of Fe(CO)<sub>5</sub> or ferrocene at elevated temperatures (800 – 1200 °C). With most CVD-processes the diameter distribution and the yield of the SWCNT can be controlled by the process parameters. Moreover it is possible with CVD to synthesize nanotubes directly on certain substrates and at specific locations making it an interesting method for the application of CNTs<sup>[79]</sup>.

None of these methods can provide a 100% pure product. Among CNTs with sometimes very broad diameter distribution usually other forms of carbon such as soot and catalyst residues are present. The purification of nanotubes is therefore an important issue where several different techniques are applied. Nanotubes can be physically sorted by length and diameter using filtration<sup>[90]</sup>, chromatography<sup>[91]</sup> or centrifugation<sup>[92]</sup>. Also a separation of metallic from semiconducting tubes is possible by means of dielectrophoresis<sup>[93]</sup>. Chemical purification however is mostly conducted via an oxidation treatment of the tubes. Most prominently is the simple yet effective method by Dujardin et al. that uses solutions of nitric acid to remove catalyst residues and amorphous carbon<sup>[94]</sup>.

#### 3.2.2.3 Functionalization methods for CNTs

With functionalization of CNTs it is possible to enhance their processability<sup>[95]</sup>. Two aspects are important in this regard. On the one hand the high tendency of nanotubes to agglomerate shall be circumvented. On the other hand the solubility of CNTs shall be increased which facilitates the chemical processing of CNT materials usually conducted in solvent media<sup>[96]</sup>.

## 3.2 Membrane materials

Several different routes towards functionalization of CNTs are known and applied. They are assembled in figure 3.12.

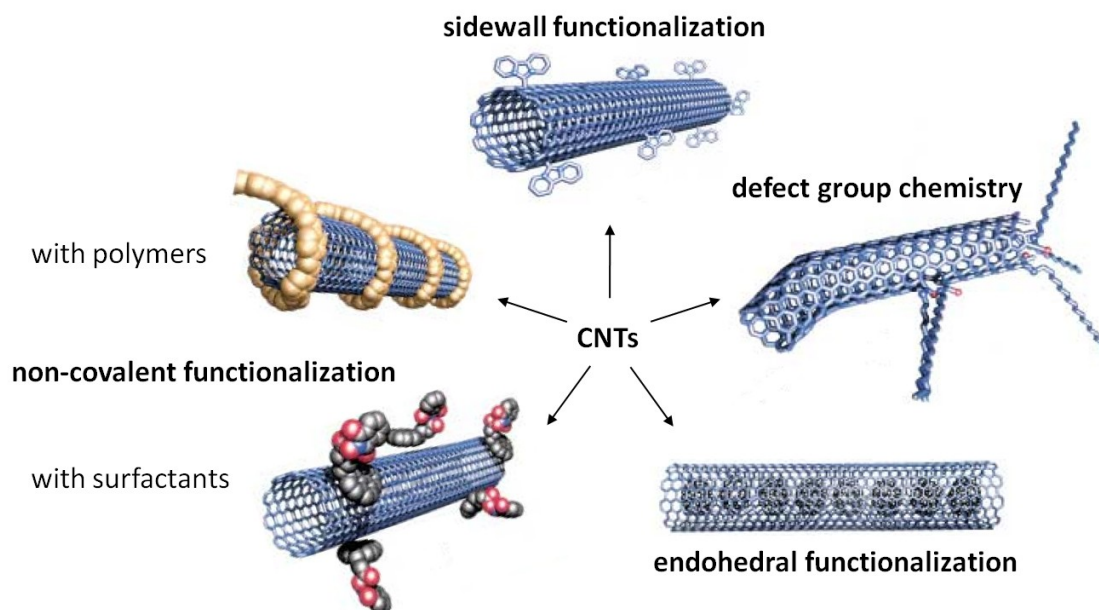


Figure 3.12: Overview of different functionalization methods for CNTs based on [95].

**Non-covalent functionalization** takes advantage of the strong  $\pi$ - $\pi$  interactions of nanotubes. Here the interaction is used to bind appropriate molecules such as polymers or surfactants onto the nanotube surface. Further modification is possible by using functional groups on these molecules. The inner cavity of CNTs is used for **endothedral functionalization**. Small enough molecules can access the cavity and be stored within or even alter the properties of the host tube. **Sidewall functionalization** is the covalent addition of molecules onto the sidewall of the tube. Hereby the hybridization of carbon changes from  $sp^2$  to  $sp^3$  relieving strain in the C-C bonds<sup>[95]</sup>. As figure 3.13 shows this strain has its origins in the pyramidalization ( $\theta_p$ ) of  $sp$ -orbitals and the misalignment of  $\pi$ -orbitals (torsion angle  $\phi$ ).

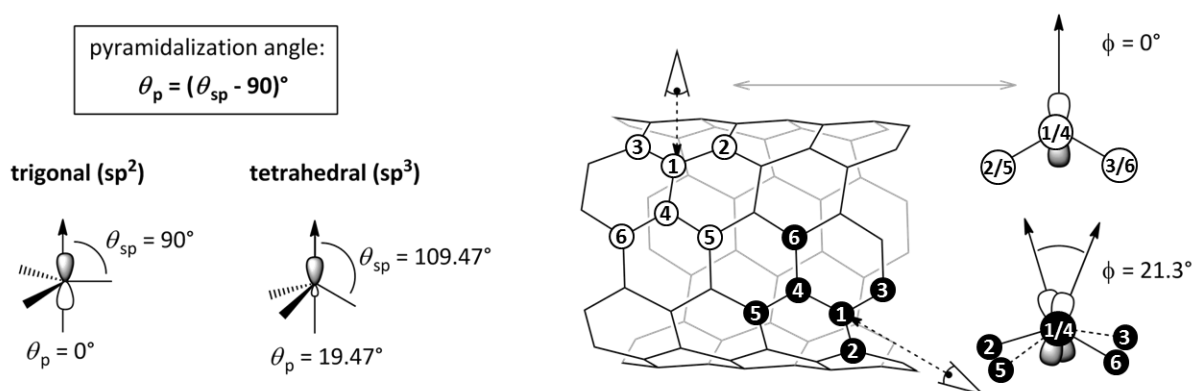


Figure 3.13: Bond strain in CNTs is caused by pyramidalization (measured by the pyramidalization angle  $\theta_p$ ) and  $\pi$ - $\pi$  misalignment due to C-C bond torsion ( $\phi$ ) based on [97].

Typically  $\theta_p$  is  $11.6^\circ$  for end caps and  $6.0^\circ$  on the sidewalls. While  $\phi$  is  $0^\circ$  for C-C bonds perpendicular to the longitudinal tube axis the misalignment can be quite big for bonds in other directions. For instance  $\phi$  is  $21.3^\circ$  in the small and thus rather closely rolled (5,5) nanotube as shown in figure 3.13 (black numerated carbon atoms)<sup>[97]</sup>. The stronger the strain, the easier the addition of a molecule is.

Possible reactants are hydrogen, fluorine, lithium, azides or carbenes among many others<sup>[96]</sup>. Moreover it is possible to functionalize CNTs using defects in their structure. This route is referred to as **defect group chemistry** and was applied in this work. The different types of defects found in CNTs are shown in figure 3.14.

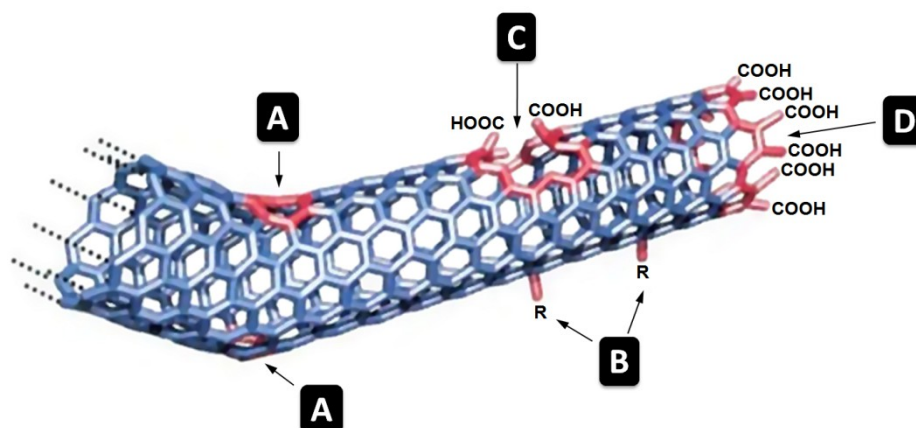


Figure 3.14: Overview of CNT defects: **A)** five- or seven-membered rings cause tube bending and lead to strained bonds. **B)** At the site of  $sp^3$ -hybridized defects a residue R is present (R = H, OH). **C)** Oxidative conditions can damage the framework leaving a hole framed with carboxylic acid groups. **D)** Open end of the tube is terminated by COOH-groups due to oxidative treatment<sup>based on [95]</sup>.

Types A and B are construction defects and thus occur during the tube formation whereas defects of types C and D are introduced when the tube is exposed to oxidative conditions<sup>[96]</sup>. The presence of five- or seven-membered rings instead of the typical six-membered ones causes a bent structure of the tube and can also lead to increased values of  $\theta_p$  and  $\phi$  (A). Hybridization defects result in  $sp^3$ -hybridized carbon atoms that possess an additional substituent R (B). Hydrogen or hydroxyl groups are commonly found here<sup>[95]</sup>. Sidewall functionalization in fact leads to this kind of defects in the CNT structure. It is however considered as an individual functionalization method. Under oxidative conditions carboxylic acid groups can be introduced into the nanotube structure. This usually eliminates carbon from the structure and leaves a hole lined with carboxylic acid groups. These defects can either be situated on the sidewall (C) or at the end of the tube (D) where the end caps are easily removed. Depending on the conditions of the oxidative treatment also nitrate, hydroxyl, hydrogen and carbonyl groups are found<sup>[95]</sup>. The oxidative purification of CNTs mentioned above also leaves defects of type C and D. Therefore also many functional groups, particularly carboxylic acid groups are introduced, which has to be considered with regard to the future application of the respective CNTs.

### 3.2.3 Titanosilicate JDF-L1

Titanosilicates are an example of zeolitic materials. Like zeolites these are microporous crystalline materials formed by a three dimensional framework with regular channels and cavities. The difference now is that zeolites are solely formed by  $SiO_4$ - or  $AlO_4$ -tetrahedra while the framework of those silicates can contain various metals in the form of different polyhedra. In the case of titanosilicates the framework is comprised of  $SiO_4$ -tetrahedra and  $TiO_5$ -pentahedra or  $TiO_6$ -octahedra<sup>[98]</sup>. Important examples are the Engelhardt titanosilicates ETS-4<sup>[99]</sup> and ETS-10<sup>[100]</sup> or the Aveiro-Manchester materials AM-1 and AM-4<sup>[101,102]</sup>. These materials are usually synthesized

## 3.2 Membrane materials

under hydrothermal conditions in Teflon-lined autoclaves at temperatures between 150 and 230 °C. Reaction times vary widely between hours and several weeks<sup>[103]</sup>. Titanosilicates exhibit interesting properties, most importantly these are a high surface area and the possibility of exchanging the charge equalizing cations. This makes them especially promising for application as shape-selective and highly active catalysts, high capacity ion exchange materials and selective adsorbents<sup>[103]</sup>. Moreover titanosilicates can also possess optical properties when -O-Ti-O-Ti-O-bonds are present like in ETS-10 for instance. These bonds can be considered as nanowires surrounded by an insulating environment of SiO<sub>2</sub><sup>[104]</sup>. In addition, Ti can be substituted by other interesting metals such as Zr, V, Sn, Nb etc. while keeping the same pentahedral or octahedral coordination<sup>[103,105]</sup>.

As mentioned before the titanosilicate used in this work is JDF-L1 (Jilin-Davy-Faraday, layered solid no.1) which is also referred to as AM-1 or disodium titanium tetrasilicate dihydrate according to its molecular composition: Na<sub>4</sub>Ti<sub>2</sub>Si<sub>8</sub>O<sub>22</sub>·4H<sub>2</sub>O. The structure was first described by Roberts et al. in 1996 and in 2007 a refinement was presented by Ferdov et al.<sup>[106]</sup>. JDF-L1 contains SiO<sub>4</sub>-tetrahedra and five coordinated Ti<sup>IV</sup> in the form of square pyramids. All four base vertices of the TiO<sub>5</sub>-square pyramids are connected to SiO<sub>4</sub>-tetrahedra and the latter are connected to two polyhedra of both species. This leads to a layered structure as shown in figure 3.15. Pores along the orientation of the layers are found in directions [100] and [010] and are formed by one TiO<sub>5</sub>-square pyramid and four SiO<sub>4</sub>-tetrahedra. A second species of pores is found across the layers along the [001] direction. These are formed by 6-membered rings of two TiO<sub>5</sub>-square pyramids connected by two pairs of SiO<sub>4</sub>-tetrahedra and exhibit a diameter of ca. 3 Å. Charge equalization of the structure is achieved by sodium cations found in between the layers located concentric in front of the aforementioned pores in [001] direction. These sodium cations are coordinated by two interlamellar water molecules and can be interchanged with other cations.

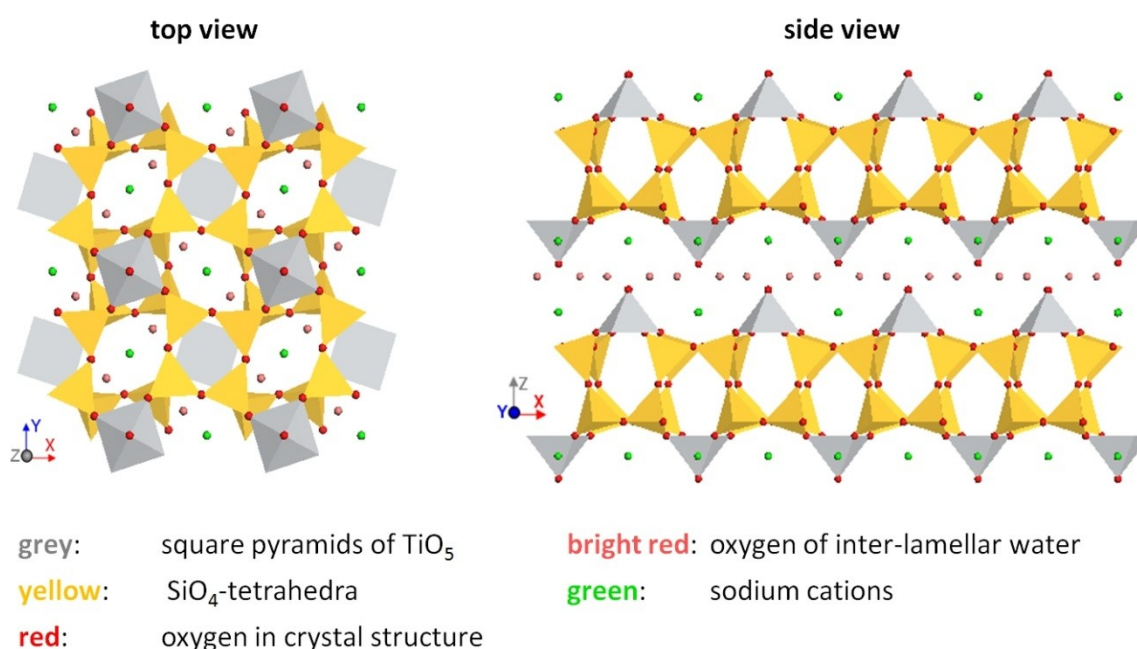


Figure 3.15: Structure of the layered titanosilicate JDF-L1 (AM-1).

The synthesis of JDF-L1 usually yields agglomerates of sheet shaped crystals with side lengths between 20 and over 150 μm and thicknesses of several μm, depending on the synthesis conditions. Rubio et al. showed that through seeded synthesis it is possible to reduce the size of the sheets<sup>[107]</sup>. By adding small quantities of ground JDF-L1 as seeds smaller agglomerates of sheets with lengths

around 2  $\mu\text{m}$  and thicknesses of ca. 100 nm were obtained. Also the reaction time of the hydrothermal synthesis was reduced through seeded synthesis. While large JDF-L1 crystal synthesis requires 93 hours, small JDF-L1 can be prepared within 6 to 24 h. It is possible to separate the individual sheet shaped crystals in the agglomerates obtained by JDF-L1 synthesis as shown in figure 3.17. For this the agglomerates are treated for 16 hours at 80  $^{\circ}\text{C}$  in a solution of the quaternary amines hexadecyltrimethylammonium bromide (cetyltrimethylammonium bromide, CTABr) and tetrapropylammonium hydroxide (TPAOH)<sup>[108]</sup>.

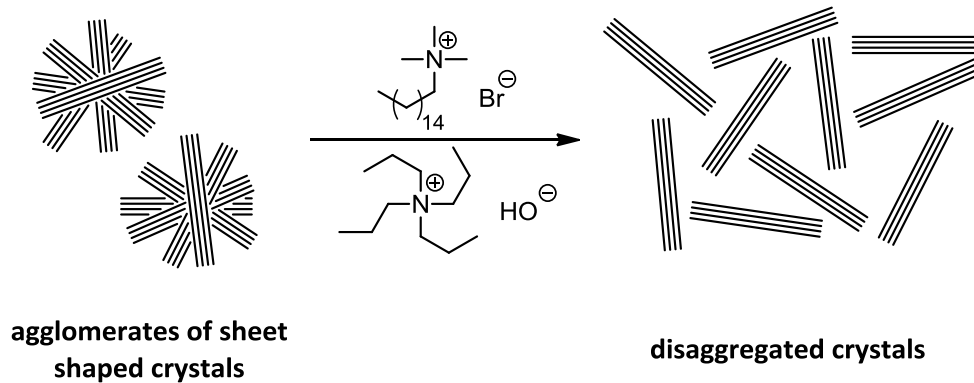


Figure 3.16: Schematic of the disaggregation process for JDF-L1. Using tertiary amines it is possible to separate the individual sheet shaped crystals from the agglomerates obtained during synthesis.

#### 3.2.4 Nanocomposites

Nanocomposites are composite materials comprising a nanoscale component incorporated into a matrix formed by a second material, usually a polymer<sup>[109]</sup>. In that case the material is referred to as a polymer nanocomposite, a term that emerged in the beginning of the 1990s<sup>[110]</sup>. In literature the term nanocomposite is also used as synonym for inorganic-organic hybrids, molecular composites or to encompass mature commercial products<sup>[110]</sup>. For a classification of the term hybrid material with regard to nanocomposites see chapter 3.2.4.1. Like nanotechnology in general also nanocomposite research benefits from the development and improvement of characterization methods that can visualize the atomic scale such as scanning tunneling and scanning probe microscopy. Also increasing computing power helps to facilitate modeling and simulating of nanoscale systems<sup>[111]</sup>. The first commercially applied nanocomposite was a polyamide/clay composite developed by Toyota around 1993 for the use in tire treads<sup>[112,113]</sup>. Also in nature examples of nanocomposites can be found. Materials such as bones, shells or wood for instance are composed of multiple phases one of which also includes particles, layers or fibers in the nanometer range<sup>[111]</sup>.

The aim of incorporating a nanometer sized phase into a matrix of e.g. a polymer is to drastically improve material properties or even achieve new ones, which would not be possible by use of a micrometer sized phase. This behavior is often called a "nano-effect". Admittedly in some cases a continuum model suffices to explain the properties gained<sup>[109]</sup>. However "nano-effect" paraphrases the fact that nanoparticles possess extremely high surface area to volume ratios and extreme aspect ratios<sup>[111]</sup>. This becomes clear considering the typical geometries of phases used to enhance material properties in composites (see figure 3.17).

## 3.2 Membrane materials

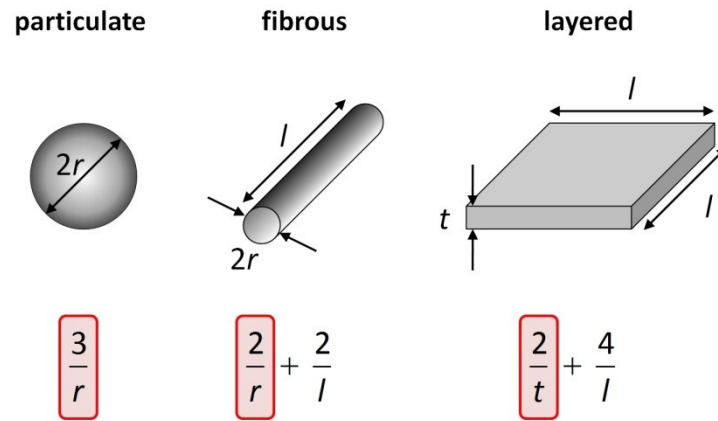


Figure 3.17: Influence of particle geometry on the surface to volume ratio for different shaped materials used for nanocomposites <sup>based on [114]</sup>.

In all cases the red highlighted term has a dominant influence on the surface area to volume ratio. For fibrous and layered materials the ratio also depends on their length, but this term is usually disregarded as it has a much smaller influence. Besides this dimension and thus also its influence on the ratio are often similar in micro- and nanoscale objects. Considering only the highlighted term the surface area to volume ratio will change by three orders of magnitude when decreasing the diameter of particulate and fibrous particles or the thickness of a layered material<sup>[114]</sup>. This results in a much lower loading requirement for nanocomposites which is an intrinsic advantage over microcomposites. The effects achieved by adding between 1 and 10 vol.-% of isotropic nanoparticles can be compared to an addition of 15 – 40 vol.-% when the same but micrometer scaled filler is used<sup>[110]</sup>. This is not only economically interesting as it increases profits. It is also important with regard to the fabrication of films and coatings where optical transparency is required. Here avoidance of the strong light scattering influence of micrometer sized particles and a reduction of filler loadings are obvious advantages<sup>[115]</sup>.

Generally the incorporation of nanoparticles shall enhance physical (barrier properties, erosion resistance, reduced flammability), thermochemical (dimensional stability under heat, thermal expansion coefficient) or processing (melt strength, surface texture) properties of composite materials<sup>[110]</sup>. In addition new characteristics can be introduced such as electrical conductivity or catalytic activity<sup>[109]</sup>. In polymer nanocomposites the nanoparticles can also influence crystallization, glass transition temperature or free volume of the polymeric matrix. Also the aging of the polymer can be altered due to modified diffusion characteristics of the material<sup>[109]</sup>. From this follows a broad field of potential applications for nanocomposites. Most prominently these are applications in electronics or computers (sensors, data storage), high-performance materials (aerospace, transportation, sports), health and medicine (tissue engineering), energy (fuel cells) or membrane separation<sup>[109,111]</sup>.

Admittedly it has been pointed out by several groups that the properties of nanocomposites are strongly dependent on the material morphology<sup>[110,116]</sup>. Practically a certain degree of disorder cannot be avoided even by thorough dispersion of the filler in the matrix. Therefore the properties usually obtained with nanocomposites lag behind what ideal filler morphology would predict<sup>[116]</sup>. Especially in potential high-technology applications a random distribution of nanoparticles prevents the necessary optimal electrical, thermal or optical properties<sup>[110]</sup>. Mostly inadequate dispersion, poor nanoparticle alignment, insufficient load transfer (between phases or to the interior of the

filler) as well as process-related failures are called to account when nanocomposite characteristics fall behind expectation<sup>[116]</sup>. Today many different approaches towards the synthesis of tailored or aligned nanocomposites are being investigated. Most of them apply supramolecular chemistry and i.a. self-assembly of molecules and nanoparticles<sup>[110]</sup>. However in this work nanocomposites with randomly dispersed fillers were investigated.

#### 3.2.4.1 Hybrid materials

The widest accepted definition of a hybrid material describes it as a material composed of two components merged on the molecular level<sup>[117]</sup>. The two components, of which one usually is of organic and the other of inorganic nature, are individual matrices or building blocks. Matrices on the one hand can either be crystalline or amorphous, organic or inorganic materials. Building blocks on the other hand are molecules or macromolecules, particles or fibers. Moreover the interaction between these components can be weak or strong. Taking into account these multifarious possibilities of different combinations the term hybrid material describes a very wide range of materials<sup>[117]</sup>. Also nanocomposites are included by this definition as will be shown. Depending on the strength of interaction between the two components hybrid materials are more precisely divided into two classes. Class I hybrid materials possess weak interaction, while class II encompasses those with strong chemical interaction<sup>[117]</sup>. From Van-der-Waals over hydrogen bonding to coordinative, ionic and covalent bonds the degree of interaction increases and sometimes energy ranges overlap. The transition between class I and II hybrid materials can therefore be seamless. A further subdivision based on structural qualities leads to the four kinds of hybrid materials shown in figure 3.18<sup>[117]</sup>.

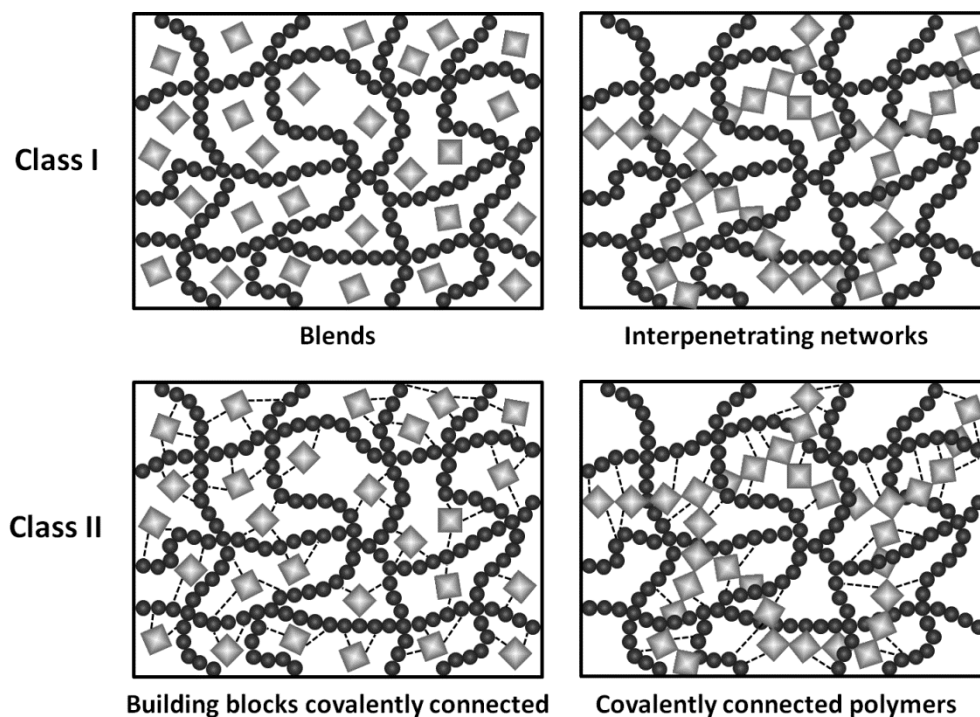


Figure 3.18: Overview of the four types of hybrid materials based on [117].

The two classes I and II of hybrid materials are subdivided into two structures each. When no strong interaction is found between the organic and inorganic building blocks of a hybrid material (class I) it

## 3.2 Membrane materials

---

is a blend, if one of the phases is present as a discrete moiety or it can be an interpenetrating network, if both phases are polymers. Class II hybrid materials can be composed of detached building blocks covalently connected with the matrix or of covalently interconnected organic and inorganic polymers<sup>[117]</sup>. According to these classifications, nanocomposites are included within the definition of hybrid materials. In most cases they are an example for blends described under class I hybrid materials. But nanocomposites can also be examples of class II hybrids if the nanoparticles are covalently connected to the matrix. Despite the overlapping definitions however, a differing use of the two terms is found in literature. Materials are commonly referred to as hybrid materials when the inorganic moiety is formed in-situ during the preparation (by e.g. sol-gel reactions). The term nanocomposite on the contrary is used when nanometer-sized materials such as CNTs, clays or nanoparticles are applied to form the inorganic phase.

### 3.2.5 Mixed matrix membranes

The two most widely used membrane materials are polymers and inorganic materials. With regard to membrane preparation they each provide different properties including advantages and drawbacks. Polymers on the one hand possess an outstanding processability allowing easy membrane fabrication. Together with at the same time low expenses this makes polymers commercially interesting and commonly well used for membrane processes despite their limited separation characteristics<sup>[27,28]</sup>. Inorganic materials on the other hand exhibit surpassing separation characteristics and the ability to withstand extreme temperature and pressure conditions. However their application is rather limited which is due to their challenging synthesis and high costs involved<sup>[118,119]</sup>. Mixed matrix membranes (MMMs) have been largely investigated as a method to combine the advantages of both materials and compensate their disadvantages respectively<sup>[120]</sup>. By incorporating a dispersed inorganic filler into a polymer matrix a membrane material shall be obtained that combines the high selectivity known from inorganic materials and the eligible mechanical properties of polymers<sup>[121]</sup>. Although as well inorganic-inorganic MMMs have been reported, where a zeolitic filler was incorporated into an amorphous silica matrix<sup>[122]</sup>, the matrix generally consists of a polymer. As filler usually micro- or nanometer scaled particles are used that can be either crystalline or amorphous. This means a MMM containing a nanosized filler phase is a nanocomposite or hybrid material respectively according to the definitions presented above. As stated before in this work the separation mechanism of the two phases in MMMs can differ depending on the materials used. The separation in inorganic materials is usually based on size-exclusion while for polymers the solution-diffusion model is applied. However the organic matrix generally outweighs the filler and with it the solution-diffusion model dominates<sup>[10]</sup>.

## 4 Experimental section

The experimental section covers all methods and techniques used in this work and describes what materials have been synthesized and how. In the beginning the synthesis of the copolyimide, the titanosilicate and the functionalization of the MWCNTs are described followed by the membrane preparation methods. Subsequently the techniques used to characterize the starting materials and membranes are specified. Eventually the experiments performed to determine membrane separation characteristics are explained. This covers the realization of gas permeation and pervaporation experiments as well as the delineation of the gas permeation and pervaporation gadgets used.

### 4.1 Copolyimide synthesis

The monomers were purchased at the companies as stated in table 4.1 and have been sublimated prior to their use as reactants in a vacuum of  $1 \times 10^{-3}$  mbar and at the temperatures listed below.

**Table 4.1: Details on used monomers and their purification methods**

Abbreviation	Monomer name	Purity	Producer	Sublimation temperature	Melting point
6FDA	4,4'-hexafluoroisopropylidene diphthalic anhydride	99 %	Alfa Aesar	215 °C	224 – 247 °C
4MPD	2,3,5,6-tetramethyl-1,4-phenylene diamine	purum, $\geq 99$ %	Fluka	195 °C	150 – 155 °C
DABA	3,5-diamino benzoic acid	$\geq 99$ %	Merck	105 °C	239 – 242 °C

The nitrogen used in the reaction was dried by first passing it through a column filled with orange gel and then a column filled with siccant (with indicator, Merck). The solvent dimethylacetamide (DMAc, synthesis grade, Merck) was purified using a dephlegmator where it was also dried over calcium hydride (92 %, Alfa Aesar). Prior to distillation the mixture has been stirred over night. A head fraction of roughly 30 mL is discarded and then the solvent used for the synthesis was distilled. For the chemical imidization triethylamine (99%, Grüssing) and acetic acid anhydride (p.a.,  $\geq 99\%$ ) have been used. For the precipitation bath and the subsequent washing of the polymer demineralized water and technical grade ethanol respectively were used.

All polymer batches have been synthesized according to the following standard synthesis procedure which is presented here exemplarily with amounts to obtain a maximum of 2.85 g (1.0 mmol) of the copolyimide at 100 % yield. The amounts used for the individual batches prepared in this work differ and are shown in detail in the appendix.

A two-neck-flask was heated out under nitrogen atmosphere and charged with 0.657 g (4.00 mmol) 4MPD and 0.152 g (1.00 mmol) DABA using 4 mL dimethylacetamide (DMAc). When the diamines were dissolved a total amount of 2.221 g (5.00 mmol) 6FDA were added slowly and rinsed with 3 mL

## ***4.2 Functionalization of carbon nanotubes***

---

of DMAc. Now the flask was covered with aluminum foil to protect the dissolved monomers from photochemical degradation. The reaction mixture was subsequently stirred over night during which it became highly viscous. Therefore another 5 mL of DMAc were added to the mixture which was then stirred for 4 h. After this a mixture of 2.079 mL (15.00 mmol) triethylamine and 1.418 mL (15.00 mmol) acetic acid anhydride was added and the chemical imidization was conducted while stirring the reaction mixture at 120 °C for 30 min. As soon as the reaction mixture has cooled down to room temperature the polymer was precipitated into a 1:1 mixture of ethanol and distilled water and subsequently milled to obtain a white powder. After washing with ethanol the polymer was at first dried at room temperature for one day. Final drying was conducted at 150 °C and 80 mbar for two days to give 2.690 g (0.94 mmol; yield: 94 %) of the copolyimide.

## **4.2 Functionalization of carbon nanotubes**

As stated previously the aim of the CNT treatment is to obtain hydroxyl-functionalized nanotubes. For this two subsequent reactions were necessary. First the oxidation of defect group on the CNTs to obtain carboxyl acid groups and second the reduction of these groups to hydroxyl groups.

### **4.2.1 Preparation of MWCNT-COOH**

The MWCNTs (Baytubes® C 150 P; Bayer Material Science) were used without further purification. In a small beaker 500 mg MWCNTs were dispersed in 20 mL distilled water using mild ultrasound treatment (Branson Sonifier W-450 D, 2 minutes at 20 % amplitude). The black dispersion was placed, together with 50 mL of concentrated nitric acid (65 %, p.a., VWR), into a 250 mL one neck flask, which was equipped with a reflux condenser. After refluxing at 120 °C for 24 hours the flask was cooled down to room temperature. In order to set a neutral pH value the MWCNTs were centrifuged at 9000 rpm for 10 minutes and subsequently washed with distilled water. This procedure was repeated three times with water and another three times with acetone to remove the remaining water. After drying at 150 °C for two days 376 mg MWCNT-COOH were obtained.

### **4.2.2 Preparation of MWCNT-OH**

200 mg of MWCNT-COOH were dispersed in 30 mL tetrahydrofuran (THF, p.a., Fluka) using mild ultrasound treatment (5 minutes at 10 % amplitude), while cooling with an ice bath. By use of further 20 mL THF the dispersion was transferred into a 100 mL two neck flask which was heated out previously under nitrogen atmosphere. Then lithium aluminium hydride (1.0 g, synthesis grade, Merck) was added and the mixture was subsequently refluxed at 80 °C for 2 hours under nitrogen atmosphere. After cooling down to room temperature 50 mL distilled water were added very slowly while the mixture was cooled with a water bath. The reaction mixture was acidified with 10 mL concentrated hydrochloric acid and stirred for 10 min. The reduced MWCNTs were washed with water and centrifuged at 9000 rpm three times to set a neutral pH. Finally another three washing and centrifugation steps are conducted using acetone. After drying for one day at 100 °C and subsequently for two days at 150 °C and 80 mbar, 154 mg MWCNT-OH were obtained as a fine black powder.

### 4.3 Preparation and modification of titanosilicate JDF-L1

In this chapter the synthesis and processing of the titanosilicate JDF-L1 are presented. The hydrothermal synthesis is described along with the disaggregation and the ion-exchange steps.

#### 4.3.1 JDF-L1 synthesis

The titanosilicate is synthesized in a hydrothermal reaction. First by combination of two solutions (A and B) a gel is prepared, which then forms the desired solid at elevated temperature in an autoclave.

Solution A consists of 10.05 g sodium silicate solution (27 wt.-% SiO<sub>2</sub>, 8 wt.-% Na<sub>2</sub>O, 65 wt.-% H<sub>2</sub>O; Merck), 1.418 g sodium hydroxide (99%, pellets; Scharlab) and 6.551 g water (demineralised). Solution B contains 6.7514 mL titanium (III) chloride solution (20 % TiCl<sub>3</sub> solution in 3 % HCl; Alfa Aesar). These two solutions are combined and a dark purple gel is formed that solidifies rapidly. The so formed gel is re-fluidized by stirring it at first for 5 minutes very vigorously and then 5 minutes at reduced speed. Now 0.077 g well grinded JDF-L1 is added as seed crystals and the mixture is stirred for another 45 minutes. Following this the homogeneity and thus the completeness of the reaction is controlled. For this purpose a small amount of the reaction mixture is taken and diluted in a ratio of 1:100 with demineralised water. If the pH-value is close to 10.5 the reaction in the gel can be considered complete and the mixture is transferred into the autoclave. Before closing the mixture inside the autoclave is degassed for 5 minutes in an ultrasonic bath. Synthesis is carried out in an oven at 230 °C for 24 hours. After this time the autoclave is cooled down under running water for 15 minutes. The reaction product, a white crystalline powder, is subsequently washed three times with demineralised water and then dried for 10 hours at 100 °C.

#### 4.3.2 Disaggregation of JDF-L1

The disaggregation of JDF-L1 was conducted using an aqueous solution of cetrimonium bromide (hexadecyltrimethylammonium bromide, CTABr) and tetrapropylammonium hydroxide (TPAOH). In a 100 mL one necked flask 2.9 g (7.96 mmol) CTABr (powder, ≥97%, Sigma-Aldrich) and 5.9 mL (11.61 mmol) TPAOH (40% in H<sub>2</sub>O, Sigma-Aldrich) are mixed with 6.13 mL demineralised water. Then 0.5 g JDF-L1 are added and the mixture is stirred vigorously for 16 hours at 80 °C. After it was left to cool down to room temperature the sediment is extracted and washed at least three times with demineralised water via centrifugation at 10,000 rpm for 10 minutes. The wet product is finally dried at 100 °C for 24 hours.

#### 4.3.3 Exchange of interlamellar cations

The interlamellar sodium cations in JDF-L1 were interchanged by exposing the disaggregated material to an amply excess of another cation in aqueous solution. Experiments were conducted to exchange sodium with the following five cations: H<sup>+</sup>, Li<sup>+</sup>, K<sup>+</sup>, Mg<sup>2+</sup> and Ca<sup>2+</sup>. No standard procedure exists covering all of the aforementioned. Certain reaction conditions are different for different cations. Basically the reaction was conducted by adding between 150 and 500 mg of the titanosilicate to 50 mL of an aqueous solution containing an excess of the cation to be interchanged

## 4.4 Membrane fabrication

---

with and subsequent stirring for varying times. This was approximately 20 minutes in case of interchanging  $\text{Na}^+$  with  $\text{H}^+$ . Here the titanosilicate has to be exposed to an acidic solution. However it is known that in too strong acidic media JDF-L1 loses its structural stability resulting in the formation of amorphous material. In order to keep this effect minimal a weak acid (acetic acid) diluted to a pH value of not lower than 3.5 was used and the pH value was monitored during the reaction. As soon as the solution reached a pH between 6 and 7 (around 10 minutes) it was carefully acidified once more to pH 4 and stirred for 10 more minutes until the pH remained unchanged and the reaction was considered finished. In case of the other cations the titanosilicate was added to a solution of the respective chloride salt and the stirring time varied between 4 and 24 hours. The used alkaline and alkaline earth chloride salts allowed a much higher excess of the cation to be interchanged with due to their high solubility. In this work a 80-fold excess of the new cation in relation to interlamellar sodium was used. As salts lithium chloride ( $\geq 99\%$ ; Sigma Aldrich), potassium chloride (Panreac, 99.5%), calcium chloride dihydrate ( $\geq 99\%$ ; Sigma Aldrich) and magnesium chloride anhydrous ( $\geq 99\%$ ; Sigma Aldrich) respectively were used. In both cases (weak acid, chloride salt) the extraction of the exchanged material was carried out via three subsequent steps of centrifugation for 10 minutes at 10,000 rpm and washing with demineralised water. The detailed preparation methods of the individually synthesised batches can be found in the appendix (see chapter 6.2).

### 4.3.4 Simultaneous disaggregation and cation exchange

Based on the finding of Rubio<sup>[123]</sup> that as-synthesized JDF-L1 can also be disaggregated using sodium hydroxide a reaction was tested to perform disaggregation and ion exchange in one step. Here the following procedure was applied. In a 50 mL one necked flask a one molar solution of different bases is prepared. Then 500 mg of as-synthesized JDF-L1 are added and the mixture is stirred for 16 hours at 80 °C. After letting the flask cool down to room temperature the sediment is extracted and washed at least three times with demineralised water via centrifugation at 10,000 rpm for 10 minutes. The wet product is finally dried at 100 °C for 24 hours. As bases NaOH (pellets, 98 %, Alfa Aesar),  $\text{NH}_3$  (solution, 25 %, Panreac),  $\text{LiOH}\cdot\text{H}_2\text{O}$  (powder, 98 %, Alfa Aesar) and KOH (pellets, 85 %, Alfa Aesar) are used.

## 4.4 Membrane fabrication

Though all membranes comprise the same copolyimide the fabrication methods differ significantly depending on whether a pure polymer or e.g. a mixed matrix membrane was to be prepared. Also different kinds of filler materials required different dispersion methods. The membrane fabrication methods used in this work are given below. In all cases the polymer 6FDA-4MPD/6FDA-DABA 4:1 was used. To simplify matters however only the much shorter term “copolyimide” is used in the following. At this point some basic information applying to all membrane preparation methods is given. The polymer solution had to be filtered using a syringe filter (PTFE, 0.45  $\mu\text{m}$  pore size, Carl Roth). This step is necessary, because during the synthesis and subsequent processing of the polymer powder dust particles are usually attracted. These hamper defect free film formation if not removed. Subsequently the filter was washed out using small additional amounts of solvent in order to reduce the loss of polymer solution due to the dead volume of the filter (100  $\mu\text{L}$  according to manufacture

specifications). As the mould for membrane casting different diameter metal rings were used. They were either placed on a PET sheet (Hostaphan® RN, colourless transparent, thickness 190 µm) or on a commercial mirror tile (20 x 20 cm). In order to keep away dust particles from contaminating the casting solution the rings were covered with a funnel whose open end was lightly plugged with tissue paper after casting of the solution.

### 4.4.1 Preparation of copolyimide membranes

In a 20 mL snap-cap vial 640 mg copolyimide (0.225 mmol) were dissolved in 6.5 mL THF and the solution was filtered through a syringe filter. Subsequently the filter was rinsed with additional 1.5 mL of THF. Now 4 mL each of the filtered solution were cast into metal rings (diameter 10 cm) lying on a piece of PET sheet, which then were covered with a funnel. After evaporation of the solvent the membranes were dried for 24 hours at 150 °C and 80 mbar in a vacuum oven.

### 4.4.2 Preparation of mixed matrix membranes

Not all investigated MMMs contained the same amount of inorganic material. However after development of the following successful general preparation method, all conditions apart from the filler load were retained for every MMM prepared within this work. Below a method is given exemplarily for the preparation of a membrane containing 8 wt.-% of inorganic material.

The copolyimide powder (1.6 g, 0.526 mmol) was dissolved in a 20 mL snap-cap vial using 16 mL THF. Subsequently the solution was filtered through a syringe filter (PTFE, 0.45 µm pore size) and the filter rinsed with additional 2 mL of THF. After portioning the solution into two snap-cap vials (9 mL each), 64 mg JDF L1 were added to both parts and the mixture was stirred over night. To ensure good dispersion the casting solution was now treated in the ultrasound bath (ELMA Transsonic 310, 35 Hz) for 30 minutes and afterwards stirred for another 30 min. These steps were repeated three times in total. Now 4 mL each of the mixture were cast into metal rings (diameter 7.5 cm) on a PET sheet and covered with a funnel. After evaporation of the solvent the membranes were dried for 24 hours at 150 °C and 80 mbar.

### 4.4.3 Preparation of MWCNT/copolyimide membranes

As for MMMs also in this case membranes containing different filler loads were prepared. After a successful preparation method was found no parameters except of the filler amounts added were altered. In the following the method is given for the preparation of a MWCNT/copolyimide membrane containing 1 wt.-% of MWCNT.

In a 20 mL snap-cap vial 0.7 g of the copolyimide (0.246 mmol) were dissolved using 10 mL THF and filtered through a syringe filter (PTFE, 0.45 µm pore size) which was subsequently rinsed with 5 mL THF. Now 7 mg of MWCNT-OH were added and the mixture was dispersed using ultra sound treatment (Sonifier 450 W) for 30 minutes at 30 % amplitude (results in 10 % power, ca. 20 W), while cooling the vial with an ice bath. After this the mixtures was stirred for 30 minutes at room temperature. These steps were repeated three times in this order. Finally two membranes were prepared from this mixture by casting 6 mL each into metal rings (diameter 10 cm) lying on a mirror

## 4.5 Characterization methods

tile. They were covered with funnels and left to evaporate the solvent over night. Final drying was conducted in the vacuum oven at 80 mbar and 150 °C for three days.

## 4.5 Characterization methods

The following chapter sums up the methods used in this work to characterize the different materials. Also, whenever this is not self explanatory, it is pointed out why and how a specific technique was used.

### 4.5.1 Characterization of basic materials

In case of the basic materials for membrane preparation it was not only necessary to find out whether or not a desired compound was synthesized. Furthermore it was important to determine several pivotal properties of the used batches. In some cases individual batches can show strong derivation in a certain characteristic, without necessarily being considered different materials. Exemplarily the molecular weight of the copolyimide should be mentioned here. Therefore it was obligatory to diagnose these properties so that possible deviant batches could be excluded.

#### 4.5.1.1 <sup>1</sup>H-NMR spectroscopy

NMR spectra were collected using a Bruker FT-NMR DRX 500. As the solvent tetrahydrofuran-d<sub>8</sub> (99.5 %, Deutero) was used. The aim of using this method was to determine the ratio of the diamino monomers in copolyimide batches. This is possible because the polymer shows aromatic as well as aliphatic <sup>1</sup>H-signals and the ratio changes depending on the content of the two diamino monomers in the copolymer structure. Figure 4.1 shows an idealized repeating unit of 6FDA-4MPD/6FDA-DABA 4:1 copolyimide with the protons numbered for allocation of the peaks. Protons indistinguishable by <sup>1</sup>H-NMR spectroscopy are marked by the same number.

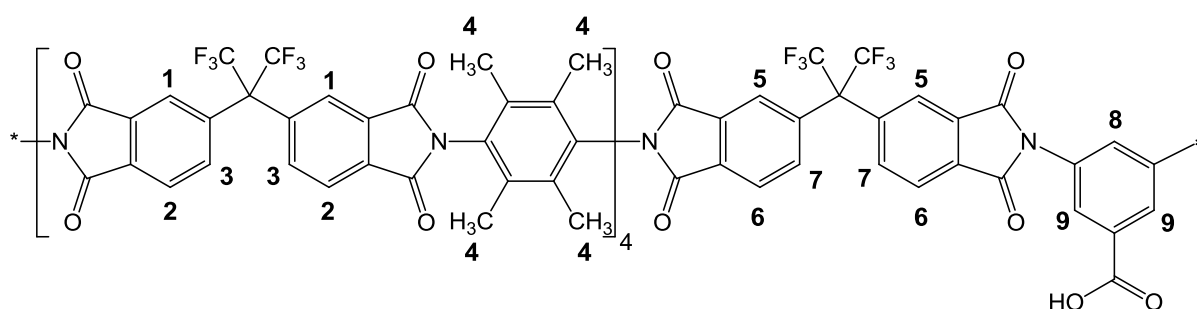


Figure 4.1: Ideal structure of the copolyimide 6FDA-4MPD/6FDA-DABA 4:1 with the proton sites numbered.

As it can be seen in the structure a repeating unit possesses 33 aromatic (#1,#2,#3 and #5 - #9) and 48 (#4) aliphatic protons. This theoretical ratio of 0.6875 should also be found in the NMR spectra as the ratio of the integrals of the aromatic and aliphatic protons. In figure 4.2 one spectrum of the copolyimide is shown exemplarily.

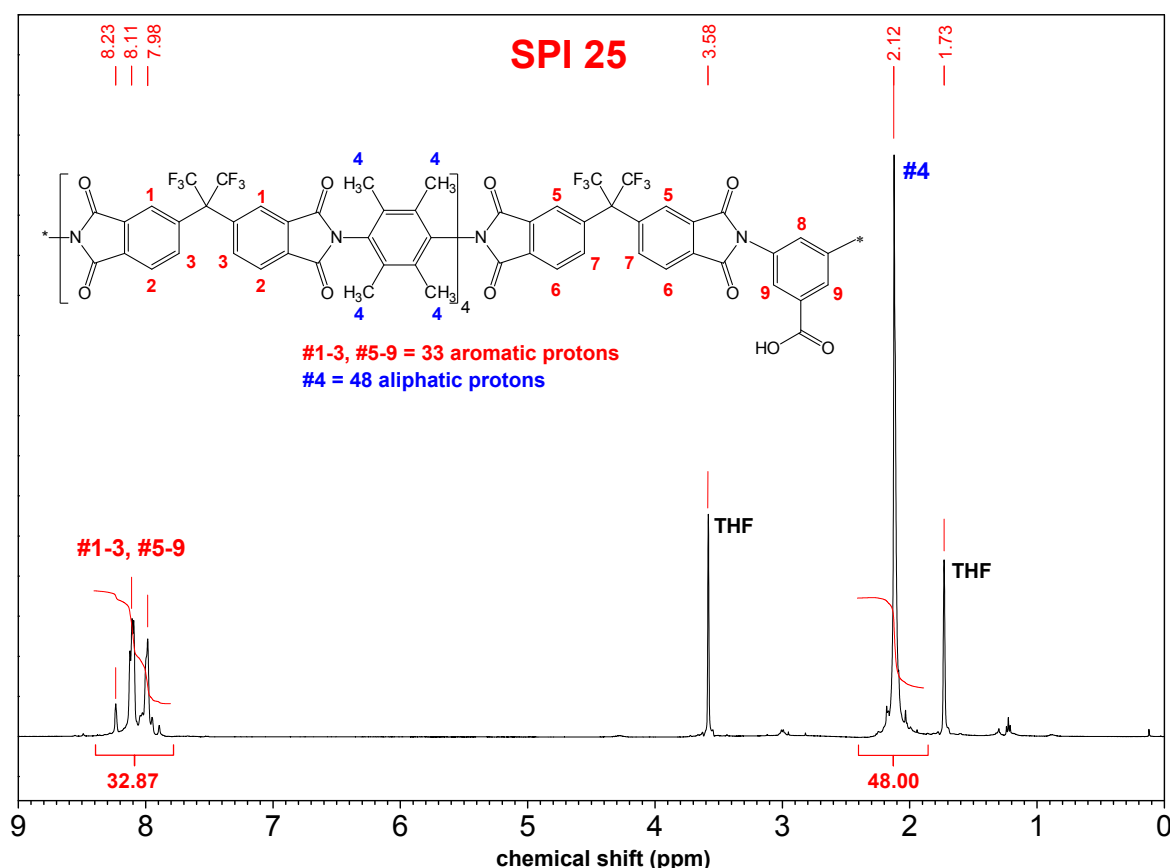


Figure 4.2: Evaluated 500 MHz  $^1\text{H}$ -NMR spectrum of batch SPI 25 of the copolyimide 6FDA-4MPD/6FDA-DABA 4:1.

For convenience the integral of the aliphatic protons was set to 48 in all spectra. In this polymer batch an experimental aromatic/aliphatic ratio of 0.6848 was found (32.87/48.00). On a percentage basis this equals a difference of 0.39 % from the theoretical ratio. From the ratio of integral also the actual diamino ratio of an individual polymer batch can be calculated. Therefore the equations to calculate the number of the aromatic and aliphatic protons respectively are needed. In the copolyimide of the type 6FDA-4MPD/6FDA-DABA  $m:n$  there are two structural elements: 6FDA-4MPD which appears  $m$ -times and 6FDA-DABA, which appears  $n$ -times. The first element contains 6 aromatic and 12 aliphatic protons while the second one contains only 9 aromatic protons. From this we can conclude the following equations:

$$H_{aromatic} = m \cdot 6 + n \cdot 9 \quad (4.1)$$

$$H_{aliphatic} = m \cdot 12 \quad (4.2)$$

If necessary any ratio of  $m:n$  with  $n \neq 1$  can be expressed as  $x:1$  by means of factorization, which reduces the equations to only one variable. This step however is not necessary in the case of 4:1. We set in  $n=1$  and obtain:

$$H_{aromatic} = m \cdot 6 + 9 \quad (4.3)$$

$$H_{aliphatic} = m \cdot 12 \quad (4.4)$$

The ratio of aromatic to aliphatic protons is therefore calculated by the two equations combined as follows:

## 4.5 Characterization methods

---

$$\frac{H_{aromatic}}{H_{aliphatic}} = \frac{6m + 9}{12m} \quad (4.5)$$

Writing this in terms of  $m$  gives us:

$$m = \frac{9}{12 \cdot \left(\frac{H_{aromatic}}{H_{aliphatic}}\right) - 6} \quad (4.6)$$

With this equation the actual diamino ratio can be calculated from the proton ratio found in the NMR spectrum. For the batch, whose spectrum is shown in figure 4.2, a ratio of 4.05:1 was determined.

It has been shown by several preceding co-workers<sup>[124–126]</sup> that this form of evaluation only makes sense for lower  $m$ , like found in this work. This is because the dependency of the aromatic/aliphatic ratio on the diamino ratio  $m:n$  shows a strong asymptotic behaviour. Information derived from this calculation becomes highly delusive for increasing  $m:n$  ratio (e.g. 49:1), because then even a very small error in the limits of integration results in a strong deviation of the experimental diamino ratio.

### 4.5.1.2 Gel permeation chromatography (GPC)

Gel permeation chromatography was conducted with tetrahydrofuran as eluent in order to determine the relative molecular weight of the copolyimide batches. The equipment consisted of a SFD Castorr 153 with a SFD S 52600 sample injector. An UV-VIS (TSP UV2000) and a refractive index detector (Shodex RI-71) were used.

### 4.5.1.3 Differential scanning calorimetry (DSC)

The glass transition temperatures  $T_g$  of the polymer batches were determined using DSC. For this a Mettler Toledo DSC 822 was used in Düsseldorf and a Mettler Toledo DSC 810 was used in Zaragoza. All measurements were conducted under nitrogen atmosphere in 70  $\mu$ L aluminium crucibles. After an initial cleaning cycle up to 200 °C with 10 K/min at least two analysis cycles were conducted up to minimum 450 °C and maximum 500 °C at heating rates between 20 and 35 K/min. In Düsseldorf the  $T_g$  was determined by an operator using the software STAR<sup>e</sup> SW. In Zaragoza the same program was used, however the software module to determine  $T_g$  automatically was not installed. Therefore a graphic evaluation was necessary. This was made as shown schematically in figure 4.3. The  $T_g$  was determined individually for all segments that showed the characteristic step effect. It can be seen in figure 4.3 A at around 420 °C. Although by theory this should also be visible in the cooling segment, in all cases only the heating segments were used for evaluation of  $T_g$  because the transition was best seen there. The glass transition temperature is defined as the turning point of the graph during the above mentioned step. The turning point however can be determined graphically using the second derivative, which has to be zero at this point. Previously the segment has to be fitted in the range of the glass transition step (figure 4.3 B). This is necessary, because the experimental data consists of individual points only and does not represent a differentiable graph. Noise would affect direct derivation leading to additional zeros points. After the fitted graph is differentiated (figure 4.3 C) the zero of this function can be determined to find  $T_g$  as seen in figure 4.3 D.

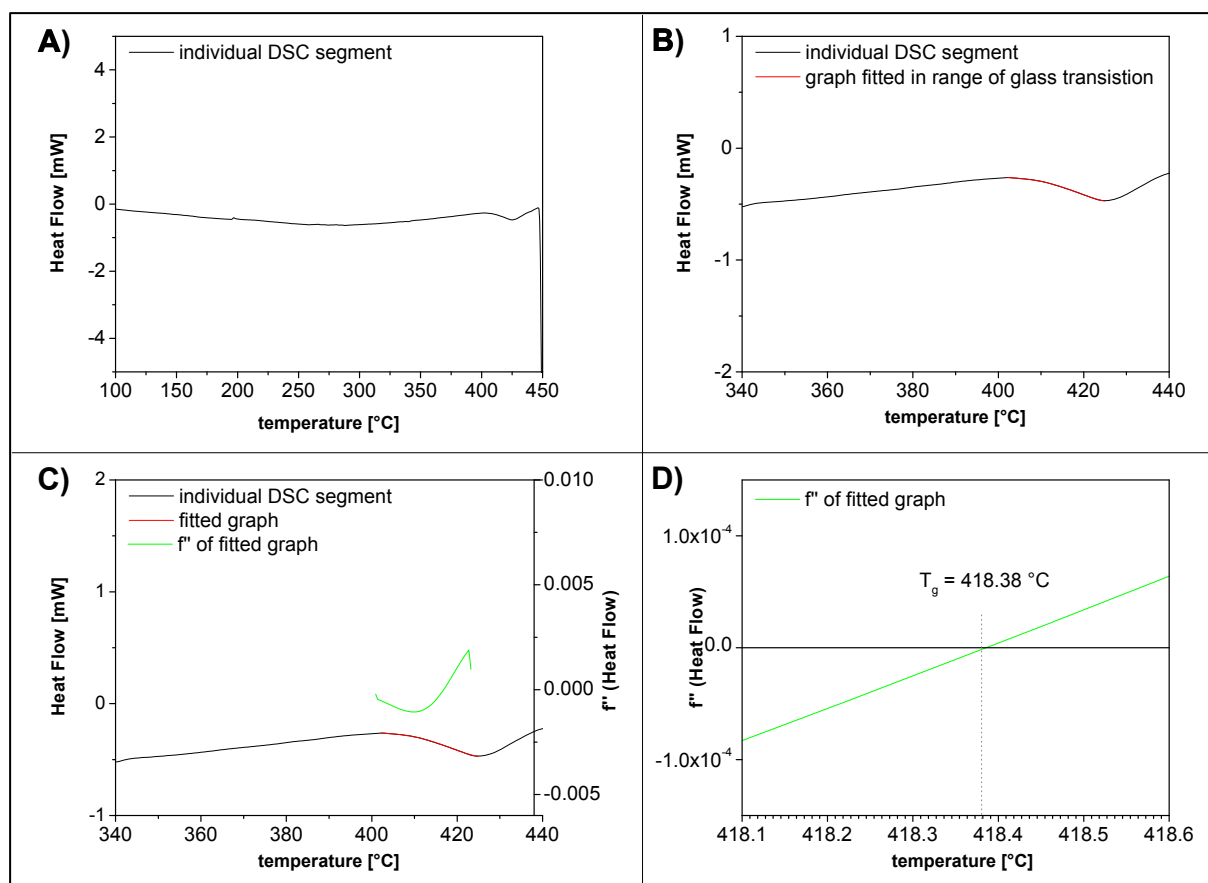


Figure 4.3: Graphic determination of the glass transition temperature from raw DSC data. A) Individual segment showing glass transition effect around 420 °C. B) Experimental data are fitted in the range of glass transition effect. C) Second derivative of fit function is drawn. D)  $T_g$  is found at zero of second derivative.

#### 4.5.1.4 Infrared spectroscopy

Infrared spectroscopy was conducted using a Shimadzu FTIR TM. The goal of using this technique was to detect functional groups in CNT samples and to gain information on the degree of functionalization. Samples were prepared as described by Mäder et al.<sup>[127]</sup>: 0.2 mg of carbon nanotubes were thoroughly mixed in a mortar with 400 mg of potassium bromide. One spectrum consisted of 200 scans at a resolution of 0.2  $\text{cm}^{-1}$ . For further processing a blank spectrum of pure KBr was subtracted and the baseline corrected.

#### 4.5.1.5 Thermogravimetric analysis

Information on the prepared membranes e.g. filler load as well as the degree of functionalization of carbon nanotubes was gained by means of thermogravimetric analysis. For this a Mettler Toledo TGA/SDTA 851e was used. Analyses were conducted in either air or nitrogen atmosphere using aluminium oxide crucibles. Subtraction of blank curves was conducted by the operating software STAR<sup>®</sup> SW, whereas evaluation of the thermograms then was carried out using Origin.

## **4.5 Characterization methods**

---

### **4.5.1.6 Electron microscopy**

Electron microscopic sample analysis was conducted at two different places. In Germany the samples were investigated at the central laboratory for scanning electron microscopy (SEM) at the University of Duisburg-Essen using an ESEM Quanta 400 FEG. In Zaragoza an ESEM Quanta 250 FEG and a TITAN STEM at the advanced microscopy laboratory of the Institute of Nanoscience of Aragon were used. The aim of electron microscopy was to obtain structural as well as morphological information of materials.

### **4.5.1.7 X-Ray diffraction**

The aim of X-ray diffraction analyses was to obtain structural information on the titanate silicate samples and their ion exchanged derivatives. The analyses were conducted by the "X-ray diffraction and fluorescence analysis" service of the support services department at the University of Zaragoza. The data was collected at room temperature on a RIGAKU "D-Max /2500" diffractometer equipped with a rotary anode. The device was operated at 40 kV and 80 mA with a copper anode and using a graphite monochromator to select the  $K_{\alpha}$  irradiation. All spectra were collected between  $2\theta$  angles of  $2.5^{\circ}$  and  $40^{\circ}$  while the step width was  $0.03^{\circ}$  (at one second per step). Moreover XRD spectra were collected using synchrotron radiation at the ESRF in Grenoble. Here the sample was filled into a capillary in powder form, which was then inserted in the beam of radiation. In order to avoid any preferential orientation of particles in the powder the capillary was rotated at elevated rounds per minute. For the analysis X-rays of the line BM25A with a wavelength of  $\lambda = 0.82637 \text{ \AA}$  were used. The spectra were collected beginning at  $2\theta$  angles of  $2^{\circ}$  and increasing up to  $30^{\circ}$  in steps of  $0.02^{\circ}$  every second<sup>[128]</sup>.

### **4.5.1.8 Elementary analysis**

Micro elementary analysis to determine oxygen content in CNTs was conducted externally at "Analytische Laboratorien" in Lindlar, Germany. An elemental analyzer "Element Rapid" equipped with a pyrolysis tube was used to completely combust the sample. The oxygen content was then detected in form of  $\text{CO}_2$  via a thermal conductivity detector. The device was operated according to the industrial standard ESTM D5291 for C,H,N-analysis.

The compositions of the titanate silicate JDF-L1 and the ion exchanged samples were analyzed via fluorescence analysis at the "X-Ray diffraction and fluorescence analysis" service of the support services department of the University of Zaragoza. A sequential x-ray fluorescence spectrometer ARL Advant XP of Thermo Electron and X-ray tubes made of rhodium were used. The program Uniquant was used for a semi quantitative analysis without standard sample (sequential analysis of elements between magnesium and uranium).

### **4.5.1.9 Adsorptive surface analyses**

The pore volume of JDF-L1 samples was analyzed by means of Ar-Adsorption. For this an ASAP 2020 equipment was used, available at the University of Zaragoza. The results were calculated with the software ASAP 2020 V3.00. Surface areas of MWCNT samples were determined via  $\text{N}_2$ -Adsorption

using a TriStar 3000 equipment. Here the software used for the calculation of results was TriStar3000 V6.08.

### 4.5.2 Membrane characterization

For the characterization of membrane films some of the above mentioned methods were used as well as further ones. The basic materials could be analyzed in powder form, while membrane samples consisted of different sized snippets of film. Powders generally are easy to apply to an analytical device. In case of membrane characterization however special sample preparation methods were required. These and any previously unmentioned characterization methods are explained in the following.

#### 4.5.2.1 Film formation tests

The film formation is tested by bending and folding a membrane film. A film is bent to half and then fold at the resulting edge. This represents an easy empirical way to obtain information on the usability of a polymer batch for membrane separation experiments. Experience has shown that a copolyimide film that does not withstand this test indicates an unsuitable polymer batch. Of every new polymer batch small films of at least 4 cm diameter were prepared as described in chapter 4.4.1 and subjected to this test.

#### 4.5.2.2 Stress-strain experiments

With stress-strain experiments the mechanical characteristics of films can be determined. In this work a Zwick/Roell Z 2.5 tensile tester was used. Membrane films with thicknesses between 30 and 70  $\mu\text{m}$  were cut into samples of 6 x 40 mm and applied to the tensile tester. The stress-strain diagrams were evaluated using Origin to obtain the Young's modulus. It is defined as the ratio of stress to strain when Hooke's Law holds. In this range the Young's modulus equates the slope of the stress-strain diagram. For the film samples this is valid at lower strains. Using Origin a linear fit was applied to the experimental data in the linear range of the stress-strain diagrams.

#### 4.5.2.3 Thermogravimetric analysis

The experimental setup was used as explained in chapter 4.5.1.5. In order to minimize the error in TGA it is best to use higher sample quantity. In the majority of cases 10 mg are considered sufficient. Filling a crucible with this amount of film snippets is difficult due to the high electrostatic behaviour of copolyimide films. The high cylindrical form of the alumina crucible used for TGA however allows applying sufficient sample quantity in from of one larger wound up snippet to the crucible. For this more convenient way a snippet of 3 cm length with a width smaller than the crucible height was cut from the sample. This was formed into a loop by holding together both ends of the snippet. Now the sample can be wound up at the middle of the loop using a pair of thin tweezers. The small coil obtained this way can easily be fitted into the crucible.

## 4.5 Characterization methods

### 4.5.2.4 Electron microscopy

In case of membrane analysis via electron microscopy especially cross-sections were of note. The facilities as described in chapter 4.5.1.6 were used. However, instead of the well known standard sample holders covered with adhesive carbon, custom-made holders from aluminium were used. These provided stable positioning of the sample in the electron microscope with the cross-section to be analyzed facing up. The samples were fixed in between two metal clamps by lying out up to three samples (each 5 mm in width) on one clamp and then joining both using two small screws. The layout of this sample holder is shown schematically in figure 4.4. The void between the two clamps adjacent to the membrane samples was filled with small amounts of conductive silver.

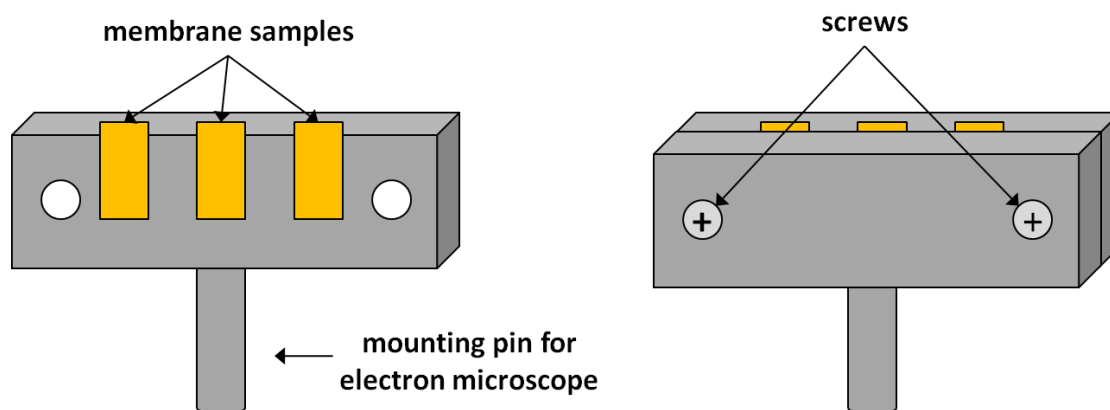


Figure 4.4: Schematic illustration of the custom-made sample holder for electron microscopy of membrane cross-sections.

In order to provide a well visible cross-section it was necessary to provide a good breaking edge of the membrane sample. For this a special breaking technique was used. At first a strip-shaped sample of 3 cm length and 0.5 cm width was cut from a membrane. Both ends of this strip were taken with tweezers to form a loop and then frozen in liquid nitrogen. After approximately one minute the sample was quickly retracted from the Dewar vessel and immediately fractured by pressing together the loop.

### 4.5.2.5 Raman spectroscopy

Raman spectra of MMMs were collected on a Jasco NSR-3100 Raman spectrometer in the University of Zaragoza. The spectrometer was equipped with ZnSe wire grid polarizers and 785 nm laser light. Spectra were recorded by irradiating the surface of the membrane with the laser and collecting with the polarizer in parallel and perpendicular orientation.



### 4.6 Pervaporation experiments

Membrane separation experiments of liquid mixtures were conducted in Düsseldorf with a custom-built pervaporation device. In the following chapters the technical set-up of this equipment is explained. Subsequently the measurement procedure is presented and finally the evaluation of the experimental data is illustrated.

#### 4.6.1 Equipment setup

The pervaporation device used in this work was constructed from scratch as a stirring cell pervaporation equipment. Like all pervaporation devices this equipment can also be divided into the feed and the permeate side, which are both separated by the membrane. Central part of this gadget is the base plate where the membrane is held over a filter paper on a porous stainless steel disk. Here feed and permeate side join. On both sides of this plate glass parts with flanges are connected and fixed with aluminium gripping jaws. On top of the base plate the two-piece glass membrane cell or stirring cell is equipped. It forms the feed side of the equipment and is composed of two glass parts with flanges joined by a metal clamping collar. Below the base plate on the permeate side a glass cap is equipped with a connection to the cooling trap and vacuum. The base plate itself lies on top of a purpose-built table serving as supporting mount. A detailed view of the base plate including the o-rings and connection of the glass parts can be found in figure 4.5.

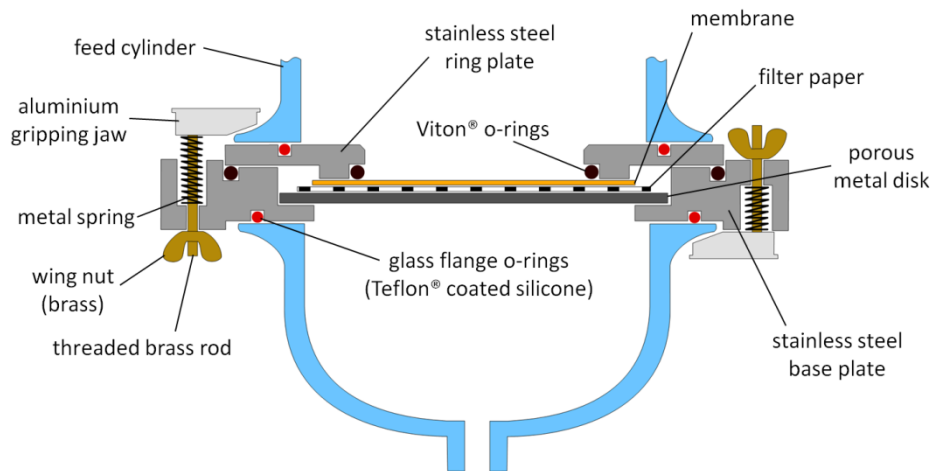


**Figure 4.5: Overview of the base plate of the pervaporation device showing the mounting of the glass parts, o-ring fittings and the membrane placement.**

The aforementioned membrane cell consists of two glass parts which are the feed cylinder and the cap. The double walled structure of the feed cylinder allows heating of the feed via a Lauda C6 laboratory thermostat which was operated with ethylene glycol. The cap possesses several glass joints where the stainless steel agitator shaft, a reflux condenser and the digital thermometer (Ebro TTX290) were connected. Also the feed sampling was conducted here via a reusable 5 mL glass syringe and a 20 cm stainless steel hollow needle. The membrane cell is filled with the feed mixture where it is stirred by the agitator (IKA RE16) and heated by the laboratory thermostat. On the permeate side a vacuum is applied using a Vacuubrand MZ 2V membrane vacuum pump providing the driving force of the mass transport. The vacuum is regulated by a Vacuubrand CVC 2 vacuum controller. To avoid untimely condensation of the permeate after passing through the membrane a

heating band is attached to the base plate and a heating cable to the stainless steel tubing which are both operated at 60 °C and regulated by a Horst HT 30 temperature controller with Ni-Cr/Ni temperature sensors. This inhibits condensation of the permeate before it reaches the sample flask in the cooling trap. Cooling in the cooling trap is achieved using a Dewar vessel with liquid nitrogen. In order to protect the vacuum pump from leaking feed in case of a membrane failure a 2 L drainage flask is equipped before the pump. A connection diagram as well as a photograph of the pervaporation device are shown in figure 4.6.

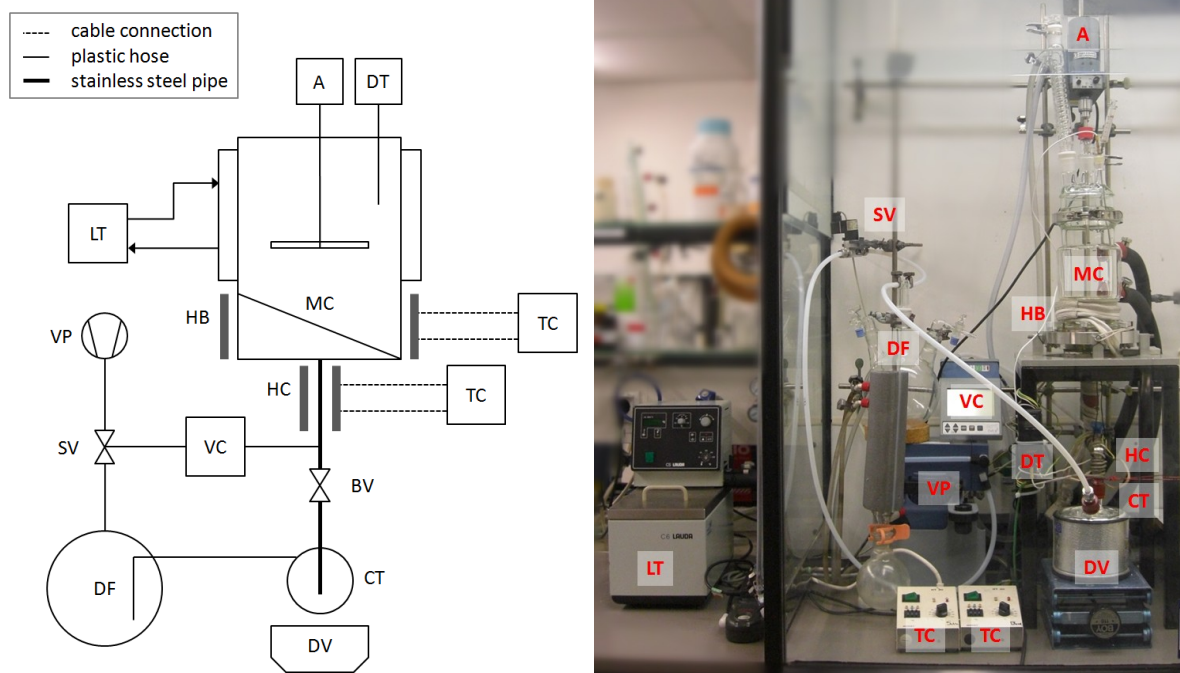


Figure 4.6: Connection diagram (left) and photograph (right) of the pervaporation device used in this work.

A: agitator	BV: ball valve	CT: cooling trap
DF: drainage flask	DT: digital thermometer	DV: Dewar vessel
HB: heating band	HC: heating cable	LT: laboratory thermostat
SV: solenoid valve	TC: temperature controller	VC: vacuum controller

### 4.6.2 Measurement procedure

In the following the operation of the pervaporation device is described. At first the preparation steps necessary to bring the equipment in operational state are explained. This includes membrane insertion and the settings of temperature and vacuum. Then the replacement of the sample flask is pointed out and at last it is described how the device was deactivated.

In order to change a membrane, possible rests of feed mixture from a previous experiment had to be removed from the membrane cell. While filling was conducted using a funnel connected to one of the glass joints on the top glass cap, emptying required an additional Teflon hose and a sealable glass container. The hose was inserted into the feed and connected to the glass container using a Schott Quickfit adapter piece. By applying a weak vacuum in the glass container the feed mixture was emptied out. In order to house a new membrane in the base plate it was necessary to completely demount the feed side. Therefore the reflux condenser and the digital thermometer had to be removed from the top cap. After the agitator was disconnected from its shaft the metal clamping collar between feed cylinder and top cap was opened so that the cap and the agitator shaft could be

## 4 Experimental section

---

removed. After unscrewing the gripping jaws of the feed cylinder the cylinder as well as the ring plate covering the membrane could be taken off. Now the porous metal disk was accessible and a membrane as well as a new filter paper could be placed on top of it. During this step a vacuum was applied on the permeate side of the device to facilitate wrinkle-free membrane placement. Next the device was closed again by undoing all above mentioned steps in reverse order: First the ring plate and the feed cylinder were placed back on the membrane and the gripping jaws were tightened. Then the glass cap with the agitator shaft was put back on the feed cylinder and fixed to it using the clamping collar. At last the agitator and its shaft were connected and the reflux condenser and the digital thermometer attached. After filling in the feed mixture the pervaporation device was ready to start with a new experimental series.

At first the thermostat and heating band as well as heating cable were switched on and set to the respective temperatures. Also the vacuum pump and controller were set to measurement conditions at 20 mbar with a  $\Delta p$  of 5 mbar. The thermostat was always set to a temperature slightly above the desired feed temperature, due to loss of heat to the environment. At temperatures of 70 °C and above the feed cylinder was covered with a shell made of polyurethane foam in order to reduce this heat loss. The room temperature in the laboratory was usually very constant so that the thermostat temperature was always operated according to the settings shown in table 4.2. During an experiment only small adjustment was necessary. Heating band and cable were always operated at 60 °C as explained above. Depending on the desired feed temperature it took between two and three hours for all necessary parts of the device to reach operating temperature.

**Table 4.2: List of temperature settings in order to obtain different feed temperatures (all values  $\pm 0.1$  °C).**

feed	60.0 °C	65.0 °C	70.0 °C	75.0 °C	80.0 °C	85.0 °C	90.0 °C
thermostat	62.3 °C	67.7 °C	72.6 °C	78.4 °C	84.0 °C	87.7 °C	94.7 °C

Once the equipment was ready to use the first measurement was started. For this the ball valve between cooling trap and membrane cell was closed and the vacuum controller switched to halt. In order to remove the sample flask all parts between the two valves (solenoid valve and ball valve) were now vented. The sample flask was removed and closed with screw caps and left to defrost. A fresh and previously weighted sample flask was connected and the vacuum was applied again. In order to avoid intense pressure variations on the membrane it was necessary to wait at least one minute before the ball valve was opened again. This time was needed by the vacuum pump to evacuate the previously ventilated area. Also this time was used to cool down the new sample flask in the Dewar vessel with liquid nitrogen. After 20 mbar were reached again the ball valve was opened and simultaneously a stopwatch was started. When the measurement time had elapsed the sample flask was replaced with a new one as described above.

After taking the last permeate sample an empty flask was connected. The heating equipment was switched off and the feed was left to cool down to room temperature. If the feed was going to be used again the vacuum controller was set to 100 mbar with a  $\Delta p$  of 50 mbar. Otherwise the feed was emptied out and the membrane was removed as explained previously.

### 4.6.3 Calculation of separation characteristics

The normalized flux  $J_n$  was calculated according to equation 4.8 using the permeate quantity in the sample flask  $m$ , the time of the experiment  $t$  as well as the thickness  $d$  and area  $A$  of the investigated membrane.

$$J_n = \frac{m \cdot d}{A \cdot t} \quad (4.8)$$

For all measurements the membrane area  $A$  was identical. The inner hole of the ring plate covering the membrane in the base plate of the pervaporation device had a diameter of 7 cm, thus providing a membrane area of 38.48 cm<sup>2</sup>. The thickness of the membrane  $d$  was determined using a micrometer screw as the average over 10 measurements. Here values ranged between 19 and 35 μm.

Toluene contents in the feed and permeate were determined by analyzing the refractive index  $n_D^{20}$  of the solutions. An Abbé refractometer with a small laboratory thermostat and tap water cooling was used. For toluene/cyclohexane mixtures  $n_D^{20}$  is between 1.4262 (pure cyclohexane) and 1.4969 (pure toluene). A calibration conducted at 20 °C by Lamers<sup>[129]</sup> already existed and was checked and confirmed by Schmeling recently<sup>[130]</sup>. The calibration data as well as the calibration curve are shown in figure 4.7.

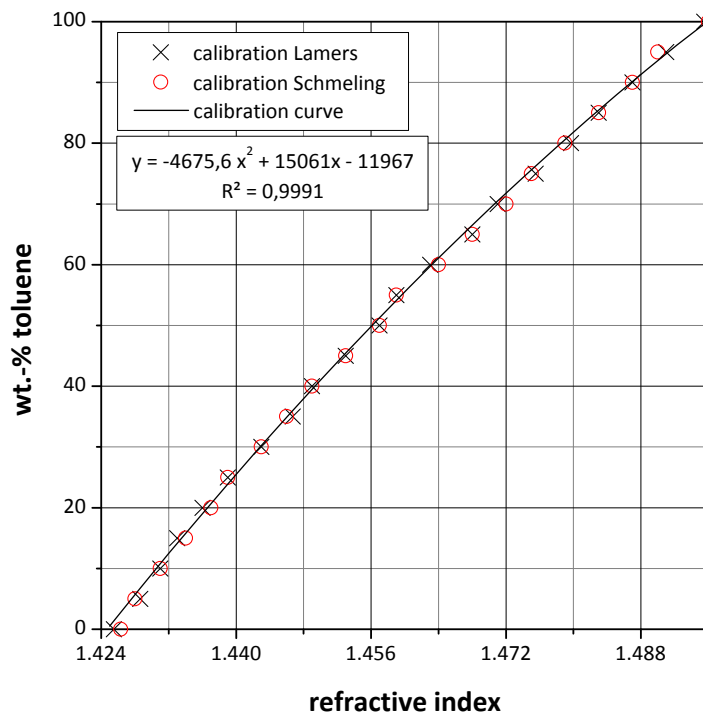


Figure 4.7: Calibration data used for the calculation of toluene content via refractive index measurement at 20 °C.

When the toluene and cyclohexane contents in feed and permeate are known, the real selectivity of the separation can be determined using equation 4.9:

$$\alpha_{real} = \frac{\left( \frac{wt. \% toluene}{wt. \% cyclohexane} \right)_{permeate}}{\left( \frac{wt. \% toluene}{wt. \% cyclohexane} \right)_{feed}} \quad (4.9)$$

### 4.7 Gas separation experiments

All membrane separation experiments with gaseous mixtures were conducted in Zaragoza with a custom built gas separation device. Technical layout and measurement procedure of this mixed gas permeation equipment are explained in the following chapters. Also it is described how the experimental data was evaluated.

#### 4.7.1 Equipment setup

The separation equipment used for mixed gas permeation experiments was constructed by the group of Prof. Coronas. A connection diagram is shown in figure 4.8. It can be seen easily that the equipment is divided into the feed and permeate side, separated by the membrane which was housed inside the central part, a stainless steel membrane cell. This cell is positioned inside an oven.

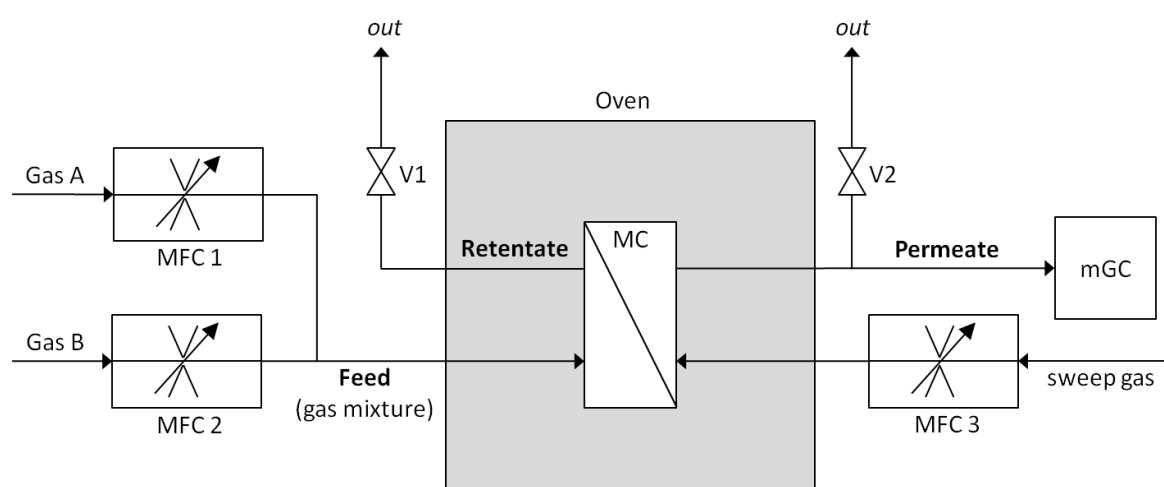


Figure 4.8: Schematic of the gas separation device used in this work.

MC: membrane cell      MFC #: mass flow controllers 1-3  
V#: ball valves 1 & 2      mGC: micro gas chromatograph

On the feed side 50/50 vol.-% oxygen/nitrogen as well as hydrogen/methane mixtures were prepared using two Alicat Scientific mass flow controllers. The feed mixtures were created from pure gas streams by setting each mass flow controller to provide a flow of 25 cm<sup>3</sup> (STP)/min, resulting in a global flow of the feed mixture of 50 cm<sup>3</sup> (STP)/min. Using the valve V1 before the retentate outlet the pressure on the feed side of the membrane was set to 340 kPa. The membrane cell consisted of two stainless steel pieces from which the bottom part offered a cavity of 4 cm in diameter to hold the membrane on top of a porous metal disc (Mott Corporation 316LSS, 20 μm nominal pore size). Like in the pervaporation equipment a filter paper was positioned between the membrane and the metal support. Top and bottom part of the membrane cell were sealed using Viton® o-rings.

The permeate side of the membrane cell was purged by a sweep gas provided by another mass flow controller. A flow of 5 cm<sup>3</sup> (STP)/min helium in oxygen/nitrogen separation experiments was applied. In hydrogen/methane experiments argon was used instead. The pressure on the permeate side had to be kept slightly above atmospheric to avoid gases from the outlet (e.g. air) to enter and contaminate the measurement. Therefore valve V2 was used to set the pressure on the permeate side to approximately 120 kPa. A computer controlled Agilent 3000A micro gas chromatograph

equipped with thermal conductivity detector was used to analyze the composition of the sweep gas stream containing the permeate.

### 4.7.2 Measurement procedure

In the following the operation of the mixed gas separation plant is explained. Generally all separation experiments were conducted at 35 °C. Prior to a new experiment a new membrane had to be inserted into the membrane cell. For this the module was placed in a small bench vice for easy removal of the eight hex head screws, used to tightly close the module. A fresh filter paper was placed on the porous metal support and on top of it the membrane which was to be analyzed. The membrane cell was then closed and mounted back into the separation plant. Now the mass flow controllers 1-3 were set to their according values. The controllers 1 and 2 were always opened and closed first. When opening the controllers this sequence allowed to immediately detect a defective membrane. In such a case no pressure rise on the feed side would be observed. Also when closing them this sequence avoids a possible pressure overload on the permeate side. This could let the membrane get out of place easily and the experiment would have to be aborted. After opening the mass flow controllers the feed and permeate pressures were adjusted using the valves V1 and V2. Now the program controlling the gas chromatograph was started and the device set to make one analysis every 10 minutes over a period of several hours. Usually after 2 hours equilibrium was achieved but the experiment was not finished until 5 to 6 hours had passed. Then the mass flow controllers were closed in the above mentioned order. When the feed and permeate pressure had declined back to atmospheric the module could be removed from the plant to allow insertion of a new membrane. If however the analysis of another gas mixture was planned, the module was left in place and instead the tubing and mass flow controllers were modified to operate under the desired gas mixture.

For some membranes a special preparation method was necessary to be able to conduct gas separation experiments. Occasionally a membrane was obtained that could not be inserted into the membrane cell as a whole. This could be necessary for two different reasons. First for some membranes strong reeling occurred during the drying process. In such cases only a part much smaller than the diameter of the membrane cell could be used. Secondly the incorporation of the titanosilicate lead to more brittle membranes, especially at higher filler loads. Sometimes such a membrane broke prior to analysis in gas separation or was so brittle that breaking could occur in the membrane cell only due to the feed pressure. In order to analyze these membranes in spite of their deficiencies they were laminated in a bigger piece of aluminium foil. Therefore a 10-15 cm long band was taken from a roll of adhesive aluminium tape (5 cm width). It was folded in the middle and a hole was cut into both layers using a circular cutter. In between these the membrane sample was placed and on the upper side the border between membrane and aluminium was sealed using epoxy resin. After drying of the resin the laminated membrane was cut to fit into the membrane cell. The membrane thickness was measured as the average over ten different spots using a micrometer screw. When the membrane was to be covered with aluminium this measurement had to be done prior to the lamination. Also this technique required a measurement of the membrane area. This was achieved by measuring the diameter of the uncovered membrane area ten times and taking the average.

## 4 Experimental section

---

### 4.7.3 Calculation of separation characteristics

Gas permeabilities were calculated on the basis of the peak areas detected by the gas chromatograph. A calibration was needed to convert peak areas into gas content in wt.-%. This calibration was checked and adjusted regularly. The individual calibration curves used in this work can be found in the appendix (see chapter 6.3). Using an excel sheet all individual analyzes of the gas chromatograph were evaluated to obtain gas permeabilities as described in the following. At first the flux  $Q_i$  of a gas component  $i$  was calculated using the mass fraction  $x_i$  obtained from the gas chromatograph. For this equation 4.10 was used and the flux and mass fraction of the sweep gas were needed.

$$Q_i = x_i \frac{Q_{sweep\ gas}}{x_{sweep\ gas}} \quad (4.10)$$

Using this value the permeability  $P_i$  of that component could be determined with aid of equation 4.11. Apart from the flux  $Q_i$  also the membrane thickness  $d$  and area  $A$ , the partial pressure difference between feed and permeate side  $\Delta p_i$  as well as the time  $t$  were needed here. As the unit of permeability the unit Barrer was used.

$$P_i = \frac{Q_i \cdot d}{A \cdot \Delta p_i \cdot t} \quad (4.11)$$

$$\left( 1 \text{ Barrer} = 10^{-10} \frac{\text{cc(STP)} \cdot \text{cm}}{\text{cm}^2 \cdot \text{cm Hg} \cdot \text{s}} \right)$$

Because the flux is calculated on basis of the sweep gas stream given in  $\text{cm}^3$  (STP)/min, as the time  $t$  60 seconds were used. The values for  $A$  and  $d$  were determined once for every membrane and  $\Delta p_i$  for every individual experiment. For all membranes the permeability was calculated as the average over all analyzes after reaching steady state. Also the selectivity for the separation of two components  $i$  and  $j$  was calculated. Here equation 4.12 was used.

$$\alpha_{i,j} = \frac{P_i}{P_j} \quad (4.12)$$

## 5 Results and discussion

In the following chapter the results of this work are presented and discussed. At first the characterization of the different basic materials is displayed. The membrane preparation and the results of membrane separation experiments are then presented separately for the MWCNT nanocomposites and the MMMs. In each section the developed membrane preparation method and characterization of the obtained membranes is described first. Subsequently the individual separation characteristics of the membranes that were investigated in the corresponding membrane processes are illustrated and discussed.

### 5.1 Basic material characterization

As pointed out in chapter 4 the basic materials were subjected to different characterization methods. The results related to the characterization of the individual materials used for membrane preparation are collected in the following.

#### 5.1.1 Copolyimide batches

In total 19 batches of the copolyimide 6FDA-4MPD/6FDA-DABA 4:1 were synthesized in this work. The copolyimide synthesis is very sensitive towards contamination which is why the outcome of different batches can vary noticeably. In order to correctly assess the comparability between individual batches the following parameters of the used polymer batches have been analyzed:

- **weight average of molecular mass  $M_w$**
- **glass transition temperature  $T_g$**
- **actual ratio of repeating units m:n**
- **film formation behavior**

The important limits for comparability in between batches and the criteria for exclusion respectively are presented in the following as well as noticeable findings regarding the analyzed parameters. A tabular overview of all batches and their corresponding characterization data can be found in the appendix in table 6.1.

The **weight averages of molecular masses** of the polymer batches prepared in this work were obtained via GPC and stretch out in the range between 30,000 and 100,000 g/mol. Correlating with  $M_w$  basically three different shapes of elution profiles are found as shown in figure 5.1.

## 5 Results and discussion

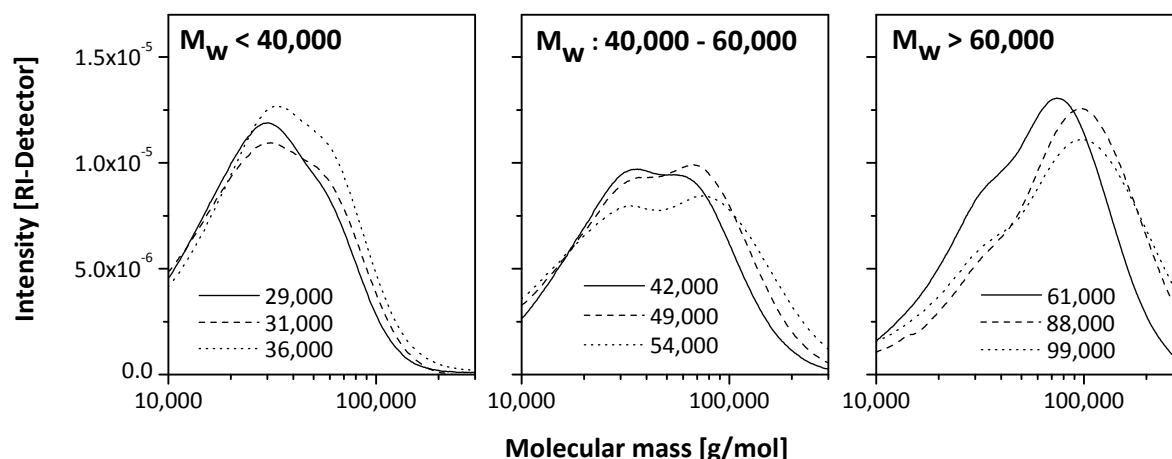


Figure 5.1: Elution profiles of copolyimide batches with different molecular weights [g/mol] prepared in this work. The bimodal graphs can be divided into three basic shapes depending on the height of  $M_w$ . For clarity reasons only a selection of the prepared copolyimide batches is presented in these graphs.

All batches possess a bimodal distribution of molecular masses with two main peaks. The first peak is found around 30,000 g/mol and a second one around 80,000 g/mol. The ratio of their intensities differs noticeably. For batches with  $M_w < 40,000$  g/mol the first peak dominates while for batches with  $M_w > 60,000$  g/mol the peak at higher masses is superior. In elution profiles of batches with  $M_w$  in between 40,000 and 60,000 g/mol the two peaks exhibit approximately the same intensity. This finding is consonant with the step-growth character of the polyimide synthesis. However it suggests that the mechanical properties of the polymer do not increase linearly with ascending  $M_w$ .

**Glass transition temperatures** were determined using DSC and values between 407 °C and 434 °C with an average (from 19 samples) of  $420.0 \pm 7.3$  °C were obtained. The data proves a high consistency of glass transition over all batches but shows no correlation between  $T_g$  and  $M_w$  as can be seen in figure 5.2. Also no dependency on other investigated parameters is found. The variation of  $T_g$  can however also be a result of contaminations in the individual polymer batches. Admittedly this means that the glass transition temperature cannot be used to obtain further information on the applicability of the polyimide batches.

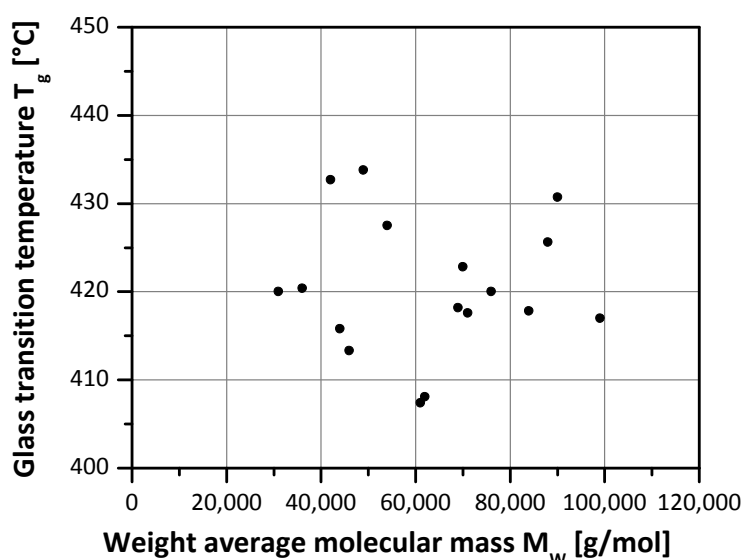


Figure 5.2: Glass transition temperatures plotted against the corresponding molecular weight averages of copolyimide batches prepared in this work. The diagram shows no relatable relationship between the two parameters.

Using  $^1\text{H-NMR}$ -spectroscopy the **actual ratio of repeating units m:n** of the copolyimide batches have been analyzed. On average (from 18 samples) a ratio of  $4.33 \pm 0.36 : 1$  is found which corresponds to an deviation of 8 % from the intended ratio of 4:1. The highest ratio is determined to be 5.56 : 1, while the lowest is 3.87 : 1. In figure 5.3 the actual diamine ratios are plotted versus the  $M_w$  of the individual batches.

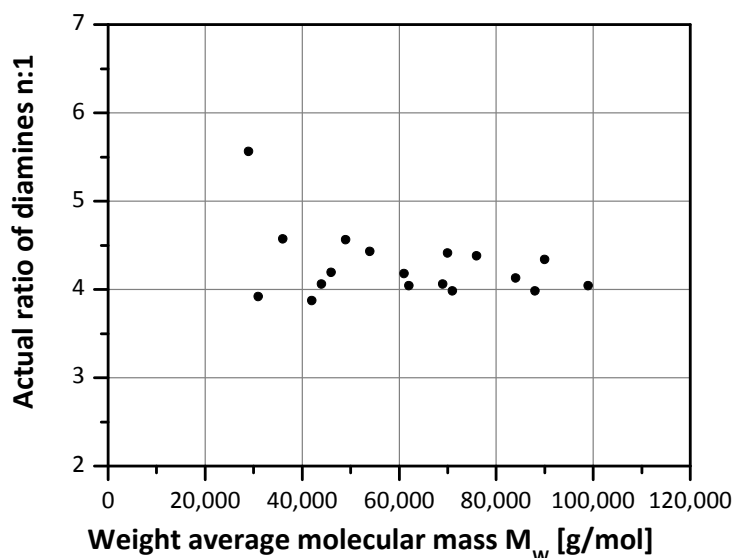


Figure 5.3: Actual ratio of diamines 4MPD/DABA versus weight average molecular mass  $M_w$

For most batches the content of 6FDA-4MPD repeating units is slightly higher than intended. Batches with lower molecular masses show a stronger deviation from the target ratio of 4:1 while at higher  $M_w$  the divergence is smaller. This is as expected from a polycondensation reaction where a high degree of polymerization is only possible with a conversion of nearly all monomers. This however requires a high purity of the reactants. Weighing errors or reactive impurities lead to a molar imbalance decreasing the maximal possible conversion and thus  $M_w$ . However the results also show that of the two diamines used in the synthesis 4MPD is the preferentially reacting one.

Beyond that every copolyimide batch was also characterized with regards to their respective **film formation behavior**. For this purpose a pure polymer film was cast which was then bended and folded. For membrane preparation only those batches were used that provided bend- and foldable pure polymer films which was the case for most batches. Polymers providing only bendable or even brittle films were discarded.

Another parameter that indicates the usability of a polymer batch is its color. In most cases the synthesis of the copolyimide 6FDA-4MPD/6FDA-DABA 4:1 yields a colorless material. However in some cases a yellow or bright yellow material is obtained. Table 5.1 shows the observed color,  $M_w$  and film formation behavior of the copolyimide batches prepared in this work.

## 5 Results and discussion

Table 5.1: Overview of film formation behavior, color and  $M_w$  of the copolyimide batches prepared in this work. Green highlighted values of  $M_w$  indicate a bend- and foldable polymer film while a red accentuation represents batches that provide only brittle films.

$M_w$ [g/mol]	Color	Batch #
29,000	yellow	SPI 18
31,000	white	SPI 24
32,000	bright yellow	SPI 28
36,000	gray beige	SPI 15
42,000	bright yellow	SPI 10
44,000	white	SPI 25
46,000	bright yellow	SPI 22
49,000	bright yellow	SPI 9
54,000	white	SPI 8
61,000	bright yellow	SPI 6

$M_w$ [g/mol]	Color	Batch #
62,000	white	SPI 2
69,000	bright yellow	SPI 13
70,000	white	SPI 11
71,000	white	SPI 23
76,000	white	SPI 4
84,000	white	SPI 26
88,000	white	SPI 5
90,000	white	SPI 1
99,000	white	SPI 7

brittle films      bend- and foldable films

All polymer batches with  $M_w$  higher than 40,000 g/mol possess good film formation behavior. This weight average molecular mass can therefore be considered as a critical minimum requisition regarding the usability of a batch of 6FDA-4MPD/6FDA-DABA 4:1 for membrane preparation. Colorless (respectively white) batches are found across the full range of molecular weights and thus no information can be deduced from this fact. On the opposite no colored batches with  $M_w$  above 70,000 g/mol were obtained. Consequently a slightly yellow color of the polymer suggests that the affected batch possesses a comparatively low  $M_w$ .

### 5.1.2 Functionalized MWCNTs

As presented before (see chapter 4.2) a two-step synthesis was used to introduce hydroxyl groups into multi walled carbon nanotubes. The individual batches of oxidized nanotubes (MWCNT-COOH) and subsequently reduced materials (MWCNT-OH) obtained in this way are distinguished by appending a consecutive letter. In order to keep track of the functionalization several analytic methods were applied to characterize the materials and visualize the introduction of functional groups.

#### 5.1.2.1 Dispersion stability of MWCNTs

The introduction of polar functional groups was expected to have impact on the dispersion stability of the nanotubes. Therefore samples of pure and functionalized MWCNTs were subjected to dispersion stability tests where 1 mg of nanotubes was dispersed in 15 mL water at low amplitude of 10 % for one minute. The re-agglomeration behavior of different samples is shown in figure 5.4.

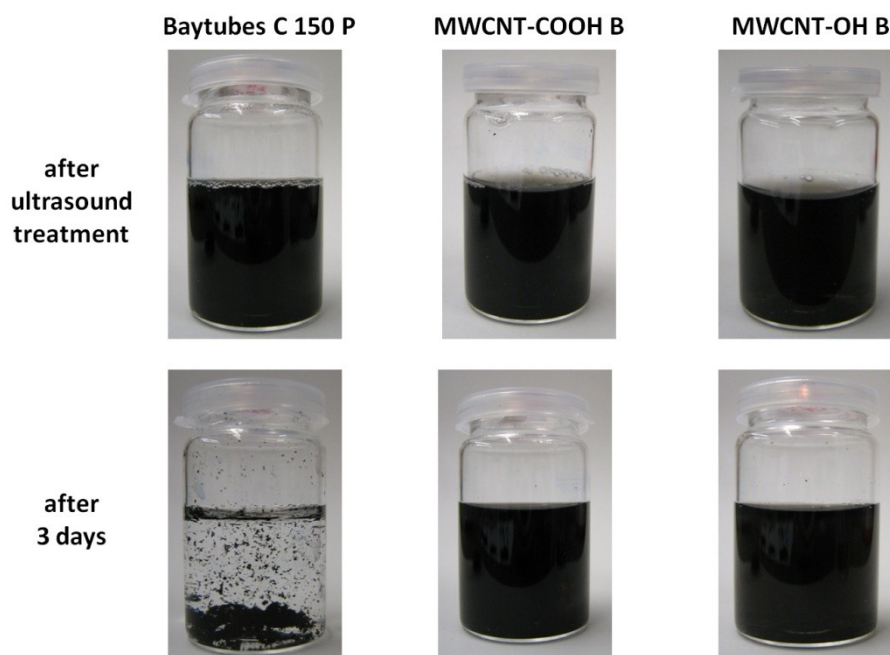


Figure 5.4: Tests regarding the agglomeration stability of MWCNT dispersions in water.

The tests show that the nanotubes in aqueous dispersions of MWCNT-COOH as well as MWCNT-OH do not agglomerate even after three days. The pure MWCNTs however are completely re-agglomerated within this period. This behavior can be explained by the introduction of polar groups on the surface of the nanotubes in MWCNT-COOH and -OH significantly increasing the dispersion stability. However this is only true for a neutral pH. At high and low pH values respectively the functionalized nanotubes agglomerate quickly (see figure 5.5). After only 30 minutes the beginning agglomeration is clearly visible and 3 days later the nanotubes are completely agglomerated.

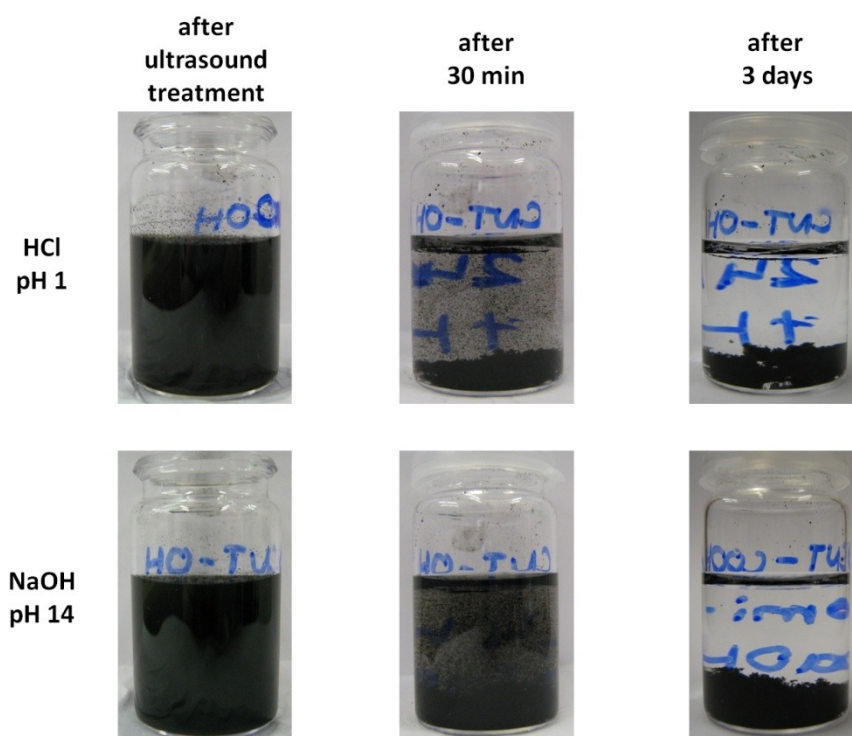


Figure 5.5: In strong acidic or basic medium the nanotubes in a dispersion of MWCNT-OH B agglomerate quickly.

## 5 Results and discussion

### 5.1.2.2 Surface analysis of MWCNTs

This assumption can be supported with results of BET analyses using nitrogen as adsorptive. The surface areas of MWCNT samples were determined. For the pure MWCNT a value of  $224.0 \text{ m}^2/\text{g}$  is found. The oxidation treatment leads to a noticeably reduced surface area of  $172.4 \text{ m}^2/\text{g}$  while the value only slightly increases to  $178.5 \text{ m}^2/\text{g}$  after the reduction treatment. This shows that functional groups are present on the surface of the nanotubes. These alter the nitrogen adsorption which leads to a significantly reduced surface area for MWCNT-COOH and MWCN-OH in comparison to pure MWCNTs.

### 5.1.2.3 Infrared spectroscopy of MWCNTs

In figure 5.1 infrared spectra of KBr-pellets from pure MWCNTs as well as two batches of MWCNT-COOH and MWCNT-OH are presented that were collected and processed as described above.

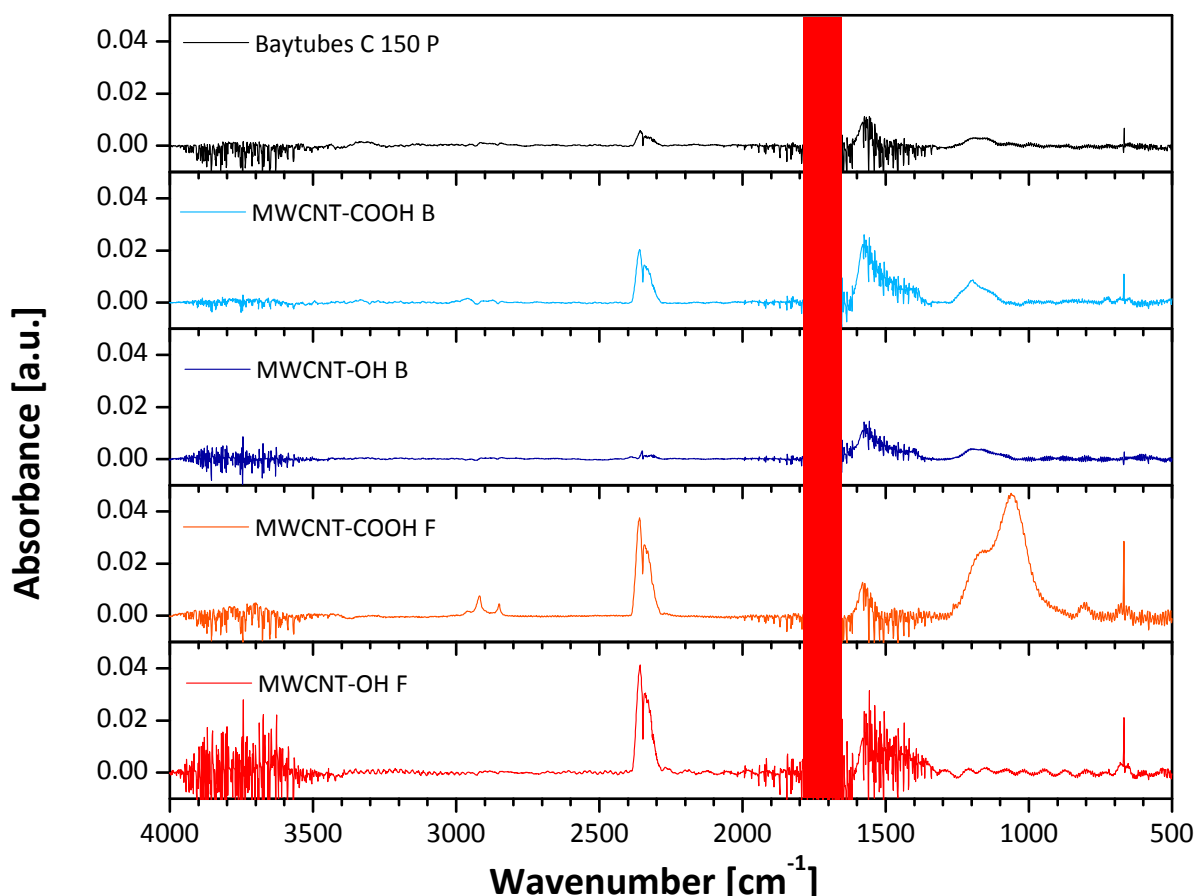


Figure 5.6: IR-spectra of potassium bromide pellets containing functionalized and unfunctionalized MWCNT samples. Stretching vibration of C=O is expected in the red highlighted area.

It is expected to find the usually intense signal related to the C=O stretching vibration if carboxyl groups are present. The collected spectra however show very low absorbances presumably due to the small content of only 0.2 mg sample on 400 mg of potassium bromide used to prepare the pellets. However in all spectra several mutual signals can be found, which are described in the following starting at high wavenumbers [ $\text{cm}^{-1}$ ]. Signals between  $4000$  and  $3500 \text{ cm}^{-1}$  are related to

intermolecular H-bonds of water molecules indicating a residual humidity left over from the functionalization treatment. However this signal is also present in the untreated MWCNTs. This rather suggests that the humidification of the KBr pellets during sample preparation was insufficiently compensated by the background, although it has been taken care to prepare all samples in similar time spans. At approximately  $2900\text{ cm}^{-1}$  symmetric as well as asymmetric vibrations of methyl groups indicate the presence of aliphatic moieties in the samples of MWCNT-COOH. The strong signals around  $2300\text{ cm}^{-1}$  are caused by insufficient compensation of  $\text{CO}_2$  through the background. Around  $1720\text{ cm}^{-1}$  the C=O stretching vibration is expected. Also in this range at ca.  $1650\text{ cm}^{-1}$  the C=C stretching vibration is found for all samples. While the latter peak is found in all spectra, a signal related to C=O stretching can only be found in the functionalized samples. Albeit all spectra show a strong noise in their signals between  $2000\text{ cm}^{-1}$  and  $1300\text{ cm}^{-1}$  making comparison difficult. Between  $1200$  and  $1100\text{ cm}^{-1}$  a peak belonging to rocking vibrations of methyl groups on aromatics is found. This particular signal is however not visible in the spectrum of MWCNT-OH F. The sharp signal at  $690\text{ cm}^{-1}$  could not be assigned to any of the structural elements expected from the samples. It could be a fragment from the processing of the spectra.

#### 5.1.2.4 Thermogravimetric analysis of MWCNTs

The IR spectra give no information regarding the actual amount of functional groups introduced through the functionalization treatment. In order to find information on the individual functionalization degrees thermogravimetric analyses in nitrogen atmosphere were conducted. The results are shown in figure 5.7.

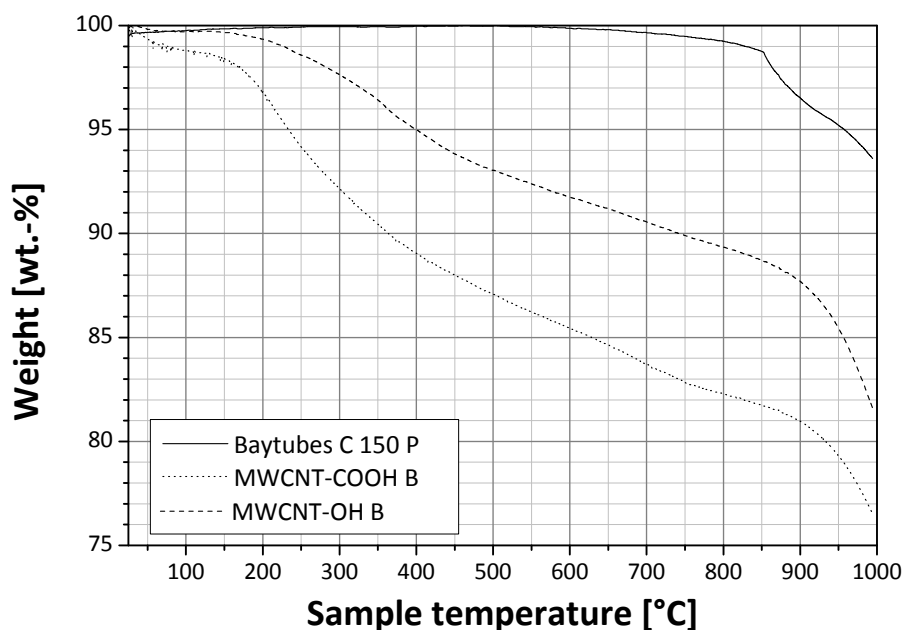


Figure 5.7: Thermogravimetric analyses of pure MWCNTs as well as COOH- and OH- functionalized samples in nitrogen atmosphere.

For pure MWCNTs no weight loss is observed up to  $600\text{ }^{\circ}\text{C}$ . Above this temperature a very small mass reduction begins which sums up to 1 wt.-% weight loss up to  $850\text{ }^{\circ}\text{C}$ . At higher temperatures the weight loss of the sample increases exponentially so that  $850\text{ }^{\circ}\text{C}$  can be considered as the decomposition temperature of Baytubes C 150 P. In case of the functionalized samples of MWCNT-COOH and MWCNT OH this behavior is also found around  $850\text{ - }900\text{ }^{\circ}\text{C}$ . Here some more

## 5 Results and discussion

significant weight losses can be observed at lower temperatures. The sample of MWCNT-COOH B loses around 1 wt.-% below 50 °C which can be explained by the presence of residual water in that particular sample. Above 150 °C in both functionalized samples (MWCNT-COOH and MWCNT-OH) a weight loss sets in, which most likely is due to the removal of functional groups e.g. decarboxylation. It is not possible to determine the actual content of functional groups via TGA because the decomposition of the nanotube above 850 °C overlaps with the weight loss related to the removal of functional groups. The weight loss up to this temperature is 18.3 wt.-% for MWCNT-COOH and 11.3 wt.-% for MWCNT-OH. The corresponding degrees of functionalization cannot be calculated from these values, because it is not known in which form the functional groups split off. However the results show that in the sample of MWCNT-COOH the mass of functional groups is much higher.

### 5.1.2.5 Elementary analyses of MWCNTs

To finally obtain quantitative information on the oxygen content of the samples elementary analysis was conducted. Results of several analyses are shown in figure 5.1.

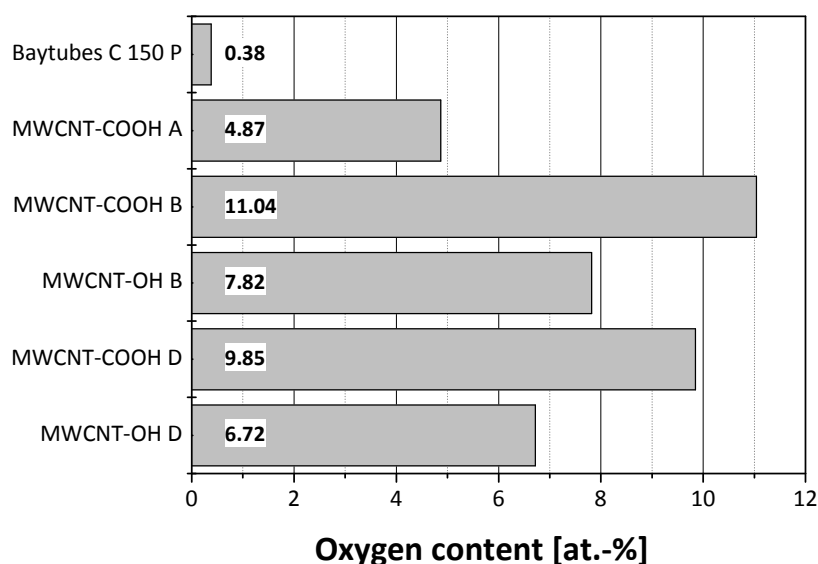


Figure 5.8: Overview of results from elementary analyses of functionalized and pure MWCNT samples.

The untreated MWCNTs possess a very low oxygen content of 0.38 at.-% while the oxidized samples of MWCNT-COOH exhibit 10 - 11 at.-%. The very first batch of carboxyl-group functionalized nanotubes (MWCNT-COOH A) is an exception. Here the reaction mixture has not been dispersed using ultrasound prior to the oxidation. This explains the much lower values in this case and the importance of the initial dispersion step of pure nanotubes in the nitric acid. The batch was therefore not used for membrane preparation. The oxygen contents in MWCNT-COOH are similar in batches B (11.04 at.-%) and D (9.85 at.-%). Also the amount of oxygen in the corresponding reduced batches of B and D are close to each other with 7.82 and 6.72 at.-%. The decrease of oxygen due to the reduction of carboxyl to hydroxyl groups is very similar and amounts to -3.22 at.-% in batch B and -3.13 at.-% in batch D. Consequently this suggests that the functionalization treatment has introduced 1 at.-% more of oxygen in batch B than in batch D. However the reductive treatment leads to the same decrease in oxygen content.

### 5.1.2.6 Electron microscopy of MWCNTs

TEM as well as SEM were used to obtain morphological information on the MWCNT samples. TEM on the one hand is best suited to investigate the structure of individual tubes. This is mainly possible due to the notably higher resolution but also because of the sample preparation, which leads to thinned out nanotubes. SEM on the other hand has a lower resolution however allows the examination of nanotube agglomerates thus providing a more extensive impression of the sample morphology. In the following an overview of each TEM (figure 5.9) as well as SEM (figure 5.10) images is presented. In both cases images of pure and functionalized MWCNTs are compared.

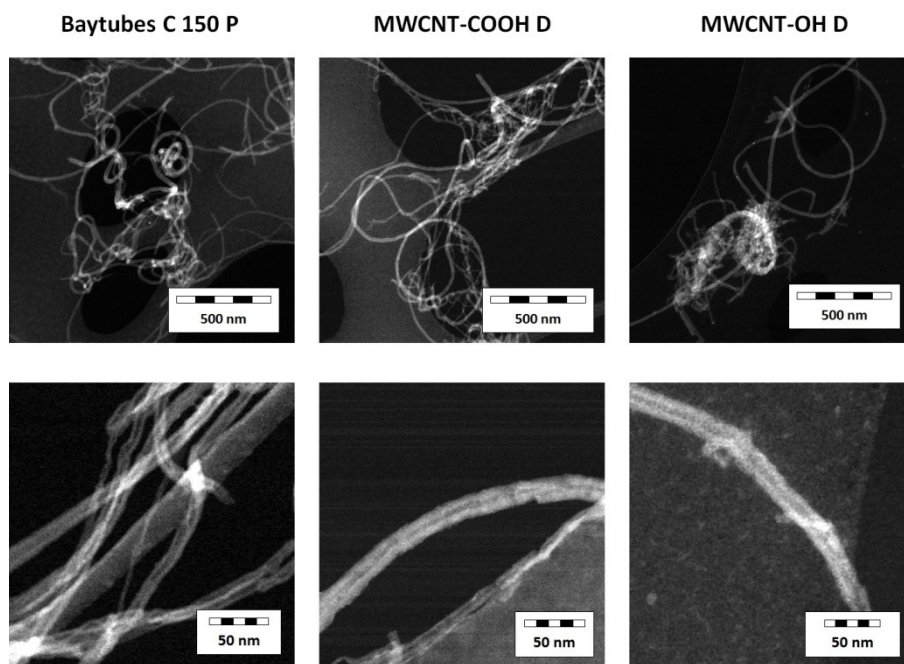


Figure 5.9: TEM images of MWCNT samples showing the morphology of nanotubes.

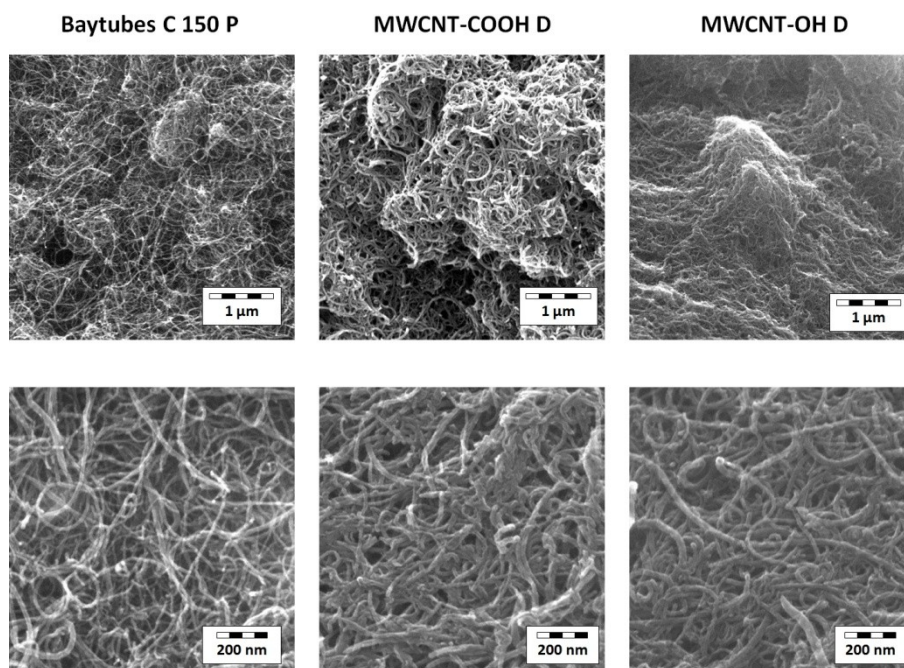


Figure 5.10: SEM images of MWCNT samples showing the morphology of nanotube agglomerates.

## 5 Results and discussion

From electron microscopic analyses it can be seen that the nanotube morphology was not noticeably affected by the functionalization procedure. TEM images of pure and functionalized samples suggest that the inner and outer diameters of the nanotubes have not been altered. The outer diameters are within specification for the pure nanotubes (13-16 nm), likewise the inner diameters (4 nm). Also the texture of nanotube agglomerates does not change as can be seen in the SEM images shown in figure 5.10. Nanotube lengths vary strongly in all samples. Short tubes of several hundred nanometers length as well as much longer ones with lengths over 1  $\mu\text{m}$  can be found. The technical data sheet for Baytubes C 150 P specifies the nanotubes length as 1 – 10  $\mu\text{m}$ .

Summing up the results of the different characterization methods applied on the MWCNT samples it can be assumed that the functionalization treatment used in this work is successful. The method introduces the desired functional groups while conserving the structural properties of the MWCNTs.

### 5.1.3 Titanosilicate materials

The titanosilicate JDF-L1 serves as the starting material for the preparation of MMMs in this work. After synthesis, this material underwent several further treatments such as disaggregation or exchange of the interlamellar cations. Consequently different characterization techniques were necessary to confirm the successful preparation of the required materials.

#### 5.1.3.1 Characterization of disaggregated JDF-L1

In order to evaluate the disaggregation procedure using quaternary amines the morphology of the titanosilicate samples was analyzed. In figure 5.11 a collection of SEM images is presented showing the texture of as-synthesized JDF-L1 and several disaggregated samples.

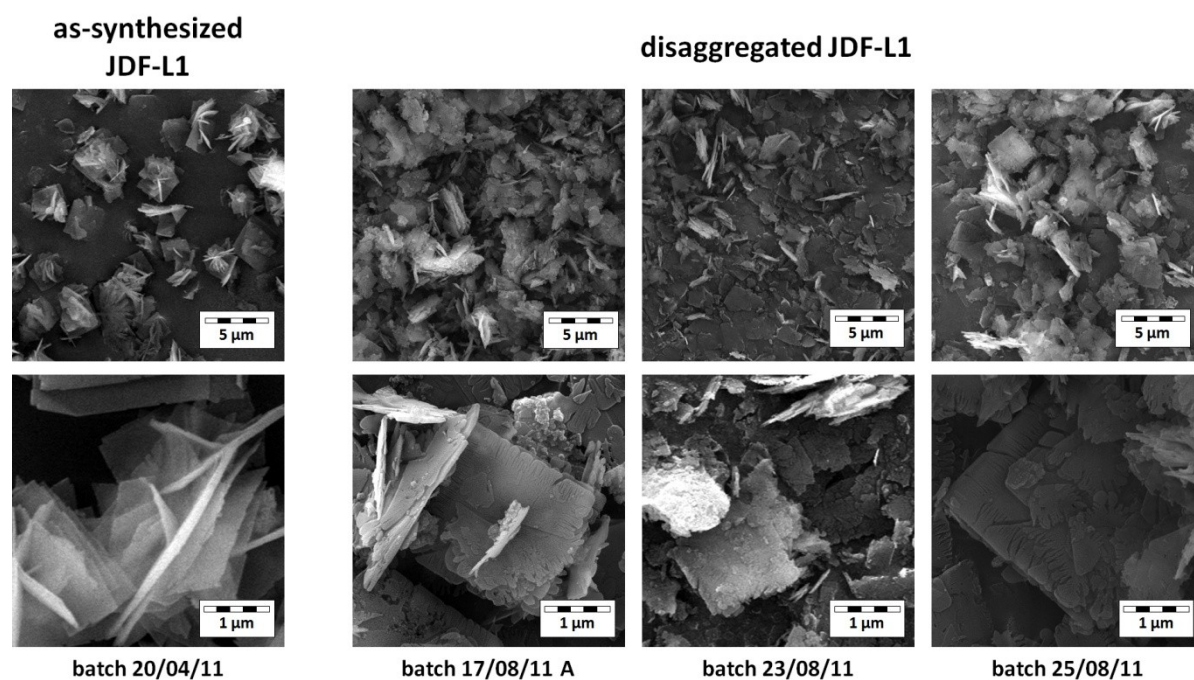


Figure 5.11: SEM images of as-synthesized and disaggregated samples of JDF-L1.



## 5 Results and discussion

fluorescence (XRF) analyses to find the exchange ratio of the interlamellar cations. For the naming of ion exchanged samples the cation that sodium was exchanged with is added as a prefix to JDF-L1 (e.g.: "(Li)-JDF-L1"). Figure 5.13 shows SEM images of all types of ion exchanged titanasilicate materials prepared in this work.

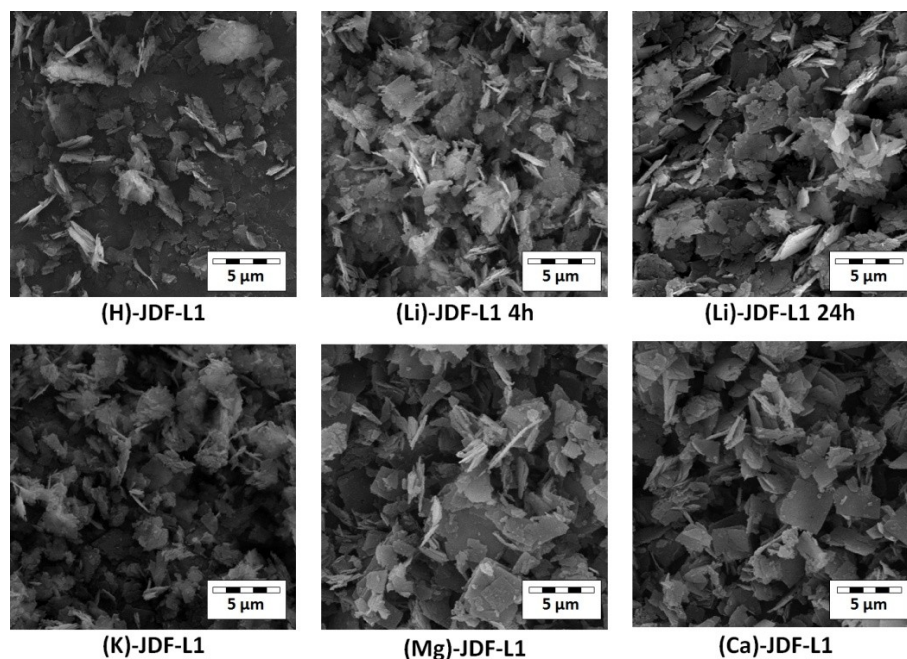


Figure 5.13: SEM images of ion-exchanged JDF-L1 samples.

It can be seen that the ion exchange procedures used in this work has only small influence on the sheet shaped structure of disaggregated JDF-L1. The samples presented above exhibit a very similar morphology compared to the disaggregated JDF-L1 shown in figure 5.11. Small damage to the sheet borders is observed together with a certain degree of sheet fragmentation, as particles with edge lengths smaller than 2 μm are found. These partial damages are likely a result of the mechanical forces applied to the samples during the prolonged stirring of the dispersion within the cation exchange solution. For (H)-JDF-L1 the XRD data shows a strong alteration of the crystal structure as seen in figure 5.14.

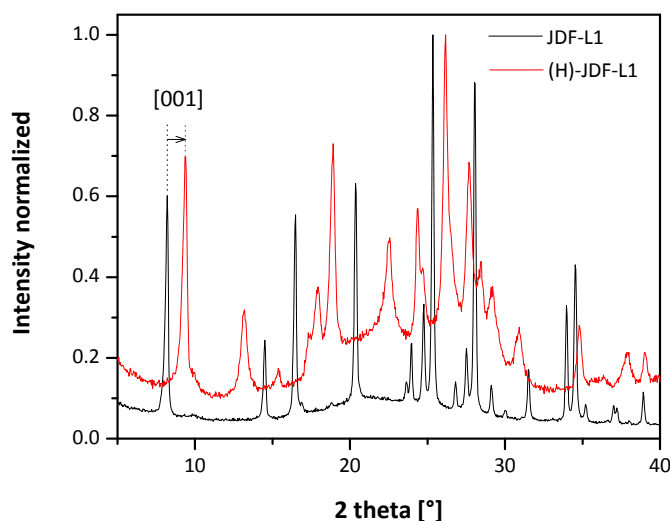


Figure 5.14: XRD spectra of disaggregated JDF-L1 and sample where  $\text{Na}^+$  was exchanged with  $\text{H}^+$ . Spectra were collected with synchrotron radiation ( $\lambda=0.82637 \text{ \AA}$ ) then adjusted to fit to  $\text{Cu K}\alpha 1$  ( $\lambda=1.54059 \text{ \AA}$ ) as used for all other XRD-spectra.

The difference in the XRD spectra after exchanging sodium cations with protons is severe. Peaks and intensities are drastically altered suggesting that the crystal structure of JDF-L1 was changed. A detailed determination of this structure would go beyond the scope of this work. However the spacing in between the layers of this sample can be assumed to be reduced compared to that of the as-synthesized JDF-L1. This is indicated by the peak related to [001] usually being the lowest signal in XRD spectra of JDF-L1. For (H)-JDF-L1 it has moved to higher angles, indicating a smaller d-spacing of the corresponding structural layers here, in agreement with the smaller ionic radius of  $H^+$  as compared to  $Na^+$ . The ion exchange with  $H^+$  conducted in acidic conditions on the one hand leads to a material with a different structure than JDF-L1. On the other hand the cation exchange procedure using aqueous solutions with an excess of certain salts has less influence on the structure as the XRD spectra in figure 5.15 show.

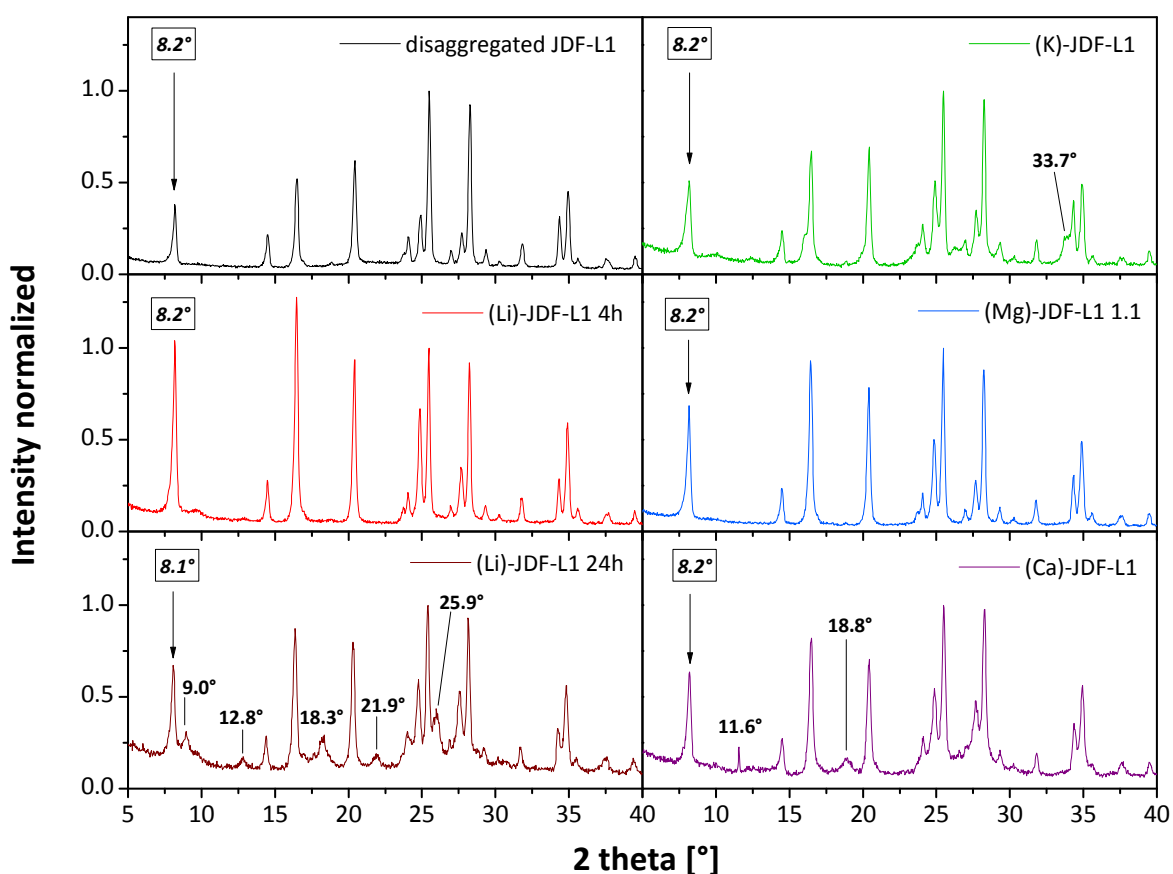


Figure 5.15: Comparison of XRD spectra of disaggregated JDF-L1 and subsequently ion exchanged titanositates.

All spectra exhibit the characteristic peaks related to the structure of JDF-L1. The introduction of other interlamellar cations does not lead to an increased or decreased distance between the layers of JDF L1 as the peak related to the direction of [001] has not been altered significantly in any of the samples. For (K)-JDF-L1 and (Ca)-JDF-L1 one or two new peaks occurred that could not be assigned to any of the related materials (signals at  $2\theta = 33.7^\circ$  and  $2\theta = 11.6^\circ, 18.8^\circ$ ). In case of (Li)-JDF-L1 two slightly different preparation methods were used. In the sample (Li)-JDF-L1 4h the titanositicate was stirred in a solution of lithium chloride for 4 hours but only a small amount of lithium was found via EDX (see figure 5.17). As a result another sample was prepared where the titanositicate dispersion was stirred for 24h in  $LiCl_2$ . Here a set of several additional peaks occurred that indicate a change of

## 5 Results and discussion

the crystal structure. In fact the novel structure is very similar to the new structure found in (H)-JDF-L1 as the comparison of both spectra in figure 5.16 shows.

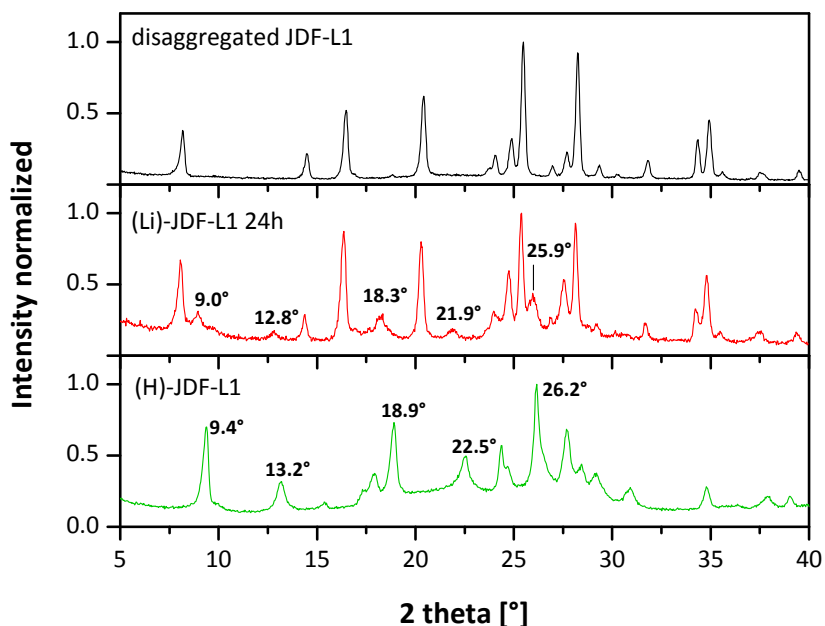


Figure 5.16: Comparison of the XRD spectra of disaggregated JDF-L1 and the ion exchanged samples (Li)-JDF-L1 24h and (H)-JDF-L1.

The XRD spectra point out that the structure of JDF-L1 dominates in the sample of (Li)-JDF-L1 24h. Although a new set of peaks is found in addition suggesting that a certain amount of the sample possesses a noticeably different structure. Positions and proportions of these novel signals are however consonant with those of (H)-JDF-L1 leading to the conclusion that the corresponding amount of (Li)-JDF-L1 24h underwent a similar structural change as the protonated sample. In any event, further research (out of scope here) would be necessary to elucidate the structural modifications observed in XRD analysis linked to the ion exchange procedures.

EDX and XRF analyses were conducted to determine the exact extent to which the interlamellar sodium cations have been exchanged in the different samples. In case of the bivalent cations also a direct tracking during the exchange reaction via conductivity measurement of the solution would make sense. However no decrease of conductivity could be observed, most presumably due to the high excess of bivalent salt. The results for EDX and XRF are presented in figure 5.17 while table 5.2 provides an overview of the ion exchange conditions and radii of the cations involved.

Table 5.2: Conditions of ion exchange procedures and ionic radii (in crystal and hydrated form) of the according cations.

sample name	cation exchanged with	time [h]	excess	ionic radius in crystal [ppm] <sup>[131]</sup>	hydrated ionic radius [ppm] <sup>[132]</sup>
JDF-L1	-	-	-	102	358
(Li)-JDF-L1 4h	Li <sup>+</sup>	4	80-fold	76	382
(Li)-JDF-L1 24h	Li <sup>+</sup>	24	80-fold	76	382
(K)-JDF-L1	K <sup>+</sup>	4	80-fold	138	331
(Mg)-JDF-L1 1.1	Mg <sup>2+</sup>	16	80-fold	72	428
(Mg)-JDF-L1 1.2	Mg <sup>2+</sup>	24	80-fold	72	428
(Mg)-JDF-L1 1.3	Mg <sup>2+</sup>	16	240-fold	72	428
(Ca)-JDF-L1	Ca <sup>2+</sup>	16	80-fold	100	412

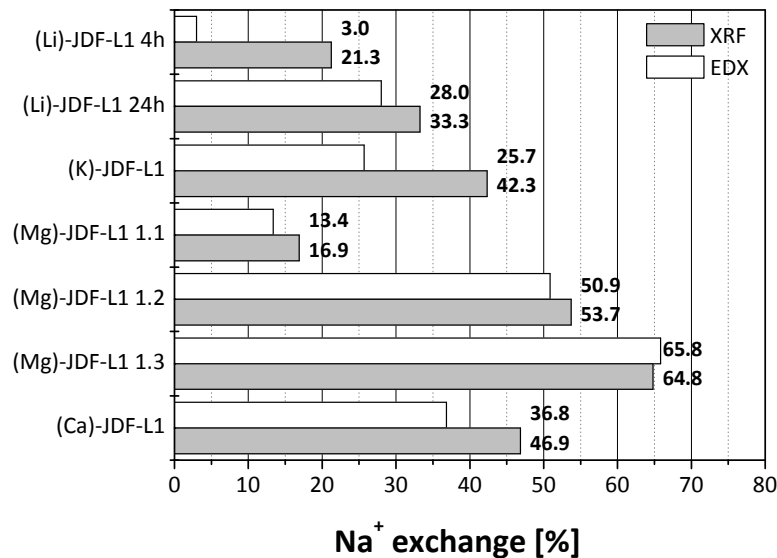


Figure 5.17: Results of elementary analyses via EDX and XRF for ion exchanged samples of JDF-L1.

The sodium exchange yield as percentage was calculated because this value considers that two sodium cations are replaced by only one bivalent cation. This allows comparison of results for mono- and bivalent cations. In all samples noticeable quantities of sodium were exchanged with the desired cations. EDX generally gives lower exchange rates than XRF data. This is most likely due to the fact that in both techniques information is obtained in very different ways. For EDX results are an average of many individual measurements of only very small regions within the sample. On the contrary XRF provides information about the bulk of the sample in each case. This might also explain why in spite of eight individual EDX measurements only a small exchange ratio of 3 % was found for the sample (Li)-JDF-L1 4h. According to XRF data however sodium cations up to 21.3 % have been exchanged, which means that preparing a new sample with a longer exchange period of 24 hours as mentioned above was not necessary. In fact the six times longer treatment period only increased the exchange rate by ca. 12 % to 33.0 % (XRF). Also for (Mg)-JDF-L1 it was attempted to achieve a higher exchange rate than what was obtained for the first sample (Mg)-JDF-L1 1.1. This sample was stirred for 16 hours in a 80-fold excess of Mg<sup>2+</sup> which resulted in an exchange rate of 13.4 % (EDX) and 16.9 % (XRF) respectively. Subsequently a prolonged stirring and a higher excess of the cation to be exchanged with were tested. Increasing either of these parameters leads to a material with a much higher

## 5 Results and discussion

exchange rate. Extending the stirring period from 16 to 24 hours leads to an exchange rate of 50.9 % (EDX) 53.7 % (XRF) (Sample: (Mg)-JDF-L1 1.2) while a  $Mg^{2+}$  excess of 240-fold instead of 80-fold results in 65.8 % (EDX) or 64.8 % (XRF) (Sample: (Mg)-JDF-L1 1.3). Moreover the exchange rates appear to be influenced by the size of the cations (table 5.2). This can be seen by the fact that the same excess (80-fold) and stirring time (4 hours) during the exchange treatment lead to a lower sodium exchange for  $Li^+$  than for  $K^+$ . The hydrated radius of lithium is 382 ppm and thus much larger than the value for sodium (358 ppm). Potassium on the contrary exhibits a lower value of 331 ppm. The same is observed in case of the bivalent cations. Under equal conditions (80-fold excess, 16 hours stirring) a smaller exchange of sodium is achieved with the larger magnesium (428 ppm) than with calcium cations (412 ppm).

In order to elucidate possible structural changes due to increasing exchange of sodium several batches were analyzed by XRD. Figure 5.18 compares the spectra of the batches of (Mg)-JDF-L1 and non ion exchanged titanasilicate.

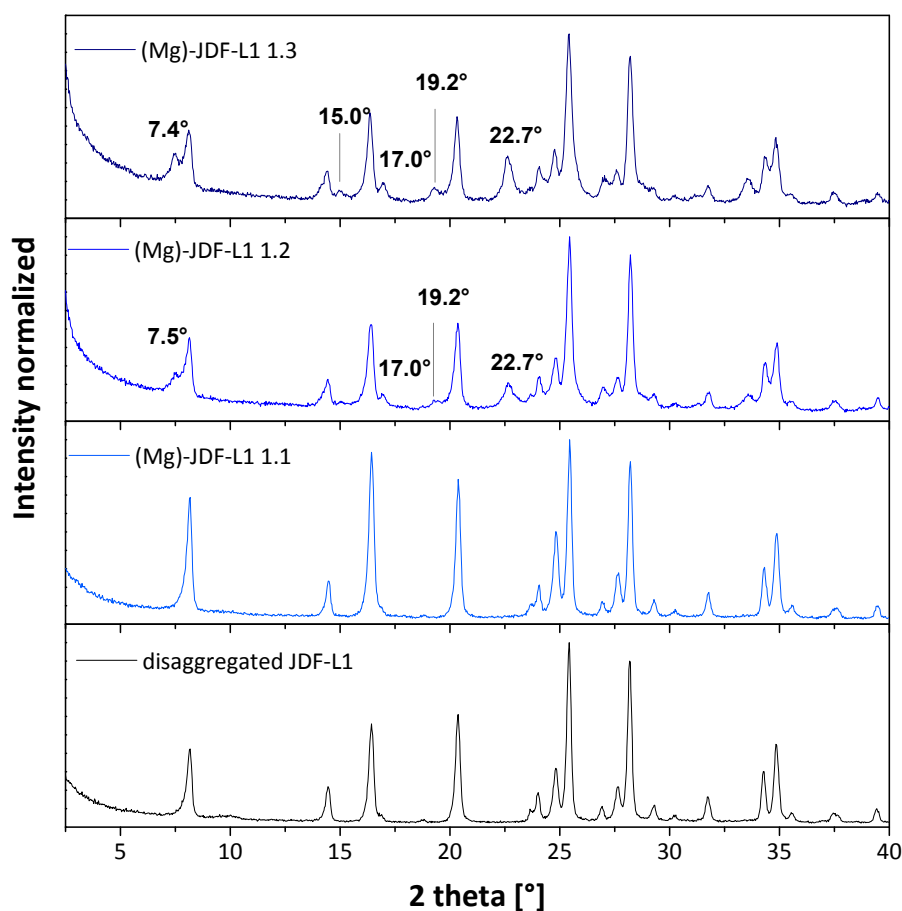


Figure 5.18: Comparison of XRD spectra of (Mg)-JDF-L1 batches with disaggregated JDF-L1.

For the first sample of (Mg)-JDF-L1 no alteration of the spectra is observed. The low sodium exchange of below 20 % has no observable influence on the structure of the titanasilicate. In the spectra of samples 2 and 3 respectively also the signals related to JDF-L1 are found. But here also a set of new peaks occurs. The sodium exchange rates in these samples are above 50 %, which suggests that the exchange of sodium with magnesium is in fact accompanied with a structural modification of JDF-L1. This effect is more noticeable with higher exchange rates. The peaks related to the altered structure are most visible in the spectrum of sample (Mg)-JDF-L1 1.3 where around 65 % of interlamellar sodium cations were exchanged with magnesium. The peak related to the

direction [001] shifts to slightly lower angles in these samples. This indicates a higher interlamellar distance due to the intercalation of magnesium cations and in any event the coexistence of two phases (i.e. JDF-L1 and (Mg)-JDF-L1).

### 5.1.3.3 Characterization of one-step disaggregated and ion exchanged JDF-L1

Apart from the method using quaternary amines an alternative procedure for the disaggregation of JDF-L1 using sodium hydroxide was found by Rubio<sup>[123]</sup>. Apparently the agglomerates in as-synthesized JDF-L1 can also be separated by stirring the material in a solution of NaOH at elevated temperatures. Based on this finding a novel approach was developed in this work to perform disaggregation and ion exchange in one step. By using lithium and potassium hydroxide it was expected to obtain a disaggregated and ion exchanged material. For this the titanosilicate was stirred for 16 hours at 80 °C in a one molar solution of the four bases NaOH, NH<sub>3</sub>, LiOH and KOH. SEM images of the materials obtained via this method are shown in figure 5.19.

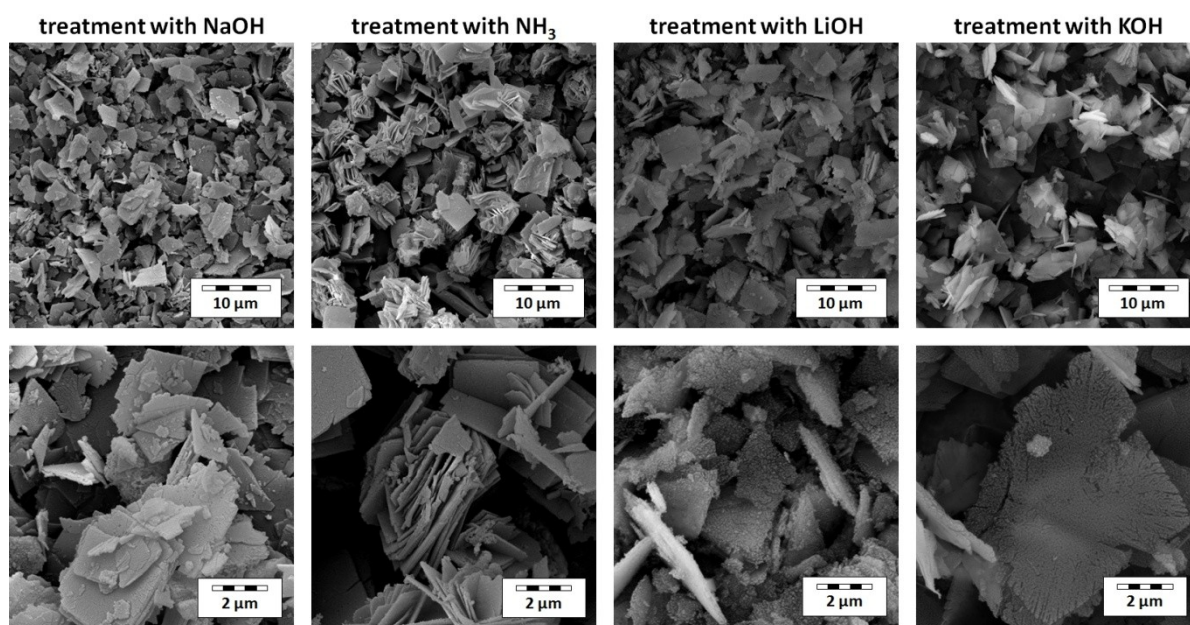


Figure 5.19: SEM images of JDF-L1 samples that underwent basic treatment in one molar solutions of different bases.

The images show that a strong base is necessary to successfully disaggregate the agglomerates in JDF-L1. A one molar solution of ammonia is too weak to induce the separation of agglomerates. The material stirred in ammonia undergoes no obvious disaggregation and appears like the as-synthesized JDF-L1. It seems that the pH is not high enough to favor the repulsion of particles due to deprotonation of silanol groups. In the cases of NaOH, LiOH and KOH however the samples mainly contain individual JDF-L1 sheets instead of agglomerates. Sheet fragmentation is observed for the samples treated with sodium and lithium hydroxide. Also a certain degree of structural damage on the sheets surface is found after treatment with LiOH and KOH due to a beginning even dissolution of the material.

To which extent an ion exchange of interlamellar sodium was performed during the disaggregation with lithium and potassium hydroxide was analyzed via EDX and XRF spectroscopy. Results of both methods are presented in figure 5.20.

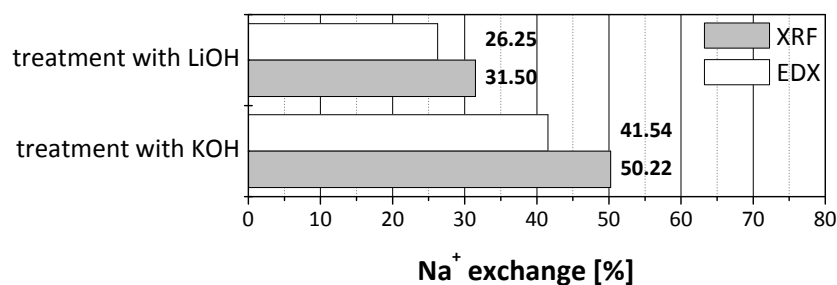


Figure 5.20: EDX and XRF data of JDF-L1 samples treated with one molar solution of lithium and potassium hydroxide.

In both materials significant amounts of the desired ions are found. An exchange with lithium took place for approximately a third of all sodium cations while in case of KOH nearly half of all interlamellar cations were exchanged with potassium. The difference shows once more that the sodium exchange rate depends on the radius of the hydrated ion. The findings made here prove that a treatment with alkali hydroxides is a successful and greener (use of organic molecules is avoided) approach to obtain disaggregated and ion-exchanged JDF-L1 in a single reaction. The materials obtained via this route were however not utilized for membrane preparation in this work. Here exclusively the materials discussed in chapter 5.1.3.2 were used.

## 5.2 MWCNT/polyimide nanocomposites for pervaporation

The following chapter describes how the preparation of membranes composed of copolyimide and functionalized MWCNTs was developed. Subsequently the separation characteristics obtained with these membranes are presented.

### 5.2.1 Development of MWCNT/copolyimide membrane preparation

Prior to this work no practical preparation method for MWCNT/copolyimide nanocomposites existed and it was necessary to gather experience in handling the materials. Consequently different preparation methods were tested with varying success which eventually led to the effective method described previously in chapter 4.4.3. The process of its development and important findings are illustrated in the following. The starting point of membrane preparation was the desire to develop a method that provides homogenous nanocomposites of copolyimide and 1 wt.-% MWCNTs based on ultra sound treatment as the most promising technique to achieve homogenous nanotube dispersions. The ultrasound generator used includes a power measuring device giving the percental value of maximal power (450 W) currently absorbed by the sample during sonication. This way the actual power applied to the membrane solutions at different amplitudes could be determined. The parameters to be modified in order to find a suitable preparation method are the sonication intensity (amplitude) and duration on the one hand and the order at which the membrane components are assembled on the other hand. The components are nanotubes, polymer and tetrahydrofuran (THF) as the solvent. In the first step several methods with different orders of assembly were investigated as listed in figure 5.21.

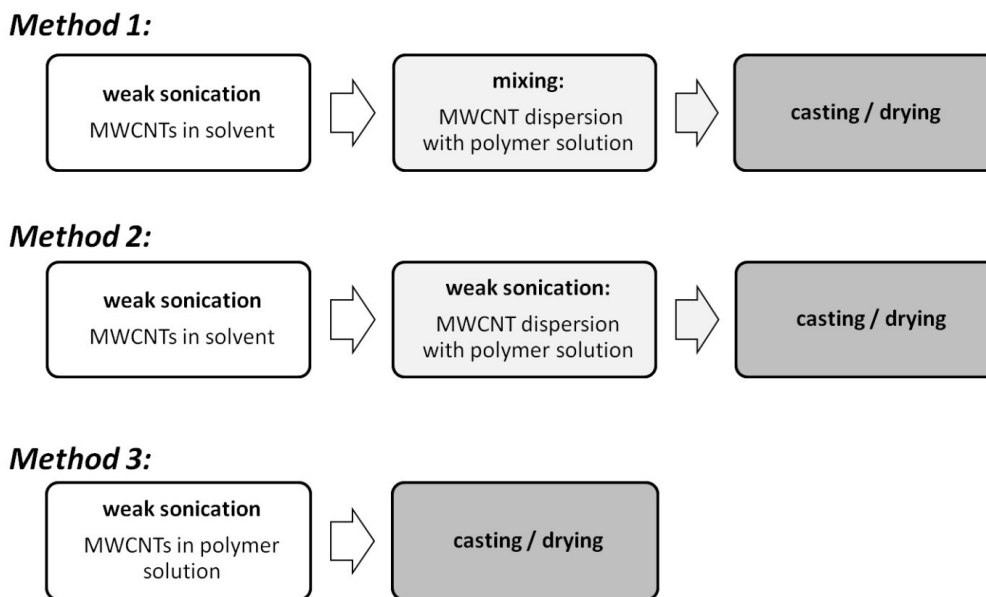


Figure 5.21: Overview of methods 1-3 for the preparation of MWCNT/copolyimide nanocomposites.

In all three methods a weak sonication was used. The ultrasound treatment was conducted at 10 % amplitude (5-10 W) for 10 minutes while cooling the sample with an ice bath. The aim was to find out whether or not a specific order of preparing the casting solution was necessary. All three methods lead to membranes exhibiting a heavily stained pattern consisting of transparent and black areas suggesting an inhomogeneous distribution of MWCNTs inside the polymer. Figure 5.22 exemplarily shows a photo of a membrane prepared according to each of the three methods mentioned above.

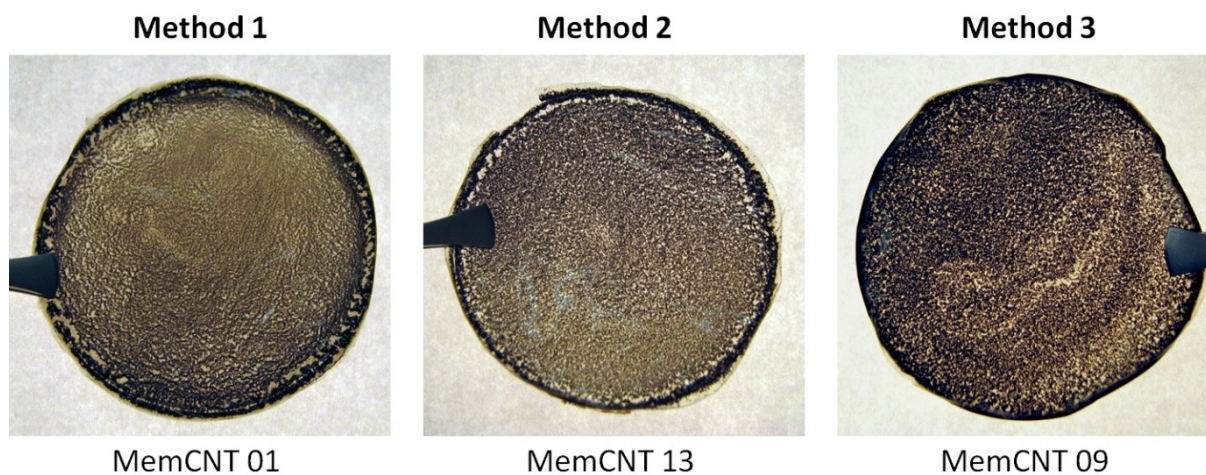


Figure 5.22: Photos of membranes prepared according to methods 1-3 exhibit a stained transparent/black structure.

Although all membrane mixtures appeared as a homogenous black dispersion during casting, only inhomogeneous membranes as shown in figure 5.22 are obtained. This means that the nanotube agglomerates were insufficiently dispersed so that to a large extent re-agglomeration occurs during solvent evaporation. Consequently this suggests that the amplitude and duration of the sonication treatment have to be increased in order to improve the preparation of MWCNT-copolyimide nanocomposites. The initial question, whether or not a specific order of combining the membrane components is necessary, could however not be answered. Albeit based on the works of Shigeta et al.<sup>[133]</sup>, who found that aromatic polyimides have a stabilizing effect on SWCNT dispersions, it was

## 5 Results and discussion

decided to focus on method 3. A similar effect is expected for the materials used in this work. Thus for all subsequent membrane preparations MWCNTs are dispersed in the copolyimide solution.

In the course of the experiments with methods 1-3 also the addition of p-toluenesulfonic acid as a cross-linking agent was investigated. Throughout the resulting membranes the same stained pattern as seen in figure 5.22 is found with even larger areas of agglomerated nanotubes. In dispersion stability tests (see figure 5.23) it was found that the addition of p-toluenesulfonic acid leads to rapid re-agglomeration of the nanotubes.

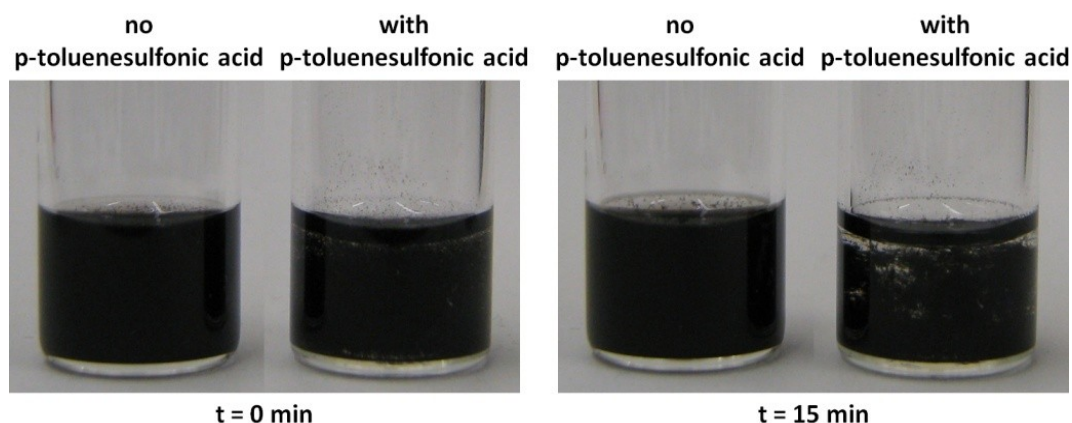


**Figure 5.23:** Addition of p-toluenesulfonic acid reduces the stability of nanotube dispersion. The mixtures consist of a solution of the copolyimide (8 wt.-%) in tetrahydrofuran and 1 wt.-% of MWCNT-OH (regarding the polymer amount). Sonication was conducted at 20 % amplitude (15-20 W) for 5 min.

This finding is in accordance with the results of dispersion stability tests of MWCNTs in water (see chapter 5.1.2.1). Here it was found that the stability of MWCNT dispersions in water is drastically reduced in acidic and basic environment. This behavior can consequently be presumed to also be true for THF as the solvent. Consequently a self catalyzed esterification of MWCNT-OH and copolyimide was chosen to prepare covalently connected nanocomposites. This step is conducted in the vacuum oven at 150° C and 80 mbar. Practically the drying period is extended from originally one to now three days.

As stated previously longer sonication treatments have to be investigated in order to achieve homogenous MWCNT/copolyimide membranes. At this point method 4 (see figure 5.24) was developed where the nanotubes were dispersed by applying strong ultra sound for 5 minutes at amplitudes up to 100 % (~90 W). When experimenting with amplitudes above 50 % (~45 W) it is found that ice bath cooling is no longer sufficient. At such high intensities even with acetone/dry ice cooling vigorous foaming of the membrane mixture is observed. As an alternative route to avoid the loss of solvent due to evaporation the higher boiling dimethylacetamide (DMAc) was tested instead of THF. Figure 5.24 states the conditions of method 4 and shows photos of membranes prepared using this instruction.

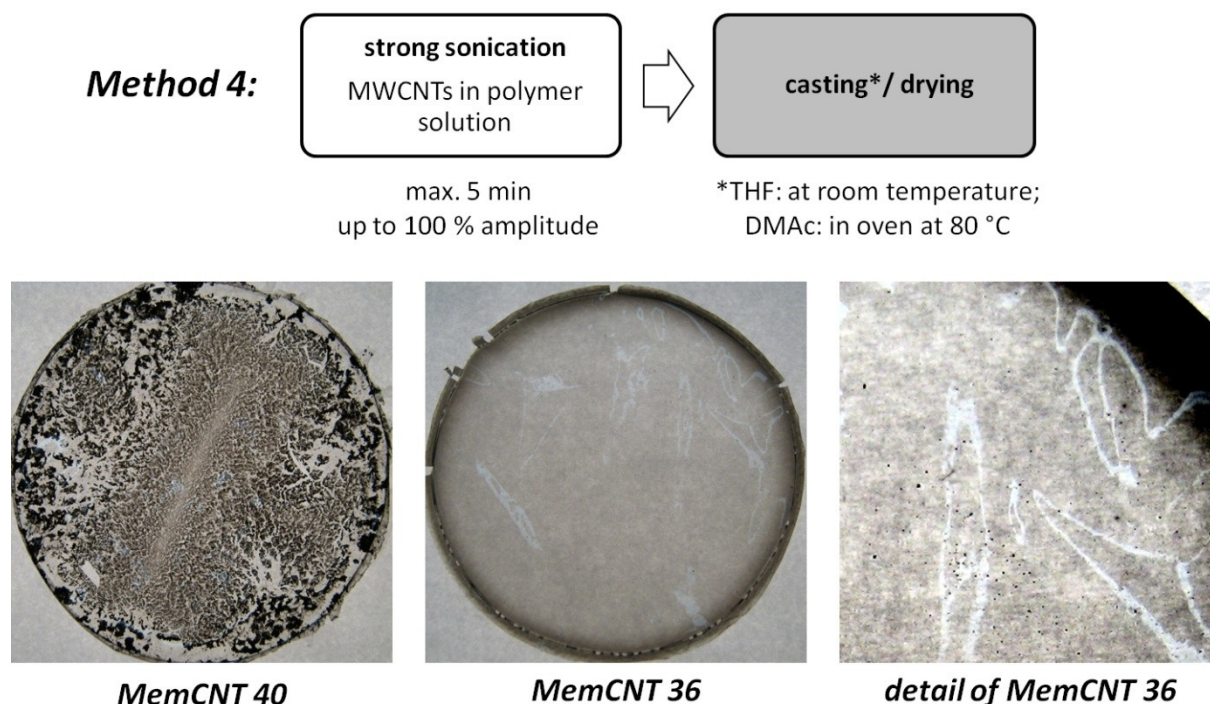


**Figure 5.24:** Preparation conditions of method 4 and photos of membranes produced using this method. DMAc was used as solvent in the case of MemCNT 40 while THF was used for MemCNT 36.

With DMAc as the solvent the foaming of the membrane mixture during sonication treatment is noticeably reduced. However the resulting membranes appear to be extremely inhomogeneous. Strong re-agglomeration occurs during the solvent evaporation step in the oven at 80 °C. It can be assumed that this is due to the elevated temperatures decreasing the dispersion stability. On the contrary apparently homogenous materials can be obtained via method 4 when using THF as the solvent. For this intensive cooling of the membrane mixture during the sonication has to be provided in order to contain foaming. Here no re-agglomeration occurs after membrane casting during solvent evaporation. However at a closer look several small black particles are found (see detail of MemCNT 36 in figure 5.24). This is possibly a result of a too short duration of the ultrasound treatment so that a certain amount of nanotubes remains undispersed. This residue of nanotubes however distorts the actual content of MWCNT in the nanocomposite. To avoid this problem a longer sonication period is necessary. Consequently the preparation conditions were altered concerning this finding. To allow thorough dispersion of MWCNTs without overheating of the mixture a much longer ultrasound treatment of 30 minutes at a lower amplitude of 30 % (45 W) was chosen and repeated three times. To prevent partial sedimentation of nanotube agglomerates the membrane mixture was also stirred in between the sonication steps. Figure 5.25 shows the conditions of the final method (method 5) and a photo of MemCNT 49 which was prepared according to these instructions.

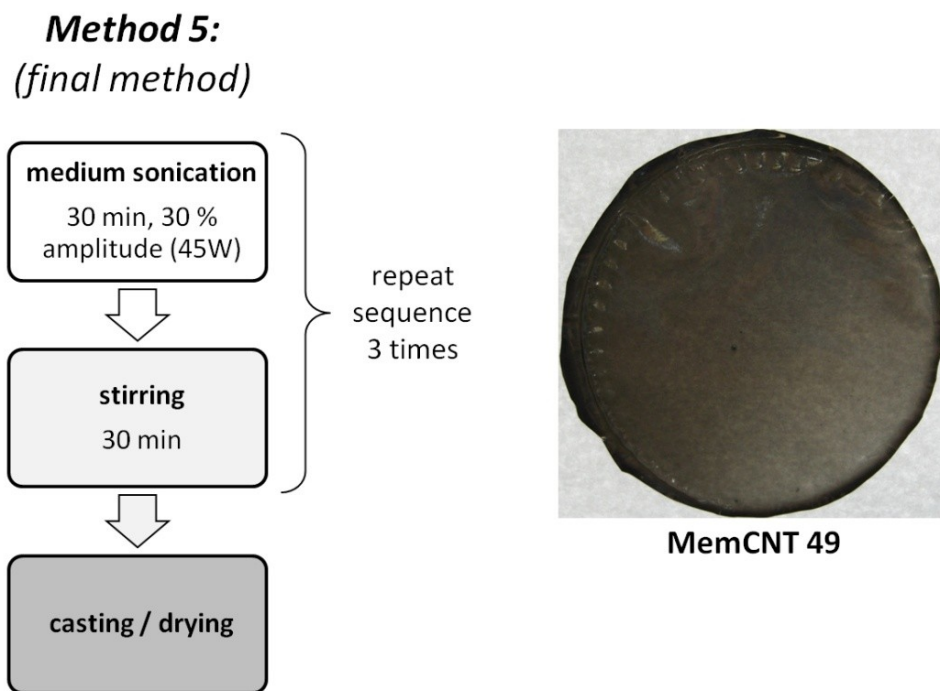


Figure 5.25: Schematic of the final preparation instruction (method 5) and photo of a membrane obtained by preparing the nanocomposite mixture according to this method.

MemCNT 49 shows that with method 5 homogenous MWCNT/copolyimide nanocomposites can be achieved. The membrane appears much darker than MemCNT 36 which has two reasons. First MemCNT 49 exhibits a thickness of 32  $\mu\text{m}$  and thus is thicker than MemCNT 36 with only 20  $\mu\text{m}$ . Secondly the nanotube loading in the case of MemCNT 49 has been dispersed much more thoroughly resulting in a stronger shading of the resulting membrane film. TGA analyses were conducted with the membranes to determine the actual content of MWCNT in the nanocomposites. Results of a pure polymer membrane and nanocomposites with 1 and 3.5 wt.-% of MWCNT-OH prepared according to method 5 are presented in figure 5.26.

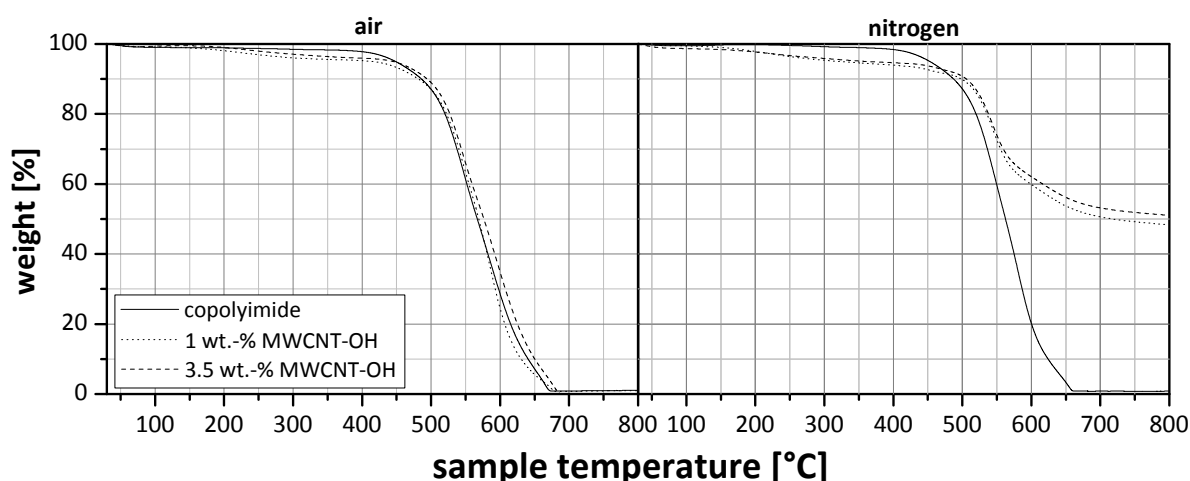


Figure 5.26: Results of TGA analyses of pure copolyimide membranes and MWCNT/copolyimide nanocomposites in air and nitrogen atmosphere. Membranes analyzed were Mem SPI 11 – 003, MemCNT 48 (1 wt.-% MWCNT-OH) and MemCNT 50 (3.5 wt.-% MWCNT-OH).

The TGA results show that in air all three samples are decomposed nearly free of residues between 670 - 690  $^{\circ}\text{C}$ . For the pure polymer sample a small residue of 1.0 % was found. A residue of 0.9 % was

obtained for the membrane containing 1 wt.-% MWCNT-OH while for the nanocomposite containing 3.5 wt.-% the value was below 0.1 % and the residue is therefore negligible. The addition of MWCNT-OH does not lead to noticeably increased residues of the nanocomposite membranes. Consequently no information regarding the MWCNT content in the samples can be deduced from this data. Under nitrogen atmosphere the pure copolyimide membrane also decomposes nearly completely and leaves a residue of again 1.0 %. Here the nanocomposite materials exhibit a much higher thermal stability which was expected from the decomposition behavior of pure nanotubes as seen in chapter 5.1.2.4. The weight of both MWCNT/copolyimide samples decreases to around 50 % at 800 °C, while the decomposition of the copolyimide on the contrary is completed at 670 °C. In case of nitrogen as atmosphere copolyimide and nanocomposites possess extremely different decomposition characteristics. Due to this no information on the actual load of MWCNT-OH can be obtained. However the results show that the incorporation of MWCNT-OH drastically increases the thermal stability of the copolyimide in nitrogen atmosphere. At 800 °C the mass of the material with 1 wt.-% MWCNT-OH has decreased to 48 wt% while at this point 51 wt.-% of the membrane containing 3.5 wt.-% are left. Both values exhibit a decreasing trend.

### 5.2.2 Pervaporation with MWCNT/copolyimide membranes

In order to obtain significant data regarding the separation characteristics of a membrane two different test series were conducted. On the one hand concentration-dependent measurements with constant temperature were executed and on the other hand the membranes were subjected to temperature-dependent measurements where the feed composition remains constant. Both experimental series provide different insight on the separation characteristics of an investigated membrane. The results obtained for pure polymer membranes and MWCNT-OH/copolyimide nanocomposites are presented in the following.

#### 5.2.2.1 Concentration-dependent measurements

For the concentration-dependent measurements the ratio of the feed components toluene and cyclohexane was varied. With every membrane in total five experiments were conducted using mixtures containing approximately 10, 30, 50 and 70 wt.-% of toluene and also with pure toluene. Pure polymer membranes (MemSPI11 05, MemSPI23 04) as well as nanocomposite membranes containing 1 wt.-% (MemCNT 48 & 49) and 3.5 wt.-% MWCNT-OH (MemCNT 50) were subjected to pervaporation experiments with the aforementioned feed-compositions. Figure 5.28 shows the separation characteristics obtained for pure polymer membranes in comparison with the results of nanocomposites containing 1 wt.-% MWCNT-OH.

## 5 Results and discussion

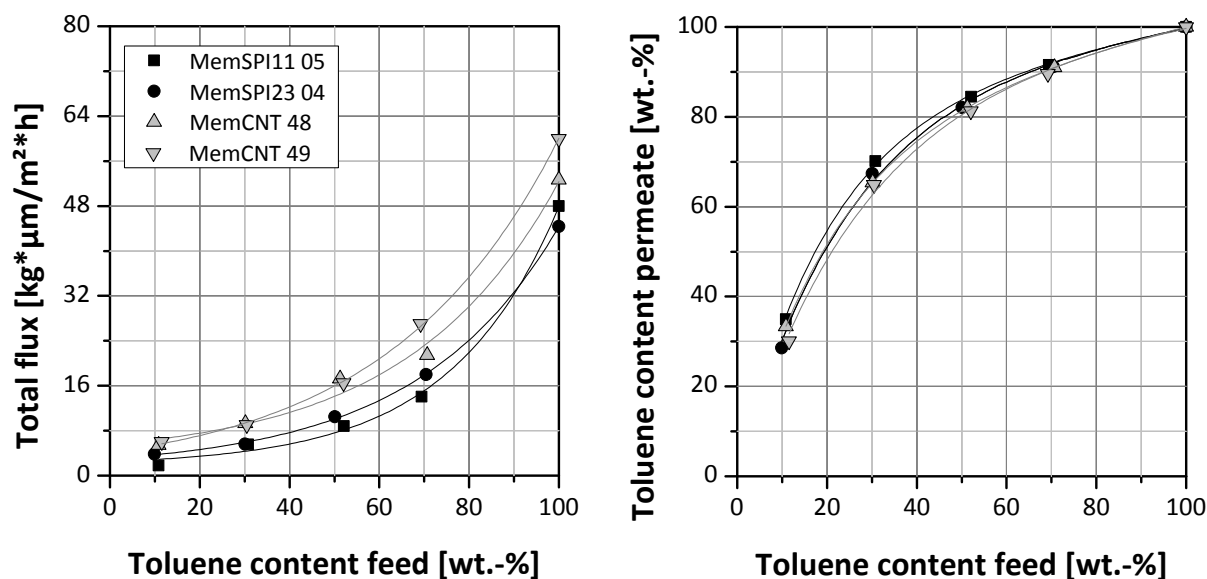


Figure 5.27: Results for pervaporation experiments in different toluene/cyclohexane mixtures with membranes prepared from the copolyimide 6FDA-4MPD/6FDA-DABA 4:1 (black symbols) and copolyimide/MWCNT nanocomposites containing 1 wt.-% MWCNT-OH (grey symbols). Experiments were conducted at a temperature of 60 °C and a permeate pressure of 25 mbar.

In case of the pure copolyimide as well as the nanocomposite containing 1 wt.-% MWCNT-OH the two analyzed membranes exhibit slightly different fluxes. However when comparing the two types of membranes the nanocomposites possess noticeably higher fluxes than the pure polymer. On the contrary very similar permeate compositions are obtained for all membranes. With nanocomposite membranes only slightly lower toluene contents are found in the permeate than with the pure copolyimide membranes. This means that by addition of MWCNTs the selectivity is marginally reduced while fluxes are drastically increased. However this increase appears to depend on the feed composition. For feed mixtures with lower toluene concentrations MWCNT/copolyimide membranes exhibit an especially high increase of the flux. In 30:70 wt.-% mixtures of toluene/cyclohexane for example fluxes of 5.5 and 5.6  $\text{kg}\cdot\mu\text{m}\cdot\text{m}^{-2}\cdot\text{h}^{-1}$  were measured with polyimide membranes whereas values of 9.3 and 9.1  $\text{kg}\cdot\mu\text{m}\cdot\text{m}^{-2}\cdot\text{h}^{-1}$  were obtained with MWCNT-OH/copolyimide nanocomposites. This means that by incorporating 1 wt.-% MWCNT-OH the fluxes increase by ca. 65 %. Also for 50:50 mixtures of toluene/cyclohexane the fluxes of pure polymer membranes are surpassed by the nanocomposite. Here values of 8.8 and 10.5  $\text{kg}\cdot\mu\text{m}\cdot\text{m}^{-2}\cdot\text{h}^{-1}$  are found for the copolyimide and fluxes of 17.3 and 16.5  $\text{kg}\cdot\mu\text{m}\cdot\text{m}^{-2}\cdot\text{h}^{-1}$  for the nanocomposite, which correspond to an increase in the range of 60 - 90%. This suggests that the nanotubes distributed within the polymer alter the membrane structure to such an effect that an accelerated permeation of the feed components is found. Considering the fact that only little change of selectivity is observed, the degree of acceleration is very similar for both toluene and cyclohexane. At higher concentrations of toluene a lower increase of flux is observed. For example with pure toluene as feed copolyimide membranes exhibit fluxes of 48.0 and 44.4  $\text{kg}\cdot\mu\text{m}\cdot\text{m}^{-2}\cdot\text{h}^{-1}$  respectively while values of 52.6 and 60.0  $\text{kg}\cdot\mu\text{m}\cdot\text{m}^{-2}\cdot\text{h}^{-1}$  are measured with the nanocomposite membranes. This corresponds to an increase in the range of only 10 – 30 %. Presumably this is due to the swelling induced by high toluene concentrations. At high toluene concentrations it can be assumed that the increase of flux will be stronger the more a membrane material is affected by swelling. The fact that MWCNT/copolyimide nanocomposites exhibit a lower increase of flux with increasing toluene concentrations compared to the pure polymer suggests a certain swelling resistance due to the addition of nanotubes. This can be explained by the formation

of covalent and hydrogen bonds between carboxyl acid groups of the copolyimide and hydroxyl groups of the nanotubes. Based on the above mentioned finding it can therefore be concluded that adding MWCNT-OH not only enhances permeability but also has a cross-linking effect on the membrane material in terms of swelling resistance towards toluene while selectivity is not noticeably affected.

To find out whether or not the separation characteristics can be enhanced further by incorporating larger amounts of nanotube pervaporation experiments with a nanocomposite containing 3.5 wt.-% MWCNT-OH were performed. The results of this experimental series are presented in figure 5.28 together with the results for the nanocomposite membranes containing 1 wt.-% of nanotubes.

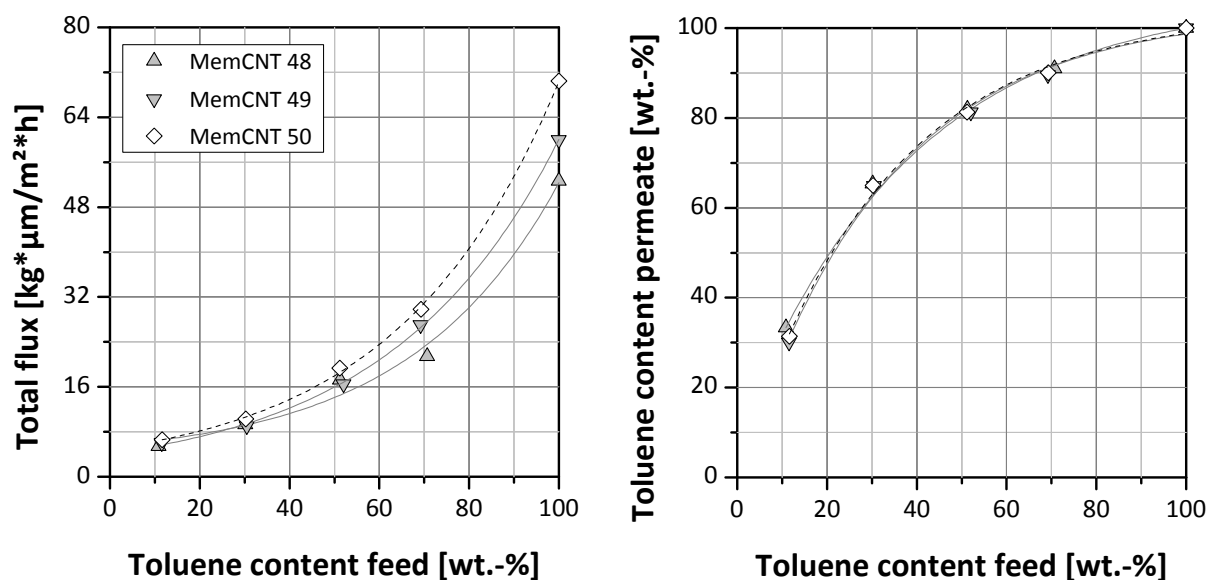


Figure 5.28: Results for pervaporation experiments in different toluene/cyclohexane mixtures with nanocomposite membranes prepared from 6FDA-4MPD/6FDA-DABA 4:1 and MWCNT-OH containing 1 wt.-% (grey symbols) and 3.5 wt.-% respectively (white symbols) of nanotubes. Experiments were conducted at a temperature of 60 °C and a permeate pressure of 25 mbar.

Although the nanotube content was tripled only slightly higher fluxes are found for the according membrane. Regarding the permeate composition very similar results compared with membranes containing 1 wt.-% nanotubes are obtained. The selectivity can therefore be considered to remain unchanged. Interestingly the membrane containing 3.5 wt.-% MWCNT-OH exhibits a more noticeable increase of fluxes at higher toluene concentrations. With 30:70 wt.-% toluene/cyclohexane mixtures a flux of  $10.3 \text{ kg}\cdot\mu\text{m}\cdot\text{m}^{-2}\cdot\text{h}^{-1}$  is found which equals to an increase of 10-15 % compared to the nanocomposites containing 1 wt.-% of nanotubes. In contrast to this the flux measured for pure toluene is  $70.4 \text{ kg}\cdot\mu\text{m}\cdot\text{m}^{-2}\cdot\text{h}^{-1}$  and thus between 20-30 % higher compared to the values of nanocomposite membranes with 1 wt.-% of MWCNT-OH. This effect suggests a slightly reduced degree of swelling resistance and thus lower cross-linking in the nanocomposites containing 3.5 wt.-%. A possible explanation could be that the much higher load of nanotubes reduces the flexibility of the membrane material due to which less functional groups can interact or cross-link.

### 5.2.2.2 Temperature-dependent measurements

For the temperature-dependent measurements a feed composition of 50:50 wt.-% toluene/cyclohexane was chosen which was kept constant throughout the test series. Several

## 5 Results and discussion

consecutive pervaporation experiments were conducted with a pure polymer membrane as well as nanocomposite membranes containing 1 wt.-% MWCNT-OH. The first measurement was conducted at a temperature of 60°C and was subsequently increased in steps of 5 °C up to 90 °C. Figure 5.29 shows the results obtained for the three analyzed membranes MemSPI23 04, MemCNT 48 and 49.

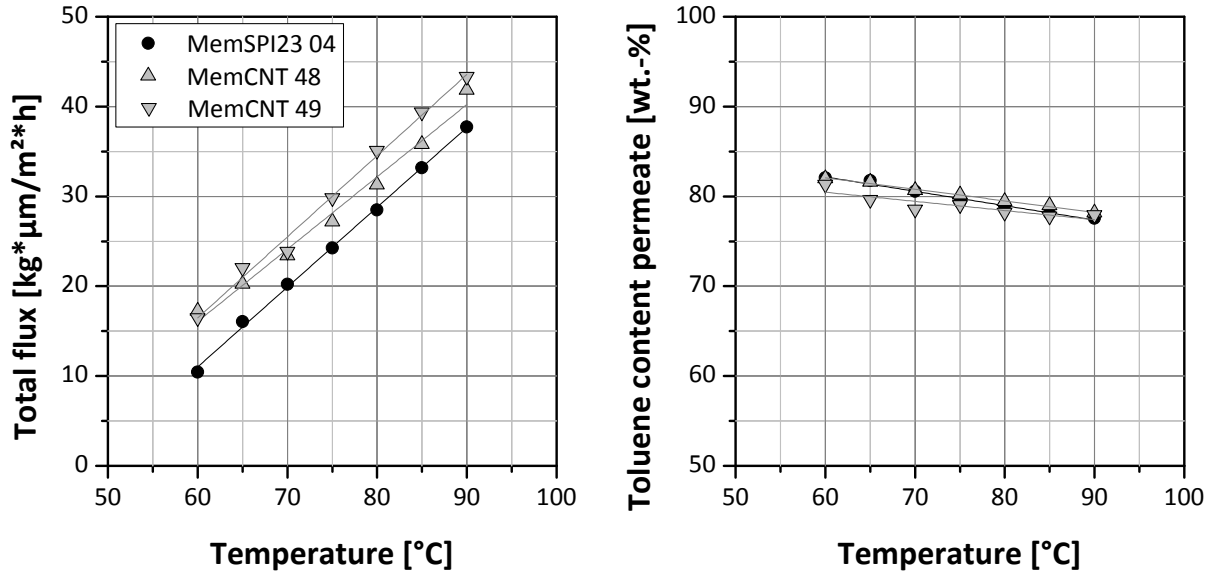


Figure 5.29: Results for temperature-dependent pervaporation experiments in 50:50 wt.-% toluene/cyclohexane mixture with a pure copolyimide membrane (black symbols) and nanocomposites containing 1 wt.-% MWCNT-OH (grey symbols). Experiments were conducted at temperatures between 60 – 90 °C and using a permeate pressure of 25 mbar.

With rising temperature a strong increase of flux is found while at the same time a small decline of the toluene concentration in the permeate is observed. For the pure copolyimide the flux increases from 10.5 to 37.7 kg·μm·m<sup>-2</sup>·h<sup>-1</sup> and for the nanocomposites from 16.5 to 43.3 kg·μm·m<sup>-2</sup>·h<sup>-1</sup>. Simultaneously the toluene content in the permeate drops approximately from 82 to 78 wt.-%. This was expected as the temperature raise generally enhances the flexibility of the membrane material as well as the diffusivity of the feed components thus enhancing the flux and reducing the selectivity. While for the permeate composition only insignificant deviation between pure polymer and nanocomposite membranes is found the fluxes of the membranes differ. Like already found in concentration-dependent measurements the MWCNT/copolyimide membranes exhibit much higher fluxes than the copolyimide membranes. However with rising temperature the flux of both membrane types increases at a similar rate.

### 5.2.2.3 Determination of activation energies for the permeation

Based on the temperature-dependent data it is possible to determine the activation energies  $E_j$  for the permeation of the individual feed components through the membrane. Here the Arrhenius equation is used and applied on the pervaporation process. According to this equation the normalized Flux  $J_n$  [kg·μm·m<sup>-2</sup>·h<sup>-1</sup>] of a component  $n$  shows the following dependency on the activation energy:

$$J_n = J_0 * \exp\left(\frac{E_j}{R * T}\right) \quad (\text{Eq. 5.1})$$

Herein  $J_0$  [ $\text{kg}\cdot\mu\text{m}\cdot\text{m}^{-2}\cdot\text{h}^{-1}$ ] is a non-dimensional pre-exponential factor.  $E_j$  is the activation energy in [ $\text{J}\cdot\text{mol}^{-1}$ ],  $R$  the gas constant [ $8.314 \text{ J}\cdot\text{mol}^{-1}\cdot\text{K}^{-1}$ ] and  $T$  the absolute temperature [K]. The separation characteristics obtained in temperature-dependent experiments are used. By plotting the normalized partial fluxes against the reciprocal absolute temperature a diagram as shown in figure 5.30 is obtained.

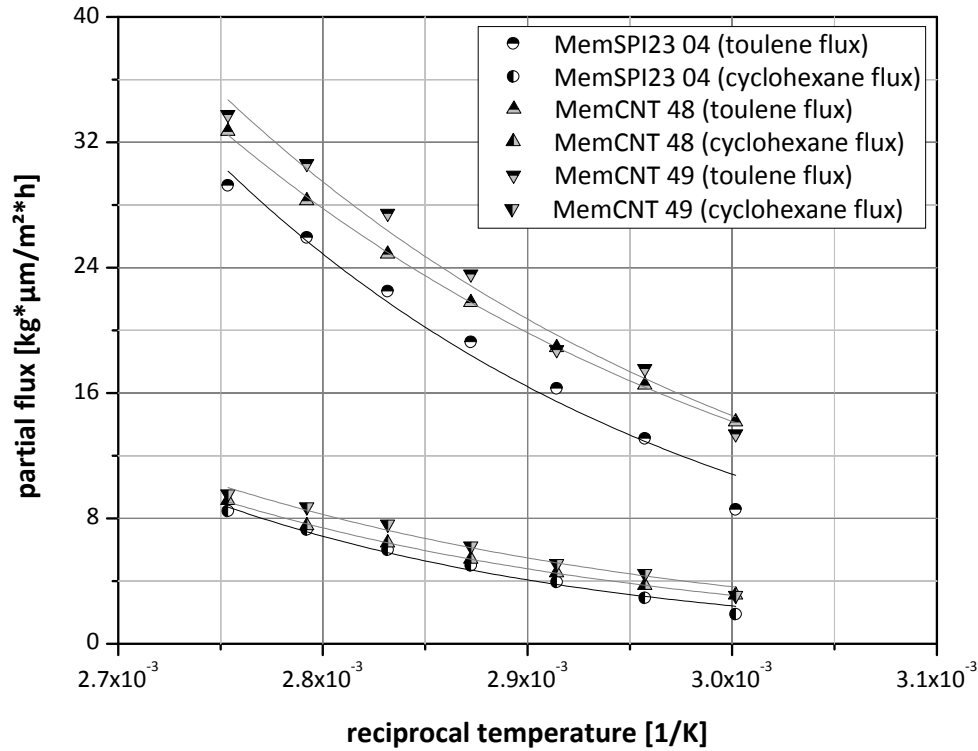


Figure 5.30: The activation energies for the permeation of the feed components are calculated using the exponential factors obtained from the fitted functions in the plot of partial fluxes vs. reciprocal temperatures. Results for pure polymer membranes (white half-filled symbols) and nanocomposites containing 1 wt.-% MWCNT-OH (grey half-filled symbols) are presented.

The equations obtained from the exponential fits can be expressed as Eq. 5.2 shows:

$$y = a * \exp(b * x) \quad (\text{Eq. 5.2})$$

The data obtained from the fit curves in figure 5.30 are presented in table 5.3.

Table 5.3: Data obtained from the exponential fit curves in figure 5.30.

Experimental series	a [ $\times 10^5$ ]	b	standard error of b	R <sup>2</sup>
MemSPI23 04 (toluene flux)	28.8	-4163.6	322.4	0.9712
MemSPI23 04 (cyclohexane flux)	146.5	-5205.1	332.1	0.9817
MemCNT 48 (toluene flux)	34.0	-3361.0	38.6	0.9993
MemCNT 48 (cyclohexane flux)	14.7	-4357.0	64.5	0.9989
MemCNT 49 (toluene flux)	5.7	-3527.4	213.8	0.9811
MemCNT 49 (cyclohexane flux)	7.8	-4092.0	295.2	0.9747

## 5 Results and discussion

Analogous to equation 5.1 the  $y$ -value corresponds to the normalized partial flux  $J_n$ ,  $a$  is the pre-exponential factor  $J_o$  and  $x$  correlates to the reciprocal absolute temperature  $1/T$ . Hence for the factor  $b$  the following equation results:

$$b = -E_J * R^{-1} \quad \text{or} \quad E_J = -b * R \quad (\text{Eq. 5.3})$$

With  $8.3145 \text{ J}\cdot\text{K}^{-1}\cdot\text{mol}^{-1}$  for  $R$  the activation energy of the permeation  $E_J$  of the individual feed components can be calculated together with the corresponding error using  $b$  and its standard error obtained together with the fit function. Table 5.4 gives an overview of all activation energies determined.

**Table 5.4: Activation energies for the permeation of toluene and cyclohexane through membranes of the copolyimide 6FDA-4MPD/6FDA-DABA 4:1 and nanocomposites of the same polymer containing 1 wt.-% MWCNT-OH.**

Membrane	$E_J$ toluene [kJ* $\text{mol}^{-1}$ ]	$E_J$ cyclohexane [kJ* $\text{mol}^{-1}$ ]	Difference of $E_J$ cyclohexane vs. $E_J$ toluene in percent
MemSPI23 04	34.6 $\pm$ 2.7	43.3 $\pm$ 2.8	20 %
MemCNT 48	27.9 $\pm$ 0.3	36.2 $\pm$ 0.5	23 %
MemCNT 49	29.3 $\pm$ 1.8	34.0 $\pm$ 2.5	14 %

The comparison shows that with nanocomposite membranes containing 1 wt.-% MWCNT-OH the activation energies for the permeation of toluene and cyclohexane are between 15 and 20 % lower than with pure polymer membranes. This supports the assumption made in chapter 5.2.2.1 that the incorporation of MWCNT-OH into the copolyimide clearly facilitates the permeability of as well toluene and cyclohexane and thus improves their fluxes significantly.

### 5.2.2.4 Summary of pervaporation results

In the pervaporation experiments it was shown that the MWCNT-OH/copolyimide nanocomposites possess superior separation characteristics compared to the pure copolyimide. The incorporation of only 1 wt.-% MWCNT-OH noticeably increases fluxes and thus the process productivity while the separation efficiency is only slightly reduced. Also the nanocomposite membranes exhibit a higher resistance towards swelling in toluene than the copolyimide which indicates that cross-linking took place during the nanocomposite preparation. In figure 5.31 the separation characteristics of the pervaporation membranes analyzed in this work are compared with data from previous works using the same copolyimide. Here pervaporation data of the pure copolyimide as well as results for diol cross-linked membranes are presented.

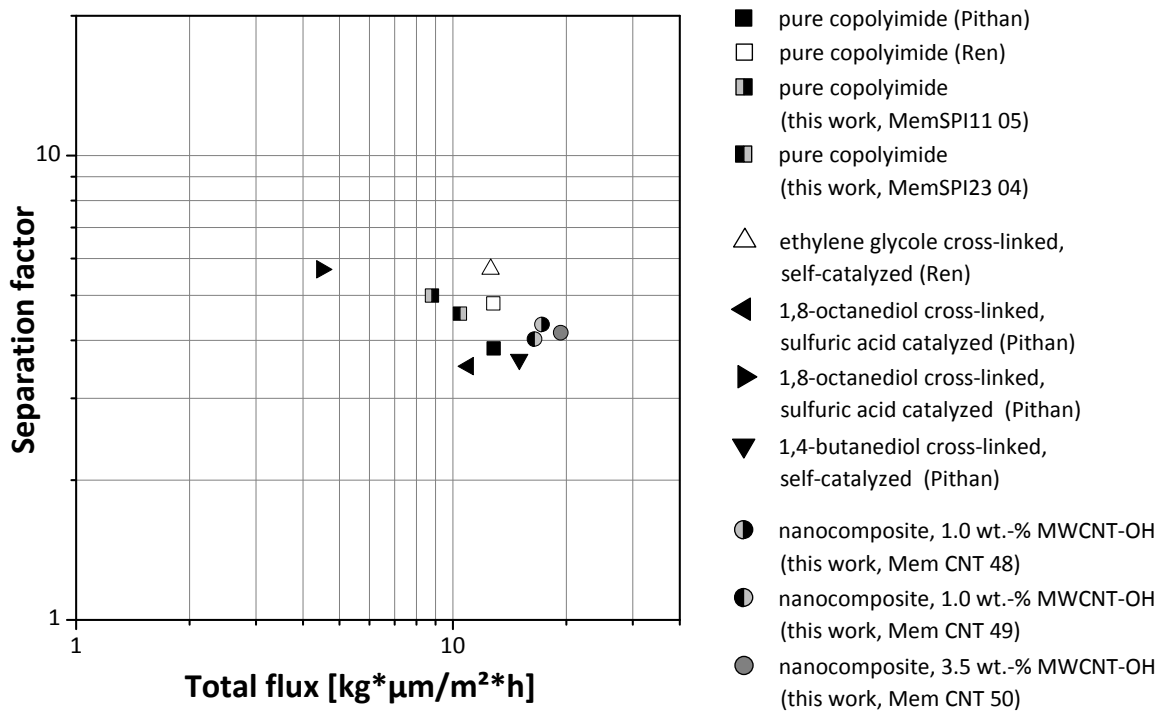


Figure 5.31: Overview of pervaporation data in the form of an upper-bond diagram for experiments with 50:50 wt.-% aromatic/alicyclic mixtures and different membranes based on the copolyimide 6FDA-4MPD/ 6FDA-DABA 4:1. All membranes were pretreated at room temperature in pure toluene for 24 h. **White symbols:** data by Ren<sup>[33]</sup> for benzene/cyclohexane mixtures ( $T = 60\text{ }^{\circ}\text{C}$ ;  $p_{\text{permeate}} = 15\text{ mbar}$ ). **Black symbols:** data by Pithan<sup>[31]</sup> for toluene/cyclohexane mixtures ( $T = 60\text{ }^{\circ}\text{C}$ ;  $p_{\text{permeate}} = 25\text{ mbar}$ ). **Grey/half-gray symbols:** data obtained within this work for toluene/cyclohexane mixtures ( $T = 60\text{ }^{\circ}\text{C}$ ;  $p_{\text{permeate}} = 25\text{ mbar}$ ).

The separation characteristics for the pure copolyimide differ between the three studies. Therefore the results for cross-linked or nanocomposite membranes should be primarily compared to the pure copolyimide results of that particular work. Generally a diol cross-linking reduces the flux of the membrane while selectivity can be lowered as well as increased. Also this cross-linking type only has a rather small influence on the separation characteristics of the corresponding pure polymer. There are however two notable exceptions. These are on the one hand the self-catalyzed 1,4-butanediol cross-linked membrane, which exhibits a slightly higher flux than the pure copolyimide membrane and on the other hand the sulfuric acid catalyzed 1,8-octanediol cross-linked membrane, for which much lower flux but a noticeably higher separation factor are found. In this work the fluxes of the pure copolyimide were lower than those found by Ren and Pithan. However the fluxes obtained with the MWCNT-OH/copolyimide nanocomposites surpass the results of all previous membranes. Admittedly the separation factors are a bit reduced by the addition of MWCNT-OH.

Based on the comparison to diol cross-linking the formation of MWCNT-OH/copolyimide nanocomposites membranes appears as the superior route to increase the separation characteristics and swelling resistance of the copolyimide 6FDA-4MPD/6FDA-DABA 4:1.

### **5.3 Gas separation with titanasilicate/copolyimide MMM**

In the following the results related to mixed matrix membranes composed of copolyimide and different titanasilicate materials are described. This encompasses the preparation of MMMs as well as the presentation of the separation characteristics obtained in gas separation experiments.

#### **5.3.1 Development of titanasilicate/copolyimide MMM membranes**

In contrast to the MWCNT/copolyimide nanocomposites where prior to this work no practical experience on membrane preparation was available for MMMs no preparation method had to be developed here. However a method had to be found which allows horizontal alignment of the sheet shaped filler material in order to increase the sieving effect introduced to the membrane. During the casting process many parameters influence the outcome of the membrane preparation. Here the concentration of the polymer solution was considered as the most promising parameter to investigate on. On the one hand it is relatively easy to control the amounts of solvent and polymer while on the other hand even small changes can have a big influence on the membrane fabrication. The solvent polymer ratio not only accounts for the duration of membrane evaporation but also influences the viscosity of the casting mixture. This again directly influences the sedimentation behavior of the filler particles. Therefore it was investigated how the filler orientation can be influenced through the solvent concentration in the casting mixture. For this reason MMMs containing between 5 and 10 wt.-% of disaggregated JDF-L1 were prepared using 10 and 13 wt.-% solutions of the copolyimide 6FDA-4MPD/6FDA-DABA 4:1 in THF. The membranes were characterized with several different techniques and the according results are presented in the following.

##### **5.3.1.1 Thermogravimetric analyses of titanasilicate containing MMMs**

The exact content of filler in the MMMs was determined via thermogravimetric analyzes. It was already found that in air as well as in nitrogen the polymer decomposes nearly free of residues at temperatures below 700 °C (see figure 5.26). The thermal stability of JDF-L1 on the contrary is much higher. For this reason the actual amounts of filler in the MMMs can be determined using TGA. The better the experimental values accord with the theoretical filler loads the better the dispersion of the titanasilicate in the casting mixtures and in the membranes respectively. Figure 5.32 shows the TGA curves of a pure copolyimide membrane and membranes containing 5, 8 and 10 wt.-% of JDF-L1. For these MMMs actual filler loads of 7.0, 8.7 and 13.0 wt.-% were determined. The deviation between the theoretic and experimental values suggests a lack of homogeneity in the casting mixture or sedimentation of the filler during membrane preparation. Moreover up to 200 °C no weight loss can be observed for all membranes analyzed here which proves that the membrane drying step sufficiently removes solvent residues.

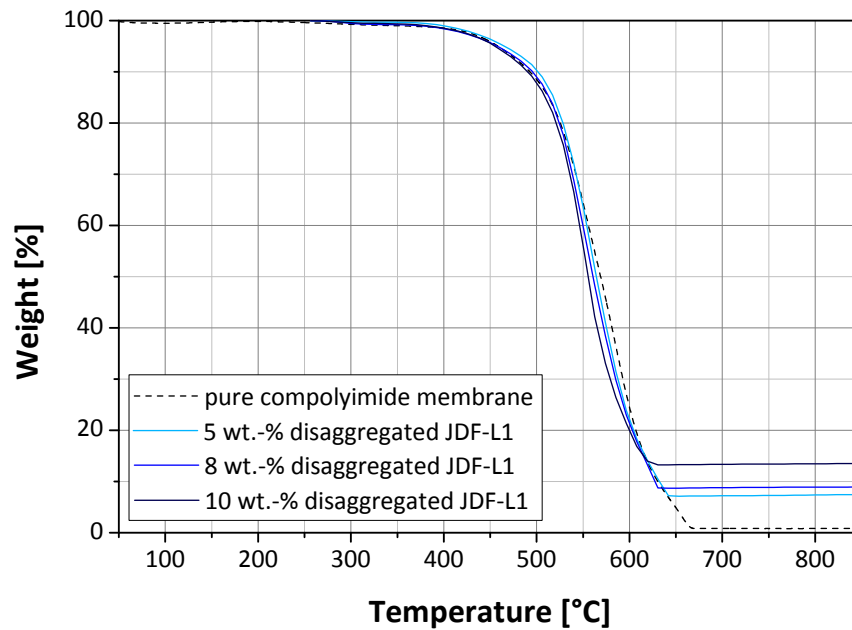


Figure 5.32: Thermogravimetric analyses of pure copolyimide membrane as well as membranes containing 5, 8 and 10 wt.-% of disaggregated JDF-L1. MMMs were prepared from a 10 wt.-% polymer solution.

### 5.3.1.2 Scanning electron microscopy of titanosilicate containing MMMs

By means of SEM analyzes it was intended to obtain information on the filler distribution within the MMMs. Also the orientation of the sheets was of interest. For this the membrane cross sections were analyzed in the electron microscope. In order to receive a reliable impression of the membrane structure a large segment covering ca. 350  $\mu\text{m}$  of a cross-section was depicted by taking nine consecutive SEM images. Contrast in the images was increased to provide better visibility of the crystal sheets within the polymer. Figure 5.33 shows the according images from a MMM containing 8 wt.-% disaggregated JDF-L1 prepared from a 10 wt.-% polymer solution. The broad overview shows a good dispersion of the sheets within the membrane. This states that the dispersion treatment chosen in the membrane preparation method suffices for the fabrication of MMM with homogeneously distributed filler particles.

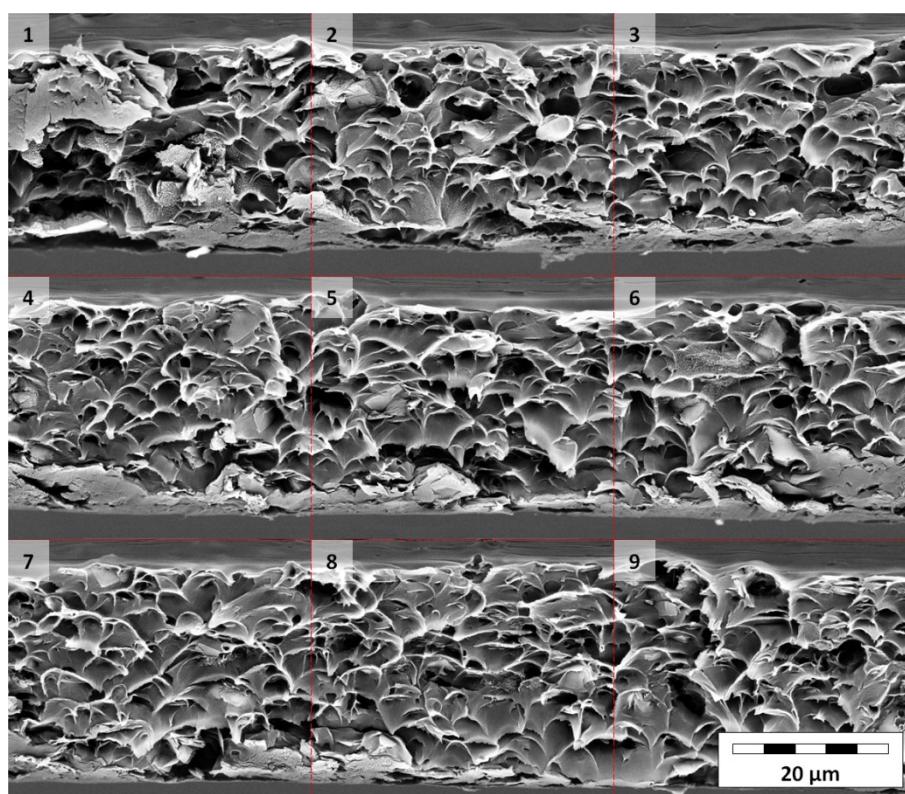


Figure 5.33: SEM image showing the cross-section of a MMM containing 8 wt.-% disaggregated JDF-L1 prepared from a 10 wt.-% polymer solution. The overview presented here is composed of nine consecutive SEM images and covers a distance of ca. 350 μm of the membrane cross-section.

The second information that was intended to be obtained from the series of SEM images is the orientation of the JDF-L1 crystal sheets. Indeed a preferentially horizontal orientation was found. In figure 5.34 exemplarily a detail of a section of image #3 in figure 5.33 is presented.

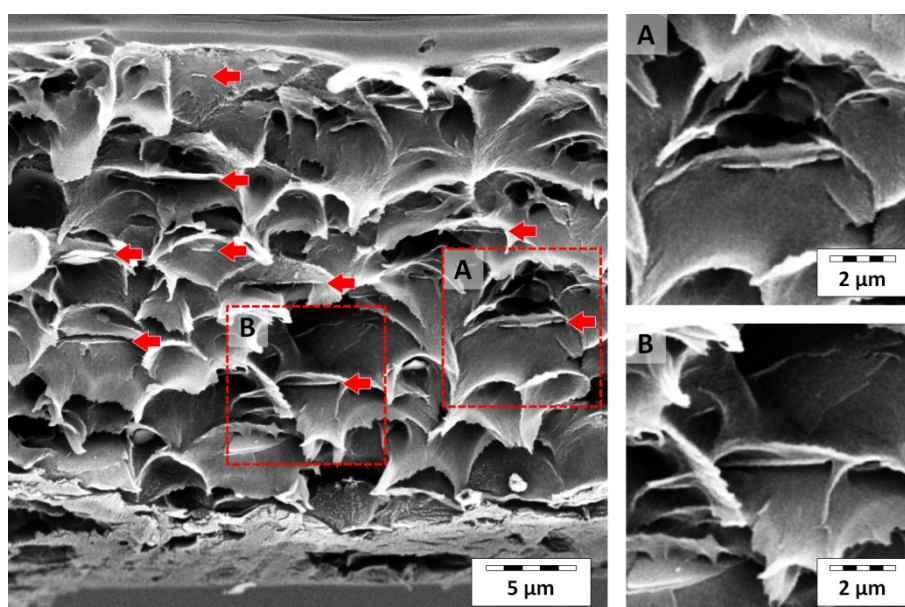


Figure 5.34: Detail of image #3 from the series of consecutive SEM images as seen in figure 5.33. The image shows preferentially horizontal orientation of JDF-L1 sheets.

In the presented area multiple horizontally oriented sheets of JDF-L1 can be found which are highlighted by red arrows for easier identification. The cut-outs A and B in figure 5.34 also show that

the crystals exhibit only very low angles of inclination. Moreover the two enlargements indicate good interaction between polymer and titanosilicate crystals.

### 5.3.1.3 Polarized light microscopy of titanosilicate containing MMMs

To compare the degree of JDF-L1 orientation in MMMs prepared from 10 and 13 wt.-% polymer solutions polarized light microscopy was applied. Figure 5.35 shows images of all MMMs in the according series obtained with the light microscope.

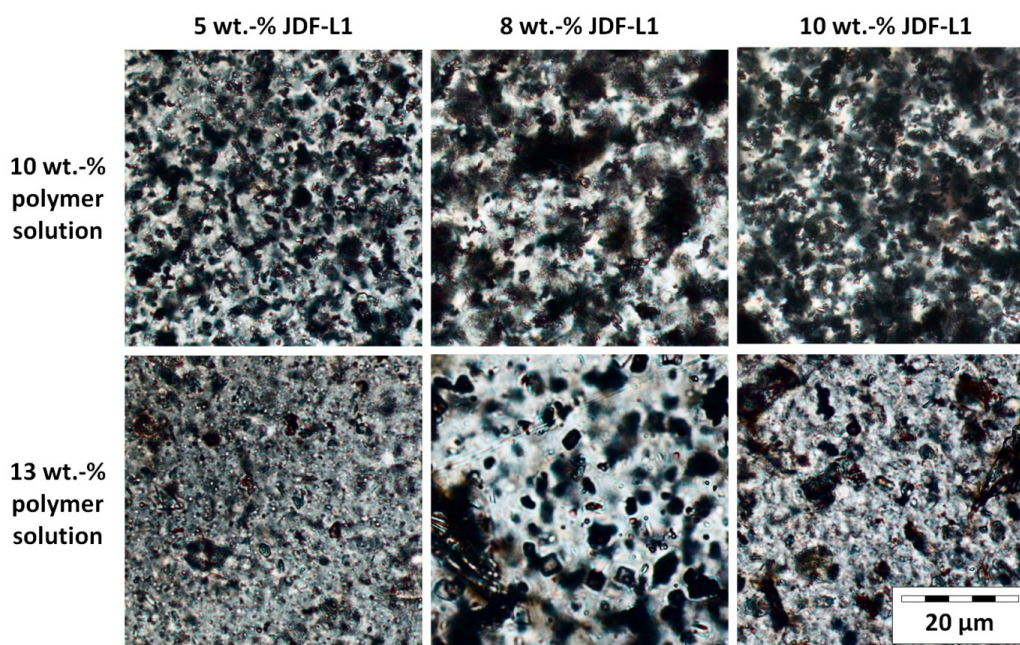


Figure 5.35: MMMs containing different amounts of JDF-L1 were examined with a polarized light microscope. Membranes are cast from copolyimide solutions of 10 wt.-% (upper row) and 13 wt.-% (lower row) in tetrahydrofuran.

Images were collected by facing the membrane surface and viewing across it using polarized light. The images visualize the structure of the MMMs. The inorganic filler JDF-L1 is visible as black particles within the transparent organic polymer. It is expected that with higher filler loads the images appear darker. However if the JDF-L1 sheets exhibit a high degree of inclination this effect will not be as visible as in membranes with predominantly horizontally aligned sheets. This is because the filler is observed more laterally when the sheets are tilted out of the viewing direction and thus appear as a smaller particles. In figure 5.35 it can clearly be seen that the MMMs cast from a 10 wt.-% polymer solution exhibit a drastic decrease of brightness with increasing filler content. According to the theory this means that the sheets of JDF-L1 are predominantly oriented perpendicular to the axis of observation and thus for the membranes a horizontal sheet orientation can be assumed. On the contrary the decrease of brightness with increasing filler load is comparably lower for the membranes cast from 13 wt.-% polymer solutions. Consequently this means that only little horizontal orientation is found here. Instead the JDF-L1 sheets exhibit much higher inclination angles.

### 5.3.1.4 X-ray diffraction of titanosilicate containing MMMs

In order to get structural information on the filler inside the membrane diffraction patterns of the MMMs were measured. The spectra are expected to possess peaks related to the structure of JDF-L1. Information on the sheet orientation can be obtained by comparing peaks intensities. If the material is predominantly horizontally oriented the peaks related to the layered structure of the material ([001], [002] and [003]) are expected to noticeably gain intensity while peaks related to other directions should appear much lower or even disappear completely. XRD patterns of the individual membrane components (polymer and filler) and a MMM are compared in figure 5.36.

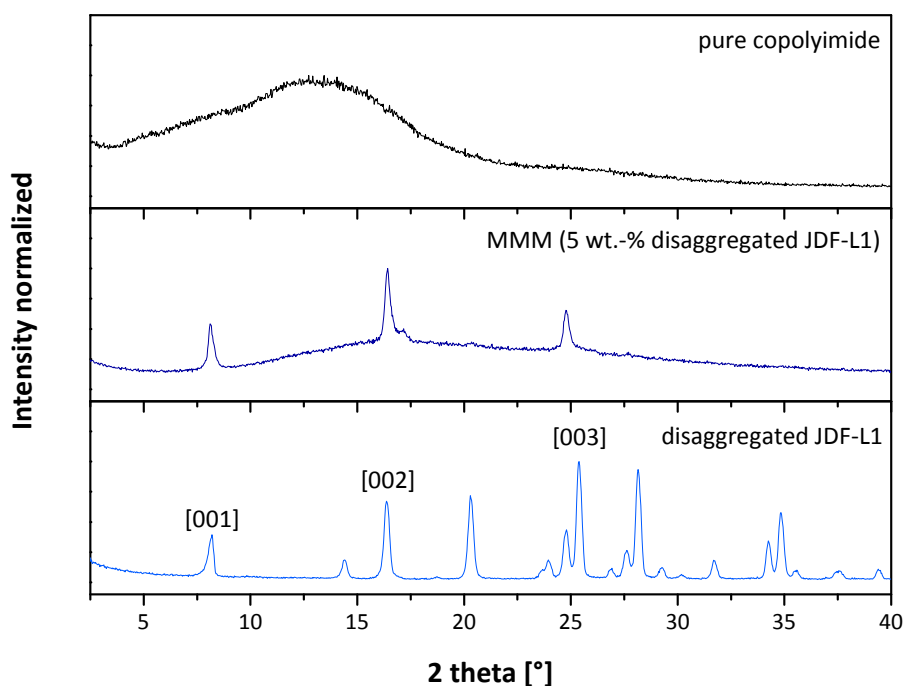


Figure 5.36: Comparison of XRD spectra of a pure copolyimide membrane, a MMM containing 5 wt.-% disaggregated JDF-L1 cast from a 13 wt.-% polymer solution and disaggregated JDF-L1.

In the mixed matrix membrane three distinct peaks are found at  $2\theta = 8.1, 16.4$  and  $24.8^\circ$  which correspond to the crystallographic directions [001], [002], and [003] of JDF-L1. The spectrum also exhibits a bulge typical for amorphous materials which is related to the copolyimide matrix. For the pure polymer a similarly broad signal with a maximum around  $2\theta = 13.0^\circ$  is observed. The presence of the three peaks in the XRD pattern of the MMM confirms that the layered structure of JDF-L1 crystal sheets is not altered by incorporating the material into the copolyimide matrix. Apart from the three above mentioned peaks no signals related to other crystallographic directions are found. The absence suggests that a noticeable degree of sheet orientation is present in the membrane. This is because a complete random sheet orientation would provide further signals. As the XRD patterns in figure 5.37 show similar findings were obtained for the other MMMs too. Moreover the fact that the broad peak attributed to the polymer is displaced to higher  $2\theta$  values suggests good interaction between the filler and the polymer. This is in good agreement with previous publications related to MMMs made from polysulfone<sup>[7,134]</sup>.

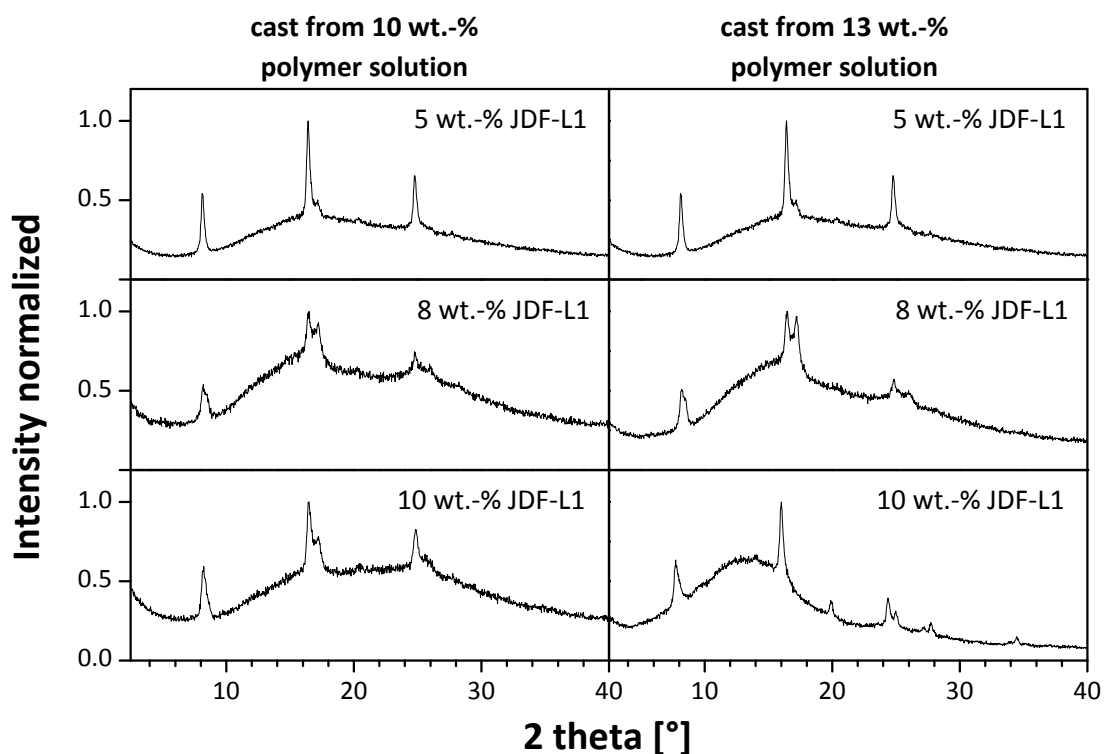


Figure 5.37: XRD patterns of MMMs containing different loads of disaggregated JDF-L1. Membranes on the left were cast from 10 wt.-% polymer solutions while membranes shown on the right were cast from 13 wt.-% polymer solutions.

Moreover angle dependent X-ray diffraction has been conducted with MMMs containing 8 wt.-% of the titanosilicate filler. As stated previously it is expected that a predominantly horizontal orientation of the crystal sheets leads to high intensities of the peaks related to the direction of the lamellar structure in JDF-L1 ([001], [002] and [003]). However in this case the intensity of these peaks is supposed to decrease by tilting the sample holder<sup>[50]</sup>. The more the sample is inclined away from the direction of the X-rays the lesser the intensity is expected to be. For this analysis the peak at  $2\theta = 8.3^\circ$ , related to [001], was chosen as the most suitable one. It possesses a high intensity and is not superimposed by the signal of the polymer like the peaks related to [002] and [003] making it the best peak to observe any angle dependency. Figure 5.38 shows the results of angle dependent XRD analyses of MMMs containing 8 wt.-% disaggregated JDF-L1 cast from either a 10 or a 13 wt.-% polymer solution. In the membrane cast from a 10 wt.-% polymer solution the peak shows a much higher intensity than in the membrane cast from a 13 wt.-% polymer solution. It can be seen that with higher inclination of the sample holder both intensities are reduced. However the decline is much stronger for the membrane cast from a 10 wt.-% polymer solution as it was expected in case of a preferential horizontal orientation of filler sheets within the polymer matrix.

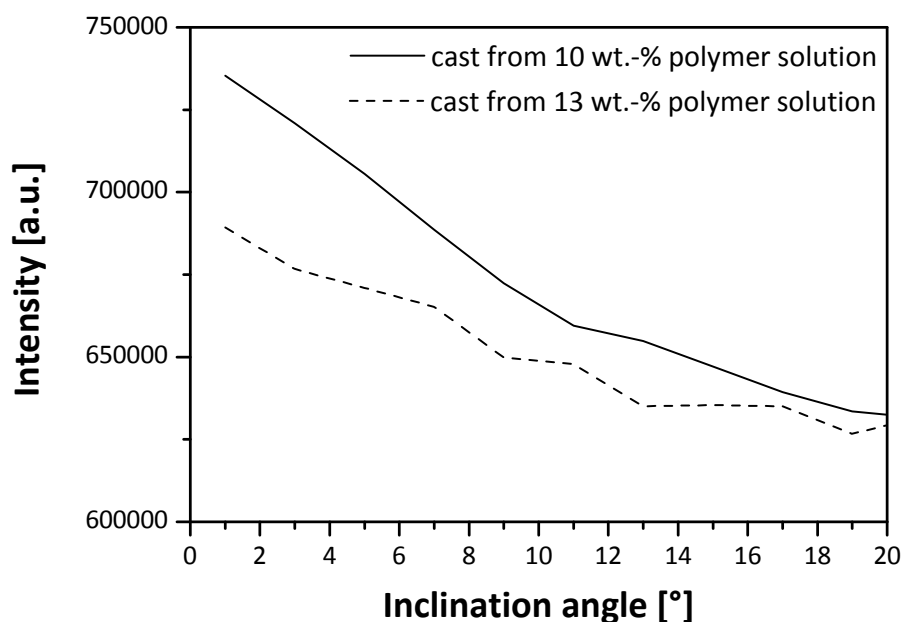


Figure 5.38: Angle dependent X-ray diffraction of MMMs cast from 10 and 13 wt.-% polymer solutions containing 8 wt.-% disaggregated JDF-L1. The intensity of the peak at  $2\theta = 8.25^\circ$ , which is related to the [001] direction, was measured at different tilt angles of the sample holder.

### 5.3.1.5 Raman spectroscopy of titanosilicate containing MMMs

To obtain further information regarding the sheet orientation within the polymer matrix polarized Raman spectroscopy was conducted. Here a beam of linear polarized laser light was aimed at the MMMs surface and the reflected signal was collected through a polarizer. From this set-up information on the structure of the sample can be deduced by comparing the Raman spectra collected with either perpendicular or parallel setting of the polarizer. If the material is randomly oriented only small differences between the two spectra is expected. On the contrary differences between the perpendicular and parallel spectrum will be observed if the material exhibits a preferential orientation. Moreover the differences will increase with a higher degree of orientation. Figure 5.39 shows the spectra of pure polymer and figure 5.40 presents the data of MMMs.

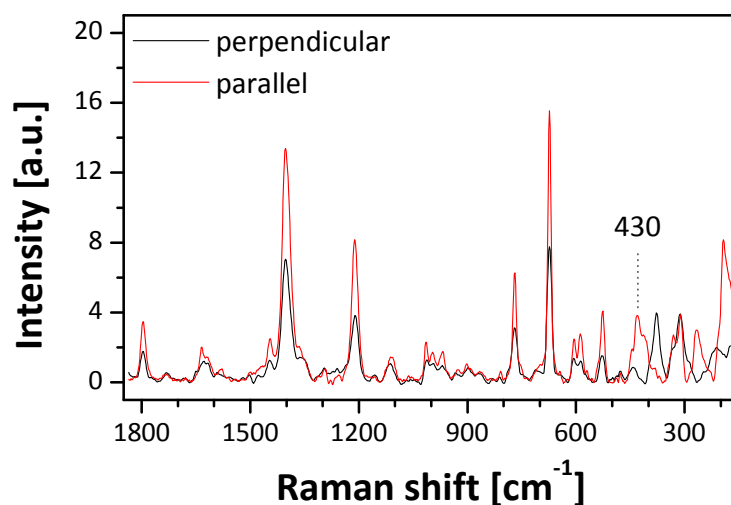


Figure 5.39: Raman spectrum of the copolyimide 6FDA-4MPD/6FDA-DABA 4:1.

For the polymer small differences between the perpendicular and parallel polarized spectrum are found. This suggests that the copolyimide itself is not randomly oriented. When comparing the spectra of polymer and MMMs it is found that in case of the copolyimide the differences between perpendicular and parallel polarization are higher in the MMM spectra. This means that the incorporation of JDF-L1 sheets increases the polymer orientation. Also it is found that most signals observed for the MMMs are related to the polymer.

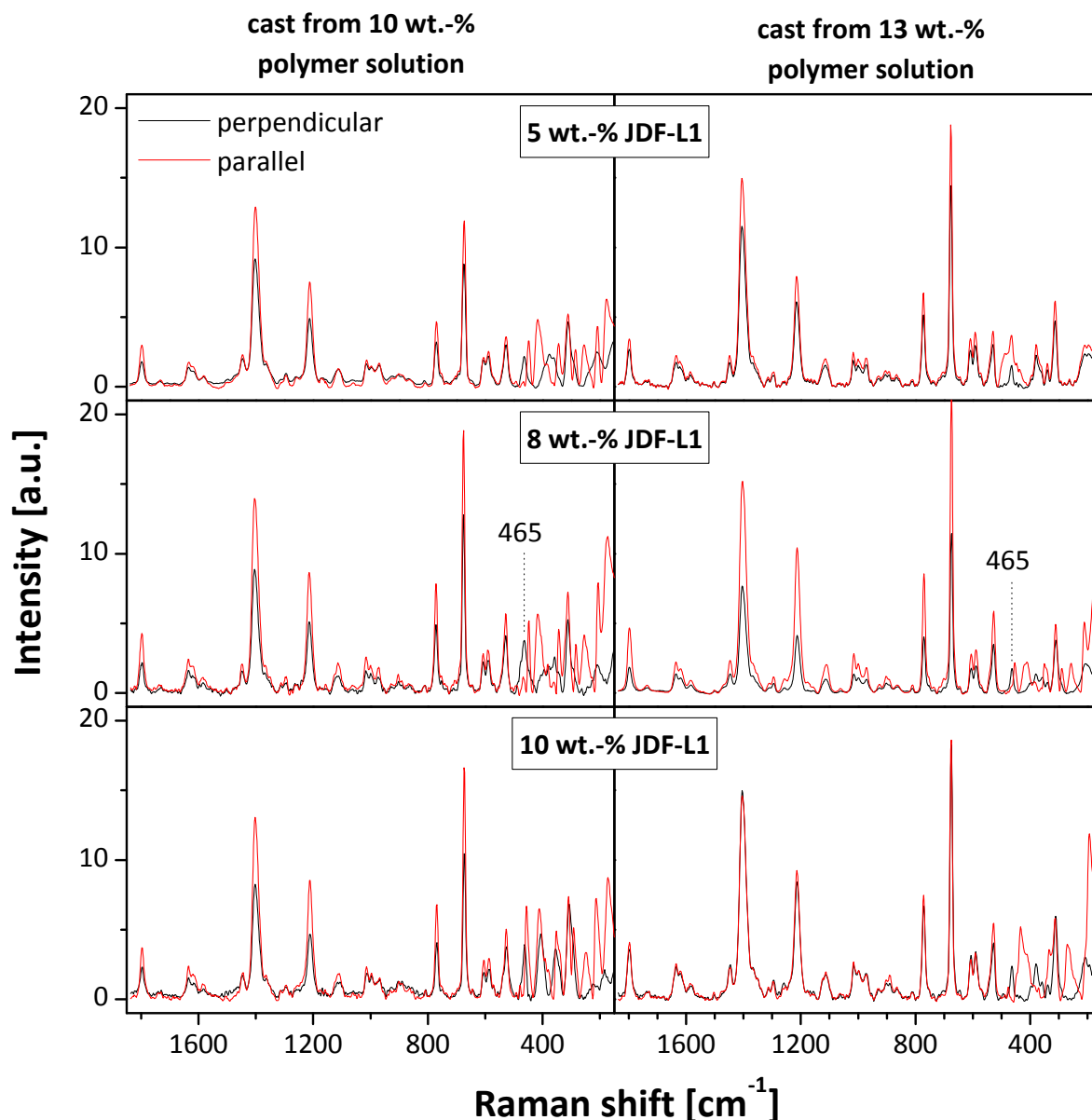


Figure 5.40: Raman spectra of MMMs containing 5, 8 and 13 wt.-% JDF-L1 and cast from 10 respectively 13 wt.-% polymer solutions.

As stated above the changes between the spectra collected with a parallel and perpendicular polarizer allow conclusions to be drawn regarding the degree of material orientation. In the present case a stronger deviation of the perpendicular spectra is related to a higher degree of horizontal orientation of the filler sheets. Most influence of the filler incorporation on the MMMs can be observed in the perpendicular spectra between 500 and 200  $\text{cm}^{-1}$ . In this range several signals disappear and others are narrowed. The perpendicular spectra show a strong polymer related signal at 430  $\text{cm}^{-1}$  which disappears under parallel polarization. This enables the observation of a

## 5 Results and discussion

characteristic peak related to JDF-L1 at  $465\text{ cm}^{-1}$ . This is well visible for MMMs with a filler load of 8 wt.-%. When comparing the MMMs cast from different concentrated polymer solution it can be seen that the aforementioned effect is stronger for the MMMs cast from 10 wt.-% polymer solutions. This is in accordance with the previously presented results obtained from X-ray diffraction.

### 5.3.1.6 Results of stress-strain experiments with MMMs

Stress-strain experiments were carried out in order to obtain information about the possible influences of the filler and its orientation on the mechanical properties of the membrane. For this the Young's moduli of pure polymer membranes and MMMs were determined. Table 5.5 provides an overview on the Young's moduli obtained from the conducted stress-strain experiments.

**Table 5.5: Results of stress-strain measurements with samples of pure polymer membranes and MMMs with different filler content cast from 10 wt.-% and 13 wt.-% polymer solution.**

Membrane	Young's modulus [MPa]	
copolyimide	batch SPI 02	2100
	batch SPI 05	2200
MMM cast from 10 wt.-% polymer solution	5 wt.-% JDF-L1	2900
	8 wt.-% JDF-L1	2600
	10 wt.-% JDF-L1	3000
MMM cast from 13 wt.-% polymer solution	5 wt.-% JDF-L1	2600
	8 wt.-% JDF-L1	2500
	10 wt.-% JDF-L1	2500

Although no correlation between Young's moduli and rising filler amount was found, the results show that the incorporation of disaggregated JDF-L1 leads to higher Young's moduli for the MMMs. Values increase from 2100 and 2200 MPa respectively for the pure polymer to 2500 - 3000 MPa for the MMMs. This is due to the comparably high stiffness of the inorganic filler which increases the force necessary to induce strain of the membrane. This finding also supports the observations made in the SEM images and in the XRD patterns that organic and inorganic phase exhibit good interaction.

### 5.3.2 Gas separation with JDF-L1/copolyimide MMMs

The results of gas separation experiments are presented and discussed in the following. Pure copolyimide membranes as well as MMMs containing titanosilicate materials as filler were applied to the separation of hydrogen/methane and oxygen/nitrogen mixtures. As seen in table 5.6 only hydrogen exhibits a kinetic diameter smaller than the pores in JDF-L1 of  $3\text{ \AA}$ .

**Table 5.6: Kinetic diameters of the gases used in gas separation experiments.**

	hydrogen	oxygen	nitrogen	methane
kinetic diameter [ $\text{\AA}$ ]	2.89	3.46	3.64	3.87

From this it is predicted that in MMMs containing JDF-L1 hydrogen will be the preferentially permeating component while the filler will form a strong barrier towards methane, oxygen and nitrogen. This effect is expected to increase with parallel orientation of the sheet shaped crystals of JDF-L1 within the polymer matrix. To evaluate this prediction different MMMs with varying types and loads of fillers were prepared and analyzed in gas separation experiments as described above (chapter 4.7). At first a series of MMMs containing between 5 and 10 wt.-% of disaggregated JDF-L1 prepared from 10 and 13 wt.-% polymer solutions are analyzed. Then MMMs containing as-synthesized and disaggregated JDF-L1 are compared. Finally cross-linking and ion exchange of the interlamellar cation were investigated as possible means to improve the so far obtained results. The according separation characteristics are presented in the following.

### 5.3.2.1 Influence of filler orientation

The characterization of MMMs suggests that in membranes cast from a 10 wt.-% polymer solution the crystal sheets of JDF-L1 are predominantly horizontally oriented, while membranes cast from a 13 wt.-% polymer solution exhibit a more random filler orientation. Gas separation experiments with hydrogen/methane and oxygen/nitrogen mixtures were conducted using MMMs containing 5, 8, or 10 wt.-% JDF-L1 in order to find out to which extent the filler load and the differences in filler orientation influence the separation characteristics. The results are presented in figure 5.41 and 5.42.

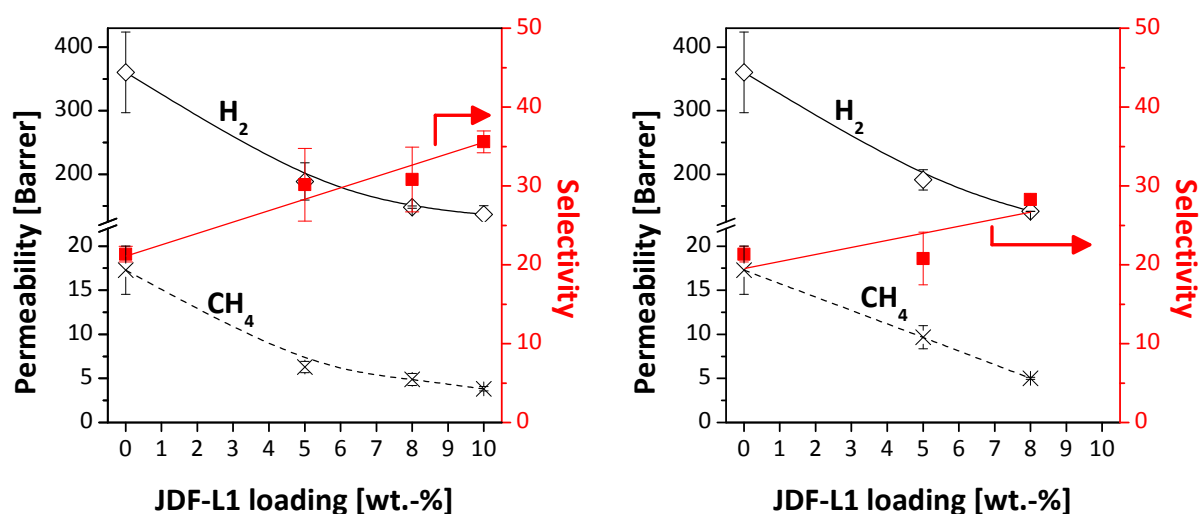


Figure 5.41: Results of H<sub>2</sub>/CH<sub>4</sub> separation experiments with MMMs cast from a 10 wt.-% (left) and 13 wt.-% (right) copolyimide solutions.

In hydrogen/methane mixtures the permeabilities of both gases decrease with higher loads of JDF-L1, as figure 5.41 shows. However the drop for CH<sub>4</sub>-permeability is much more drastic than for H<sub>2</sub>-permeability which leads to a notable increase of H<sub>2</sub>/CH<sub>4</sub> selectivity. From this it can be assumed that the sheet crystals act as an efficient barrier for methane while hydrogen molecules can permeate through the filler. This is in accordance to the behavior expected on basis of kinetic diameters. In comparison to the membranes cast from a 10 wt.-% polymer solution (figure 5.41, left) a lower gain of selectivity with increasing filler loads is found for the MMMs cast from a 13 wt.-% polymer solution (figure 5.41, right). This coincides with the previous characterization results pointing out that a higher degree of horizontal orientation is present in the MMMs cast from 10 wt.-% polymer solutions. The higher the degree of horizontal filler orientation, the stronger the barrier effect on methane and the higher the increase of selectivity is expected. Especially in case of

## 5 Results and discussion

the MMMs containing 5 wt.-% JDF-L1 the difference is obvious. For the membranes cast from a 10 wt.-% polymer solution  $H_2$  and  $CH_4$  permeabilities of 189 and 6.3 Barrer respectively and a  $H_2/CH_4$  selectivity of 30.2 are found while the MMM with the same load cast from a 13 wt.-% polymer solution exhibits  $H_2$  and  $CH_4$  permeabilities of 191 and 9.7 Barrer respectively and a  $H_2/CH_4$  selectivity of 20.8. For comparison the permeabilities of the pure polymer are 360 Barrer for  $H_2$  and 17.3 for  $CH_4$  which yield a  $H_2/CH_4$  selectivity of 21.3. The fact that a predominant horizontal filler orientation leads to a higher reduction of  $CH_4$  permeability suggests that  $H_2$  can actually permeate through the filler. Anyhow the results show that both horizontally oriented as well as non preferentially oriented filler sheets enhance the tortuousness of the molecular transport path across the membrane improving the separation characteristics.

Figure 5.42 presents the results of gas separation experiments with oxygen/nitrogen mixtures. Here again the data obtained for MMMs cast from 10 wt.-% polymer solution are shown in the left, while the results for membranes cast from 13 wt.-% polymer solutions are presented in the right diagram.

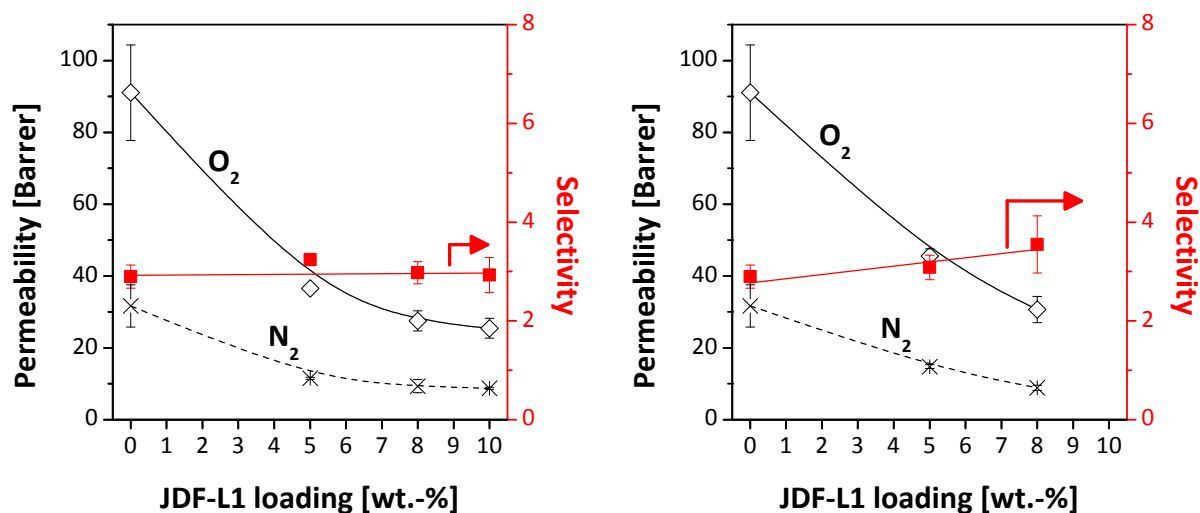


Figure 5.42: Results of  $O_2/N_2$  separation experiments with MMMs cast from a 10 wt.-% (left) and 13 wt.-% (right) copolyimide solutions.

Considering the kinetic diameters shown in table 5.6 and the size of pores in JDF-L1 transverse to the layers (3 Å) it is expected that none of the molecules used here can permeate through the filler. In fact with increasing filler loads the permeability of both gases is reduced at the same degree leaving the selectivity merely unaffected. When comparing the results for MMMs cast from 10 and 13 wt.-% polymer solutions it can be seen that the orientation has only little influence on the  $O_2/N_2$  selectivity. A value of 2.9 is found for the pure polymer while selectivities for the MMMs are between 2.9 and 3.5. Admittedly a stronger barrier effect on the permeation of the feed components is found for the MMMs cast from 10 wt.-% polymer solutions which exhibit a higher degree of horizontal orientation. The permeability of the pure copolyimide is 91.0 Barrer and is decreased in case of all MMMs. For membranes containing 5 and 8 wt.-% of JDF-L1 that were cast from a 10 wt.-% polymer solution  $O_2$  permeabilities of 36.6 respectively 27.5 Barrer were found which are lower than those measured for MMMs prepared from 13 wt.-% polymer solutions (45.6 and 30.7 Barrer).

In both investigated mixtures (figures 5.41 and 5.42) it is found that the results obtained for pure polymer membranes exhibit much larger errors than those for the MMMs. This is presumably due to the diameter of the membrane samples, which was bigger in case of the pure polymer membranes. Although all membranes were cast on an adjustable and leveled out table, unevenness of the casting

support cannot be ruled out completely. With 3.9 cm the diameters of pure polymer membranes were four times larger than those of the MMMs samples, which were around 1 cm. It is supposed that this leads to a more inconsistent thickness and thus a higher measurement inaccuracy in case of pure polymer membranes.

### 5.3.2.2 Influence of disaggregation

In order to evaluate the importance of thorough filler disaggregation MMMs containing 8 wt.-% as-synthesized JDF-L1 were prepared and analyzed in gas separation with mixtures of  $H_2/CH_4$  and  $O_2/N_2$ . In figure 5.43 the results are presented compared to the separation characteristics of the pure polymer and MMMs containing 8 wt.-% of disaggregated JDF-L1.

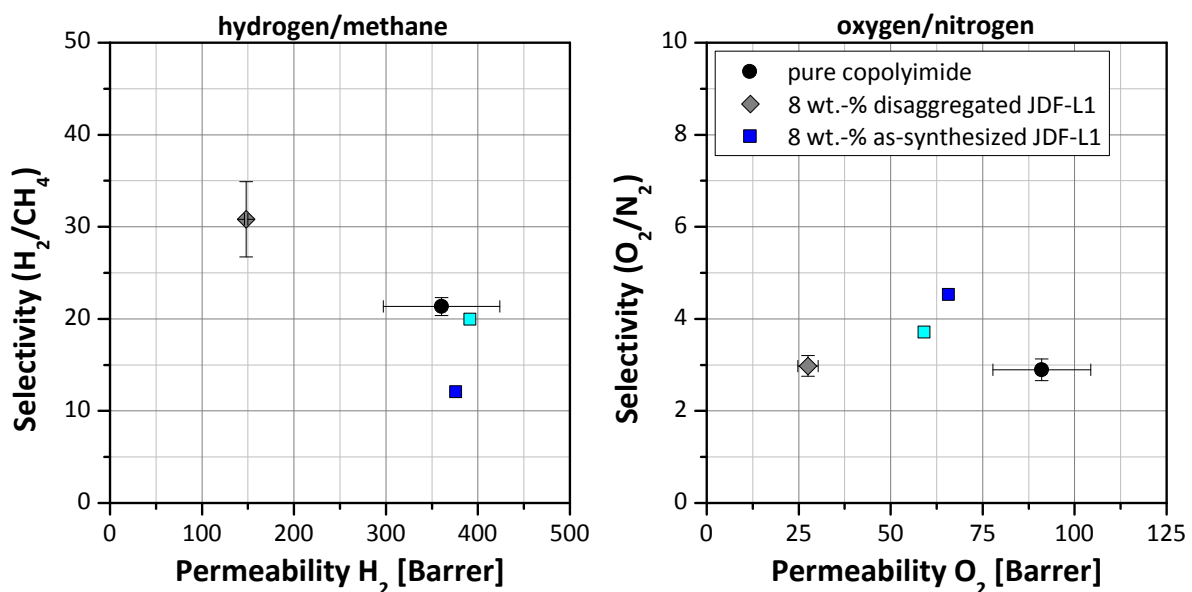


Figure 5.43: Results of gas separation experiments with copolyimide membranes and MMMs cast from a 10 wt. % copolyimide solutions containing 8 wt.-% of either as-synthesized (blue squares) or disaggregated JDF-L1 (grey diamonds). For comparison pure polymer data is presented too (black spheres).

The results obtained with the two MMMs containing as-synthesized JDF-L1 differ noticeably in both mixtures. This might be due to the difficulty to prepare homogeneous MMMs with this material. The JDF-L1 agglomerates possess much larger dimensions than the sheet shaped crystals obtained after disaggregation. Therefore the filler here is more heavily subjected to sedimentation during membrane fabrication and especially membrane casting leading to inhomogeneous membranes. For  $H_2/CH_4$  mixtures hydrogen permeabilities of 376 and 391 Barrer are found for the membranes containing as-synthesized JDF-L1 which is similar to the value of pure copolyimide (360 Barrer). In terms of  $H_2/CH_4$  selectivity however very different values are obtained for the two MMMs. While one membrane exhibits a  $H_2/CH_4$  selectivity of 20 thus similar to the pure polymer (21.3), the other MMM possesses a much lower selectivity of only 12.1 which is possibly a result of membrane inhomogeneity. The comparison of MMMs containing 8 wt.-% as-synthesized and disaggregated JDF-L1 shows that the separation of agglomerates is crucial to obtain a filler material capable of providing increased separation characteristics as shown in chapter 5.3.2.1.

In  $O_2/CH_4$  mixtures a barrier effect due to the incorporation of as-synthesized JDF-L1 is observable as both MMMs exhibit lower permeabilities than the pure polymer. In detail the  $O_2$  permeability is

## 5 Results and discussion

decreased from 91.0 Barrer for the pure polymer to 65.7 respectively 59.1 Barrer. However the membrane containing disaggregated JDF-L1 exhibits an even lower  $O_2$  permeability of only 27.5 Barrer. While polymer and MMMs containing disaggregated-JDF-L1 exhibit  $O_2/CH_4$  selectivities of 2.9 and 3.0 respectively for the two membranes containing as-synthesized JDF-L1 slightly higher values of 4.5 and 3.7 are found. The results obtained with oxygen/nitrogen mixtures also point out the importance of filler disaggregation. The barrier effect leading to decreased permeabilities is much higher in case of 8 wt.-% disaggregated JDF-L1 than in case of as-synthesized JDF-L1.

### 5.3.2.3 Influence of cross-linking

Cross-linking usually leads to a more interconnected membrane material able to withstand swelling (see chapter 0). Due to the enhanced interconnection such membranes commonly exhibit lower permeabilities but higher selectivities. Therefore cross-linking was investigated as means to further improve the trend observed for MMMs containing JDF-L1 as filler (chapter 5.3.2.1). For this ethylene glycol was added to the casting mixture allowing covalent linkage of polymer chains through esterification of the diol and carboxyl acid groups on the polymer chains located on the DABA repeating units. The results of  $H_2/CH_4$  gas separation with cross-linked MMMs containing 5 and 10 wt.-% disaggregated JDF-L1 are compared to non cross-linked MMMs in figure 5.44.

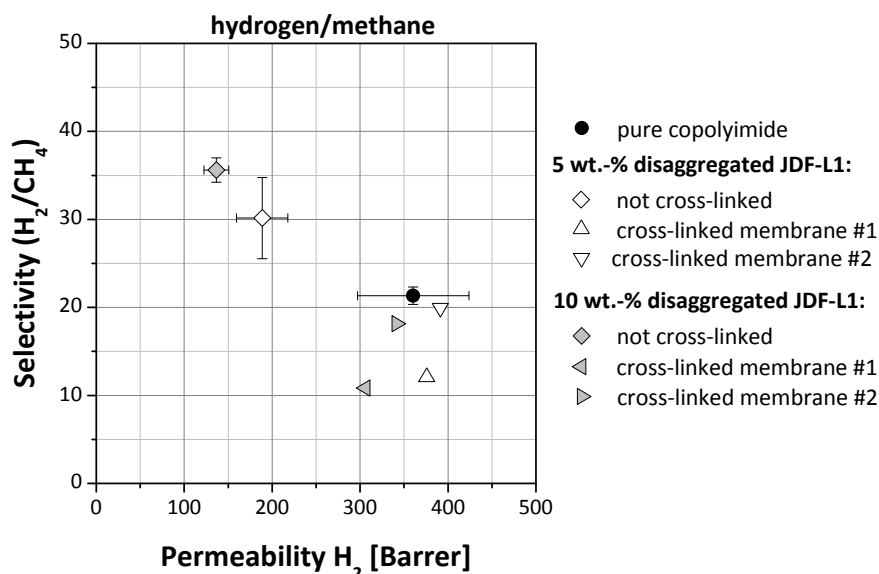


Figure 5.44: Results of gas separation experiments with non cross-linked and ethylene glycol cross-linked MMMs containing 5 wt.-% (white symbols) and 10 wt.-% disaggregated JDF-L1 respectively (grey symbols). Also the data of pure copolyimide membranes is shown for comparison (black spheres).

For each filler load two cross-linked membranes were investigated in gas separation. It can be seen that the results for these membranes differ distinctly suggesting that cross-linking increases membrane inhomogeneity. For the cross-linked membranes a higher filler load leads to lower permeabilities and selectivities. However permeabilities are similar to the values of the pure polymer (360 Barrer). For cross-linked MMMs containing 5 wt.-% JDF-L1 permeabilities of 376 and 391 Barrer are found and values of 306 and 341 Barrer are measured for cross-linked MMMs containing 10 wt.-% JDF-L1. The selectivities are lower than the value found for the pure polymer (21.3). Here 12.1 and 20.0 are measured for MMMs with a filler load of 5 wt.-% and values of 10.8 respectively 18.2 were determined for MMMs containing 10 wt.-% JDF-L1. These results also support the initial

assumption that cross-linking leads to strong inhomogeneity in the membranes. This is presumably due to the enhanced chain stiffness in the polymer which impedes interaction between organic and inorganic matrices, also hindering preferential horizontal orientation of the filler in the MMMs. Therefore voids can be present between polymer and filler which drastically reduce selectivity and increase permeability.

### 5.3.2.4 Influence of interlamellar cation

The aim of exchanging the interlamellar sodium cation in JDF-L1 was to increase the separation characteristics of MMMs containing disaggregated JDF-L1 as presented in chapter 5.3.2.1. It was found that the permeation of  $\text{CH}_4$ ,  $\text{O}_2$  and  $\text{N}_2$  is efficiently hindered in MMMs containing well dispersed individual crystals sheets of JDF-L1 while  $\text{H}_2$  can permeate through the filler to a certain extent. This discrimination drastically increases the selectivity of the material. Cation exchange was now investigated as a method to further increase the deviance of  $\text{H}_2$  and  $\text{CH}_4$  permeability by facilitating the hydrogen permeation. The interlamellar cation is positioned in a central position in front of the pores across the layered structure (see Figure 3.15) of the titanosilicate. Based on the assumption that a molecule is permeating through the filler structure the interlamellar cation will affect the permeation path. By incorporating different cations at this crucial position it is expected to alter the permeation of hydrogen through the filler. As presented in chapter 5.1.3.2 different filler materials based on JDF-L1 with exchanged interlamellar cations were prepared. Gas separation experiments using mixtures of  $\text{H}_2/\text{CH}_4$  and  $\text{O}_2/\text{N}_2$  were conducted with MMMs containing 8 wt.-% of these materials and the results are presented in figures 5.45 and 5.46.

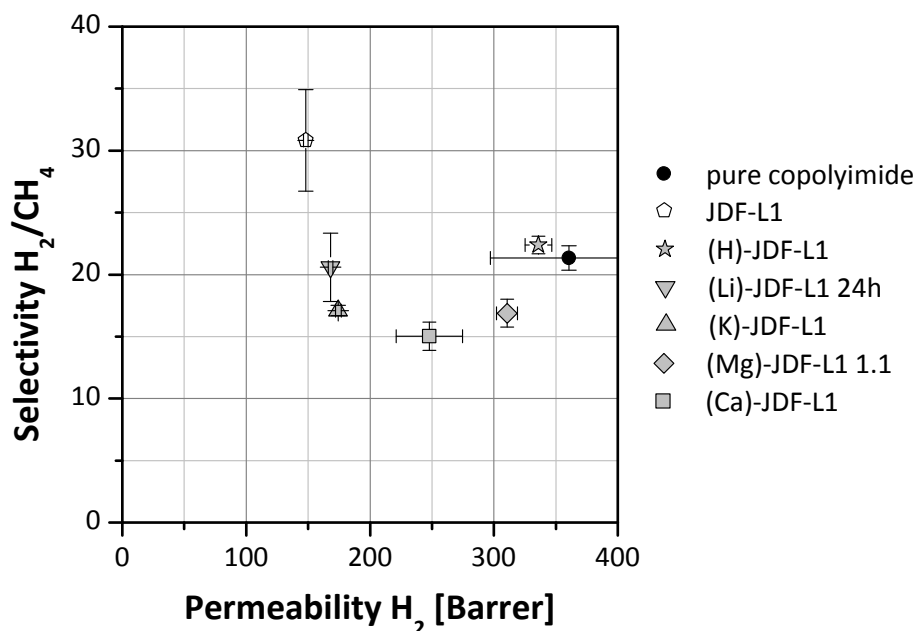


Figure 5.45: Results of  $\text{H}_2/\text{CH}_4$  gas separation experiments with MMMs containing 8 wt.-% of different ion exchanged samples of JDF-L1 (grey symbols). For comparison also results of pure copolyimide membranes (black spheres) and MMMs containing 8 wt.-% disaggregated JDF-L1 (white pentagons) are shown.

In hydrogen/methane mixtures  $\text{H}_2$  permeabilities of 168 and 174 Barrer respectively are found for MMMs containing fillers with the monovalent interlamellar cations lithium and potassium. These values are similar to the value of MMMs containing non ion exchanged JDF-L1 (148 Barrer). On the contrary much higher  $\text{H}_2$  permeabilities are found for membranes containing bivalent cations. With

## 5 Results and discussion

(Mg)-JDF-L1 1.1 a  $H_2$  permeability of 311 Barrer is found and 248 Barrer for (Ca)-JDF-L1. For MMMs containing (H)-JDF-L1 as the filler a  $H_2$  permeability of 336 Barrer and a  $H_2/CH_4$  selectivity of 22.4 are measured which are very similar to the values of pure polymer membranes (360 Barrer and a selectivity of 21.3). This suggests that neither the permeation of  $H_2$  nor  $CH_4$  molecules is hindered by the filler (H)-JDF-L1. With filler materials containing bivalent cations also higher  $CH_4$  permeabilities are found. For (Mg)-JDF-L1 1.1 and (Ca)-JDF-L1 values of 18.5 and 16.5 Barrer are measured while 8.23 and 10.2 Barrer are determined for (Li)-JDF-L1 24h and (K)-JDF-L1. All these permeabilities are generally higher than for MMMs containing disaggregated JDF-L1, where the  $CH_4$  permeability is 4.9 Barrer. Therefore no increase of  $H_2/CH_4$  selectivity is found for MMMs containing ion exchanged filler as it is the case for membranes with disaggregated JDF-L1. Instead in most cases the selectivity even decreases compared to pure polymer membranes. The lowest values with monovalent interlamellar cations are measured for (K)-JDF-L1 with 17.1 and in case of bivalent interlamellar cations for (Ca)-JDF-L1 with 15.0. The highest selectivity of the ion exchanged materials was found for MMMs containing (Li)-JDF-L1 24h with 20.6. This is similar to the value of pure polymer membranes (21.3). The results show that for  $H_2/CH_4$  mixtures a gain of selectivity is only found with non ion exchanged JDF-L1 which however is accompanied by a noticeable reduction of permeabilities. In all ion exchanged materials a loss of the strong barrier effect of the filler towards methane is observed as all measured  $CH_4$  permeabilities exceed by far the value of disaggregated JDF-L1. In case of monovalent cations however the  $H_2$  permeabilities are similar to the value for non ion exchanged JDF-L1, suggesting that neither the treatment with lithium nor potassium significantly alters the permeation of hydrogen through the filler. An exchange of interlamellar sodium with a bivalent cation however noticeably increases the permeability of hydrogen. But at the same time it reduces the barrier effect towards methane. These unexpected results can be explained by the damage inflicted on the JDF-L1 sheet particles by the ion exchange treatment, as evidenced by the according SEM images (see chapter 5.1.3.2). This damaging may have produced meso- and/or macroporosity responsible for the increase of both  $H_2$  and  $CH_4$  permeabilities.

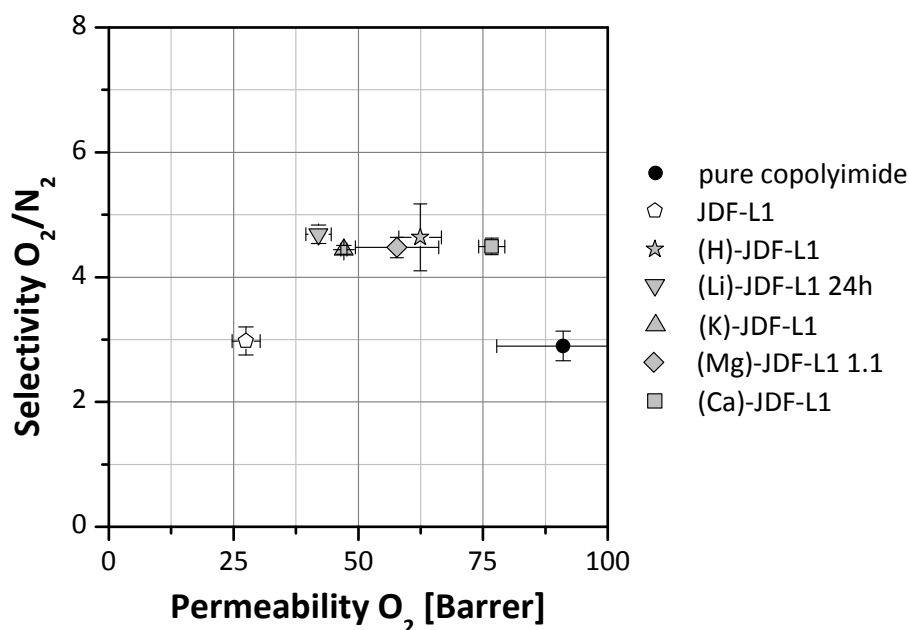


Figure 5.46: Results of  $O_2/N_2$  gas separation experiments with MMMs containing 8 wt.-% of different ion exchanged samples of JDF-L1 (grey symbols). For comparison also results of pure copolyimide membranes (black spheres) and MMMs containing 8 wt. % disaggregated JDF-L1 (white pentagons) are shown.

In oxygen/nitrogen mixtures all MMMs containing ion exchanged titanosilicates as filler exhibit permeabilities higher than MMMs with disaggregated JDF-L1 and lower than those of pure polymer membranes. However the N<sub>2</sub> permeabilities are comparatively lower so that higher O<sub>2</sub>/N<sub>2</sub> selectivities are found. While pure polymer membranes possess an O<sub>2</sub>/N<sub>2</sub> selectivity of 2.9 and MMMs with non ion exchanged JDF-L1 one of 3.0, all five ion exchanged materials exhibit selectivities between 4.4 as found for (K)-JDF-L1 and 4.7 as found for (Li)-JDF-L1 24h. Again in this mixture MMMs with bivalent interlamellar cations exhibit higher permeabilities than those containing monovalent cations. Oxygen permeabilities of 57.8 and 76.8 Barrer are determined for (Mg)-JDF-L1 1.1 and (Ca)-JDF-L1 while values of 42.0 and 47.1 Barrer are found for (Li)-JDF-L1 24h and (K)-JDF-L1. With MMMs containing (H)-JDF-L1 as filler permeabilities of 62.4 Barrer for oxygen and 13.6 Barrer for N<sub>2</sub> are measured. These values are comparable to those of MMMs with bivalent interlamellar cations. The results obtained for O<sub>2</sub>/N<sub>2</sub> mixtures suggest that in all cases the ion exchange treatment decreases the barrier effect of the titanosilicate filler towards both feed gases. Oxygen permeabilities are much higher than in MMMs with non ion exchanged JDF-L1 while nitrogen permeabilities increase only marginally leading to slightly higher O<sub>2</sub>/N<sub>2</sub> selectivities. The highest permeabilities are measured with MMMs containing filler materials in which the interlamellar sodium was exchanged with either protons or bivalent cations.

In both investigated gas mixtures membranes in which sodium was exchanged with a bivalent cation (Mg, Ca) exhibit higher permeabilities than MMMs containing a monovalent interlamellar cation (Li, K). For MMMs with (H)-JDF-L1 as filler the separation characteristics are more similar to those of MMMs containing bivalent cations or even pure polymer membranes in case of H<sub>2</sub>/CH<sub>4</sub>. In chapter 5.1.3.2 severe structural changes are observed for (H)-JDF-L1 which are also found partially for (Li)-JDF-L1 24h. It cannot be ruled out that through these structural changes the position of the interlamellar cation or even the pore size itself is affected. The loss of the barrier function of the titanosilicate filler therefore can in both cases be attributed to the altered structure. Moreover in case of (H)-JDF-L1 the extremely small size of the interlamellar cation (protons) has to be considered too. MMMs containing potassium, magnesium and calcium also exhibit noticeably different separation characteristics than MMMs with non ion exchanged JDF-L1 even though in XRD no structural changes were observed for these materials. This suggests that the increased permeabilities in these cases are rather related to the nature of the interlamellar cation. In case of magnesium and calcium the essential difference presumably is the ionic valence. In terms of charge equalization one bivalent cation replaces two sodium cations leaving a certain amount of interlamellar cation positions unoccupied due to the ion exchange. As a result the permeation of a feed component through pores adjacent to such an unoccupied position can be facilitated. Taking into account the ionic radii in crystal for the interlamellar cations used in ion exchange treatment (table 5.7) it is found that potassium exhibits the by far largest ionic radius with 138 ppm. It also is the only cation larger than sodium.

**Table 5.7: Ionic radii in crystal<sup>[131]</sup> for the cations used in this work as interlamellar ions for charge equalization in JDF-L1.**

	Li <sup>+</sup>	Na <sup>+</sup>	K <sup>+</sup>	Mg <sup>2+</sup>	Ca <sup>2+</sup>
<b>ionic radius in crystal [ppm]</b>	76	102	138	72	100

## 5 Results and discussion

Although no structural changes were observed in XRD the separation characteristics of MMMs containing (K)-JDF-L1 are very similar to those of MMMs with (Li)-JDF-L1 24h. From this it can be concluded that a larger interlamellar cation than sodium (radius in crystal) as well as the structural changes observed for (H)- and (Li)-JDF-L1 24h both lead to higher permeabilities of methane, nitrogen and oxygen.

Finally the improvement of  $O_2/N_2$  selectivity achieved with some of the ion exchanged materials suggests that the damage caused by the ion exchange treatment (see chapter 5.1.3.2) is of mesoporous nature as it is able to promote  $O_2$  over  $N_2$  transport. Also in this regard further research would be needed to elucidate the influence of the ion exchange processes on the textural and chemical properties of the modified filler.

### 5.3.2.5 Summary of gas separation results

As already mentioned in the beginning of this work (see chapter 2.3) a good way to compare gas separation results of different membranes is in the form of upper bound diagrams, which were introduced by Robeson in the beginning of the 1990s. In the following the results obtained for MMMs containing different loads of disaggregated JDF-L1 cast from 10 and 13 wt.-% polymer solution as well as for MMMs containing ion exchanged JDF-L1 are presented in this way in comparison to Robeson's upper bounds of 1991 and 2008. The results for the gas mixture  $H_2/CH_4$  are shown in figure 5.47 and the results for  $O_2/N_2$  mixtures are collected in figure 5.48.

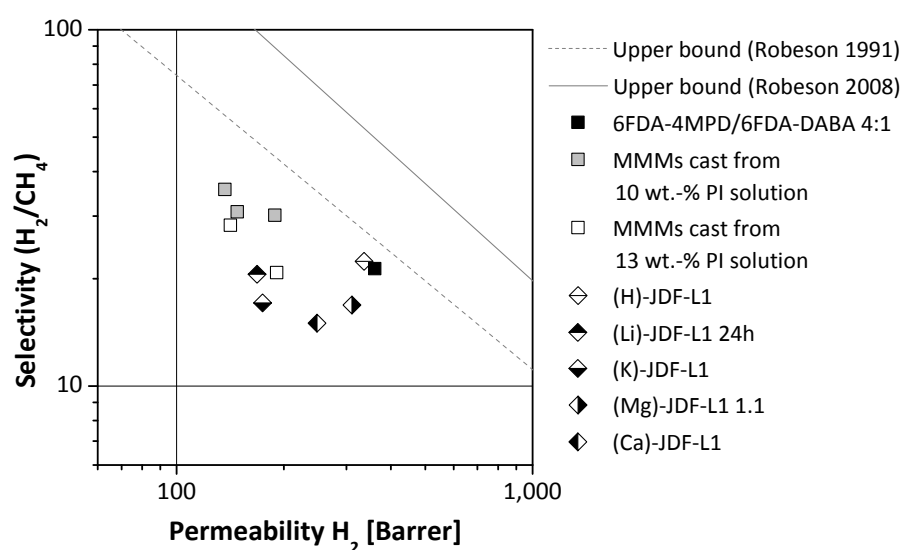
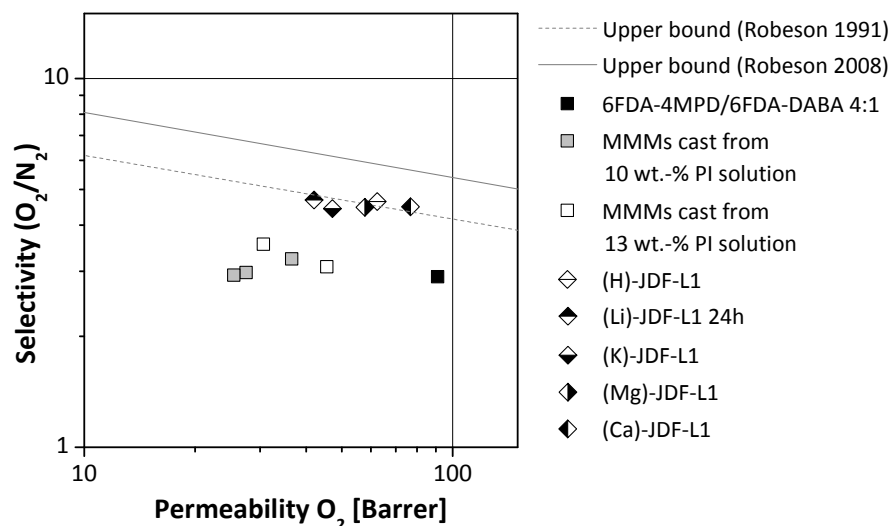


Figure 5.47: Upper bound diagram for the gas mixture  $H_2/CH_4$  presenting the results of gas separation experiments conducted in this work.

With MMMs cast from differently concentrated polymer solution (10 and 13 wt.-%) and loads of JDF-L1 between 5 and 10 wt.-% lower permeabilities but higher selectivities were found. This trend is most visible in the upper bound diagram for the data points related to MMMs cast from 10 wt.-% polymer solutions. From pure polymer to MMMs containing disaggregated JDF-L1 the data points move parallel to the upper bound itself (from black to grey squares). For MMMs cast from 13 wt.-% polymer solutions however a much lower gain of selectivity was found so that the shift of data points from pure polymer to the MMMs appears more horizontally (from black to white squares) than in case of the MMMs cast from 10 wt.-% polymer solutions. For the MMMs containing ion exchanged

JDF-L1 samples as filler the results are further apart from the upper bound. This is because the membranes exhibit lower permeability as well as selectivity compared to pure polymer. As already mentioned a big exception is found for (H)-JDF-L1. For the corresponding MMM separation characteristics very similar to the pure polymer are determined despite containing 8 wt.-% titanosilicate.



**Figure 5.48: Upper bound diagram for the gas mixture  $O_2/N_2$  presenting the results of gas separation experiments conducted in this work**

The diagrams displaying the gas separation results obtained with  $O_2/N_2$  mixtures show that the data points associated to MMMs cast from 10 and 13 wt.-% polymer solution are further apart from the upper bound than pure polymer. This is because due to the strong barrier effect the permeability was decreased while selectivity remained unaltered. On the contrary the results obtained for MMMs containing samples of ion exchanged JDF-L1 are very close or even slightly above to the upper bound of 1991. The reason for this is the small gain of selectivity and comparably small loss of permeability.



## 6 Appendix

### 6.1 Copolyimide synthesis

Copolyimide batches with various scheduled quantities were prepared according to the procedure described in chapter 4.1. The theoretic and actual quantities of solvents and reacting agents used for the preparation of the individual batches are presented below in table form.

**Batch: SPI 1**

	<b>M</b> [g/mol]	ratio	<b>n</b> [mmol]	<b>n</b> [mmol] actual	<b>m</b> [g]	<b>m</b> [g] actual	<b>V</b> [ml] actual	<b>V</b> [ml]
6FDA	444.25	5	<b>5.000</b>	5.000	<b>2.221</b>	2.221		
4MPD	164.25	4	<b>4.000</b>	4.000	<b>0.657</b>	0.657		
DABA	152.13	1	<b>1.000</b>	1.000	<b>0.152</b>	0.152		
triethylamine	101.19	15	<b>15.000</b>	15.000	<b>1.518</b>	1.518	2.079	<b>2.079</b>
acetic acid anhydride	102.09	15	<b>15.000</b>	15.000	<b>1.531</b>	1.531	1.418	<b>1.418</b>
dimethylacetamide							12.000	
6FDA-4MPD/ 6FDA-DABA 4:1	2850.18		<b>1.000</b>	<b>0.944</b>	<b>2.850</b>	2.690		

**Yield: 94.4%**

**Batch: SPI 2**

	<b>M</b> [g/mol]	ratio	<b>n</b> [mmol]	<b>n</b> [mmol] actual	<b>m</b> [g]	<b>m</b> [g] actual	<b>V</b> [ml] actual	<b>V</b> [ml]
6FDA	444.25	5	<b>5.000</b>	5.000	<b>2.221</b>	2.221		
4MPD	164.25	4	<b>4.000</b>	4.000	<b>0.657</b>	0.657		
DABA	152.13	1	<b>1.000</b>	1.000	<b>0.152</b>	0.152		
triethylamine	101.19	15	<b>15.000</b>	15.000	<b>1.518</b>	1.518	2.079	<b>2.079</b>
acetic acid anhydride	102.09	15	<b>15.000</b>	15.000	<b>1.531</b>	1.531	1.418	<b>1.418</b>
dimethylacetamide							10.000	
6FDA-4MPD/ 6FDA-DABA 4:1	2850.18		<b>1.000</b>	<b>0.989</b>	<b>2.850</b>	2.820		

**Yield: 98.9%**

## 6 Appendix

### Batch: SPI 4

	<b>M</b> [g/mol]	ratio	<b>n</b> [mmol]	<b>n</b> [mmol] actual	<b>m</b> [g]	<b>m</b> [g] actual	<b>V</b> [ml] actual	<b>V</b> [ml]
6FDA	444.25	5	<b>5.000</b>	5.000	<b>2.221</b>	2.221		
4MPD	164.25	4	<b>4.000</b>	4.000	<b>0.657</b>	0.657		
DABA	152.13	1	<b>1.000</b>	1.000	<b>0.152</b>	0.152		
triethylamine	101.19	15	<b>15.000</b>	15.000	<b>1.518</b>	1.518	2.079	<b>2.079</b>
acetic acid anhydride	102.09	15	<b>15.000</b>	15.000	<b>1.531</b>	1.531	1.418	<b>1.418</b>
dimethylacetamide							11.000	
6FDA-4MPD/ 6FDA-DABA 4:1	2850.18		<b>1.000</b>	<b>0.993</b>	<b>2.850</b>	2.830		

Yield: **99.3%**

### Batch: SPI 5

	<b>M</b> [g/mol]	ratio	<b>n</b> [mmol]	<b>n</b> [mmol] actual	<b>m</b> [g]	<b>m</b> [g] actual	<b>V</b> [ml] actual	<b>V</b> [ml]
6FDA	444.25	5	<b>5.000</b>	5.000	<b>2.221</b>	2.221		
4MPD	164.25	4	<b>4.000</b>	4.000	<b>0.657</b>	0.657		
DABA	152.13	1	<b>1.000</b>	1.000	<b>0.152</b>	0.152		
triethylamine	101.19	15	<b>15.000</b>	15.000	<b>1.518</b>	1.518	2.079	<b>2.079</b>
acetic acid anhydride	102.09	15	<b>15.000</b>	15.000	<b>1.531</b>	1.531	1.418	<b>1.418</b>
dimethylacetamide							16.000	
6FDA-4MPD/ 6FDA-DABA 4:1	2850.18		<b>1.000</b>	<b>0.923</b>	<b>2.850</b>	2.631		

Yield: **92.3%**

### Batch: SPI 6

	<b>M</b> [g/mol]	ratio	<b>n</b> [mmol]	<b>n</b> [mmol] actual	<b>m</b> [g]	<b>m</b> [g] actual	<b>V</b> [ml] actual	<b>V</b> [ml]
6FDA	444.25	5	<b>10.000</b>	10.000	<b>4.443</b>	4.443		
4MPD	164.25	4	<b>8.000</b>	8.000	<b>1.314</b>	1.314		
DABA	152.13	1	<b>2.000</b>	2.000	<b>0.304</b>	0.304		
triethylamine	101.19	15	<b>30.000</b>	30.000	<b>3.036</b>	3.036	4.158	<b>4.158</b>
acetic acid anhydride	102.09	15	<b>30.000</b>	30.000	<b>3.063</b>	3.063	2.836	<b>2.836</b>
dimethylacetamide							29.000	
6FDA-4MPD/ 6FDA-DABA 4:1	2850.18		<b>2.000</b>	<b>1.750</b>	<b>5.737</b>	5.010		

Yield: **87.5%**

**Batch: SPI 7**

	<b>M</b> [g/mol]	ratio	<b>n</b> [mmol]	<b>n</b> [mmol] actual	<b>m</b> [g]	<b>m</b> [g] actual	<b>V</b> [ml] actual	<b>V</b> [ml]
6FDA	444.25	5	<b>5.000</b>	5.000	<b>2.221</b>	2.222		
4MPD	164.25	4	<b>4.000</b>	4.010	<b>0.657</b>	0.658		
DABA	152.13	1	<b>1.000</b>	1.000	<b>0.152</b>	0.152		
triethylamine	101.19	15	<b>15.000</b>	15.000	<b>1.518</b>	1.518	2.079	<b>2.079</b>
acetic acid anhydride	102.09	15	<b>15.000</b>	15.000	<b>1.531</b>	1.531	1.418	<b>1.418</b>
dimethylacetamide							17.000	
6FDA-4MPD/ 6FDA-DABA 4:1	2850.18		<b>1.000</b>	<b>0.980</b>		2.800		

Yield: **98.0%****Batch: SPI 8**

	<b>M</b> [g/mol]	ratio	<b>n</b> [mmol]	<b>n</b> [mmol] actual	<b>m</b> [g]	<b>m</b> [g] actual	<b>V</b> [ml] actual	<b>V</b> [ml]
6FDA	444.25	5	<b>5.000</b>	5.000	<b>2.221</b>	2.221		
4MPD	164.25	4	<b>4.000</b>	4.000	<b>0.657</b>	0.657		
DABA	152.13	1	<b>1.000</b>	1.000	<b>0.152</b>	0.152		
triethylamine	101.19	15	<b>15.000</b>	15.000	<b>1.518</b>	1.518	2.085	<b>2.079</b>
acetic acid anhydride	102.09	15	<b>15.000</b>	15.000	<b>1.531</b>	1.531	1.418	<b>1.418</b>
dimethylacetamide							17.000	
6FDA-4MPD/ 6FDA-DABA 4:1	2850.18		<b>1.000</b>	<b>0.970</b>		2.782		

Yield: **97.0%****Batch: SPI 9**

	<b>M</b> [g/mol]	ratio	<b>n</b> [mmol]	<b>n</b> [mmol] actual	<b>m</b> [g]	<b>m</b> [g] actual	<b>V</b> [ml] actual	<b>V</b> [ml]
6FDA	444.25	5	<b>10.000</b>	10.000	<b>4.443</b>	4.443		
4MPD	164.25	4	<b>8.000</b>	8.000	<b>1.314</b>	1.314		
DABA	152.13	1	<b>2.000</b>	2.000	<b>0.304</b>	0.304		
triethylamine	101.19	15	<b>30.000</b>	30.000	<b>3.036</b>	3.036	4.170	<b>4.160</b>
acetic acid anhydride	102.09	15	<b>30.000</b>	29.990	<b>3.063</b>	3.062	2.836	<b>2.840</b>
dimethylacetamide							15.000	
6FDA-4MPD/ 6FDA-DABA 4:1	2850.18		<b>2.000</b>	<b>1.958</b>	<b>5.580</b>	5.580		

Yield: **97.9%**

## 6 Appendix

### Batch: SPI 10

	<b>M</b> [g/mol]	ratio	<b>n</b> [mmol]	<b>n</b> [mmol] actual	<b>m</b> [g]	<b>m</b> [g] actual	<b>V</b> [ml] actual	<b>V</b> [ml]
6FDA	444.25	5	<b>15.000</b>	15.000	<b>6.664</b>	6.664		
4MPD	164.25	4	<b>12.000</b>	12.000	<b>1.971</b>	1.971		
DABA	152.13	1	<b>3.000</b>	3.000	<b>0.456</b>	0.456		
triethylamine	101.19	15	<b>45.000</b>	30.000	<b>4.554</b>	3.036	6.238	<b>6.238</b>
acetic acid anhydride	102.09	15	<b>45.000</b>	30.000	<b>4.594</b>	3.063	4.254	<b>4.254</b>
dimethylacetamide							25.000	
6FDA-4MPD/ 6FDA-DABA 4:1	2850.18		<b>3.000</b>	<b>2.800</b>	<b>8.551</b>	7.985		
			<b>Yield:</b>	<b>93.3%</b>				

### Batch: SPI 11

	<b>M</b> [g/mol]	ratio	<b>n</b> [mmol]	<b>n</b> [mmol] actual	<b>m</b> [g]	<b>m</b> [g] actual	<b>V</b> [ml] actual	<b>V</b> [ml]
6FDA	444.25	5	<b>12.710</b>	12.710	<b>5.646</b>	5.646		
4MPD	164.25	4	<b>10.170</b>	10.170	<b>1.670</b>	1.671		
DABA	152.13	1	<b>2.540</b>	2.540	<b>0.387</b>	0.387		
triethylamine	101.19	15	<b>38.130</b>	38.130	<b>3.858</b>	3.858	5.285	<b>5.285</b>
acetic acid anhydride	102.09	15	<b>38.130</b>	38.130	<b>3.893</b>	3.892	3.604	<b>3.604</b>
dimethylacetamide							30.000	
6FDA-4MPD/ 6FDA-DABA 4:1	2850.18		<b>2.540</b>	<b>2.450</b>	<b>7.245</b>	6.980		

**Yield: 96.3%**

### Batch: SPI 13

	<b>M</b> [g/mol]	ratio	<b>n</b> [mmol]	<b>n</b> [mmol] actual	<b>m</b> [g]	<b>m</b> [g] actual	<b>V</b> [ml] actual	<b>V</b> [ml]
6FDA	444.25	5	<b>15.000</b>	15.000	<b>6.664</b>	6.664		
4MPD	164.25	4	<b>12.000</b>	12.000	<b>1.971</b>	1.971		
DABA	152.13	1	<b>3.000</b>	3.000	<b>0.456</b>	0.456		
triethylamine	101.19	15	<b>45.000</b>	45.000	<b>4.554</b>	4.554	6.238	<b>6.238</b>
acetic acid anhydride	102.09	15	<b>45.000</b>	45.000	<b>4.594</b>	4.594	4.254	<b>4.254</b>
dimethylacetamide							30.000	
6FDA-4MPD/ 6FDA-DABA 4:1	2850.18		<b>3.000</b>	<b>2.910</b>	<b>8.551</b>	8.281		

**Yield: 96.9%**

**Batch: SPI 15**

	<b>M</b> [g/mol]	ratio	<b>n</b> [mmol]	<b>n</b> [mmol] actual	<b>m</b> [g]	<b>m</b> [g] actual	<b>V</b> [ml] actual	<b>V</b> [ml]
6FDA	444.25	5	<b>15.000</b>	15.000	<b>6.664</b>	6.664		
4MPD	164.25	4	<b>12.000</b>	12.000	<b>1.971</b>	1.971		
DABA	152.13	1	<b>3.000</b>	3.000	<b>0.456</b>	0.456		
triethylamine	101.19	15	<b>45.000</b>	45.000	<b>4.554</b>	4.554	6.238	<b>6.238</b>
acetic acid anhydride	102.09	15	<b>45.000</b>	45.000	<b>4.594</b>	4.595	4.254	<b>4.254</b>
dimethylacetamide							30.000	
6FDA-4MPD/ 6FDA-DABA 4:1	2850.18		<b>3.000</b>	<b>2.910</b>	<b>8.551</b>	8.280		

Yield: 96.9%

**Batch: SPI 18**

	<b>M</b> [g/mol]	ratio	<b>n</b> [mmol]	<b>n</b> [mmol] actual	<b>m</b> [g]	<b>m</b> [g] actual	<b>V</b> [ml] actual	<b>V</b> [ml]
6FDA	444.25	5	<b>15.000</b>	15.000	<b>6.664</b>	6.664		
4MPD	164.25	4	<b>12.000</b>	12.000	<b>1.971</b>	1.971		
DABA	152.13	1	<b>3.000</b>	3.000	<b>0.456</b>	0.456		
triethylamine	101.19	15	<b>45.000</b>	45.000	<b>4.554</b>	4.554	6.238	<b>6.238</b>
acetic acid anhydride	102.09	15	<b>45.000</b>	45.010	<b>4.594</b>	4.595	4.255	<b>4.254</b>
dimethylacetamide							30.000	
6FDA-4MPD/ 6FDA-DABA 4:1	2850.18		<b>3.000</b>	<b>2.910</b>	<b>8.551</b>	8.280		

Yield: 96.9%

**Batch: SPI 22**

	<b>M</b> [g/mol]	ratio	<b>n</b> [mmol]	<b>n</b> [mmol] actual	<b>m</b> [g]	<b>m</b> [g] actual	<b>V</b> [ml] actual	<b>V</b> [ml]
6FDA	444.25	5	<b>9.000</b>	9.001	<b>3.998</b>	3.999		
4MPD	164.25	4	<b>7.200</b>	7.201	<b>1.183</b>	1.183		
DABA	152.13	1	<b>1.800</b>	1.800	<b>0.274</b>	0.274		
triethylamine	101.19	15	<b>27.000</b>	27.003	<b>2.732</b>	2.732	3.743	<b>3.743</b>
acetic acid anhydride	102.09	15	<b>27.000</b>	26.997	<b>2.756</b>	2.756	2.552	<b>2.552</b>
dimethylacetamide							17.000	
6FDA-4MPD/ 6FDA-DABA 4:1	2850.18		<b>1.800</b>	<b>1.636</b>	<b>5.130</b>	4.662		

Yield: 90.8%

## 6 Appendix

### Batch: SPI 23

	<b>M</b> [g/mol]	ratio	<b>n</b> [mmol]	<b>n</b> [mmol] actual	<b>m</b> [g]	<b>m</b> [g] actual	<b>V</b> [ml] actual	<b>V</b> [ml]
6FDA	444.25	5	<b>7.000</b>	7.000	<b>3.110</b>	3.110		
4MPD	164.25	4	<b>5.600</b>	5.600	<b>0.920</b>	0.920		
DABA	152.13	1	<b>1.400</b>	1.400	<b>0.213</b>	0.213		
triethylamine	101.19	15	<b>21.000</b>	21.000	<b>2.125</b>	2.120	2.911	<b>2.911</b>
acetic acid anhydride	102.09	15	<b>21.000</b>	20.999	<b>2.144</b>	2.144	1.985	<b>1.985</b>
dimethylacetamide							20.000	
6FDA-4MPD/ 6FDA-DABA 4:1	2850.18		<b>1.400</b>	<b>1.350</b>	<b>3.9903</b>	3.8490		

**Yield: 96.5%**

### Batch: SPI 24

	<b>M</b> [g/mol]	ratio	<b>n</b> [mmol]	<b>n</b> [mmol] actual	<b>m</b> [g]	<b>m</b> [g] actual	<b>V</b> [ml] actual	<b>V</b> [ml]
6FDA	444.25	5	<b>8.000</b>	8.000	<b>3.554</b>	3.554		
4MPD	164.25	4	<b>6.400</b>	6.400	<b>1.051</b>	1.051		
DABA	152.13	1	<b>1.600</b>	1.600	<b>0.243</b>	0.243		
triethylamine	101.19	15	<b>24.000</b>	24.001	<b>2.429</b>	2.429	3.327	<b>3.327</b>
acetic acid anhydride	102.09	15	<b>24.000</b>	24.004	<b>2.450</b>	2.450	2.269	<b>2.269</b>
dimethylacetamide							20.000	
6FDA-4MPD/ 6FDA-DABA 4:1	2850.18		<b>1.600</b>	<b>1.568</b>	<b>4.5603</b>	4.4610		

**Yield: 97.8%**

### Batch: SPI 25

	<b>M</b> [g/mol]	ratio	<b>n</b> [mmol]	<b>n</b> [mmol] actual	<b>m</b> [g]	<b>m</b> [g] actual	<b>V</b> [ml] actual	<b>V</b> [ml]
6FDA	444.25	5	<b>8.000</b>	8.000	<b>3.554</b>	3.554		
4MPD	164.25	4	<b>6.400</b>	6.400	<b>1.051</b>	1.051		
DABA	152.13	1	<b>1.600</b>	1.600	<b>0.243</b>	0.243		
triethylamine	101.19	15	<b>24.000</b>	24.001	<b>2.429</b>	2.429	3.327	<b>3.327</b>
acetic acid anhydride	102.09	15	<b>24.000</b>	24.004	<b>2.450</b>	2.451	2.269	<b>2.269</b>
dimethylacetamide							20.000	
6FDA-4MPD/ 6FDA-DABA 4:1	2850.18		<b>1.600</b>	<b>1.568</b>	<b>4.5603</b>	4.4680		

**Yield: 98.0%**

**Batch: SPI 26**

	<b>M</b> [g/mol]	ratio	<b>n</b> [mmol]	<b>n</b> [mmol] actual	<b>m</b> [g]	<b>m</b> [g] actual	<b>V</b> [ml] actual	<b>V</b> [ml]
6FDA	444.25	5	<b>7.900</b>	7.900	<b>3.510</b>	3.510		
4MPD	164.25	4	<b>6.320</b>	6.320	<b>1.038</b>	1.038		
DABA	152.13	1	<b>1.580</b>	1.580	<b>0.240</b>	0.240		
triethylamine	101.19	15	<b>23.700</b>	23.698	<b>2.398</b>	2.398	3.285	<b>3.285</b>
acetic acid anhydride	102.09	15	<b>23.700</b>	23.697	<b>2.420</b>	2.419	2.240	<b>2.240</b>
dimethylacetamide							25.000	
6FDA-4MPD/ 6FDA-DABA 4:1	2850.18		<b>1.580</b>	<b>1.575</b>	<b>4.503</b>	4.488		

Yield: 99.6%

**Batch: SPI 28**

	<b>M</b> [g/mol]	ratio	<b>n</b> [mmol]	<b>n</b> [mmol] actual	<b>m</b> [g]	<b>m</b> [g] actual	<b>V</b> [ml] actual	<b>V</b> [ml]
6FDA	444.25	5	<b>7.900</b>	7.900	<b>3.510</b>	3.510		
4MPD	164.25	4	<b>6.320</b>	6.320	<b>1.038</b>	1.038		
DABA	152.13	1	<b>1.580</b>	1.580	<b>0.240</b>	0.240		
triethylamine	101.19	15	<b>23.700</b>	23.698	<b>2.398</b>	2.398	3.285	<b>3.285</b>
acetic acid anhydride	102.09	15	<b>23.700</b>	23.697	<b>2.420</b>	2.419	2.240	<b>2.240</b>
dimethylacetamide							18.000	
6FDA-4MPD/ 6FDA-DABA 4:1	2850.18		<b>1.580</b>	<b>1.555</b>	<b>4.503</b>	4.431		

Yield: 98.4%

## 6 Appendix

Table 6.1: Tabular overview of the characterization data of all copolyimide batches used in this work.

Batch	color	mass [g]	yield [%]	film formation	GPC	DSC	NMR	
							$H_{\text{aliph}}/H_{\text{arom}}$	actual amount of 4MPD
SPI 1	white	2.69	94.4	bend- and foldable	90 000	430.7	0.6729	4.34
SPI 2	white	2.82	98.9	bend- and foldable	62 000	408.1	0.6858	4.04
SPI 4	white	2.83	99.3	bend- and foldable	76 000	420.0	0.6713	4.38
SPI 5	white	2.63	92.3	bend- and foldable	88 000	425.6	0.6885	3.98
SPI 6	bright yellow	5.01	87.9	bend- and foldable	61 000	407.4	0.6794	4.18
SPI 7	white	2.80	98.2	bend- and foldable	99 000	417.0	0.6858	4.04
SPI 8	white	2.78	97.5	bend- and foldable	54 000	427.5	0.6692	4.43
SPI 9	bright yellow	5.58	97.9	bend- and foldable	49 000	433.8	0.6646	4.56
SPI 10	bright yellow	7.98	93.4	bend- and foldable	42 000	432.7	0.6938	3.87
SPI 11	white	7.00	81.8	bend- and foldable	70 000	422.8	0.6702	4.41
SPI 13	bright yellow	8.28	96.9	bend- and foldable	69 000	418.2	0.6848	4.06
SPI 15	beige	8.28	96.9	brittle films	36 000	420.4	0.6642	4.57
SPI 18	yellow	8.28	96.9	brittle films	29 000	discarded	0.635	5.56
SPI 22	bright yellow	4.66	90.8	bend- and foldable	46 000	413.3	0.6792	4.19
SPI 23	white	3.85	96.5	bend- and foldable	71 000	417.6	0.6885	3.98
SPI 24	white	4.46	97.8	brittle films	31 000	420.0	0.6913	3.92
SPI 25	white	4.47	98	bend- and foldable	44 000	415.8	0.6848	4.06
SPI 26	white	4.49	99.6	bend- and foldable	84 000	417.8	0.6815	4.13
SPI 28	bright yellow	4.43	98.4	bend- and foldable	32 000	<i>discarded</i>		

Batches 18 and 28 were discarded with regard to membrane preparation. However the characterization results were used.

## 6.2 Exchange of interlamellar cations in disaggregated JDF-L1

The interlamellar sodium cations in JDF-L1 were exchanged with several other cations according to the following preparation synthesis regulations.

### 6.2.1 Preparation of (H)-JDF-L1

	M [g/mol]	ratio	n [mmol]	m [mg]	V [ml]
disaggregated JDF-L1				500	
demineralized water					~ 750
tetrahydrofuran					~ 100
acetic acid (conc.)					< 1

In a 300 mL Erlenmeyer flask 500 mg disaggregated JDF-L1 are mixed with 50 mL demineralized water and stirred for 3 minutes. By adding 2 drops of concentrated acetic acid the pH value of the suspension is lowered to 3.5 and the mixture is stirred for 5 minutes. Subsequently the pH is nearly neutral (measured: 6.0) and is once more lowered by addition of two drops of concentrated acetic acid to now 4.0. After stirring the mixture for 10 minutes the pH remains constant and the reaction is finished. In a adequate flask the suspension is now diluted with 400 mL demineralized water which increases the pH value to 6.5. The product is extracted via centrifugation at 10,000 rpm for 17 minutes. The liquid is discarded and the solid residue suspended with demineralized water. Centrifugation is repeated two times with water (5 minutes) and one time with tetrahydrofuran (10 minutes). The cleaned suspension is left to sediment in a beaker for 2 hours. The solid residue is then obtained through decantation. The sedimentation step is repeated once more with tetrahydrofuran and the residue is then left to dry at room temperature.

**Product mass: 271 mg**

### 6.2.2 Preparation of (Li)-JDF-L1 4h

	M [g/mol]	ratio	n [mmol]	m [g]	V [ml]
disaggregated JDF-L1	863.42	1	0.29	0.250	
demineralized water					~ 500
tetrahydrofuran					~ 50
lithium chloride (≥ 99 %, Sigma Aldrich)	42.39	80	23.16	0.982	

In a 100 mL Erlenmeyer flask 0.982 g lithium chloride (23.16 mmol) are dissolved in 50 mL demineralized water, then 250 mg disaggregated JDF-L1 are added. The mixture is stirred for 4 hours and the solid is subsequently obtained via centrifugation at 10.000 rpm for 10 minutes. The solid

## 6 Appendix

---

residue is cleaned using centrifugation three more times with water and then two times with tetrahydrofuran. The final residue is left to dry at room temperature.

**Product mass: 186 mg**

### 6.2.3 Preparation of (Li)-JDF-L1 24h

	M [g/mol]	ratio	n [mmol]	m [g]	V [ml]
disaggregated JDF-L1	863.42	1	0.29	0.250	
demineralized water					~ 500
tetrahydrofuran					~ 50
lithium chloride (≥ 99 %, Sigma Aldrich)	42.39	80	23.16	0.982	

In a 100 mL Erlenmeyer flask 0.982 g lithium chloride (23.16 mmol) are dissolved in 50 mL demineralized water, then 250 mg disaggregated JDF-L1 are added. The mixture is stirred for 24 hours and the solid is subsequently obtained via centrifugation at 10.000 rpm for 10 minutes. The solid residue is cleaned using centrifugation three more times with water and then two times with tetrahydrofuran. The final residue is left to dry at room temperature.

**Product mass: 173 mg**

### 6.2.4 Preparation of (K)-JDF-L1

	M [g/mol]	ratio	n [mmol]	m [g]	V [ml]
disaggregated JDF-L1	863.42	1	0.58	0.5	
demineralized water					~ 500
tetrahydrofuran					~ 50
Potassium chloride (Panreac, 99.5 %)	74.56	80	46.32	3.45	

In a 300 mL Erlenmeyer flask 3.45 g potassium chloride (46.32 mmol) are dissolved in 100 mL demineralized water and then 500 mg disaggregated JDF-L1 are added. The mixture is stirred for 4 hours, subsequently filtered and then washed three times with 100 mL demineralized water and two times with 20 mL tetrahydrofuran. The filter cake is suspended with 10 mL tetrahydrofuran and left to dry at room temperature.

**Product mass: 407 mg**

### 6.2.5 Preparation of (Mg)-JDF-L1 1.1

	M [g/mol]	ratio	n [mmol]	m [g]	V [ml]
disaggregated JDF-L1	863.42	1	0.17	0.15	
demineralized water					~ 500
tetrahydrofuran					~ 50
magnesium chloride anhydrous (≥ 99 %, Sigma Aldrich)	95.21	40	6.95	0.662	

In a 100 mL Erlenmeyer flask 0.662 g magnesium chloride (6.95 mmol) are dissolved in 30 mL demineralized water, then 150 mg disaggregated JDF-L1 are added. The mixture is stirred for 16 hours and the solid is subsequently obtained via centrifugation at 10.000 rpm for 10 minutes. The solid residue is cleaned using centrifugation three more times with water and then two times with tetrahydrofuran. The final residue is left to dry at room temperature.

**Product mass: 122 mg**

### 6.2.6 Preparation of (Mg)-JDF-L1 1.2

	M [g/mol]	ratio	n [mmol]	m [g]	V [ml]
disaggregated JDF-L1	863.42	1	0.17	0.15	
demineralized water					~ 500
tetrahydrofuran					~ 50
magnesium chloride anhydrous (≥ 99 %, Sigma Aldrich)	95.21	40	6.95	0.662	

In a 100 mL Erlenmeyer flask 0.662 g magnesium chloride (6.95 mmol) are dissolved in 30 mL demineralized water, then 150 mg disaggregated JDF-L1 are added. The mixture is stirred for 24 hours and the solid is subsequently obtained via centrifugation at 10.000 rpm for 10 minutes. The solid residue is cleaned using centrifugation three more times with water and then two times with tetrahydrofuran. The final residue is left to dry at room temperature.

**Product mass: 137 mg**

### 6.2.7 Preparation of (Mg)-JDF-L1 1.3

	M [g/mol]	ratio	n [mmol]	m [g]	V [ml]
disaggregated JDF-L1	863.42	1	0.17	0.15	
demineralized water					~ 500
tetrahydrofuran					~ 50
magnesium chloride anhydrous (≥ 99 %, Sigma Aldrich)	95.21	120	20.40	1.942	

In a 100 mL Erlenmeyer flask 1.942 g magnesium chloride (6.95 mmol) are dissolved in 30 mL demineralized water, then 150 mg disaggregated JDF-L1 are added. The mixture is stirred for 16 hours and the solid is subsequently obtained via centrifugation at 10.000 rpm for 10 minutes. The solid residue is cleaned using centrifugation three more times with water and then two times with tetrahydrofuran. The final residue is left to dry at room temperature.

**Product mass: 145 mg**

### 6.2.8 Preparation of (Ca)-JDF-L1

	M [g/mol]	ratio	n [mmol]	m [g]	V [ml]
disaggregated JDF-L1	863.42	1	0.17	0.15	
demineralized water					~ 500
tetrahydrofuran					~ 50
calcium chloride dihydrate (≥ 99 %, Sigma Aldrich)	74.56	40	6.95	1.02	

In a 100 mL Erlenmeyer flask 1.02 g calcium chloride (6.95 mmol) are dissolved in 30 mL demineralized water, then 150 mg disaggregated JDF-L1 are added. The mixture is stirred for 16 hours and the solid is subsequently obtained via centrifugation at 10.000 rpm for 10 minutes. The solid residue is cleaned using centrifugation three more times with water and then two times with tetrahydrofuran. The final residue is left to dry at room temperature.

**Product mass: 138 mg**

## 6.3 Calibration data for gas separation experiments

The correlation of peak areas obtained from gas chromatography and actual gas content in the permeate stream was necessary for the evaluation of gas separation experiments. The calibrations have been updated several times and the calibration data used is presented in chronologic order hereafter.

### 6.3.1 Calibration data oxygen/nitrogen

Calibration #1

oxygen content [%]	peak area oxygen	nitrogen content [%]	peak area nitrogen
1.000	39304.6	1.000	41121.1
0.091	3941.3	0.091	4199.0
0.039	1745.0	0.039	1853.4
0.015	876.3	0.015	769.6
0.01	711.3	0.01	531.7
0.007	349.5	0.007	377.6
0.000	0.0	0.000	0.0
calibration equation: $y = 39144x + 152.69$ $R^2 = 0.9999$		calibration equation: $y = 41009x + 115.52$ $R^2 = 1$	
file: 2009-08 CalibradoMGC_2.xls			

Calibration #2

oxygen content [%]	peak area oxygen	nitrogen content [%]	peak area nitrogen
1.000	41213.0	1.000	40043.0
0.053	1794.5	0.053	1552.5
0.015	590.7	0.015	506.0
0.010	391.0	0.010	381.0
0.007	285.0	0.007	273.0
0.000	0.0	0.000	0.0
calibration equation: $y = 41281x - 82.903$ $R^2 = 0.9999$		calibration equation: $y = 40154x - 132.27$ $R^2 = 0.9998$	
file: 2010-06 CalibradoMGCs_05_10.xls			

Calibration #3

oxygen content [%]	peak area oxygen	nitrogen content [%]	peak area nitrogen
1.000	42739.0	1.000	49483.0
0.053	2180.0	0.053	2337.0
0.015	685.3	0.015	750.7
0.010	472.3	0.010	526.3
0.007	354.3	0.007	396.0
0.000	0.0	0.00	0.0
calibration equation: $y = 42717x + 16.933$ $R^2 = 1$		calibration equation: $y = 49504x - 32.748$ $R^2 = 1$	
file: 2011-05 CalibradoMGCs_03_11.xls			

Calibration #4

oxygen content [%]	peak area oxygen	nitrogen content [%]	peak area nitrogen
3.0003	120008.0	0.990	48816.0
2.4021	96978.4	0.793	39355.6
1.8990	76740.8	0.494	25708.0
1.2999	52237.2	0.299	15768.3
0.7496	30175.3	0.100	6457.7
calibration equation: $y = 40045x + 335.97$ $R^2 = 0.9999$		calibration equation: $y = 47584x + 1759.2$ $R^2 = 0.9998$	
file: 2011-06 CalibradoMGC_high-permeability_O2-N2_07-11.xls			

## 6 Appendix

### 6.3.2 Calibration data hydrogen/methane

Calibration #1

hydrogen content [%]	peak area hydrogen	methane content [%]	peak area methane
0.000	0.0	0.000	0.0
0.150	1283.7	0.010	75.6
0.260	2237.1	0.020	169.2
1.640	14686.9	0.050	453.1
4.260	38899.1	0.200	1804.5
10.000	87454.0	0.500	5542.1
		0.690	9126.3
		1.000	20876.7
calibration equation: $y = 8777x + 239.06$ $R^2 = 0.9996$		calibration equation: $y = 17367x + 22.418$ $R^2 = 0.9961$	
file: 2009-08 Calibraciones_11_2008.xls			

Calibration #2

hydrogen content [%]	peak area hydrogen	methane content [%]	peak area methane
18.370	168200.0	4.306	7912.5
8.260	77691.0	1.316	2405.0
4.310	40294.0	0.498	914.9
2.440	22719.0	0.118	247.8
0.990	9202.0	0.045	57.0
0.330	2989.0	0.000	0.0
0.000	0.0		
calibration equation: $y = 9177x + 389.59$ $R^2 = 0.9998$		calibration equation: $y = 1836.9x - 0.3151$ $R^2 = 1$	
file: 2010-06 CalibradosMGCs_05_10.xls			

Calibration #3

hydrogen content [%]	peak area hydrogen	methane content [%]	peak area methane
13.040	110929.5	4.306	69670.0
8.260	70329.0	1.316	22174.0
2.9100	23468.0	0.498	8334.0
0.990	7776.6	0.118	2034.0
0.330	2788.0	0.000	0.0
calibration equation: $y = 8555.9x - 637.27$ $R^2 = 0.9999$		calibration equation: $y = 16155x + 290.35$ $R^2 = 0.9998$	
file: 2010-07 Calibraciones_05_10.xls~RF297257cd.xls			

Calibration #4

hydrogen content [%]	peak area hydrogen	methane content [%]	peak area methane
10.110	109223.2	4.306	55879.1
8.260	89740.4	1.316	17289.4
2.910	34414.5	0.498	6876.1
0.990	12900.9	0.118	1653.4
0.330	4318.9	0.050	683.9
		0.00	0.0
calibration equation: $y = 10627x + 2075.6$ $R^2 = 0.9996$		calibration equation: $y = 12953x + 157.93$ $R^2 = 0.9999$	
file: 2010-09 Calibraciones_08_10.xls			

Calibration #5

hydrogen content [%]	peak area hydrogen	methane content [%]	peak area methane
18.03	177970.3	5.000	11253.0
13.79	135915.0	4.348	9434.8
9.09	91822.0	3.030	6587.0
5.00	50778.0	1.961	4079.0
2.44	24084.0	1.333	2811.8
0.99	9764.0	0.500	1128.0
0.52	4919.0	0.100	308.4
0.00	0.0	0.000	0.0
calibration equation: $y = 9881.9x + 305.8$ $R^2 = 0.9998$		calibration equation: $y = 2209.9x - 44.83$ $R^2 = 0.9987$	
file: 2011-05 CalibradoMGCs_03_11.xls			

Calibration #6

hydrogen content [%]	peak area hydrogen	methane content [%]	peak area methane
19.84	1071812.0	1.00	11238.0
17.87	962828.8	0.90	10163.1
15.87	854162.2	0.80	8933.3
13.89	753005.0	0.70	7798.2
11.90	654442.4	0.60	6738.4
9.91	522609.0	0.50	5403.0
7.50	383002.6	0.30	3210.1
5.00	246478.9	0.20	2147.6
2.50	53917.2	0.10	631.3
calibration equation: $y = 57617x - 56247$ $R^2 = 0.998$		calibration equation: $y = 11710x - 413.76$ $R^2 = 0.9991$	
file: 2011-06 CalibradoMGC_high-permeability_H2_CH4_05-11.xls			



## 7 Bibliography

- [1] T. Melin, "Membrantechnik" *Chemie Ingenieur Technik* **2003**, 75, 1464–1467.
- [2] M. Ajhar, S. Bütehorn, F. Krull, M. Lumey, S. Lyko, F. Salehi, T. Westermann, T. Melin, "Membrantechnik" *Chemie Ingenieur Technik* **2006**, 78, 1794–1801.
- [3] M. Kraume, T. Peters, "Entwicklungen und Perspektiven druckgetriebener Membranverfahren" *Chemie Ingenieur Technik* **2005**, 77, 473–485.
- [4] H. Strathmann, "Membrane separation processes: Current relevance and future opportunities" *AIChE Journal* **2001**, 47, 1077–1087.
- [5] D. Paul, "Polymermembranen für die Stofftrennung" *Chemie in unserer Zeit* **1998**, 32, 197–205.
- [6] R. Mahajan, R. Burns, M. Schaeffer, W. J. Koros, "Challenges in Forming Successful Mixed Matrix Membranes with Rigid Polymeric Materials" *Journal of Applied Polymer Science* **2002**, 86, 881–890.
- [7] B. Zornoza, C. Téllez, J. Coronas, "Mixed matrix membranes comprising glassy polymers and dispersed mesoporous silica spheres for gas separation" *Journal of Membrane Science* **2011**, 368, 100–109.
- [8] A. Galve, D. Sieffert, C. Staudt, M. Ferrando, C. Güell, C. Téllez, J. Coronas, "Combination of ordered mesoporous silica MCM-41 and layered titanosilicate JDF-L1 fillers for 6FDA-based copolyimide mixed matrix membranes" *Journal of Membrane Science* **2013**, 431, 163–170.
- [9] T. C. Merkel, B. D. Freeman, R. J. Spontak, Z. He, I. Pinnau, P. Meakin, A. J. Hill, "Ultraporous, reverse-selective nanocomposite membranes." *Science (New York, N.Y.)* **2002**, 296, 519–22.
- [10] C. M. Zimmerman, A. Singh, W. J. Koros, "Tailoring Mixed Matrix Composite Membranes for Gas Separations" *Journal of membrane science* **1997**, 137, 145–154.
- [11] B. Zornoza, B. Seoane, J. M. Zamara, C. Téllez, J. Coronas, "Combination of MOFs and zeolites for mixed-matrix membranes" *ChemPhysChem* **2011**, 12, 2781–2785.
- [12] H. B. T. Jeazet, C. Staudt, C. Janiak, "A method for increasing permeability in O<sub>2</sub>/N<sub>2</sub> separation with mixed-matrix membranes made of water-stable MIL-101 and polysulfone." *Chemical Communications* **2012**, 48, 2140–2.
- [13] P. Gorgojo, D. Sieffert, C. Staudt, C. Tellez, J. Coronas, "Exfoliated zeolite Nu-6(2) as filler for 6FDA-based copolyimide mixed matrix membranes" *Journal of Membrane Science* **2012**, 411–412, 146–152.
- [14] R. Mahajan, D. Q. Vu, W. J. Koros, "Mixed Matrix Membrane Materials: An Answer to the Challenges Faced by Membrane Based Gas Separations Today?" *J. Chin. Inst. Chem. Eng.* **2002**, 33, 77.
- [15] B. Smitha, D. Suhanya, S. Sridhar, M. Ramakrishna, "Separation of Organic-Organic Mixtures by Pervaporation—a Review" *Journal of membrane Science* **2004**, 241, 1–21.
- [16] T. Melin, R. Rautenbach, *Membranverfahren - Grundlagen Der Modul- Und Anlagenauslegung*, Springer, Berlin, Heidelberg, **2007**.
- [17] S. H. HAMID, M. A. ALI, "Comparative Study of Solvents for the Extraction of Aromatics from Naphtha" *Energy Sources* **1996**, 18, 65–84.

## 7 Bibliography

---

- [18] L. S. White, C. R. Wildemuth, "Aromatics Enrichment in Refinery Streams Using Hyperfiltration" *Industrial & Engineering Chemistry Research* **2006**, *45*, 9136–9143.
- [19] L. Lin, Y. Zhang, Y. Kong, "Recent advances in sulfur removal from gasoline by pervaporation" *Fuel* **2009**, *88*, 1799–1809.
- [20] L. S. White, "Development of large-scale applications in organic solvent nanofiltration and pervaporation for chemical and refining processes" *Journal of Membrane Science* **2006**, *286*, 26–35.
- [21] G. Wytze Meindersma, A. (J. G. ). Podt, A. B. de Haan, "Selection of ionic liquids for the extraction of aromatic hydrocarbons from aromatic/aliphatic mixtures" *Fuel Processing Technology* **2005**, *87*, 59–70.
- [22] J. P. Garcia Villaluenga, a. Tabe-Mohammadi, "A review on the separation of benzene/cyclohexane mixtures by pervaporation processes" *Journal of Membrane Science* **2000**, *169*, 159–174.
- [23] D. Roizard, A. Nilly, P. Lochon, "Preparation and study of crosslinked polyurethane films to fractionate toluene–n-heptane mixtures by pervaporation" *Separation and Purification Technology* **2001**, *22-23*, 45–52.
- [24] L. Aouinti, D. Roizard, G. H. Hu, F. Thomas, M. Belbachir, "Investigation of pervaporation hybrid polyvinylchloride membranes for the separation of toluene–n-heptane mixtures — case of clays as filler" *Desalination* **2009**, *241*, 174–181.
- [25] H. Ye, J. Li, Y. Lin, J. Chen, C. Chen, "PERVAPORATION SEPARATION FOR TOLUENE/n-HEPTANE MIXTURE BY POLYIMIDE MEMBRANES CONTAINING FLUORINE" *Chinese Journal of Polymer Science* **2008**, *26*, 705.
- [26] C. P. Ribeiro, B. D. Freeman, D. S. Kalika, S. Kalakkunnath, "Aromatic polyimide and polybenzoxazole membranes for the fractionation of aromatic/aliphatic hydrocarbons by pervaporation" *Journal of Membrane Science* **2012**, *390-391*, 182–193.
- [27] L. M. Robeson, "Correlation of Separation Factor Versus Permeability for Polymeric Membranes" *Journal of Membrane Science* **1991**, *62*, 165–185.
- [28] L. M. Robeson, "The Upper Bound Revisited" *Journal of Membrane Science* **2008**, *320*, 390–400.
- [29] D. Katarzynski, C. Staudt, "Permeation Properties of Different Aromatic Substances in Multicomponent Aromatic/Aliphatic Pervaporation Experiments" *Desalination* **2006**, *200*, 23–25.
- [30] D. Katarzynski, F. Pithan, C. Staudt, "Pervaporation of Multi Component Aromatic/Aliphatic Mixtures through Copolyimide Membranes" *Separation Science and Technology* **2008**, *43*, 59–70.
- [31] F. Pithan, Neuartige Copolyimidmembranen Für Die Pervaporation Zum Einsatz in Der Aromaten/Aliphaten-Trennung Und Der Prozesswasseraufbereitung, Doctoral Thesis, Universität Heidelberg, **2003**.
- [32] F. Pithan, C. Staudt-Bickel, S. Hess, R. N. Lichtenthaler, "Polymeric Membranes for Aromatic/Aliphatic Separation Processes" *ChemPhysChem* **2002**, *3*, 856–862.
- [33] J. Ren, C. Staudt-Bickel, R. N. Lichtenthaler, "Separation of Aromatics/Aliphatics with Crosslinked 6FDA-Based Copolyimides" *Separation and Purification Technology* **2001**, *22-23*, 31–43.
- [34] F. Peng, C. Hu, Z. Jiang, "Novel Poly(vinyl alcohol)/Carbon Nanotube Hybrid Membranes for Pervaporation Separation of Benzene/Cyclohexane Mixtures" *Journal of Membrane Science* **2007**, *297*, 236–242.

- [35] F. Peng, F. Pan, H. Sun, L. Lu, Z. Jiang, "Novel Nanocomposite Pervaporation Membranes Composed of Poly(vinyl alcohol) and Chitosan-Wrapped Carbon Nanotube" *Journal of Membrane Science* **2007**, *300*, 13–19.
- [36] P. Bernardo, E. Drioli, G. Golemme, "Membrane Gas Separation: A Review/State of the Art" *Industrial & Engineering Chemistry Research* **2009**, *48*, 4638–4663.
- [37] R. W. Baker, "Future Directions of Membrane Gas Separation Technology" *Industrial & Engineering Chemistry Research* **2002**, *41*, 1393–1411.
- [38] R. J. Gardner, R. A. Crane, J. F. Hannan, "Hollow Fiber Permeator For Separating Gases" *Chemical Engineering Progress* **1997**, *73*, 76–78.
- [39] Air Products, "Prism Membrane Hydrogen Recovery & Purification," can be found under <http://www.airproducts.com/products/Gases/supply-options/prism-membrane-hydrogen-recovery-and-purification.aspx>, (accessed: 04/24/2013), **2013**.
- [40] Air Liquide, "Hydrogen membrane - Refineries," can be found under <http://www.medal.airliquide.com/en/hydrogen-membrane-gas-separation/hydrogen-membrane-refineries.html>, (accessed: 04/24/2013), **2013**.
- [41] W. J. Koros, R. Mahajan, "Pushing the Limits on Possibilities for Large Scale Gas Separation: Which Strategies?" *Journal of Membrane Science* **2001**, *181*, 141–141.
- [42] K. Tanaka, M. N. Islam, M. Kido, H. Kita, K.-I. Okamoto, "Gas Permeation and Separation Properties of Sulfonated Polyimide Membranes" *Polymer* **2006**, *47*, 4370–4377.
- [43] M. Macchione, J. C. Jansen, G. De Luca, E. Tocci, M. Longeri, E. Drioli, "Experimental analysis and simulation of the gas transport in dense Hyflon® AD60X membranes: Influence of residual solvent" *Polymer* **2007**, *48*, 2619–2635.
- [44] L. G. Toy, K. Nagai, B. D. Freeman, I. Pinnau, Z. He, T. Masuda, M. Teraguchi, Y. P. Yampolskii, "Pure-Gas and Vapor Permeation and Sorption Properties of Poly[1-phenyl-2-[p-(trimethylsilyl)phenyl]acetylene] (PTMSDPA)" *Macromolecules* **2000**, *33*, 2516–2524.
- [45] I. Pinnau, L. G. Toy, "Gas and vapor transport properties of amorphous perfluorinated copolymer membranes based on 2,2-bis(trifluoromethyl)-4,5-difluoro-1,3-dioxole/tetrafluoroethylene" *Journal of Membrane Science* **1996**, *109*, 125–133.
- [46] K. Nagai, A. Higuchi, T. Nakagawa, "Gas permeability and stability of poly(1-trimethylsilyl-1-propyne-co-1-phenyl-1-propyne) membranes" *Journal of Polymer Science Part B: Polymer Physics* **1995**, *33*, 289–298.
- [47] L. Yang, J. Fang, N. Meichin, K. Tanaka, H. Kita, K. Okamoto, "Gas Permeation Properties of Thianthrene-5, 5, 10, 10-tetraoxide-containing Polyimides" *Polymer* **2001**, *42*, 2021–2029.
- [48] K. Tanaka, M. Okano, H. Toshino, H. Kita, K.-I. Okamoto, "Effect of Methyl Substituents on Permeability and Permselectivity of Gases in Polyimides Prepared from Methyl-Substituted Phenylenediamines" *Journal of Polymer Science Part B: Polymer Physics* **1992**, *30*, 907–914.
- [49] T.-S. Chung, L. Y. Jiang, Y. Li, S. Kulprathipanja, "Mixed matrix membranes (MMMs) comprising organic polymers with dispersed inorganic fillers for gas separation" *Progress in Polymer Science* **2007**, *32*, 483–507.
- [50] C. Yang, W. H. Smyrl, E. . Cussler, "Flake Alignment in Composite Coatings" *Journal of Membrane Science* **2004**, *231*, 1–12.
- [51] H.-K. Jeong, W. Krych, H. Ramanan, S. Nair, E. Marand, M. Tsapatsis, "Fabrication of Polymer/Selective-Flake Nanocomposite Membranes and Their Use in Gas Separation" *Chemistry of Materials* **2004**, *16*, 3838–3845.

## 7 Bibliography

---

- [52] S. Choi, J. Coronas, Z. Lai, D. Yust, F. Onorato, M. Tsapatsis, "Fabrication and Gas Separation Properties of Polybenzimidazole (PBI)/Nanoporous Silicates Hybrid Membranes" *Journal of Membrane Science* **2008**, *316*, 145–152.
- [53] C. Rubio, C. Casado, P. Gorgojo, F. Etayo, S. Uriel, C. Téllez, J. Coronas, "Exfoliated Titanosilicate Material UZAR-S1 Obtained from JDF-L1" *European Journal of Inorganic Chemistry* **2010**, *1*, 159 – 163.
- [54] J. Choi, M. Tsapatsis, "MCM-22/silica selective flake nanocomposite membranes for hydrogen separations" *Journal of the American Chemical Society* **2010**, *132*, 448–9.
- [55] A. Mixa, *Polymermembranen Bei Der Entfernung Organischer Schadstoffe in Der Prozesswasseraufbereitung*, Diploma Thesis, Universität Düsseldorf, **2005**.
- [56] J. G. Wijmans, R. W. Baker, "The solution-diffusion model: a review" *Journal of Membrane Science* **1995**, *107*, 1–21.
- [57] T. Graham, "On the absorption and dialytic separation of gases by colloid septa" *Philosophical Transactions of the Royal Society of London* **1866**, *156*, 399–439.
- [58] R. C. Binning, R. J. Lee, J. F. Jennings, E. C. Martin, "Separation of Liquid Mixtures by Permeation" *Industrial & Engineering Chemistry* **1961**, *53*, 45–50.
- [59] R. J. Pace, A. Datyner, "Statistical Mechanical Model for Diffusion of Simple Penetrants in Polymers. I. Theory" *Journal of Polymer Science: Polymer Physics Edition* **1979**, *17*, 437–451.
- [60] A. Fick, "On liquid diffusion" *Journal of Membrane Science* **1995**, *100*, 33–38.
- [61] J. G. Wijmans, "Letter to the Editor" *Journal of Membrane Science* **2003**, *220*, 1–3.
- [62] R. W. Baker, J. G. Wijmans, Y. Huang, "Permeability, permeance and selectivity: A preferred way of reporting pervaporation performance data" *Journal of Membrane Science* **2010**, *348*, 346–352.
- [63] E. H. Immergut, H. F. Mark, "Principles of Plasticization", in: *Plasticization and Plasticizer Processes*, AMERICAN CHEMICAL SOCIETY, **1965**, pp. 1 – 26.
- [64] N. Schmeling, R. Konietzny, D. Sieffert, P. Rölling, C. Staudt, "Functionalized copolyimide membranes for the separation of gaseous and liquid mixtures." *Beilstein journal of organic chemistry* **2010**, *6*, 789–800.
- [65] W. Caseri, "Polyimide in: Thieme Römpf Online," can be found under <http://www.roempp.com/prod/?ID=RD-16-03328>, (accessed: 11/27/2012), **2012**.
- [66] H. Dominghaus, *Die Kunststoffe Und Ihre Eigenschaften*, Springer-Verlag, Berlin Heidelberg, **2005**.
- [67] W. W. Wright, M. Hallden-Abberton, "Polyimides", in: *Ullmann's Encyclopedia of Industrial Chemistry* (Ed.: J.E. Bailey), WILEY-VCH, **2005**, pp. 39 – 58.
- [68] M. T. Bogert, R. R. Renshaw, "4-AMINO-o-PHTHALIC ACID AND SOME OF ITS DERIVATIVES" *Journal of the American Chemical Society* **1908**, *30*, 1135 – 1144.
- [69] W. M. Edwards, I. M. Robinson, *Polyimides of Pyromellitic Acid*, **1955**, U.S. Patent US2710853.
- [70] C. E. Sroog, A. L. Endrey, S. V. Abramo, C. E. Berr, W. M. Edwards, K. L. Olivier, "Aromatic Polypyromellitimides from Aromatic Polyamic Acide" *Journal of Polymer Science Part A* **1965**, *3*, 1373–1390.
- [71] A. L. Endrey, *Aromatic Polyimide Particles From Polycyclic Diamines*, **1965**, U.S. Patent US3179631.

- [72] J. de Abajo, J. G. de la Campa, "Processable Aromatic Polyimides", in: *Progress in Polyimide Chemistry I* (Ed.: H.R. Kircheldorf), Springer-Verlag, Berlin Heidelberg, **1999**, pp. 23 – 59.
- [73] I. Bettermann, C. Staudt, "Desulphurization of kerosene: Pervaporation of benzothiophene/n-dodecane mixtures" *Journal of Membrane Science* **2009**, *343*, 119–127.
- [74] D. Katarzynski, C. Staudt, "Temperature-Dependent Separation of Naphthalene/n-Decane Mixtures using 6FDA–DABA-Copolyimide Membranes" *Journal of Membrane Science* **2010**, *348*, 84–90.
- [75] S. Iijima, T. Ichihashi, "Single-shell carbon nanotubes of 1-nm diameter" *Nature* **1993**, *363*, 603–605.
- [76] D. S. Bethune, C. H. Klang, M. S. de Vries, G. Gorman, R. Savoy, J. Vazquez, R. Beyers, "Cobalt-catalysed growth of carbon nanotubes with single-atomic-layer walls" *Nature* **1993**, *363*, 605–607.
- [77] M. Monthieux, V. L. Kuznetsov, "Who should be given the credit for the discovery of carbon nanotubes?" *Carbon* **2006**, *44*, 1621–1623.
- [78] D. M. Guldi, N. Martín, *Carbon Nanotubes and Related Structures*, Wiley-VCH Verlag GmbH & Co. KGaA, Weinheim, **2010**.
- [79] O. Hampe, "Kohlenstoff-Nanoröhren in: Thieme Römpf Online," can be found under <http://www.roempp.com/prod/?ID=RD-11-02803>, (accessed: 11/30/2012), **2012**.
- [80] X. Zhao, Y. Liu, T. Suzuki, R. O. Jones, Y. Ando, "Smallest Carbon Nanotube Is 3 Å in Diameter" *Physical review letters* **2004**, *92*, 125501–125502.
- [81] X. Wang, Q. Li, J. Xie, Z. Jin, J. Wang, Y. Li, K. Jiang, S. Fan, "Fabrication of Ultralong and Electrically Uniform Single-Walled Carbon Nanotubes on Clean Substrates" *Nano letters* **2009**, *9*, 3137–41.
- [82] M.-F. Yu, O. Lourie, M. J. Dyer, K. Moloni, T. F. Kelly, R. S. Ruoff, "Strength and Breaking Mechanism of Multiwalled Carbon Nanotubes Under Tensile Load" *Science* **2000**, *287*, 637–640.
- [83] P. Kim, L. Shi, A. Majumdar, P. McEuen, "Thermal Transport Measurements of Individual Multiwalled Nanotubes" *Physical Review Letters* **2001**, *87*, 2–5.
- [84] W. Krätschmer, L. D. Lamb, K. Fostiropoulos, D. R. Huffman, "Solid C<sub>60</sub>: a new form of carbon" *Nature* **1990**, *347*, 354–358.
- [85] M. Terrones, "SCIENCE AND TECHNOLOGY OF THE TWENTY-FIRST CENTURY: Synthesis, Properties, and Applications of Carbon Nanotubes" *Annual Review of Materials Research* **2003**, *33*, 419–501.
- [86] C. Journet, W. K. Maser, P. Bernier, A. Loiseau, M. Lamy de la Chapelle, S. Lefrant, P. Deniard, R. Lee, J. E. Fischer, "Large-scale production of single-walled carbon nanotubes by the electric-arc technique" *Nature* **1997**, *388*, 756–758.
- [87] H. W. Kroto, J. R. Heath, S. C. O'Brien, R. F. Curl, R. E. Smalley, "C<sub>60</sub>: Buckminsterfullerene" *Nature* **1985**, *318*, 162–163.
- [88] A. Thess, R. Lee, P. Nikolaev, H. Dai, P. Petit, J. Robert, C. Xu, Y. H. Lee, S. G. Kim, A. G. Rinzler, et al., "Crystalline Ropes of Metallic Carbon Nanotubes" *Science* **1996**, *273*, 483–487.
- [89] P. Nikolaev, M. J. Bronikowski, R. K. Bradley, F. Rohmund, D. T. Colbert, K. A. Smith, R. E. Smalley, "Gas-phase catalytic growth of single-walled carbon nanotubes from carbon monoxide" *Chemical Physics Letters* **1999**, *313*, 91–97.

## 7 Bibliography

---

- [90] J.-M. Bonard, T. Stora, J.-P. Salvetat, F. Maier, T. Stöckli, C. Duschl, L. Forró, W. A. de Heer, A. Châtelain, "Purification and size-selection of carbon nanotubes" *Advanced Materials* **1997**, *9*, 827–831.
- [91] D. A. Heller, R. M. Mayrhofer, S. Baik, Y. V. Grinkova, M. L. Usrey, M. S. Strano, "Concomitant length and diameter separation of single-walled carbon nanotubes." *Journal of the American Chemical Society* **2004**, *126*, 14567–14573.
- [92] M. S. Arnold, S. I. Stupp, M. C. Hersam, "Enrichment of single-walled carbon nanotubes by diameter in density gradients." *Nano letters* **2005**, *5*, 713–718.
- [93] R. Krupke, F. Hennrich, H. v. Löhneysen, M. M. Kappes, "Separation of metallic from semiconducting single-walled carbon nanotubes." *Science (New York, N.Y.)* **2003**, *301*, 344–347.
- [94] E. Dujardin, T. W. Ebbesen, A. Krishnan, M. M. J. Treacy, "Purification of Single-Shell Nanotubes" *Advanced Materials* **1998**, *10*, 611–613.
- [95] A. Hirsch, "Functionalization of Single-Walled Carbon Nanotubes" *Angewandte Chemie International Edition* **2002**, *41*, 1853–1859.
- [96] S. Banerjee, T. Hemraj-Benny, S. S. Wong, "Covalent Surface Chemistry of Single-Walled Carbon Nanotubes" *Advanced Materials* **2005**, *17*, 17–29.
- [97] S. Niyogi, M. A. Hamon, H. Hu, B. Zhao, P. Bhowmik, R. Sen, M. E. Itkis, R. C. Haddon, "Chemistry of Single-Walled Carbon Nanotubes" *Accounts of Chemical Research* **2002**, *35*, 1105–1113.
- [98] J. Coronas, "Zeolites and Porous-tailored Materials" - *Lecture in the Course of the PhD.net Workshop "Frontiers of Nanocomposite Materials"*, Düsseldorf, **2008**.
- [99] S. M. Kuznicki, V. A. Bell, S. Nair, H. W. Hillhouse, R. M. Jacubinas, C. M. Braunbarth, B. H. Toby, M. Tsapatsis, "A titanosilicate molecular sieve with adjustable pores for size-selective adsorption of molecules." *Nature* **2001**, *412*, 720–4.
- [100] S. M. Kuznicki, *LARGE-PORED CRYSTALLINE TITANIUM MOLECULAR SIEVE ZEOLITES*, **1989**, U.S. Patent 4,853,202.
- [101] J. Rocha, P. Brandão, Z. Lin, A. P. Esculcas, A. Ferreira, M. W. Anderson, "Synthesis and Structural Studies of Microporous Titanium–Niobium–Silicates with the Structure of Nenadkevichite" *The Journal of Physical Chemistry* **1996**, *100*, 14978–14983.
- [102] Z. Lin, J. Rocha, P. Brandão, A. Ferreira, A. P. Esculcas, J. D. P. de Jesus, A. Philippou, M. W. Anderson, "Synthesis and Structural Characterization of Microporous Umbite, Penkvilksite, and Other Titanosilicates" *The Journal of Physical Chemistry B* **1997**, *101*, 7114–7120.
- [103] J. Rocha, M. W. Anderson, "Microporous Titanosilicates and other Novel Mixed Octahedral-Tetrahedral Framework Oxides" *European Journal of Inorganic Chemistry* **2000**, *2000*, 801–818.
- [104] C. Lamberti, "Electron-hole reduced effective mass in monoatomic ...–O–Ti–O–Ti–O–... quantum wires embedded in the siliceous crystalline matrix of ETS-10" *Microporous and Mesoporous Materials* **1999**, *30*, 155–163.
- [105] J. Rocha, Z. Lin, "Microporous Mixed Octahedral-Pentahedral-Tetrahedral Framework Silicates" *Reviews in Mineralogy and Geochemistry* **2005**, *57*, 173–201.
- [106] S. Ferdov, U. Kolitsch, C. Lengauer, E. Tillmanns, Z. Lin, R. a. Sá Ferreira, "Refinement of the layered titanosilicate AM-1 from single-crystal X-ray diffraction data" *Acta Crystallographica Section E Structure Reports Online* **2007**, *63*, i186–i186.

- [107] C. Rubio, C. Casado, S. Uriel, C. Téllez, J. Coronas, "Seeded Synthesis of Layered Titanosilicate JDF-L1" *Materials Letters* **2009**, *63*, 113–115.
- [108] A. Galve, D. Sieffert, E. Vispe, C. Téllez, J. Coronas, C. Staudt, "Copolyimide mixed matrix membranes with oriented microporous titanosilicate JDF-L1 sheet particles" *Journal of Membrane Science* **2011**, *370*, 131–140.
- [109] D. R. Paul, L. M. Robeson, "Polymer Nanotechnology: Nanocomposites" *Polymer* **2008**, *49*, 3187–3204.
- [110] R. A. Vaia, J. F. Maguire, "Polymer Nanocomposites with Prescribed Morphology: Going beyond Nanoparticle-Filled Polymers" *Chemistry of Materials* **2007**, *19*, 2736–2751.
- [111] F. Hussain, M. Hojjati, M. Okamoto, R. E. Gorga, "Review article: Polymer-matrix Nanocomposites, Processing, Manufacturing, and Application: An Overview" *Journal of Composite Materials* **2006**, *40*, 1511–1575.
- [112] A. Usuki, Y. Kojima, M. Kawasumi, A. Okada, Y. Fukushima, T. Kurauchi, O. Kamigaito, "Synthesis of nylon 6-clay hybrid" *Journal of Materials Research* **1993**, *8*, 1179–1184.
- [113] A. Usuki, M. Kawasumi, Y. Kojima, A. Okada, T. Kurauchi, O. Kamigaito, "Swelling behavior of montmorillonite cation exchanged for  $\omega$ -amino acids by  $\epsilon$ -caprolactam" *Journal of Materials Research* **1993**, *8*, 1174–1178.
- [114] E. T. Thostenson, C. Li, T.-W. Chou, "Nanocomposites in context" *Composites Science and Technology* **2005**, *65*, 491–516.
- [115] G. Schmidt, M. M. Malwitz, "Properties of Polymer–Nanoparticle Composites" *Current Opinion in Colloid and Interface Science* **2003**, *8*, 103–108.
- [116] D. W. Schaefer, R. S. Justice, "How Nano Are Nanocomposites?" *Macromolecules* **2007**, *40*, 8501–8517.
- [117] G. Kickelbick, "Introduction to Hybrid Materials", in: *Hybrid Materials. Synthesis, Characterization, and Applications*, Wiley-VCH Verlag GmbH & Co. KGaA, Weinheim, **2007**, pp. 1–48.
- [118] S. A. Hashemifard, A. F. Ismail, T. Matsuura, "Prediction of Gas Permeability in Mixed Matrix Membranes using Theoretical Models" *Journal of Membrane Science* **2010**, *347*, 53–61.
- [119] J. Gascon, F. Kapteijn, B. Zornoza, V. Sebastián, C. Casado, J. Coronas, "Practical Approach to Zeolitic Membranes and Coatings: State of the Art, Opportunities, Barriers, and Future Perspectives" *Chemistry of Materials* **2012**, *24*, 2829–2844.
- [120] E. Cussler, "Membranes containing selective flakes" *Journal of Membrane Science* **1990**, *52*, 275–288.
- [121] J. A. Sheffel, M. Tsapatsis, "A model for the performance of microporous mixed matrix membranes with oriented selective flakes" *Journal of Membrane Science* **2007**, *295*, 50–70.
- [122] T. Bein, K. Brown, G. C. Frye, C. J. Brinker, "Molecular Sieve Sensors for Selective Detection at the Nanogram Level" *Journal of the American Chemical Society* **1989**, *111*, 7640–7641.
- [123] C. Rubio, Síntesis y Aplicación De Titanosilicatos y Estañosilicatos Laminares y Deslaminados, Doctoral Thesis, University of Zaragoza, **2012**.
- [124] I. Bettermann, Entschwefelung Von Kerosin: Untersuchungen Zur Permeation Mehrkerniger, Schwefelhaltiger Aromaten, Doctoral Thesis, University of Düsseldorf, **2009**.
- [125] D. Katarzynski, Pervaporation Komplexer Aromaten Am Beispiel Von Naphthalin/n-Decan-Mischungen, Doctoral Thesis, Universität Düsseldorf, **2008**.

## 7 Bibliography

---

- [126] P. Rölling, Untersuchungen Zu Hydrophilen Membranmaterialien Und Elektrophilen Scavengern Im Industriellen Einsatz, Doctoral Thesis, University of Düsseldorf, **2010**.
- [127] J. Rausch, R.-C. Zhuang, E. Mäder, "Surfactant assisted dispersion of functionalized multi-walled carbon nanotubes in aqueous media" *Composites Part A: Applied Science and Manufacturing* **2010**, *41*, 1038–1046.
- [128] A. Galve Guinea, Estudio Estructural De Materiales Laminares y Su Aplicación En Membranas Mixtas Material Laminar-Polímero, Doctoral Thesis, University of Zaragoza, **2012**.
- [129] M. Lamers, Steuerung Der Trenneigenschaften Polymerer Membranen Durch Supramolekulare Komplexbildung Mit Cyclodextrinen, Doctoral Thesis, University of Düsseldorf, **2007**.
- [130] N. Schmeling, Synthese Und Charakterisierung Von Ionisch Und Photochemisch Vernetzbaren Polymermaterialien, Doctoral Thesis, University of Düsseldorf, **2012**.
- [131] R. D. Shannon, "Revised effective ionic radii and systematic studies of interatomic distances in halides and chalcogenides" *Acta Crystallographica Section A* **1976**, *32*, 751–767.
- [132] A. Volkov, S. Paula, D. Deamer, "Two mechanisms of permeation of small neutral molecules and hydrated ions across phospholipid bilayers" *Bioelectrochemistry and Bioenergetics* **1997**, *42*, 153–160.
- [133] M. Shigeta, M. Komatsu, N. Nakashima, "Individual Solubilization of Single-Walled Carbon Nanotubes Using Totally Aromatic Polyimide" *Chemical Physics Letters* **2006**, *418*, 115–118.
- [134] S. Castarlenas, P. Gorgojo, C. Casado-Coterillo, S. Masheshwari, M. Tsapatsis, C. Téllez, J. Coronas, "Melt Compounding of Swollen Titanosilicate JDF-L1 with Polysulfone To Obtain Mixed Matrix Membranes for H<sub>2</sub>/CH<sub>4</sub> Separation" *Industrial & Engineering Chemistry Research* **2013**, *52*, 1901–1907.

# 8 List of figures and tables

## 8.1 List of figures

<i>Figure 2.1: Life-cycle curve for several membrane processes displaying the sale as a function of the development state of a process</i> <sup>based on [3,4]</sup> .....	9
<i>Figure 2.2: Schematic of the permeation of a binary mixture through a porous (left) and a solution diffusion membrane (right)</i> <sup>based on [5]</sup> . The transmembrane flux through a porous membrane is described as a function of pressure $p$ and pore diameter $d$ . The permeability $P$ of a solution diffusion membrane depends on solubility $S$ and diffusivity $D$ of the feed components.....	11
<i>Figure 2.3: Presentation of different separation characteristics for the pervaporation of toluene/<i>n</i>-heptane mixtures with 20 - 50 wt.-% aromatic content at 80°C in the style of an upper bound diagram. Membrane data sources are as follows: polyurethanes (star) by Roizard et al.<sup>[23]</sup>, PVC membranes (triangle) by Aouinti et al.<sup>[24]</sup>, fluorinated polyimides (square) by Ye et al.<sup>[25]</sup> and aromatic polyimides by Ribeiro et al.<sup>[26]</sup> .....</i>	13
<i>Figure 2.4: Structures and monomers comprising polymers with outstanding hydrogen/methane separation characteristics. ....</i>	15
<i>Figure 2.5: Diagram showing the Robeson upper bound correlation for the membrane based separation of hydrogen and methane<sup>[28]</sup>. A selection of membrane materials close or above the upper bound is shown<sup>[42-48]</sup> .....</i>	16
<i>Figure 2.6: Scheme of the desired nanocomposite membranes comprised of the copolyimide 6FDA-4MPD/6FDA-DABA 4:1 and functionalized MWCNTs.....</i>	19
<i>Figure 2.7: Schematic of permeation paths through mixed matrix membranes for gas molecules smaller (hydrogen) and larger (methane) than the pore size of the filler. On the left the MMM contains an agglomerated filler while on the right nanosheets are used which extend the permeation path of the larger gas molecules. ....</i>	19
<i>Figure 3.1: Schematic illustration of a membrane separation process for a mixture composed of a higher permeable component (blue spheres) and a lower permeable one (yellow spheres)</i> <sup>based on [55]</sup> . 21	21
<i>Figure 3.2: Schematic of the mass streams and states of matter in gas separation and pervaporation. The rectangular box is commonly used to depict a membrane module with separated feed and permeate side. The diagonal line represents the membrane.....</i>	22
<i>Figure 3.3: Depiction of the permeation across a membrane according to the three underlying steps of the solution-diffusion model.....</i>	23
<i>Figure 3.4: Schematic of the plasticization of a polymer with and without cross-linking.</i> <sup>Based on [64]</sup> ..... 27	27
<i>Figure 3.5: Chemical structures of linear and cyclic polyimides. In the linear structure the imide group is exemplarily highlighted in red.....</i>	28
<i>Figure 3.6: Structures of the commercial polyimides Kapton and P84.....</i>	29

## 8.1 List of figures

---

Figure 3.7: Two step synthesis for aromatic polyimides. The rests X and Y represent aromatic groups. ....	29
Figure 3.8: Structure of the copolyimide 6FDA-4MPD/6FDA-DABA 4:1. ....	30
Figure 3.9: Structures of single and multi walled carbon nanotubes. The ends of CNTs can either be open or closed with end caps. ....	31
Figure 3.10: Theoretic construction and structure of the CNTs (10,0), (7,3) and (5,5) as examples of the three possible CNT structures. Also the electronic properties of the tubes are related to the direction of $C_h$ . ....	31
Figure 3.11: Schematics of the three major synthesis methods for the production of CNTs. ....	32
Figure 3.12: Overview of different functionalization methods for CNTs <sup>based on [95]</sup> . ....	34
Figure 3.13: Bond strain in CNTs is caused by pyramidalization (measured by the pyramidalization angle $\theta_p$ ) and $\pi$ - $\pi$ misalignment due to C-C bond torsion ( $\phi$ ) <sup>based on [97]</sup> . ....	34
Figure 3.14: Overview of CNT defects: A) five- or seven-membered rings cause tube bending and lead to strained bonds. B) At the site of $sp^3$ -hybridized defects a residue R is present ( $R = H, OH$ ). C) Oxidative conditions can damage the framework leaving a hole framed with carboxylic acid groups. D) Open end of the tube is terminated by COOH-groups due to oxidative treatment <sup>based on [95]</sup> . ....	35
Figure 3.15: Structure of the layered titanosilicate JDF-L1 (AM-1). ....	36
Figure 3.16: Schematic of the disaggregation process for JDF-L1. Using tertiary amines it is possible to separate the individual sheet shaped crystals from the agglomerates obtained during synthesis. ....	37
Figure 3.17: Influence of particle geometry on the surface to volume ratio for different shaped materials used for nanocomposites <sup>based on [114]</sup> . ....	38
Figure 3.18: Overview of the four types of hybrid materials <sup>based on [117]</sup> . ....	39
Figure 4.1: Ideal structure of the copolyimide 6FDA-4MPD/6FDA-DABA 4:1 with the proton sites numbered. ....	46
Figure 4.2: Evaluated 500 MHz $^1H$ -NMR spectrum of batch SPI 25 of the copolyimide 6FDA-4MPD/6FDA-DABA 4:1. ....	47
Figure 4.3: Graphic determination of the glass transition temperature from raw DSC data. A) Individual segment showing glass transition effect around 420 °C. B) Experimental data are fitted in the range of glass transition effect. C) Second derivative of fit function is drawn. D) $T_g$ is found at zero of second derivative. ....	49
Figure 4.4: Schematic illustration of the custom-made sample holder for electron microscopy of membrane cross-sections. ....	52
Figure 4.5: Overview of the base plate of the pervaporation device showing the mounting of the glass parts, o-ring fittings and the membrane placement. ....	54
Figure 4.6: Connection diagram (left) and photograph (right) of the pervaporation device used in this work. ....	55
Figure 4.7: Calibration data used for the calculation of toluene content via refractive index measurement at 20 °C. ....	57
Figure 4.8: Schematic of the gas separation device used in this work. ....	58

Figure 5.1: Elution profiles of copolyimide batches with different molecular weights [g/mol] prepared in this work. The bimodal graphs can be divided into three basic shapes depending on the height of  $M_w$ . For clarity reasons only a selection of the prepared copolyimide batches is presented in these graphs..... 62

Figure 5.2: Glass transition temperatures plotted against the corresponding molecular weight averages of copolyimide batches prepared in this work. The diagram shows no relatable relationship between the two parameters..... 62

Figure 5.3: Actual ratio of diamines 4MPD/DABA versus weight average molecular mass  $M_w$ ..... 63

Figure 5.4: Tests regarding the agglomeration stability of MWCNT dispersions in water. .... 65

Figure 5.5: In strong acidic or basic medium the nanotubes in a dispersion of MWCNT-OH B agglomerate quickly..... 65

Figure 5.6: IR-spectra of potassium bromide pellets containing functionalized and unfunctionalized MWCNT samples. Stretching vibration of C=O is expected in the red highlighted area. .... 66

Figure 5.7: Thermogravimetric analyses of pure MWCNTs as well as COOH- and OH- functionalized samples in nitrogen atmosphere..... 67

Figure 5.8: Overview of results from elementary analyses of functionalized and pure MWCNT samples. .... 68

Figure 5.9: TEM images of MWCNT samples showing the morphology of nanotubes. .... 69

Figure 5.10: SEM images of MWCNT samples showing the morphology of nanotube agglomerates.. 69

Figure 5.11: SEM images of as-synthesized and disaggregated samples of JDF-L1..... 70

Figure 5.12: Comparison of XRD spectra of as-synthesized and disaggregated JDF-L1..... 71

Figure 5.13: SEM images of ion-exchanged JDF-L1 samples..... 72

Figure 5.14: XRD spectra of disaggregated JDF-L1 and sample where  $Na^+$  was exchanged with  $H^+$ . Spectra were collected with synchrotron radiation ( $\lambda=0.82637 \text{ \AA}$ ) then adjusted to fit to  $Cu K\alpha 1$  ( $\lambda=1.54059 \text{ \AA}$ ) as used for all other XRD-spectra..... 72

Figure 5.15: Comparison of XRD spectra of disaggregated JDF-L1 and subsequently ion exchanged titanosilicates. .... 73

Figure 5.16: Comparison of the XRD spectra of disaggregated JDF-L1 and the ion exchanged samples (Li)-JDF-L1 24h and (H)-JDF-L1..... 74

Figure 5.17: Results of elementary analyses via EDX and XRF for ion exchanged samples of JDF-L1... 75

Figure 5.18: Comparison of XRD spectra of (Mg)-JDF-L1 batches with disaggregated JDF-L1. .... 76

Figure 5.19: SEM images of JDF-L1 samples that underwent basic treatment in one molar solutions of different bases..... 77

Figure 5.20: EDX and XRF data of JDF-L1 samples treated with one molar solution of lithium and potassium hydroxide. .... 78

Figure 5.21: Overview of methods 1-3 for the preparation of MWCNT/copolyimide nanocomposites.79

Figure 5.22: Photos of membranes prepared according to methods 1-3 exhibit a stained transparent/black structure. .... 79

## 8.1 List of figures

---

- Figure 5.23: Addition of *p*-toluenesulfonic acid reduces the stability of nanotube dispersion. The mixtures consist of a solution of the copolyimide (8 wt.-%) in tetrahydrofuran and 1 wt.-% of MWCNT-OH (regarding the polymer amount). Sonication was conducted at 20 % amplitude (15-20 W) for 5 min. .... 80
- Figure 5.24: Preparation conditions of method 4 and photos of membranes produced using this method. DMAc was used as solvent in the case of MemCNT 40 while THF was used for MemCNT 36.81
- Figure 5.25: Schematic of the final preparation instruction (method 5) and photo of a membrane obtained by preparing the nanocomposite mixture according to this method. .... 82
- Figure 5.26: Results of TGA analyses of pure copolyimide membranes and MWCNT/copolyimide nanocomposites in air and nitrogen atmosphere. Membranes analyzed were Mem SPI 11 – 003, MemCNT 48 (1 wt.-% MWCNT-OH) and MemCNT 50 (3.5 wt.-% MWCNT-OH). .... 82
- Figure 5.27: Results for pervaporation experiments in different toluene/cyclohexane mixtures with membranes prepared from the copolyimide 6FDA-4MPD/6FDA-DABA 4:1 (black symbols) and copolyimide/MWCNT nanocomposites containing 1 wt.-% MWCNT-OH (grey symbols). Experiments were conducted at a temperature of 60 °C and a permeate pressure of 25 mbar. .... 84
- Figure 5.28: Results for pervaporation experiments in different toluene/cyclohexane mixtures with nanocomposite membranes prepared from 6FDA-4MPD/6FDA-DABA 4:1 and MWCNT-OH containing 1 wt.-% (grey symbols) and 3.5 wt.-% respectively (white symbols) of nanotubes. Experiments were conducted at a temperature of 60 °C and a permeate pressure of 25 mbar. .... 85
- Figure 5.29: Results for temperature-dependent pervaporation experiments in 50:50 wt.-% toluene/cyclohexane mixture with a pure copolyimide membrane (black symbols) and nanocomposites containing 1 wt.-% MWCNT-OH (grey symbols). Experiments were conducted at a temperatures between 60 – 90 °C and using a permeate pressure of 25 mbar. .... 86
- Figure 5.30: The activation energies for the permeation of the feed components are calculated using the exponential factors obtained from the fitted functions in the plot of partial fluxes vs. reciprocal temperatures. Results for pure polymer membranes (white half-filled symbols) and nanocomposites containing 1 wt.-% MWCNT-OH (grey half-filled symbols) are presented. .... 87
- Figure 5.31: Overview of pervaporation data in the form of an upper-bond diagram for experiments with 50:50 wt.-% aromatic/alicyclic mixtures and different membranes based on the copolyimide 6FDA-4MPD/ 6FDA-DABA 4:1. All membranes were pretreated at room temperature in pure toluene for 24 h. White symbols: data by Ren<sup>[33]</sup> for benzene/cyclohexane mixtures ( $T = 60\text{ °C}$ ;  $p_{\text{permeate}} = 15\text{ mbar}$ ). Black symbols: data by Pithan<sup>[31]</sup> for toluene/cyclohexane mixtures ( $T = 60\text{ °C}$ ;  $p_{\text{permeate}} = 25\text{ mbar}$ ). Grey/half-gray symbols: data obtained within this work for toluene/cyclohexane mixtures ( $T = 60\text{ °C}$ ;  $p_{\text{permeate}} = 25\text{ mbar}$ ). .... 89
- Figure 5.32: Thermogravimetric analyses of pure copolyimide membrane as well as membranes containing 5, 8 and 10 wt.-% of disaggregated JDF-L1. MMMs were prepared from a 10 wt.-% polymer solution. .... 91
- Figure 5.33: SEM image showing the cross-section of a MMM containing 8 wt.-% disaggregated JDF-L1 prepared from a 10 wt.-% polymer solution. The overview presented here is composed of nine consecutive SEM images and covers a distance of ca. 350  $\mu\text{m}$  of the membrane cross-section. .... 92
- Figure 5.34: Detail of image #3 from the series of consecutive SEM images as seen in figure 5.33. The image shows preferentially horizontal orientation of JDF-L1 sheets. .... 92

<i>Figure 5.35: MMMs containing different amounts of JDF-L1 were examined with a polarized light microscope. Membranes are cast from copolyimide solutions of 10 wt.-% (upper row) and 13 wt.-% (lower row) in tetrahydrofuran. ....</i>	93
<i>Figure 5.36: Comparison of XRD spectra of a pure copolyimide membrane, a MMM containing 5 wt% disaggregated JDF-L1 cast from a 13 wt.-% polymer solution and disaggregated JDF-L1. ....</i>	94
<i>Figure 5.37: XRD patterns of MMMs containing different loads of disaggregated JDF-L1. Membranes on the left were cast from 10 wt.-% polymer solutions while membranes shown on the right were cast from 13 wt.-% polymer solutions. ....</i>	95
<i>Figure 5.38: Angle dependant X-ray diffraction of MMMs cast from 10 and 13 wt.-% polymer solutions containing 8 wt.-% disaggregated JDF-L1. The intensity of the peak at <math>2\theta = 8.25^\circ</math>, which is related to the [001] direction, was measured at different tilt angles of the sample holder.....</i>	96
<i>Figure 5.39: Raman spectrum of the copolyimide 6FDA-4MPD/6FDA-DABA 4:1. ....</i>	96
<i>Figure 5.40: Raman spectra of MMMs containing 5, 8 and 13 wt.-% JDF-L1 and cast from 10 respectively 13 wt.-% polymer solutions. ....</i>	97
<i>Figure 5.41: Results of <math>H_2/CH_4</math> separation experiments with MMMs cast from a 10 wt.-% (left) and 13 wt.-% (right) copolyimide solutions. ....</i>	99
<i>Figure 5.42: Results of <math>O_2/N_2</math> separation experiments with MMMs cast from a 10 wt.-% (left) and 13 wt.-% (right) copolyimide solutions. ....</i>	100
<i>Figure 5.43: Results of gas separation experiments with copolyimide membranes and MMMs cast from a 10 wt. % copolyimide solutions containing 8 wt.-% of either as-synthesized (blue squares) or disaggregated JDF-L1 (grey diamonds). For comparison pure polymer data is presented too (black spheres). ....</i>	101
<i>Figure 5.44: Results of gas separation experiments with non cross-linked and ethylene glycol cross-linked MMMs containing 5 wt.-% (white symbols) and 10 wt.-% disaggregated JDF-L1 respectively (grey symbols). Also the data of pure copolyimide membranes is shown for comparison (black spheres). ....</i>	102
<i>Figure 5.45: Results of <math>H_2/CH_4</math> gas separation experiments with MMMs containing 8 wt.-% of different ion exchanged samples of JDF-L1 (grey symbols). For comparison also results of pure copolyimide membranes (white squares) and MMMs containing 8 wt.-% disaggregated JDF-L1 (black spheres) are shown. ....</i>	103
<i>Figure 5.46: Results of <math>O_2/N_2</math> gas separation experiments with MMMs containing 8 wt.-% of different ion exchanged samples of JDF-L1 (grey symbols). For comparison also results of pure copolyimide membranes (white squares) and MMMs containing 8 wt.-% disaggregated JDF-L1 (black spheres) are shown. ....</i>	104
<i>Figure 5.47: Upper bound diagram for the gas mixture <math>H_2/CH_4</math> presenting the results of gas separation experiments conducted in this work.....</i>	106
<i>Figure 5.48: Upper bound diagram for the gas mixture <math>O_2/N_2</math> presenting the results of gas separation experiments conducted in this work.....</i>	107

## 8.2 List of tables

---

### 8.2 List of tables

<i>Table 2.1: Most commonly used materials for membrane fabrication<sup>[5]</sup> .....</i>	<i>10</i>
<i>Table 4.1: Details on used monomers and their purification methods .....</i>	<i>41</i>
<i>Table 4.2: List of temperature settings in order to obtain different feed temperatures (all values <math>\pm 0.1</math> °C). .....</i>	<i>56</i>
<i>Table 5.1: Overview of film formation behavior, color and <math>M_w</math> of the copolyimide batches prepared in this work. Green highlighted values of <math>M_w</math> indicate a bend- and foldable polymer film while a red accentuation represents batches that provide only brittle films.....</i>	<i>64</i>
<i>Table 5.2: Conditions of ion exchange procedures and ionic radii (in crystal and hydrated form) of the according cations. ....</i>	<i>75</i>
<i>Table 5.3: Data obtained from the exponential fit curves in figure 5.30. ....</i>	<i>87</i>
<i>Table 5.4: Activation energies for the permeation of toluene and cyclohexane through membranes of the copolyimide 6FDA-4MPD/6FDA-DABA 4:1 and nanocomposites of the same polymer containing 1 wt.-% MWCNT-OH.....</i>	<i>88</i>
<i>Table 5.5: Results of stress-strain measurements with samples of pure polymer membranes and MMMs with different filler content cast from 10 wt.-% and 13 wt.-% polymer solution. ....</i>	<i>98</i>
<i>Table 5.6: Kinetic diameters of the gases used in gas separation experiments.....</i>	<i>98</i>
<i>Table 5.7: Ionic radii in crystal<sup>[131]</sup> and hydrated ionic radii<sup>[132]</sup> for the cations used in this work as interlamellar ions for charge equalization in JDF-L1.....</i>	<i>105</i>
<i>Table 6.1: Tabular overview of the characterization data of all copolyimide batches used in this work. ....</i>	<i>116</i>